UNIVERSITÉ DE STRASBOURG

École doctorale
Physique, chimie-physique
ED 182
Université de Strasbourg

ÉCOLE DOCTORALE ED182 – Physique et Chimie-Physique
UMR 7178

THÈSE présentée par :

Emma MONPRIBAT

soutenue le : **30 septembre 2024**

pour obtenir le grade de : **Docteure de l'Université de Strasbourg**
Discipline/ Spécialité : Physique Subatomique

Contribution of the subcoulomb fusion reaction to the stellar evolution and nucleosynthesis

THÈSE dirigée par :

Mme COURTIN Sandrine	Professeure, Université de Strasbourg

RAPPORTEURS :

M GORIELY Stéphane	Chercheur qualifié, F.R.S - FNRS
Mme REDON Nadine	Directrice de recherches, CNRS

AUTRES MEMBRES DU JURY :

Mme LANCON Ariane	Professeure, Université de Strasbourg

À J., A. et B., étoiles les plus brillantes de mon ciel

Contents

Contents v

List of Figures vii

List of Tables xiii

List of Publications and Communications xv

Introduction 1

1 Nuclear reactions and their astrophysical importance 5
- 1.1 Astrophysical context . . . 6
  - 1.1.1 Nucleosynthesis . . . 6
  - 1.1.2 Stellar evolution . . . 7
  - 1.1.3 Burning phases . . . 12
- 1.2 Importance of Nuclear Physics . . . 24
  - 1.2.1 Reaction rates . . . 24
  - 1.2.2 Deep sub-barrier cross section . . . 27
  - 1.2.3 Impact on astrophysical scenarios . . . 38
- 1.3 Résumé du chapitre . . . 43
  - 1.3.1 Contexte astrophysique . . . 43
  - 1.3.2 Importance de la physique nucléaire . . . 45

2 Carbon fusion measurement 49
- 2.1 $^{12}C + ^{12}C$ fusion reaction . . . 51
  - 2.1.1 Exit channels . . . 51
  - 2.1.2 State of the art . . . 53
- 2.2 Detection methods . . . 55
  - 2.2.1 Distinct measurement . . . 55
  - 2.2.2 Coincidence method . . . 59
- 2.3 The STELLA experiment . . . 60
  - 2.3.1 Reaction chamber . . . 61
  - 2.3.2 Carbon targets . . . 63
  - 2.3.3 Charged particle detectors . . . 65
  - 2.3.4 Gamma-ray detectors: UK-FATIMA collaboration . . . 72
  - 2.3.5 Vacuum system . . . 74

2.3.6 Acquisition systems and synchronization 77
2.3.7 Andromede facility 82
2.4 Résumé du chapitre 83
2.4.1 La réaction de fusion ^{12}C + ^{12}C 84
2.4.2 Méthodes de détection 84
2.4.3 L'expérience STELLA 85

3 The ^{12}C + ^{12}C fusion reaction cross section with the STELLA project 89
3.1 Data analysis 90
3.1.1 Calibration 90
3.1.2 Charge sharing 93
3.1.3 Angular distribution 98
3.2 Data normalization 99
3.2.1 Current integrator 100
3.2.2 Target thickness 102
3.2.3 Systematic uncertainties 102
3.3 Determination of the total fusion cross section at $E_{\mathrm{rel}} = 4.76$ MeV . . . 103
3.3.1 Event selection 103
3.3.2 Angular distribution 105
3.3.3 Total cross section 105
3.4 Résumé du chapitre 113
3.4.1 Analyse des données 113
3.4.2 Normalisation des données 114
3.4.3 Détermination de la section efficace totale à $E_{\mathrm{rel}} = 4.76$ MeV . . 115

4 New reaction rates and their impact on stellar evolution 117
4.1 Determination of ^{12}C + ^{12}C nuclear reaction rates 118
4.1.1 Fusion excitation response function 118
4.1.2 STELLA sensitivity 121
4.1.3 Reaction rate 125
4.2 Impact on stellar evolution 130
4.2.1 Impact on global stellar evolution 130
4.2.2 Impact on detailed nucleosynthesis 139
4.3 Résumé du chapitre 145
4.3.1 Détermination des taux de réactions pour ^{12}C + ^{12}C 145
4.3.2 Impacts sur l'évolution stellaire 146

Conclusion 149

List of Figures

1.1 Periodic table color coded to sugest the nuclear origin of all elements. Credit: NASA/CXC/K. Divona; Reference: SDSS blog, J. Johnson. From [1] . . . 7

1.2 Structure of a 25 $M_\odot$ star of solar metallicity, shortly before core collapse. Only the main constituents in each layer are shown. Minor constituents are set in thin rectangle. Weak s-process component is set in thick rectangle. Subscripts C and S stand for core and shell burning, respectively. The diagonally arranged numbers indicate the interior mass for each burning shell. From [2]. . . . 8

1.3 Kippenhan diagrams for non-rotating 25 (top) and 40 (bottom) $M_\odot$ models. The black zones corresponds to convective regions. From [3]. . . 10

1.4 Stellar evolution of low-mass (left cycle) and high-mass (right cycle) stars. From [4]. . . . 11

1.5 Hertzprung-Russel diagram with the temperatures of stars against their luminosity. The position of a star in the diagram provides information about its present stage and its mass. Credit: ESO. From [5]. . . . 12

1.6 Energy levels of ^{4}He, ^{8}Be and ^{12}C. From [2]. . . . 16

1.7 Energy levels of ^{12}C and ^{16}O. From [2]. . . . 17

1.8 Top: Partial nuclear chart highligthing the created nuclei during C-burning. The arrows represent the time-integrated net abundance flows for a 25 $M_\odot$ star. Bottom: Evolution of the chemical abundance during C-burning for a 25 $M_\odot$ star for a constant temperature and density of $T = 0.9$ GK and $\rho = 10^5$ g/cm^3, respectively. Both are from [2]. . . . 19

1.9 Evolution of chemical abundance during Ne-burning for a 25 $M_\odot$ star for a constant temperature and density of $T = 1.5$ GK and $\rho = 5 \times 10^6$ g/cm^3, respectively. From [2]. . . . 21

1.10 Evolution of chemical abundance during O-burning for a 25 $M_\odot$ star for a constant temperature and density of $T = 2.2$ GK and $\rho = 3 \times 10^6$ g/cm^3, respectively. From [2]. . . . 23

1.11 Evolution of chemical abundance during Si-burning for a 25 $M_\odot$ star for a constant temperature and density of $T = 3.6$ GK and $\rho = 3 \times 10^7$ g/cm^3, respectively. From [2]. . . . 24

1.12 Representation of the Gamow peak (green), defined by the convolution of the Maxwell-Boltzmann distribution (blue) and the tunneling through the Coulomb barrier (red). The Gamow peak can be fitted by a gaussian, with a mean E_0. From [6]. 28
1.13 Top: Ikeda diagram showing α-cluster states in several nuclei, with their associated excitation energy in MeV. From [7]. Bottom: Molecular configurations computed with theory. The bottom lign corresponds to the ground state of each nuclei. The ^{12}C-^{12}C cluster state in the ^{24}Mg is framed in black. From [8]. 30
1.14 Comparaison of excitation functions for ^{12}C + ^{12}C, ^{12}C + ^{13}C and ^{13}C + ^{13}C systems, with CC-calculations. From [9]. 31
1.15 Level densities as a function of the excitation energy in ^{24}Mg, ^{25}Mg and ^{32}S. From [10]. 32
1.16 Cross section for ^{64}Ni + ^{64}Ni fusion reaction. Adapted from [11]. 34
1.17 Top: Nuclear potential as a function of the distance for ^{64}Ni + ^{64}Ni system. Bottom: Cross section for ^{64}Ni + ^{64}Ni fusion reaction. Both figures are from [12]. 35
1.18 Top: Interaction potential for ^{48}Ca + ^{48}Ca. Bottom: Cross section for ^{48}Ca + ^{48}Ca fusion reaction. Both figures are from [13]. 36
1.19 Top: S-factor for ^{12}C + ^{12}C fusion reaction, represented with different theoretical models. Bottom: Zoom on the sub-barrier measurements. From [14]. 37
1.20 Top: Reaction rates for ^{12}C + ^{12}C obtained with different extrapolations. Bottom: Reaction rates for ^{12}C + ^{12}C obtained with different extrapolations normalized with CF88 rate. From [15]. 40
1.21 Limit mass $M_{\mathrm{L}}/M_{\odot}$ for the carbon ignition as a function of the metallicity Z, following the CF88 reaction rate in red and the CF88 reaction rate with a resonance at $E_{\mathrm{com}} = 1.4$ MeV. Figure from [6] and data from [16]. 41
1.22 Carbon ignition curves in a core of a massive ^{12}C-^{16}O white dwarf, with CF88 model and fusion hindrance model [17]. Adapted from [18] by [6]. 42

2.1 Energy level diagram of the ^{12}C + ^{12}C fusion reaction at $E_{\mathrm{com}} \approx 1.2 - 2.8$ MeV. Adapted from [19]. 52
2.2 Excitation fonctions for the ^{12}C + ^{12}C reaction from [20], for the different fusion reaction channels. The black arrow indicate the Coulomb barrier at $E_{\mathrm{Coulomb}} = 6.6$ MeV. The inset shows a suggested 1D quasi-molecular potential. 53
2.3 Compilation of total astrophysical S(E)-factors of the ^{12}C + ^{12}C reaction obtained with direct measurements. The theoretical models are from [17; 21]. Experimental data are taken from [22; 23; 24]. The letter in brackets indicates the reaction product detected: light particle (p) or γ rays (γ). The two black rectangles indicate the position of the Gamow window for the stellar temperatures $T = 0.5$ GK ($E_{\mathrm{Gamow}} = 1.5 \pm 0.3$ MeV) and $T = 0.9$ GK ($E_{\mathrm{Gamow}} = 2.25 \pm 0.48$ MeV). 54

2.4 Angular distribution for protons and α particles, at $E_{\text{com}} = 4.25$ MeV. From [22]. 56
2.5 S^*-factor for proton and α channels at deep sub-barrier energies. From [24]. 58
2.6 Compilation of total astrophysical factors S(E) of the ^{12}C + ^{12}C reaction obtained with direct measurements. The theoretical models are from [17; 21]. Experimental data are taken from [22; 23; 24; 25; 26; 27; 28]. The brackets indicates the reaction product detected: light particle (p), γ rays (γ) or both in coincidence (coincidence). The two black rectangles indicate the position of the Gamow window for the stellar temperatures $T \approx 0.5$ GK ($E_{\text{Gamow}} = 1.5 \pm 0.3$ MeV) and $T \approx 0.9$ GK ($E_{\text{Gamow}} = 2.52 \pm 0.48$ MeV). 60
2.7 The STELLA experiment. 61
2.8 3D CAD representation of the STELLA reaction chamber. From [6] . 62
2.9 3D CAD representation of the inside of the STELLA reaction chamber. From [29] 63
2.10 3D CAD representation of the rotative targets system of the STELLA experiment. From [6] 64
2.11 Left: Picture of a target in the target holder before irradiation. Right: Picture of a target after irradiation. The irradiated area is lighter than the area that is not impacted by the beam. 65
2.12 Photograph of the STELLA experiment's reaction chamber taken during the 2022 experimental campaign. 66
2.13 Photography of the junction side of a S3 type DSSSD. The 24 rings and the connections to the pins at the bottom of the detector are visible. From [6] 67
2.14 Scheme of the S3 Printed-Circuit Board (PCB), designed and mounted at IPHC. The ohmic side is on the left, the junction side on the right. From [6] 68
2.15 Angular distribution for α_0 for the ^{12}C + ^{12}C fusion, at $E_{\text{com}} = 5.38$ MeV by J. Nippert [28]. The red circle indicates the angular range probed by PIXEL. 69
2.16 Left: 3D view of the BB10 detector. Right: 3D view of the Super-X3 detector. Both pictures are from [30]. 70
2.17 Angular distributions in the laboratory frame for the ^{12}C + ^{12}C Mott scattering. From [6]. 71
2.18 Schema of a $LaBr_3$(Ce) scintillator. From [27] 72
2.19 Top: 3D CAD representation od the UK-FATIMA detectors on the cylindrical configuration support. Bottom: 3D CAD representation of the first ring of detectors of the cylindrical configuration. The green lines show the trajectory of three γ rays from the target. Both figures are from [29] 75
2.20 Scheme of the structure allowing the manipulation of the scintillators array. Fromé[6] 76
2.21 Scheme of the working principle of a polarized silicon particle detector. From [6]. 78

2.22 Top: Triggering system with a simple trigger threshold applied on a preamplifier signal. Bottom: Triggering system with a digital trigger threshold applied on an integrated differential signal. Both figures are from [6]. 79
2.23 Left: Arbitrary signal with exponential decrease. Right: Trapezoid signal using the Jordanov algorithm. Both figures are from [6]. 80
2.24 Scheme of a scintillator with the associated PMT. The scintillator converts the high energy incident γ in a low energy light, and the PMT convert this light into a electrical signal. From [31]. 80
2.25 Scheme of the clock distribution for a synchronized STELLA-FATIMA-PIXEL acquisition. Credits M. Richer. 81
2.26 Scheme of the synchronization pulse distribution in the STELLA-FATIMA-PIXEL acquisition system. Credits M. Richer. 82
2.27 Andromede facility. In operation the tank is closed. 83

3.1 3α calibration fit for a typical strip of the S3F detector. The obtained fit parameters are $p_0 = (6.458 \pm 0.001) \times 10^{-4}$ and $p_1 = -3.470 \pm 0.011$. The defaut QDC channel output is negative. 91
3.2 Kinematic energy calculation of α particules in black and protons in red producted at $E_{\text{lab}} = 9.6$ MeV. 92
3.3 High energy calibration fit for a typical strip of the S3B detector at $E_{\text{lab}} = 9.6$ MeV. The obtained fit parameters are $p_0 = (4.092 \pm 0.004) \times 10^{-4}$ and $p_1 = (9.933 \pm 3.435) \times 10^{-2}$. The defaut QDC chnanel output is negative. 93
3.4 Angular differential energy spectra calibrated with high energy in S3F (top) and S3B (bottom) at $E_{\text{lab}} = 9.6$ MeV. Black and red lines represent the kinematics calculations for the α and proton exit channels, respectively. The ground state transitions are at the highest energy, followed by excitation levels with decreasing particle energy. 94
3.5 Scheme representing the principle of charge sharing: in the left drawing no charge sharing occurs, in the middle drawing the charges are distributed over two strips. The diagram on the right represents the amount of charges collected by every strips in the latter scenario. From [28]. 95
3.6 Top: Correlation of active rings of S3B for the detection of multiplicity-two events. Bottom: Correlation of particles energies for multiplicity-two events for S3B in neighbouring strips. $E_{\text{lab}} = 9.6$ MeV. 96
3.7 Effect of charge sharing on particles spectra, for S3F (top) and S3B (bottom). $E_{\text{lab}} = 9.6$ MeV. 97
3.8 Angular distribution for α_0 at $E_{\text{lab}} = 10.75$ MeV. 99
3.9 Scheme of the Faraday cups system used to measure the beam intensities I_1 and I_2 and charge state q_1 and q_2 before and after the target, respectively. From [6]. 100
3.10 Particle spectra in S3F (top) and S3B (bottom). The vertical lines show the kinematic calculations for α in black and proton in red. $E_{\text{rel}} = 4.76$ MeV. 104

3.11 Angular distribution for α_0 (top) and α_1 (bottom). $E_{\rm rel} = 4.76$ MeV. . 106
3.12 Angular distribution for p_0 (top) and p_1 (bottom). $E_{\rm rel} = 4.76$ MeV. . . 107
3.13 Total cross section for the α channel (top) and the proton channel (bottom). Experimental data from [22; 27; 28] are represented. $E_{\rm rel}$ = 4.76 MeV. 109
3.14 Total cross section for the α exit channel, determined with α_0 (top) and α_1 (bottom). Experimental data from [22; 27; 28] are represented. $E_{\rm rel} = 4.76$ MeV. 110
3.15 Total cross section for the proton exit channel, determined with p_0 (top) and p_1 (bottom). Experimental data from [22; 27; 28] are represented. $E_{\rm rel} = 4.76$ MeV. 111
3.16 Angular differential energy spectra for S3B detector $E_{\rm lab} = 9.6$ MeV. Black, red et blue lines represent the kinematics calculations for the α exit channel, proton exit channels and from deuterium contaminant, respectively. The ground state transitions are at the highest energy, followed by excitation levels with decreasing particle energy. 113

4.1 Cross sections for alpha (a) and proton (b) channel, obtained with STELLA (red points) [32]. Adjustments made for the Hin model (red curve) and HinRes model (green curve) are compared with the cross section from the CF88 model (blue curve) [21]. Data points at the lowest energy for protons and the second lowest for the α channel are upper limits (vertical black lines). 121
4.2 Top: Gamow energy as a function of the temperature. Lower and upper limit are given by a Gaussian approximation of the Gamow peak proposed in [2]. The two black lines represent the upper and lower limits energies reached by STELLA experiment. Bottom: Gamow window for the reaction fusion ^{12}C + ^{12}C at $T = 0.77$ GK, as a function of the relative energy. 123
4.3 Top: Gamow window (black) and approximation from Illiadis [2] (red) for the reaction fusion ^{12}C + ^{12}C at $T = 0.77$ GK. The 1/e width (here Δ) and the 1σ width are also represented for the approximation. Bottom: Zoom on the top of both curves. 124
4.4 Reaction rates (top) and normalized reaction rates to $N_A\langle\sigma v\rangle)_{\rm CF88}$ (bottom), without (Hin; red curve) and with (HinRes; green curve) the added resonance [32]. The reaction rate from the CF88 model is also presented (blue curve). The shaded areas around the curves are the uncertainties (see text). Orange hatched areas show the temperature region explored by the STELLA experiment. The black arrows show the regions where carbon fusion occurs, for two stellar models (12 and 25 $M_\odot$), for both the Hin and HinRes models (see Fig. 4.5). 127
4.5 Central temperature evolution during the C-burning phase for 12 $M_\odot$ and 25 $M_\odot$ models with different ^{12}C + ^{12}C reaction rates. The evolution is given as a function of the mass fraction of carbon at the centre that decreases as a function of time. From [32]. 132

4.6 Evolution of central temperature as a function of central density for 12 $M_\odot$ and 25 $M_\odot$ models with different ^{12}C + ^{12}C reaction rates. From [32]. . . . 132

4.7 Kippenhahn diagrams for the centre of 25 $M_\odot$ models during the end of C-burning phase with Hin (top) and HinRes (bottom) ^{12}C + ^{12}C reaction rates. The grey shaded area shows the convective zones. The red dashed line shows the limits of the C-burning zones (defined where $\epsilon_{\mathrm{C}} \geq 10^2$erg g^{-1}s^{-1}). From [32]. . . . 133

4.8 Top: Core abundance profile at the end of central C-burning for $12M_\odot$ models with different ^{12}C + ^{12}C reaction rates. Bottom: Abundances profile at the end of C-burning for $25M_\odot$ models with different ^{12}C + ^{12}C reaction rates. From [32]. . . . 135

4.9 Left: Abundances relative to CF88 models in the supernova ejecta of the 25 $M_\odot$ models for different ^{12}C + ^{12}C reaction rates, based on the structure obtained at the end of the C-burning phase. Right: The same abundances but for the total mass content in the ejecta. From [32]. . . 136

4.10 Energy production at the mid-point of C-burning (when half the central ^{12}C has been consumed since the beginning of C-burning) for 25 $M_\odot$ models for different ^{12}C + ^{12}C reaction rates. The CF88, Hin and HinRes models are plotted in solid, dashed, and dotted lines, respectively. From [32]. . . . 138

4.11 Comparisons between the abundances before (green) and at the end of the core C-burning phase (black, red and blue) obtained with three different sets of rates for the ^{12}C + ^{12}C reactions. The dashed vertical lines highlight from left to right the carbon ($Z = 6$), neon ($Z = 10$), sodium ($Z = 11$), magnesium ($Z = 12$), iron ($Z = 26$), strontium ($Z = 38$), barium ($Z = 56$), and lead ($Z = 82$). From [32]. . . . 140

4.12 Abundances obtained at the end of the C-burning phase normalised to the final abundances obtained using the CF88 rate. Only the elements with a mass fraction greater than 10^{-8} (in either the first or second model) are considered. From [32]. . . . 142

4.13 Ratio of the reaction channels in the valid temperature range for carbon burning for CF88, the Hin and HinRes in the One-Layer code. From [33]. . . . 143

4.14 Mass fractions at the end of the core C-burning phase of a 17 $M_\odot$ star. The grey line refers to the initial abundances, extracted from the CF88 GENEC model at core C-ignition. The bottom panels show the abundances normalised to the ones of the CF88 model. Top: nucleosynthesis using the same (ρ, T) path from CF88 model. Bottom: nucleosynthesis using the consistent (ρ, T) paths from each GENEC model. From [34]. 144

List of Tables

1.1 The three pp chains. The different steps are described from the top to the bottom. From [35]. 13
1.2 The four CNO cycles. The different steps are described from the top to the bottom. From [35]. 14

2.1 Angular coverage (in % of 4π) of $LaBr_3(Ce)$ scintillators according different configurations and number of detectors in the first ring. From [6]. 73
2.2 Efficiency of the photoelectric peak with respect to the energy for 36 scintillators in the cylindrical configuration. ϵ_{sing} is the efficiency from single spectra analysis, and ϵ_{sum} is the sum of the total energy deposit in the array. From [6]. 74

3.1 Correction factor f_{cor} in respect to the beam intensity I_{beam}. 101
3.2 Fraction of the measured excited states for the α and proton exit channels. Fusion data from [22]. 108

4.1 Cross sections measured by STELLA, for α exit channel and proton exit channel. Data from [27]. 120
4.2 Parameters of cross sections for $^{12}C + {}^{12}C$ fusion reaction using different models from data interpolation. From [32]. 120
4.3 Integrals for the Gamow peak and the approximation from Illiadis [2], on an interval totally covering both peaks and the $E_0 \pm \sigma$ range, and ratio between these integrals for both curves. 122
4.4 Reaction rates for the $^{12}C + {}^{12}C$ fusion reaction according to different models. Reaction rates are in $cm^3s^{-1}mol^{-1}$ and temperatures in GK. From [32]. 129
4.5 Parameters for recommended, lower and upper reaction rates in the case of Hin model. From [32]. 130
4.7 Central C-burning lifetime for different $^{12}C + {}^{12}C$ reaction rates. From [32]. 137

List of Publications and Communications

Publications

- **E. Monpribat**, S. Martinet, S. Courtin, M. Heine, S. Ekstrom, D. G. Jenkins, A. Choplin, P. Adsley, D. Curien, M. Moukaddam, J. Nippert, S. Tsiatsiou, G. Meynet, *A new ^{12}C + ^{12}C nuclear reaction rate: Impact on stellar evolution*, Astronomy&Astrophysics **660**:A47, 2022

- M. Heine, G. Fruet, S. Courtin, D. G. Jenkins, P. Adsley, A. Brown, R. Canavan, W. N. Carford, E. Charon, D. Curien, S. Della Negra, J. Duprat, F. Hammache, J. Lesrel, G. Lotay, A. Meyer, **E. Monpribat**, D. Montanari, L. Morris, M. Moukaddam, J. Nippert, Zs. Podolyak, P. H. Regan, I. Ribaud, M. Richer, M. Rudigier, R. Shearman, N. de Séréville, C. Stodel, *Direct Measurement of Carbon Fusion at Astrophysical Energies with Gamma-Particle Coincidences*, EPJ Web of Conferences **260** 01004, 2022

- **E. Monpribat**, A. Choplin, S. Martinet, S. Courtin, M. Heine, P. Adsley, D. Curien, T. Dumont, S. Ekstrom, D. G. Jenkins, M. Moukaddam, J. Nippert, S. Tsiatsiou, G. Meynet, *A new ^{12}C + ^{12}C reaction rate: Impact on stellar evolution*, EPJ Web of Conferences **279** 11016, 2023

- S. Courtin, M. Heine, **E. Monpribat**, J. Nippert, *Carbon burning at stellar energies*, Journal of Physics: Conferences Series **2586** 012114, 2023

- **E. Monpribat**, T. Dumont, A. Bonhomme, M. Heine, J. Nippert, S. Courtin, *A new ^{12}C + ^{12}C reaction rate from the STELLA collaboration: how to determine astrophysical parameters with nuclear experiments?*, SF2A-2023: Proceedings of the Annual meeting of the French Society of Astronomy and Astrophysics pp.435-438, 2023

- J. Nippert, A. Bonhomme, S. Courtin, D. Curien, E. Gregor, M. Heine, **E. Monpribat**, T. Dumont, C. Stodel *Recent Results on Direct Measurement of the ^{12}C + ^{12}C Fusion Cross section at Deep Sub-barrier Energies with STELLA*, Acta Physica Polonica B Proceedings Supplement **17** 3-A33, 2024

- T. Dumont, **E. Monpribat**, S. Courtin, A. Choplin, A. Bonhomme, S. Ekstrom, M. Heine, D. Curien, J. Nippert, G. Meynet, *Massive star evolution with a new*

^{12}C + ^{12}C nuclear reaction rate, Astronomy&Astrophysics **688**:A115, 2024

- J. Nippert, S. Courtin, M. Heine, D.G. Jenkins, P. Adsley, A. Bonhomme, R. Canavan, D. Curien, T. Dumont, E. Gregor, **E. Monpribat**, L. Morrison, M. Moukaddam, M. Richer, M. Rudigier, J.G. Vega Romero, W.N. Catford, P. Cotte, S. Della Negra, G. Haefner, F. Hammache, J. Lesrel, S. Pascu, Zs Podolyak, P.H. Regan, I. Ribaud, N. de Séréville, C. Stodel, J. Vesic, *Complementing the picture of deep sub-barrier ^{12}C + ^{12}C fusion with STELLA*, submitted to Physical Review C

- D. Brugnara, G. Montagnoli, A.M. Stefanini, M. Del Fabbro, F. Angelini, A. Bonhomme, J. Benito, M. Balogh, S. Courtin, G. Colucci, L. Corradi, R. Depalo, A. Ertoprak, E. Fioretto, A. Gozzelino, B. Gongora Servin, A. Gottardo, F. Galtarossa, M. Heine, M. Mazzocco, D. Mengoni, B. Million, **E. Monpribat**, R. Nicolas Del Alamo, M. Polettini, J. Pellumaj, E. Pilotto, S. Pigliapoco, M. Rocchini, K. Rezynkina, S. Szilner, D. Stramaccioni, A. Trzcinska, L. Zago, I. Zanon, *Fusion dynamics far below the barrier for ^{12}C + ^{28}Si*, submitted to Nuclear Physics Section A

Conferences

- XXth International Workshop on Nuclear Astrophysics, *New ^{12}C + ^{12}C nuclear reaction rates: impact on stellar evolution*, Ringberg Germany, 11/2021

- Journée Andromède 2022, *Carbon and oxygen burning towards astrophysical energies*, Orsay France, 01/2022

- Nuclear Physics in Astrophysics X, *New ^{12}C + ^{12}C nuclear reaction rates: impact on stellar evolution*, CERN Switzerland, 09/2022

- AG GdR Resanet, *New ^{12}C + ^{12}C nuclear reaction rates: impact on stellar evolution*, Lyon France, 09/2022

- Journées SF2A 2023, *A new ^{12}C + ^{12}C nuclear reaction rate from the STELLA collaboration: how to determine astrophysical parameters with nuclear experiments?*, Strasbourg France, 06/2023

Introduction

On m'a dit : "Tu n'es que cendre et poussières." On a oublié de me dire qu'il s'agissait de poussières d'étoiles.

Hubert Reeves, *Poussière d'étoiles*

Among all the questions in contemporary physics, the origin of elements, and therefore the origin of life, is certainly of the most fundamental, primitive, animalistic, and essential one. Where do they come from, and how did they form? How and where did the myriad of atoms that make up our bodies come into existence? To this question, Hubert Reeves answered that we are all made of stardust [36]. But what is the connection between the twinkling stars scattered across the celestial vault and the hands writing this manuscript?

In 1957, G. Burbidge, M. Burbidge, W. Fowler and F. Hoyle [37], and A. Cameron [38], going against the other theories assuming that all chemical elements were formed during the primordial phases of the Universe, published pioneering studies that remain, over 60 years later, trully references in nuclear astrophysics. In these articles, they postulated and justified that the vast majority of elements are synthesised within stars during their lifetime and death, based on the then well-known fact that nuclear reactions occur in these celestial bodies.

Stars are like cauldrons in the Universe, enriching it, helping it to evolve and enabling the creation of increasingly complex bodies, thanks to the nuclear reactions that take place within them. These reactions, and fusion reactions in particular, are responsible for producing the energy that allows stars to have long lifetime, which can reach several billion years, as is the case for our Sun. By changing the chemical composition of stars, these reactions also govern the evolution of stars: the latter will differ based on their initial mass, since the nuclear processes involved will be different.

The direct link between the evolution of stars and the nuclear reactions within them is the nuclear reaction rate. This profoundly astrophysical and nuclear quantity is calculated from reaction cross sections, and plays an essential role in stellar evolution codes. In addition to the commonly used reaction rates, Caughlan & Fowler [21], Angulo *et al.* [39] (Nacre) and Xu *et al.* [40] (NacreII), new rates are regularly published, refining our knowledge and our approach to the physics of stars.

Thus, precise knowledge of the nuclear reactions that take place within stars is needed to understand their evolution and death. Certain reactions are particularly crucial for stellar evolution, such as the fusion reaction $^{12}C + ^{12}C$. Indeed, this reaction takes place in many different astrophysical sites: the core C-burning phase [41; 42; 15; 43], shell C-burning [44; 45; 46], white dwarfs accretion and SN Ia supernovæ [47; 48; 49], explosive nucleosynthesis [50] and superbursts [51; 52]. In addition, this reaction marks the start of the carbon combustion phase, a key phase in the evolution of stars. The activation or non-activation of this reaction in a star will determine the life path it takes, and therefore strongly influence the development of the star's chemical composition and, consequently, the interstellar medium.

However, the properties of the $^{12}C + ^{12}C$ fusion reaction when it occurs in stars are still poorly understood. In fact, the energy ranges at which this fusion reaction takes place in stars, the energies of astrophysical interest, are well below the Coulomb barrier of the reactions studied [53]: the cross sections sought are therefore very small, of the order of the picobarn, and difficult to measure. In addition, at these energies, this reaction has many resonant structures, possibly linked to the formation of a nuclear molecules. Several research teams have tried for more than 50 years to determine these cross sections, either experimentally or theoretically, but have been unable to obtain any usable results in the region of interest because the data show large error bars [54].

The work carried out during this thesis and presented in this manuscript concerns the study of the $^{12}C + ^{12}C$ fusion reaction, from its experimental measurement in the laboratory to the determination of new stellar reaction rate and the study of its impact on the evolution of stars. It was carried out as part of the STELLA collaboration, whose project is to measure the cross sections of fusion reactions at energies of astrophysical interest [29]. The initial results of this experiment, obtained using a particle-γ coincidence method, are very promising, with improved error bars [27; 28]. With these results, it is now possible to determine new stellar reaction rates.

In Chapter 1, the importance of nuclear reactions for the evolution of stars will be discussed. To this end, a description of the astrophysical context will be given, with definitions of nucleosynthesis, stellar evolution and the different phases of stellar combustion. Secondly, the link with nuclear physics will be established, with the definition of the stellar reaction rate, but also of the nuclear behaviour that can have an impact on the same, and therefore on the evolution of stars.

Chapter 2 will be devoted to the $^{12}C + ^{12}C$ fusion reaction, and to its measurement at energies of astrophysical interest. The various measurement techniques will be described, along with their intrinsic limitations. The strength of the coincidence method, and in particular of the STELLA experiment, will then be described. The details of the set up will be presented: the reaction chamber, the target system, the different types of detectors and the data acquisition system. During this thesis, an experimental campaign took place over 3 months in the spring of 2022, under the difficult pandemic conditions.

The analysis of the results obtained with STELLA during this experimental campaign will be the subject of Chapter 3 of this manuscript. The energy spectra will be detailed, from calibration to event selection. Data normalisation will also be discussed.

Finally, the obtention of a total cross section will be presented.

The last chapter, Chapter 4, will be dedicated to the new stellar reaction rate. Due to the COVID-19 pandemic and the resulting delay in the experiment, this rate is obtained from previously published STELLA data [27]. Its determination will be fully detailed, and its relevance to the study of the evolution of massive stars will be presented. Its impact on stellar evolution will then be discussed, based on two simulation works, one with GENEC [55], the second with a code presenting a network of nuclear reactions [56] in order to follow nucleosynthesis during the carbon burning phase.

This manuscript will end with a conclusion on the work carried out, and prospects for the future, both in nuclear physics and in stellar astrophysics.

Chapter 1

Nuclear reactions and their astrophysical importance

Contents

1.1 Astrophysical context 6
1.1.1 Nucleosynthesis 6
1.1.2 Stellar evolution 7
Paths of life 7
Hydrostatic equilibrium 9
1.1.3 Burning phases 12
Hydrogen burning 12
Helium burning 14
Carbon burning 17
Advanced burning stages and supernovæ 20
1.2 Importance of Nuclear Physics 24
1.2.1 Reaction rates 24
Definition 24
Gamow window and S-Factor 26
1.2.2 Deep sub-barrier cross section 27
Resonances 28
Fusion hindrance 33
1.2.3 Impact on astrophysical scenarios 38
Evolution of massives stars 38
Binary systems and type Ia supernovæ 39
1.3 Résumé du chapitre 43
1.3.1 Contexte astrophysique 43
1.3.2 Importance de la physique nucléaire 45

Nuclear physics and nuclear reactions play an essential role in stellar evolution, and therefore in the evolution of the Universe. If they are not directly responsible of the stars luminosity, they have an important impact in their lifetime, evolution, composition. Furthermore, astrophysical models and theory tend to show that, depending on their initial masses, stars have distinct and defined end-of-life scenarios. For example, some given nuclear reactions are only accessible to certain stars.

Fusion reactions are of the uttermost important nuclear reactions for stellar evolution. Knowing the properties of these nuclear reactions would provide a much better understanding of the fusion mechanisms at work in stars, and therefore a better understanding of the evolution of the Universe in general. In this regard, experimental nuclear physics, with the determination of reaction rates, *i.e.* an essential parameter for astrophysicists and simulations of stellar evolution, is greatly important for astrophysics.

In addition, recent studies have shown that nuclear structures, such as resonances or fusion hindrance, might have an impact on the reaction rate [15; 25]. As a result, refining the excitation functions for the nuclear reactions that occur in stars, and thus highlighting the structures of these cross sections, also have an important role to play in understanding the evolution of stars.

1.1 Astrophysical context

1.1.1 Nucleosynthesis

Nucleosynthesis is the process in which the chemical elements are produced. It takes place through different nuclear reactions, such as nuclear fusion or fission, neutron and proton capture, photodisintegration, spallation, decay, at different times and places [37; 38; 57].

The lightest, and so first elements of the periodic table were produced in the first few minutes after the Big-Bang, throughout the whole Universe [53]. During this period, high temperature and pressure enabled the formation of helium and small quantities of lithium from existing hydrogen, throught the so-called Big Bang nucleosynthesis, or primordial nucleosynthesis. After about 20 minutes, the expansion of the Universe led to its cooling, and to the decoupling of photons, the nuclear reactions thus stopped.

After this initial nucleosynthesis, the formation of the first stars is the next event to offer suitable conditions for nuclear reactions to occur and hence the formation of elements. Indeed, througth their evolution phases, stars are the cauldron in which a lot of nuclear processes take place. This element production is known as the stellar nucleosynthesis. This nucleosynthesis can take place in very different environments: the lighest elements are produced during the quiescent nucleosynthesis, that occurs in cores and shells of stars at the hydrostatic equilibrium, through nuclear fusion, photodisintegration, neutron capture during stellar burning phases. Elements heavier than iron are produced during supernovæ nucleosynthesis, also known as explosive nucleosynthesis, through different processes, as proton-capture process and neutron-

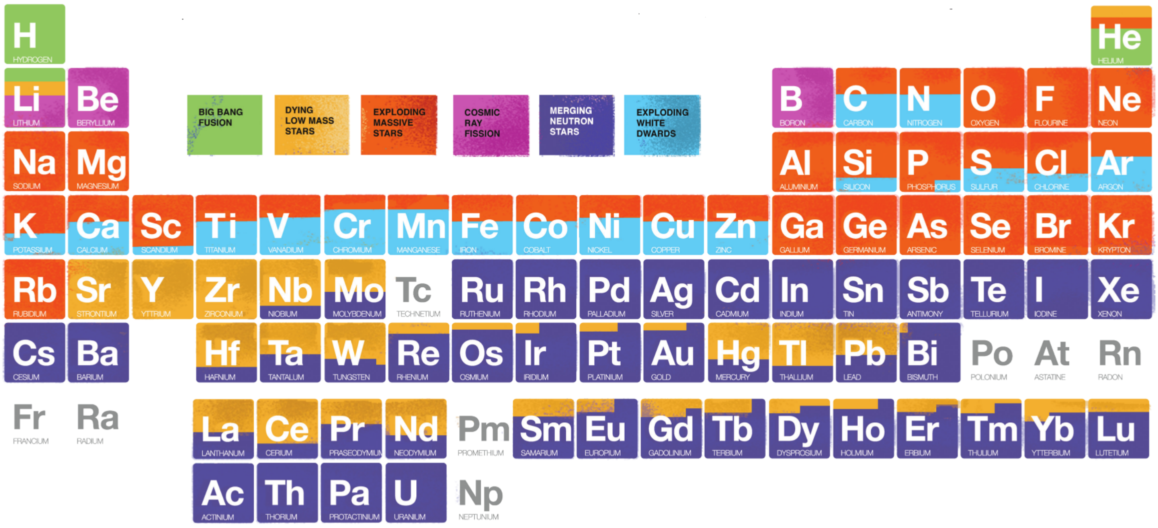

Figure 1.1: Periodic table color coded to sugest the nuclear origin of all elements. Credit: NASA/CXC/K. Divona; Reference: SDSS blog, J. Johnson. From [1]

capture process, that gather s-process, i-process and r-process for slow, intermediate and rapid, respectively.

Other astrophysical objects can be at the origin of temperature and pressure that allow elements formation. Accretion disks of black holes is a place of elements synthesis, as the neutron star mergers, also called kilonovæ, and black hole mergers. They have been recently highlighted as a major source of heavy elements [58; 59].

The last astrophysical phenomenom leading to nucleosynthesis is the cosmic ray spallation, or l-process [37]. During it, a cosmic ray impacts with an atom. This process occurs mainly in interstellar medium, but also on Earth. A few light isotopes are produces through it, as lithium, berylium and boron.

Figure 1.1 shows the Periodic table, color coded to highlight the processes behind the formation of the different chemicals elements, and theirs production sites.

This graphic shows the importance of stars for elements formation: these elements can be formed during different stellar processes, that occur for different types of stars, and different evolutionary stages. The stellar nucleosynthesis is deeply linked to stars evolution.

1.1.2 Stellar evolution

Paths of life

The stellar nucleosynthesis includes all the nuclear reactions that occur during the different phases of stars evolution, and that lead to the formation of a large majority of chemical elements. One can distinct two types of stellar nucleosynthesis: the quiescent one, during which the stars are in hydrostatic equilibrium, and the explosive one, also

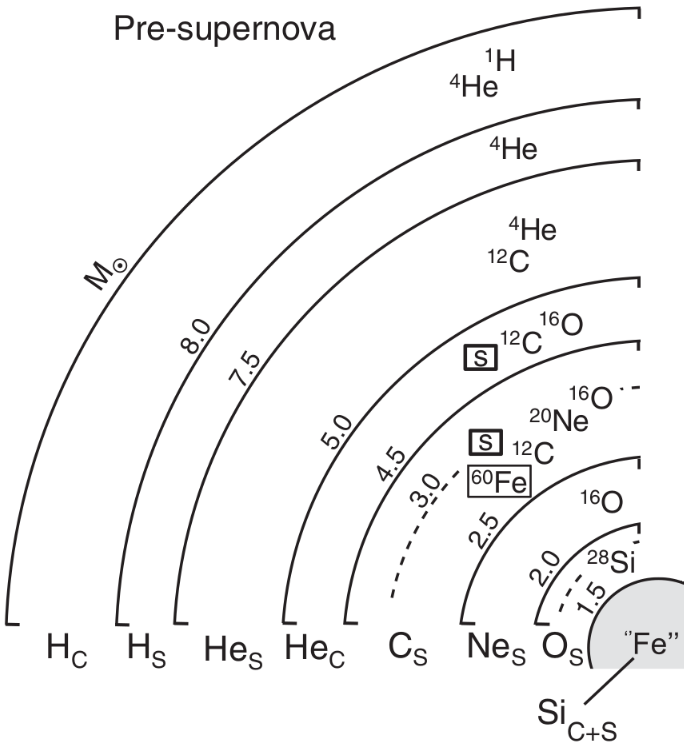

Figure 1.2: Structure of a 25 $M_{\odot}$ star of solar metallicity, shortly before core collapse. Only the main constituents in each layer are shown. Minor constituents are set in thin rectangle. Weak s-process component is set in thick rectangle. Subscripts C and S stand for core and shell burning, respectively. The diagonally arranged numbers indicate the interior mass for each burning shell. From [2].

called supernova nucleosynthesis.

Quiescent stellar nucleosynthesis is the process that takes place during most of a star's life. It is one of the causes of the hydrostatic equilibrium of stars. Under its own gravity, a star will collapse and contract. This contraction causes an increase in pressure within the star, leading to a rise in temperature. This temperature eventually becomes high enough for fusion reactions to take place in the star's core. The energy released by these reactions then counteracts the effect of gravitational collapse, thanks in particular to the radiation pressure generated by the gamma rays emitted during fusion [2]. Once the fuel in the core is exhausted, the reactions stop and the star starts again to collapse. The temperature rises, and new reactions take place, either in the core from the products of previous reactions, or in the outer shells if the temperature permits. The star's structure is then made up of successive layers with different chemical compositions, known as a "shell structure".

Figure 1.2 shows a snapshot of the pre-supernova structure of a 25 $M_{\odot}$, where $1M_{\odot} = 2 \times 10^{30}$ kg corresponds to the mass of the Sun, with solar metallicity ($Z_{\odot} = 0.0134$ [60]) as predicted by one-dimensional, spherically symmetric models [61], shortly before core collapse [2]. The main components fo each layer are shown, as well as the minor constituents in thin rectangle and the weak s-process component in thick rectangles. Nuclear burning takes place in thin regions (burning shells) at the interface of different compositional layers. The composition resulting from burning stages is indicated at the bottom (C and S stand for core and shell, respectively). The diagonally arranged numbers indicate the interior mass for each burning shell.

This structure is clearly distinguishable in the Kippenhahn diagrams in Fig. 1.3 [3]. These diagrams represent the evolution of the internal structure of a star, with the mass in a sphere with radius r in y-axis and the time in x-axis. The black zones correspond to convective regions, and the white zones to radiative ones. In both diagrams the different burning stages are indicated below the x-axis. The evolution of a 25 and a 40 $M_{\odot}$ are represented in the upper and bottom panels respectively, from the formation of the star to its core collapse.

These diagrams show the evolution of the stellar structure during the different burning phases, through the mode of energy transport.

The synthetized elements during this nucleosynthesis essentially depend on the initial mass M_i of the considered star. Two possible cases are observed.

If the star has an initial mass $M_i < 8\ M_{\odot}$ it will fuse its hydrogen into helium, then the latter into carbon and oxygen. No other fusion reaction takes place in such an object, as its initial mass does not allow a sufficient increase in temperature. The remnant of such a process is a white dwarf, an object whose hydrostatic equilibrium is due to electron degeneracy pressure.

If the star's initial mass is greater than $M_i > 10 - 12\ M_{\odot}$, which is considered as massive star, then it is capable of successively burning all its constituent elements in the core, up to iron. As iron is the most stable element in the periodic table of elements, its fusion is endothermic at stellar core temperatures, and does not occur during phases of quiet stellar nucleosynthesis. The star ends its life as a supernova, and its remnant may be a neutron star or a black hole.

The evolution of stars with an initial mass of $M_i = 8 - 10\ M_{\odot}$ is not precisely predicted. Indeed, numerical models for these stars are unable to determine whether the stellar fate will be white dwarfs or supernovæ as other parameters of the star, such as its rotation or metallicity, play an important role in this case. However, current observations show that these stars can evolve into white dwarfs, neutron stars or black holes [2].

These two path of life of stars are respresented in Fig. 1.4. The left cycle shows the evolution of stars with initial masses $M_i < 8\ M_{\odot}$, and the right cycle the evolution of massive stars.

Hydrostatic equilibrium

The life of a star begins with the collapse of a cloud of gas, mostly hydrogen, under its own gravity. At the center of this collapsing cloud, the pressure of the gas increases, as does its temperature. Potential energy is then converted into kinetic energy during

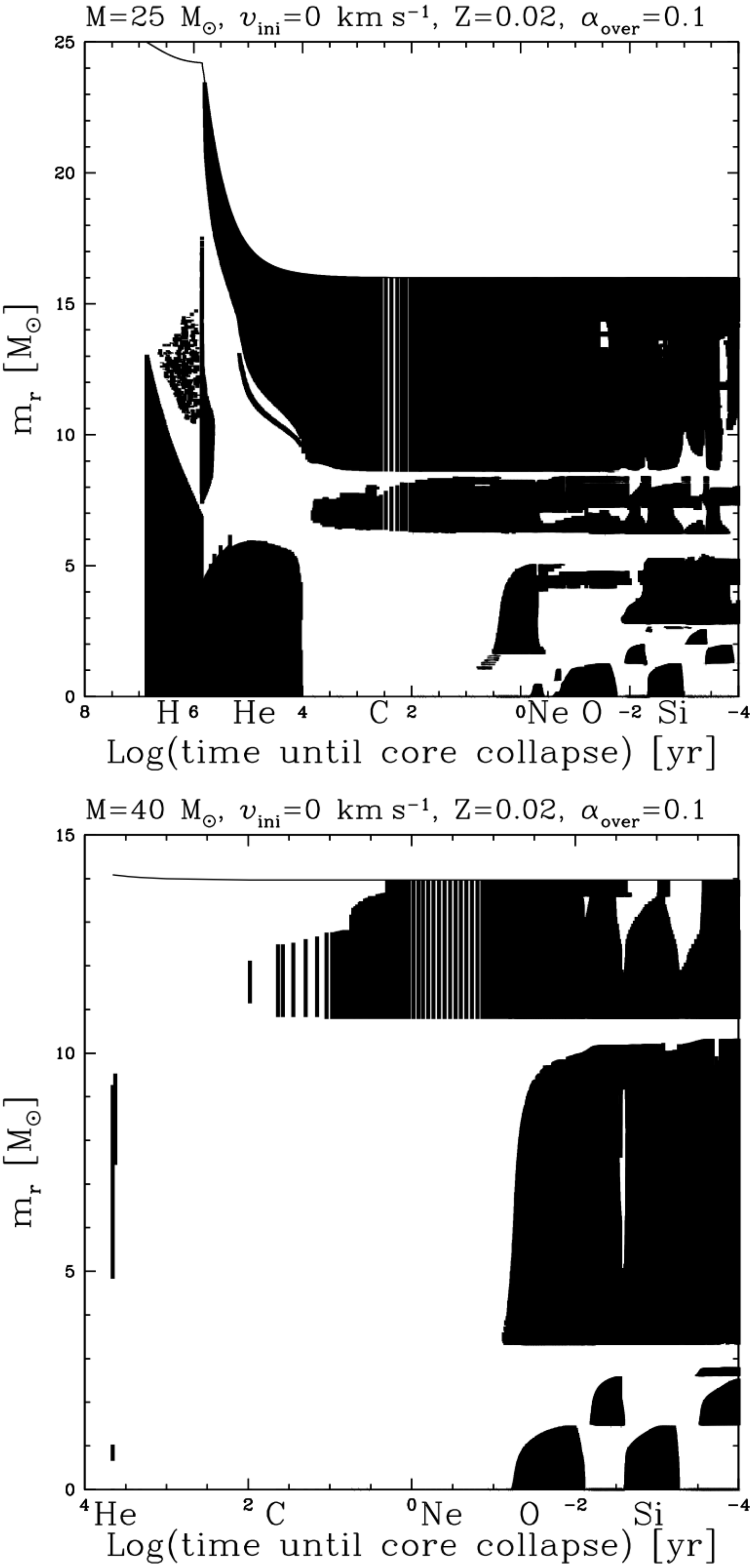

Figure 1.3: Kippenhan diagrams for non-rotating 25 (top) and 40 (bottom) $M_\odot$ models. The black zones corresponds to convective regions. From [3].

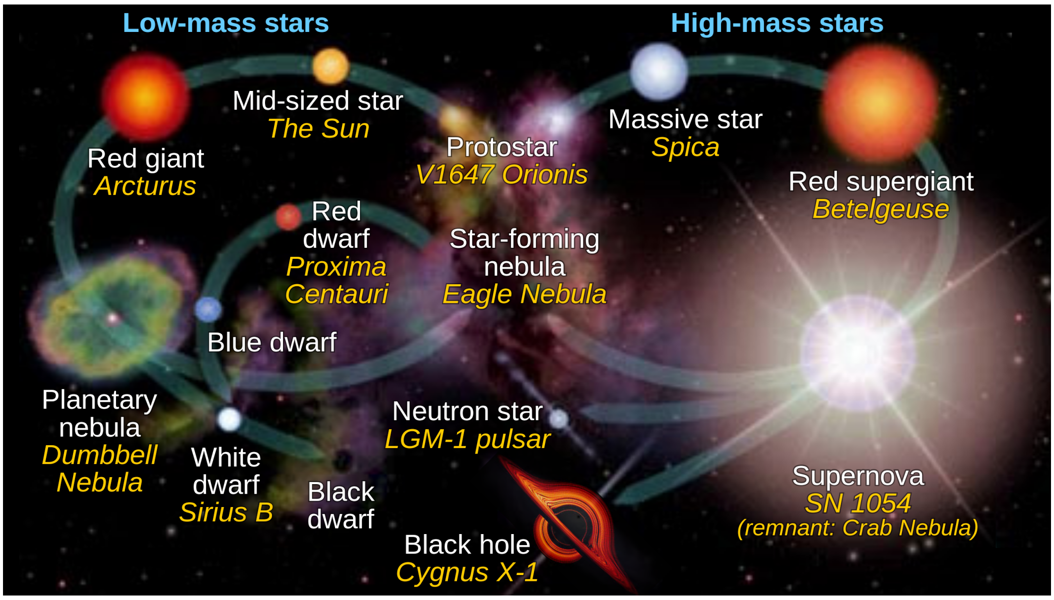

Figure 1.4: Stellar evolution of low-mass (left cycle) and high-mass (right cycle) stars. From [4].

the infall. The temperature, and therefore the kinetic energy of the atoms of the gas, increases until the forces of pressure counterbalance the star's gravitational collapse. The star then reaches a state of equilibrium, described by the hydrostatic equilibrium equation [62]:

$$\frac{\mathrm{d}P(r)}{\mathrm{d}r} = -\frac{GM(r)}{r^2}\rho(r), \tag{1.1}$$

where $P(r)$ and $\rho(\mathrm{r})$ are the pressure and density at a given radius r, $M(r)$ the total mass contained in a sphere of radius r, and G the universal constant of gravity.

Because of this equilibrium, a star is a system in a stationary regime of energy transport, and cannot accumulate energy at any given point. Considering L_r the "outgoing energy - incoming energy" balance per unit time of a spherical surface of radius r, we have:

$$L_{r+\mathrm{d}r} - L_r = 4\pi r^2 q(r)\ \mathrm{d}r, \tag{1.2}$$

that gives:

$$\frac{\mathrm{d}L_r}{\mathrm{d}r} = 4\pi r^2 q, \tag{1.3}$$

where q is a rate of energy production, typically nuclear, per unit of volume. Nuclear physics is therefore essential to solve these equations.

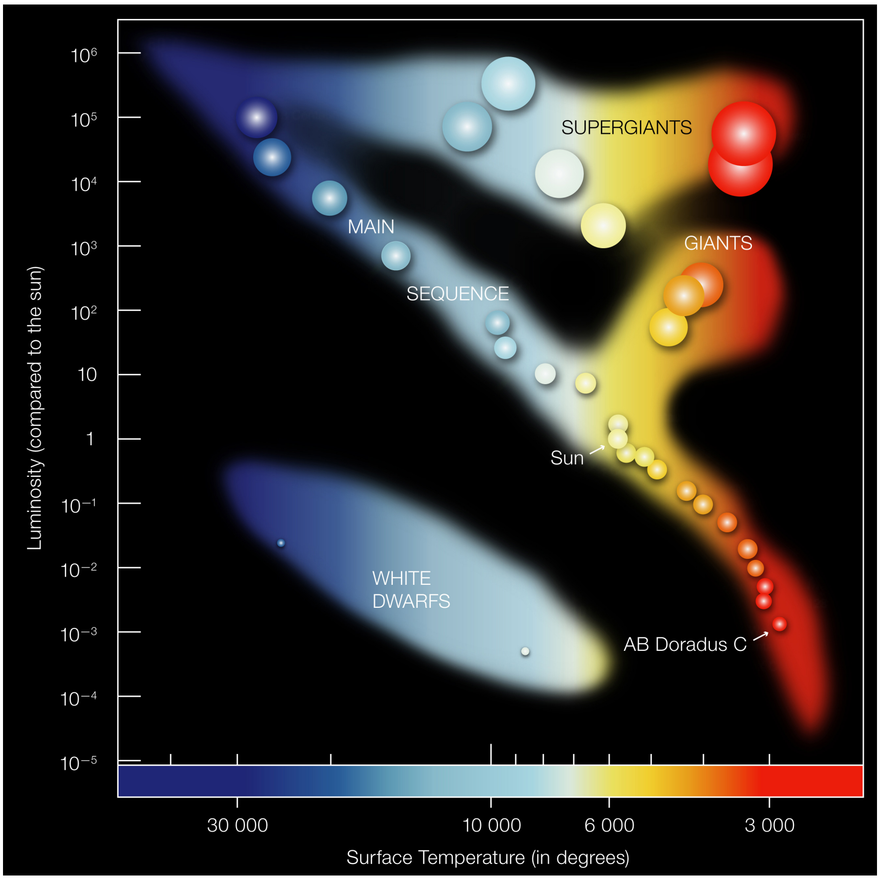

Figure 1.5: Hertzprung-Russel diagram with the temperatures of stars against their luminosity. The position of a star in the diagram provides information about its present stage and its mass. Credit: ESO. From [5].

1.1.3 Burning phases

As seen previously, stellar evolution is deeply connected to the nuclear reactions taking place within stars.

One of the tools that can be used to better understand this connection is the Hertzprung-Russel diagram, or HR diagram, shown in Fig. 1.5. In this diagram, the stars are naturally arranged according to their surface temperature, on the x-axis, and according to their luminosity, on the y-axis.

The stars are grouped into categories, the latter can be a good indication of nuclear burning that take place in the stars.

In this way, the evolution of stars can be broken down into several precise burning phases, each involving the combustion of a particular element.

Hydrogen burning

The hydrogen burning phase, or H-burning, is the first burning phase that a star will see. It corresponds to the Main Sequence of the life of stars, which is the diagonal structure in Fig. 1.5. The name Main Sequence comes from the fact that, due to the dominant abundance of hydrogen, a star will spend most of its lifetime on this stage.

Indeed, the lifetime of H-burning varies greatly depending on the initial mass of the star: from a few hundred million years for the most massive stars to more than 10 billion years for the lightest.

During this phase, four ^{1}H hydrogen nuclei are transformed into a ^{4}He helium nucleus. This reaction releases a total energy of $Q_{4^1\mathrm{H}\to^4\mathrm{He}} = 26.731$ MeV.

Although at the beginning of its life a star is composed mainly of ^{1}H ($\geq 75\%$), the probability of direct fusion of four nuclei is very low. Fusion is therefore possible through a series of interactions between nuclei and particles. Two main processes are responsible for hydrogen combustion: proton-proton chains and CNO cycles.

Proton-proton chains:

There are three series of proton-proton chains, or pp chains, leading to the formation of ^{4}He. These three series are grouped together in Tab. 1.1.

For each of the three chains, the first reaction is the fusion of two ^{1}H nuclei in a deuterium nucleus, noted d. This reaction involves the transformation of a proton into a neutron, process that occurs through the weak interaction. This explains the low probability of this reaction to occur, and then the long lifetime of stars.

pp1 chain	pp2 chain	pp3 chain
p(p,e$^+\nu$)d	p(p,e$^+\nu$)d	p(p,e$^+\nu$)d
d(p,γ)^{3}He	d(p,γ)^{3}He	d(p,γ)^{3}He
^{3}He(^{3}He,2p)α	^{3}He(^{4}He,γ)^{7}Be	^{3}He(^{4}He,γ)^{7}Be
	^{7}Be(e$^-$,ν)^{7}Li	^{7}Be(p,γ)^{8}B
	^{7}Li(p,α)α	^{8}B($\beta^+\nu$)^{8}Be
		^{8}Be(α)α

Table 1.1: The three pp chains. The different steps are described from the top to the bottom. From [35].

The second reaction for all chains is a proton capture by the deuterium, creating a ^{3}He nucleus. The third reaction is differents for the chains. In pp1, the direct fusion of two ^{3}He forms a ^{4}He nucleus. But for pp2 and pp3, this reaction involves the fusion of ^{3}He + ^{4}He. It is then necessary to have sufficient density of α particles in the medium in order to have these chains: the ^{4}He acts as catalyser.

The relative contribution of the various pp chains to the H-burning strongly depends on the conditions and the chemical composition of the stellar medium.

CNO cycles:

On top of hydrogen and helium, stars are composed of a number of heavier elements, produced by the nucleosynthesis of stars of previous generations. Stars may therefore initially be composed of small quantities of carbon, nitrogen or oxygen. These nuclei can then act as catalysts for the reaction $4^1\text{H} \rightarrow^4 \text{He}$.

Four different cycles may occur, called CNO cycles, for Carbon-Nitrogen-Oxygen. They are listed in Tab. 1.2.

CNO1	CNO2	CNO3	CNO4
^{12}C(p,γ)^{13}N	^{14}N(p,γ)^{15}O	^{15}N(p,γ)^{16}O	^{16}O(p,γ)^{17}F
^{13}N($\beta^+\nu$)^{13}C	^{15}O($\beta^+\nu$)^{15}N	^{16}O(p,γ)^{17}F	^{17}F($\beta^+\nu$)^{17}O
^{13}C(p,γ)^{14}N	^{15}N(p,γ)^{16}O	^{17}F($\beta^+\nu$)^{17}O	^{17}O(p,γ)^{18}F
^{14}N(p,γ)^{15}O	^{16}O(p,γ)^{17}F	^{17}O(p,γ)^{18}F	^{18}F($\beta^+\nu$)^{18}O
^{15}O($\beta^+\nu$)^{15}N	^{17}F($\beta^+\nu$)^{17}O	^{18}F($\beta^+\nu$)^{18}O	^{18}O(p,γ)^{19}F
^{15}N(p,α)^{12}C	^{17}O(p,α)^{14}N	^{18}O(p,α)^{15}N	^{19}F(p,α)^{16}O

Table 1.2: The four CNO cycles. The different steps are described from the top to the bottom. From [35].

The amount of heavy elements stays constant during the processes. Thus, depending of the mass and the temperature of the star, the CNO cycles can be responsible for a non-negligible energy release. In fact, they may be more favoured than the pp chains. For example, for stars with core temperatures above $T > 20$ MK, the CNO1 cycle is responsible for greater energy production than the pp1 chain [2].

Helium burning

Once the H-burning phase is over, and the core of the star is composed mainly of helium, the star will contract and its core temperature will rise, until helium fusion is possible. The star will then enter the helium burning phase, or He-burning, and will no longer lie on the Main Sequence diagonal on the HR diagram, but will be categorised as a Giant or Supergiant depending on its initial mass.

As for the H-burning, the lifetime of the He-burning phase strongly depends on the initial mass of the star.

Four main reactions take place in the core during this burning phase:

$$^{4}\text{He}(\alpha\alpha,\gamma)^{12}\text{C} \qquad (Q = 7274.7\,\text{keV}), \tag{1.4}$$
$$^{12}\text{C}(\alpha,\gamma)^{16}\text{O} \qquad (Q = 7161.9\,\text{keV}), \tag{1.5}$$
$$^{16}\text{O}(\alpha,\gamma)^{20}\text{Ne} \qquad (Q = 4729.8\,\text{keV}), \tag{1.6}$$
$$^{20}\text{Ne}(\alpha,\gamma)^{24}\text{Mg} \qquad (Q = 9316.6\,\text{keV}). \tag{1.7}$$

The first two reactions are the most important, as they determine the abundances of carbon and oxygen, the fourth and third most abundant elements, respectively.

During this burning, the H-burning will take place in an outer layer of the star, in the H-shell burning.

3α reaction:

As in the case of H-burning and pp chains, it is unlikely that carbon can be produced by the direct fusion of three helium nuclei. This process will therefore take place in two stages.

First of all, two ^{4}He nuclei will fuse into a ^{8}Be nucleus, with the reaction:

$$^{4}\mathrm{He} + {}^{4}\mathrm{He} \rightarrow {}^{8}\mathrm{Be} \qquad (Q = -91.84\,\mathrm{keV}). \tag{1.8}$$

The ^{8}Be is unstable in its fundamental state, with a half-life $T_{1/2} \sim 8 \times 10^{-17}$ s. As a result, it disintegrates into two α as soon as it is formed.

However, the very high density of particles within a star allows the continuous formation of ^{8}Be. In this way, a balance is formed between the creation and destruction of ^{8}Be, ensuring its constant presence.

It is therefore possible for this ^{8}Be to capture an α through the reaction:

$$^{4}\mathrm{He} + {}^{8}\mathrm{Be} \rightarrow {}^{12}\mathrm{C} + \gamma \qquad (Q = 7366.57\,\mathrm{keV}). \tag{1.9}$$

Due to the cross section of the ^{8}Be(α,γ)^{12}C reaction, the abundance of ^{12}C observed in the Universe is only possible through the presence of an excited state around $E_{\mathrm{ex}} = 7.6 - 7.7$ MeV in the ^{12}C nucleus, see Fig. 1.6. This excited state, known as the 'Hoyle state', will be discussed further in section 1.2. Its experimental measurement followed its prediction by a few years later [63; 64].

^{12}C(α,γ)^{16}O reaction:

The 3α reaction induces the creation of ^{12}C, a nucleus that will allow the production of oxygen. With the creation of carbon and the destruction of helium, the density and temperature conditions evolve to a stage where the ^{12}C(α,γ)^{16}O reaction is favoured over the 3α reaction.

However, observations of the abundances of carbon and oxygen in the Universe indicate a ratio of [2]:

$$N_{^{12}\mathrm{C}}/N_{^{16}\mathrm{O}} \approx 0.4, \tag{1.10}$$

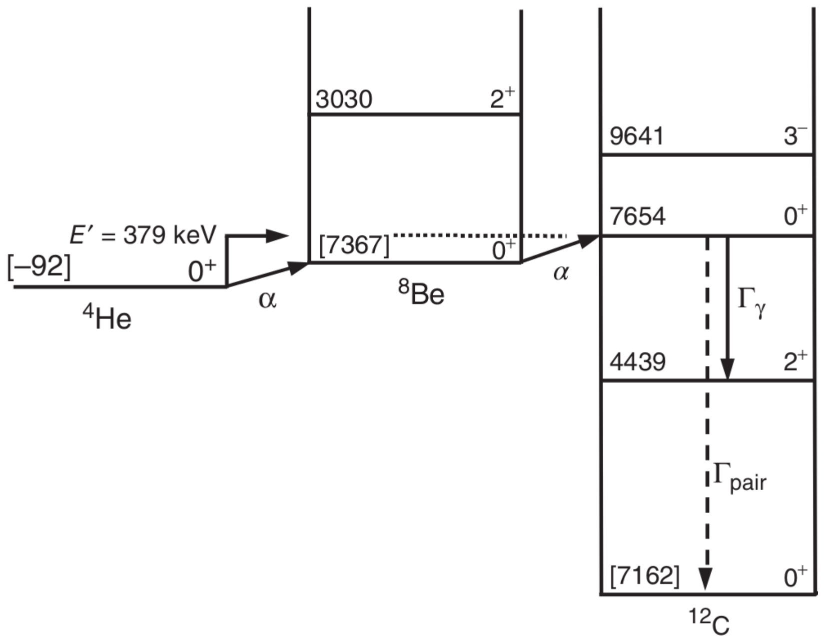

Figure 1.6: Energy levels of ^{4}He, ^{8}Be and ^{12}C. From [2].

where $N_{^{12}\mathrm{C}}$ and $N_{^{16}\mathrm{O}}$ are the abundances of ^{12}C and ^{16}O, respectively. So only a fraction of the ^{12}C is consumed by this reaction. This can be explained by intrinsic properties of the ^{16}O core.

With the typical temperatures of stellar interiors during the He-burning phase, $T =\ 0.2$ GK, the energy at which the reaction takes place is around 300 keV. Thus, taking into account the Q value, we obtain an excitation energy of the order of $E_{\mathrm{ex}} \approx 7.4$ MeV in the oxygen nucleus.

However, as can be seen from the excitation diagram shown in Fig. 1.7, no excited states are present in this energy region. The states at $E_{\mathrm{ex}} = 7117$ keV $(\mathrm{J}^{\pi} = 1^{-})$ and $E_{\mathrm{ex}} = 6917$ keV $(\mathrm{J}^{\pi} = 2^{+})$ have very little influence on this reaction.

Again, nuclear physics may explains how the astrophysical observations are possible.

Stars with an initial mass $M_i < 8M_{\odot}$ will stop evolving at the end of the He-burning phase. This is because their mass is too low for them to acquire a collapse energy capable of exceeding the degeneracy pressure of the electrons. The temperature can therefore no longer rise to sufficiently high level to begin the next phase of combustion.

These stars, like the Sun, will then end up as white dwarfs, an inert object composed of carbon, oxygen and nitrogen, whose hydrostatic equilibrium is maintained by the degeneracy pressure. These objects are placed on the bottom left on the HR diagram.

However, this equilibrium is only valid for masses of less than 1.4 $M_{\odot}$, known as the Chandrasekhar mass. If the mass of the white dwarf was to exceed this limit, by accreting matter from a companion for example, it would give rise to a nova or a type Ia supernova, and induce explosive nucleosynthesis.

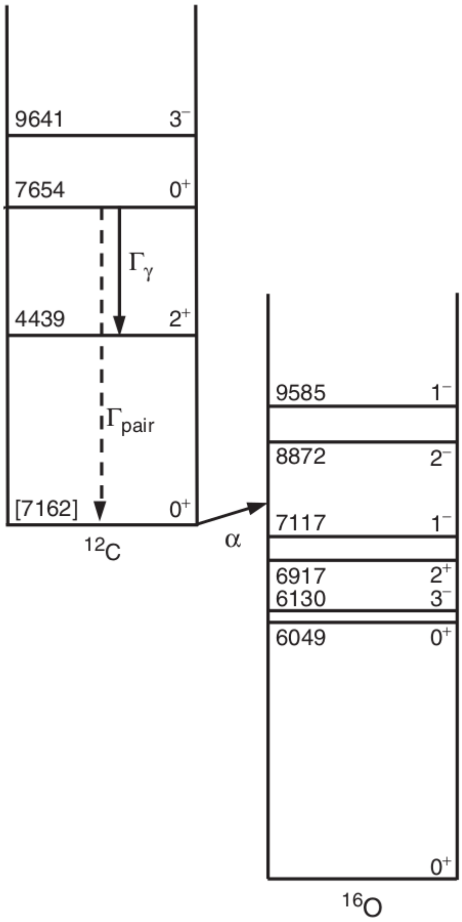

Figure 1.7: Energy levels of ^{12}C and ^{16}O. From [2].

Carbon burning

If the initial mass of the star is high enough, *i.e.* with a initial mass $M_i > 8\ M_\odot$, then the pressure of electron degeneracy will be overcome. The pressure at the centre of the star will continue to increase until the temperature allows new fusion reactions to take place. As the star's core is mainly made up of carbon and oxygen, the reactions that are then possible are ^{12}C + ^{12}C, ^{12}C + ^{16}O or ^{16}O + ^{16}O fusion reactions. It is the ^{12}C + ^{12}C reaction that will take place first, because of its lowest Coulomb barrier $E_{\text{Coulomb}} = 6.6$ MeV.

The star will therefore enter the carbon-burning phase, or C-burning. It will then remain in the Giants or Supergiants branch of the HR diagram.

The ^{12}C + ^{12}C fusion reaction results in the formation of an ^{24}Mg nucleus, with a Q value $Q = 13.93$ MeV. As the ^{24}Mg nucleus has a high excitation energy, it will evacuate this energy *via* three main exit channels:

$$
\begin{aligned}
{}^{12}\mathrm{C} + {}^{12}\mathrm{C} \rightarrow {}^{24}\mathrm{Mg}^* &\rightarrow {}^{20}\mathrm{Ne}^* + \alpha \qquad (Q = 4.62\,\mathrm{MeV}), && (1.11)\\
&\rightarrow {}^{23}\mathrm{Na}^* + p \qquad (Q = 2.24\,\mathrm{MeV}), && (1.12)\\
&\rightarrow {}^{23}\mathrm{Mg}^* + n \qquad (Q = -2.62\,\mathrm{MeV}). && (1.13)
\end{aligned}
$$

Other processes are possible, such as ^{12}C(^{12}C,γ)^{24}Mg or ^{12}C(^{12}C,^{8}Be)^{16}O, but are considerably less important [2].

Carbon fusion generally takes place at temperatures of the order of $T = 0.6-1$ GK depending on the initial mass of the star. Under these conditions the ^{12}C(^{12}C, n)^{23}Mg reaction is endothermic and therefore negligible [65].

The reactions ^{12}C(^{12}C,α)^{20}Ne, ^{12}C(^{12}C,p)^{23}Na and ^{12}C(^{12}C,n)^{23}Mg are called the primary reactions of C-burning. The released light particles will then be available to interact with the nuclei present in the stellar medium, such as the ashes from the He-burning reactions or the ^{20}Ne and ^{23}Na nuclei produced during the primary C-burning reactions. These reactions are called secondary reactions.

The top panel of Fig. 1.8 shows a partial nuclear chart, with the number of proton on the y-axis and the number of neutrons on the x-axis. The primary and secondary reactions that occur during C-burning in the core of a star of 25 $M_\odot$ are represented. The net abundance of the elements transformed during the C-burning, *i.e.* the difference of abundances after and before the C-burning, is represented by the width of the arrows.

The main abundance flows are caused by the primary reactions ^{12}C(^{12}C,α)^{20}Ne and ^{12}C(^{12}C,p)^{23}Na. An important part of the light particles liberated will be consumed by the secondary reactions ^{23}Na(p,α)^{20}Ne et ^{16}O(α,γ)^{20}Ne.

Less important, flows are caused by (p,γ), (α,γ), (α,n) and (n,p) reactions and β^+-decay.

The primary reaction ^{12}C(^{12}C,n)^{23}Mg is also visible as a weak flow. Indeed, removing this reaction from the network has only small effects on the major isotopes. However, this reaction may become important at higher temperatures, as in shell carbon burning.

The evolution of chemical abundances during the C-burning is represented on the bottom panel of Fig. 1.8. The star considered has a core temperature of $T = 0.9$ GK and a central density $\rho = 10^5$ g/cm^3, typical for a star with initial mass $M_i = 25\ M_\odot$.

Among the nuclei with the larger enrichment, there are the ^{20}Ne and ^{23}Na from the primary reactions. The ^{24}Mg is produced in particular by the secondary reactions ^{23}Na(p,γ)^{24}Mg and ^{20}Ne(α,γ)^{24}Mg.

With ^{12}C, the ^{22}Ne quantity strongly decreases during the C-burning. It is transformed into ^{25}Mg through the ^{22}Ne(α,n)^{25}Mg reaction. This reaction is particularly interesting because it contributes significantly to the neutron enrichment of the stellar medium at high temperature. These neutrons will then be at the origin of a large

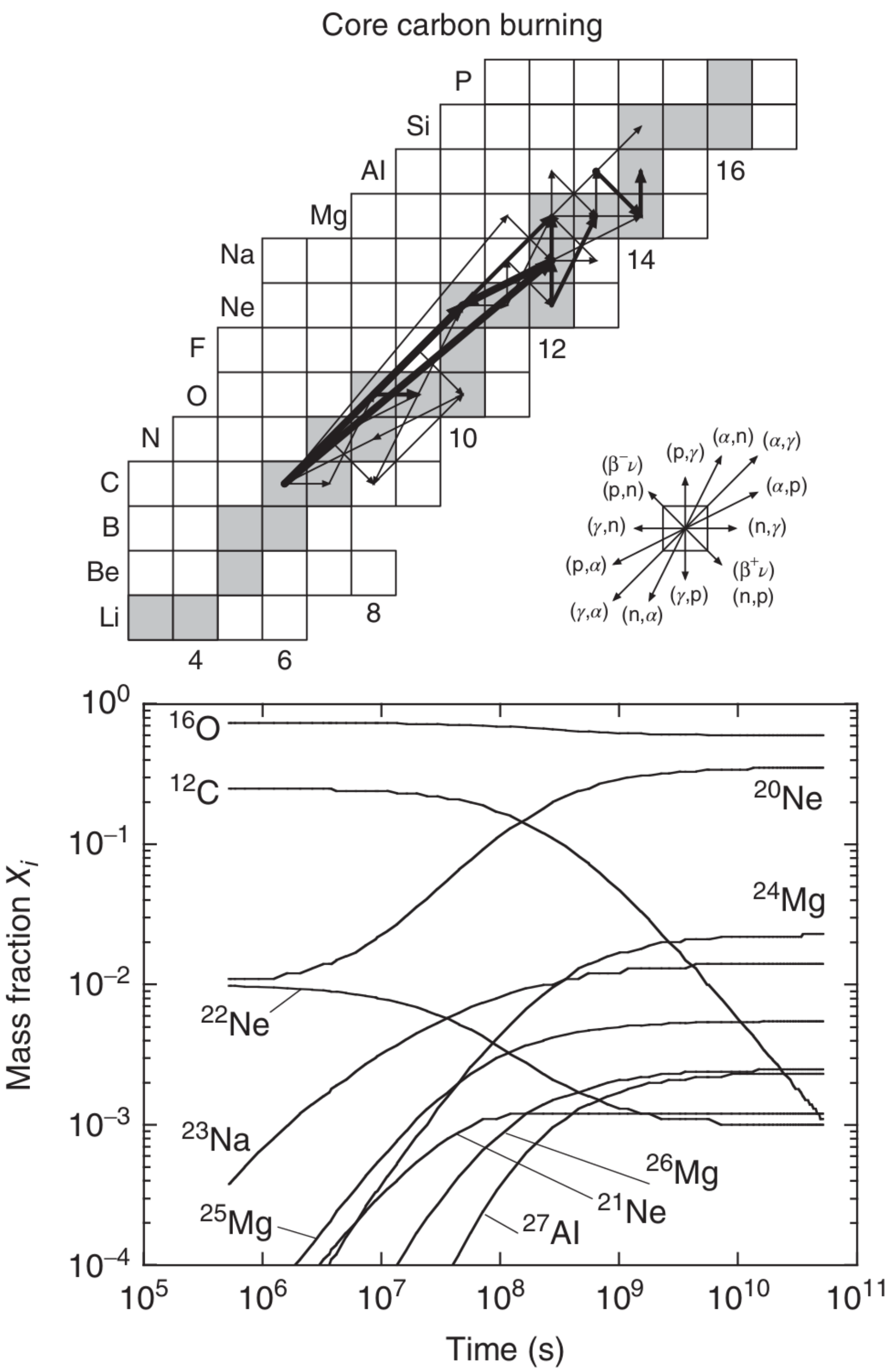

Figure 1.8: Top: Partial nuclear chart highligthing the created nuclei during C-burning. The arrows represent the time-integrated net abundance flows for a 25 $M_{\odot}$ star. Bottom: Evolution of the chemical abundance during C-burning for a 25 $M_{\odot}$ star for a constant temperature and density of $T = 0.9$ GK and $\rho = 10^5$ g/cm^3, respectively. Both are from [2].

number of neutron-induced processes, especially during shell C-burning [42]. For the core C-burning, neutron will be expected to be product by ^{13}C.

The C-burning phase has a lifetime around 1600 years, *i.e.* $t = 5 \times 10^{10}$ s for a typical 25 $M_\odot$ star [2], before the amount of carbon becomes negligible.

Thus, the C-burning and its start are largely dominated by nuclear physics, and more particularly the cross section of the ^{12}C + ^{12}C fusion reaction. However, this reaction is extremely difficult to study in the laboratory, and the results obtained to date are not precise enough to effectively constrain theoretical models, as will be discussed in the next chapter.

There are still major uncertainties surrounding this phase, such as the temperature and density required for it to start. This makes it difficult to determine the mass limit of stars that can begin the C-burning phase, and hence the more advanced burning phases leading to supernovæ.

Advanced burning stages and supernovæ

After C-burning, the star will undergo several subsequent phases of combustion before the end of its life. The main phases it will go through are the neon, oxygen and silicon burning phases, before its core collapses and it explodes into a supernovæ.

During these stages the star will be in the Giant or Supergiants branch of the HR diagram.

Neon burning:

At the end of the C-burning phase, the core of the star is mainly composed of ^{16}O, ^{20}Ne, ^{23}Na and ^{24}Mg. It will then contract and the temperature and density will increase. Although the next most likely nuclear reaction is ^{16}O + ^{16}O fusion, this is not the case. Indeed, before reaching the conditions necessary for this fusion to start, the temperature in the core will reach values where the photodisintegration of the nuclei by photons from the stellar medium becomes dominant ($T < 1$ GK).

Photons in the stellar medium follow the Planck energy distribution, for which the probability of finding N_γ photons with energies between E_γ and $E_\gamma + \mathrm{d}E_\gamma$ per unit volume in a gas at temperature T is defined by:

$$N_\gamma \mathrm{d}E_\gamma = \frac{8\pi}{(hc)^3} \frac{E_\gamma^2}{\exp(E_\gamma/k_B T) - 1} \mathrm{d}E_\gamma. \tag{1.14}$$

At $T = 1.5$ GK, the typical temperature of stellar environments during this phase [53], photons with energies of a few MeV will be able to interact with the nuclei in the star. Among these, ^{20}Ne is the nucleus for which the α emission threshold is the lowest $Q_\alpha = -4.73$ MeV, unlike the emission threshold in the other nuclei which are between 7 and 14 MeV, and the probability of obtaining a photon at these energies is therefore too low.

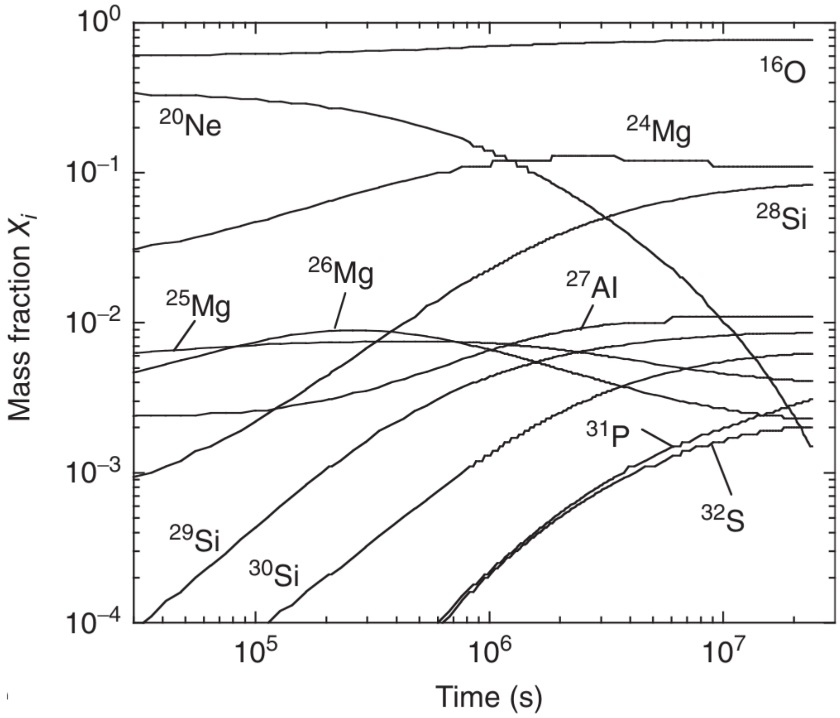

Figure 1.9: Evolution of chemical abundance during Ne-burning for a 25 $M_\odot$ star for a constant temperature and density of T = 1.5 GK and ρ = 5 × 10^6 g/cm^3, respectively. From [2].

The reaction network therefore consists of the primary reaction:

$$^{20}\mathrm{Ne}(\gamma,\alpha)^{16}\mathrm{O} \qquad (Q = -4730.7\,\mathrm{keV}), \tag{1.15}$$

and the secondary reactions:

$$^{20}\mathrm{Ne}(\alpha,\gamma)^{24}\mathrm{Mg}(\alpha,\gamma)^{28}\mathrm{Si} \qquad (Q_{^{20}\mathrm{Ne}(\alpha,\gamma)} = 9316\,\mathrm{keV}), \tag{1.16}$$
$$(Q_{^{24}\mathrm{Mg}(\alpha,\gamma)} = 9984\,\mathrm{keV}), \tag{1.17}$$
$$^{23}\mathrm{Na}(\alpha,\mathrm{p})^{26}\mathrm{Mg}(\alpha,\mathrm{n})^{29}\mathrm{Si} \qquad (Q_{^{23}\mathrm{Na}(\alpha,\mathrm{p})} = 1821\,\mathrm{keV}), \tag{1.18}$$
$$(Q_{^{26}\mathrm{Mg}(\alpha,\mathrm{n})} = 34\,\mathrm{keV}). \tag{1.19}$$

This set of reactions is known as the neon burning phase, or Ne-burning.

The evolution of chemical abundances during the Ne-burning phase is shown in Fig. 1.9, for a star with contant temperature and density $T = 1.5$ GK and $\rho = 5 \times 10^6$ g/cm^3, respectively, typical for 25 $M_\odot$ star. At the end of this phase, the core will be composed mainly of ^{16}O, ^{24}Mg and ^{28}Si, with smaller quantities of other nuclei such as ^{27}Al and ^{29,30}Si, synthesised by successive capture of α particles, protons and neutrons, in competition with β-decays and electron capture [53].

The lifetime of Ne-burning is around 280 days, *i.e.* $t = 2.4 \times 10^7$ s for a typical 25 $M_\odot$ star [2].

Oxygen burning:

At the end of the Ne-burning phase, the star will contract again, and the temperature will rise sufficiently to start oxygen burning, and then enter the oxygen burning phase, or O-burning. This phase takes place at typical temperatures of $T = 1.5 - 2.7$ GK depending on the mass of the star, with $T = 2.2$ GK for a 25 $M_\odot$ star [2].

This phase is similar to the C-burning one, in that a fusion reaction between heavy ions, in this case ^{16}O + ^{16}O, is the primary process that sustains all the nuclear burning.

The ^{16}O + ^{16}O fusion reaction results in the formation of a ^{32}S nucleus, with a Q value $Q = 16.5$ MeV. Since the ^{32}S nucleus has a high excitation energy, it will evacuate its energy via the most likely primary reactions:

$$
\begin{aligned}
{}^{16}\mathrm{O}({}^{16}\mathrm{O},\mathrm{p})^{31}\mathrm{P} &\qquad (Q = 7678\,\mathrm{keV}), &(1.20)\\
{}^{16}\mathrm{O}({}^{16}\mathrm{O},2\mathrm{p})^{30}\mathrm{Si} &\qquad (Q = 381\,\mathrm{keV}), &(1.21)\\
{}^{16}\mathrm{O}({}^{16}\mathrm{O},\alpha)^{28}\mathrm{Si} &\qquad (Q = 9594\,\mathrm{keV}), &(1.22)\\
{}^{16}\mathrm{O}({}^{16}\mathrm{O},2\alpha)^{24}\mathrm{Mg} &\qquad (Q = -390\,\mathrm{keV}), &(1.23)\\
{}^{16}\mathrm{O}({}^{16}\mathrm{O},\mathrm{d})^{30}\mathrm{P} &\qquad (Q = -2409\,\mathrm{keV}), &(1.24)\\
{}^{16}\mathrm{O}({}^{16}\mathrm{O},\mathrm{n})^{31}\mathrm{S} &\qquad (Q = 1499\,\mathrm{keV}). &(1.25)
\end{aligned}
$$

The light particles formed will quickly become involved in secondary reactions with the ashes from the Ne-burning or the daughter particles from the primary reactions. Thus, series of interactions (p,γ), (α,γ), (p,n),... as well as β-decay lead to the production of nuclei in the 30 < A < 40 region.

Figure 1.10 shows the chemical abundance evolution during the O-burning phase, with contant temperature and density of $T = 2.2$ GK et $\rho = 3 \times 10^6$ g/cm^3 respectively, typical for a 25 $M_\odot$ star. At the end of this stage, the core is mainly composed of ^{28}Si, ^{32}S, ^{36,38}Ar and ^{40}Ca [2].

The O-burning phase has a lifetime of about 162 days, *i.e.* $t = 1.4 \times 10^7$ s for a typical 25 $M_\odot$ star. It marks the end of fusion reactions between heavy ions in the cores of massive stars. This is explain by the fact that the Coulomb barriers between the species present at this stage of stellar evolution are too high.

Silicon burning:

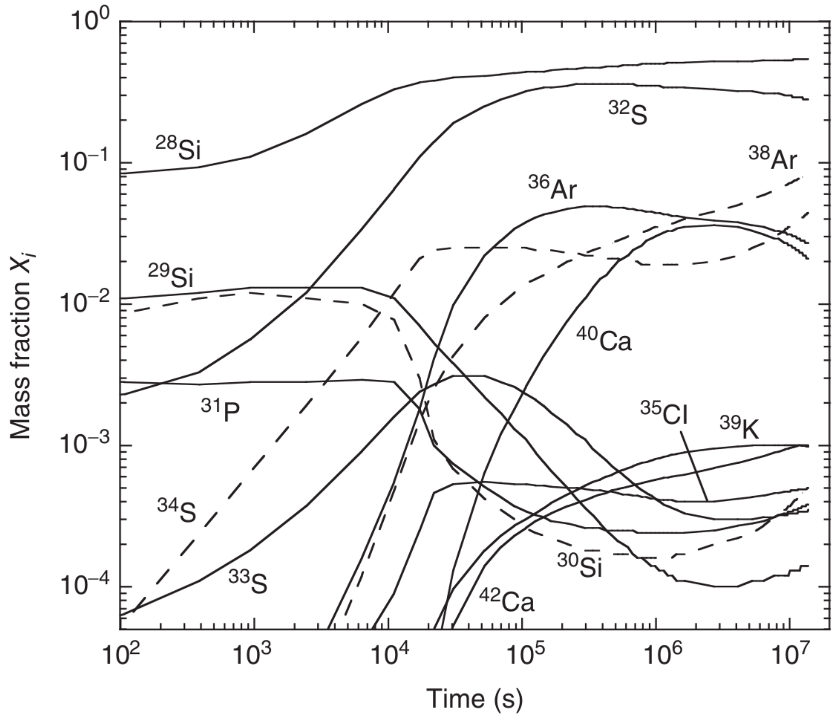

Figure 1.10: Evolution of chemical abundance during O-burning for a 25 $M_\odot$ star for a constant temperature and density of $T = 2.2$ GK and $\rho = 3 \times 10^6$ g/cm^3, respectively. From [2].

The process marking the start of the phase following that of O-burning is the photodisintegration of the two most abundant species at the heart of the star, *i.e.* ^{28}Si and ^{32}S, known as the silicon burning phase or Si-burning.

This phase begins when the temperature reaches the typical value of $T = 3$ GK [53], with the photodisintegration of ^{28}Si. The latter has the lowest proton, neutron and α separation energies [66], and will be destroyed first *via* the reactions (γ,p) and (γ,α) mainly.

The light particles emitted after photodisintegration will then interact with the nuclei present in the stellar medium. The evolution of chemical species during Si-burning is shown in Fig. 1.11 for a 25 $M_\odot$ star, with constant temperature and density of $T = 3.6$ GK and $\rho = 3 \times 10^7$ g/cm^3, respectively. At the end of this phase the core of the star is mainly composed by nuclei around iron and nickel, mass region where the species are the most strongly bound in the nuclei chart.

Silicon burns very quickly, the ^{28}Si is indeed consumed in just a few hours for a typical 25 $M_\odot$ [2].

Explosive burning and supernovæ:

After the Si-burning, the nuclear reactions at the heart of the star stop very quickly.

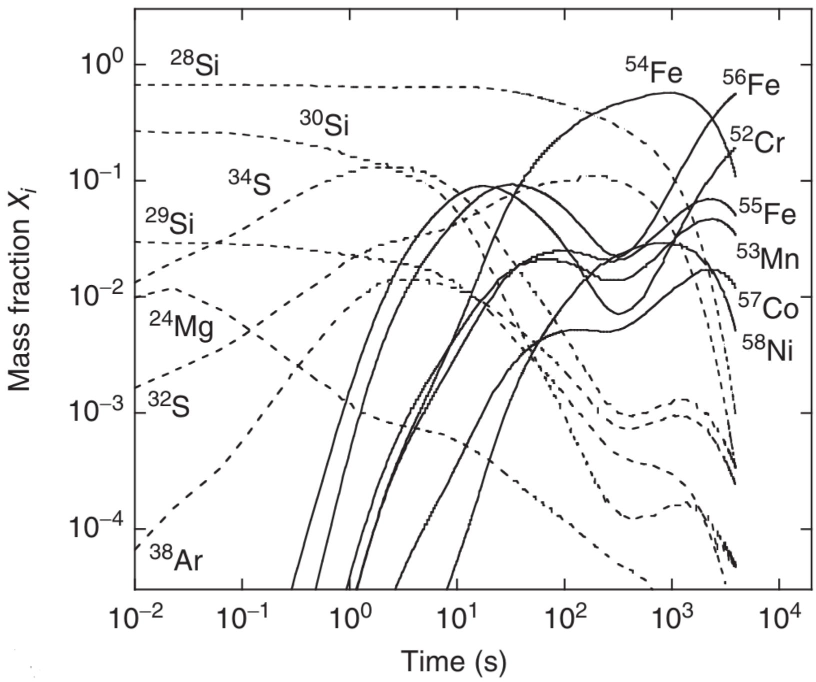

Figure 1.11: Evolution of chemical abundance during Si-burning for a 25 $M_\odot$ star for a constant temperature and density of $T = 3.6$ GK and $\rho = 3 \times 10^7$ g/cm^3, respectively. From [2].

The core will collapse in on itself under the effect of gravitational contraction. The density will then increase dramatically, until it reaches the stage where the electrons contained in the plasma recombine with the protons in the nuclei, in general giving rise to a neutron star. This event, known as a supernova, greatly enriches the interstellar medium.

This end of life is the site of explosive nucleosynthesis, and allows the formation of a large multitude of intermediate and heavy nuclei, through various processes such as p-capture and n-capture [53].

The neutron stars that emerge from this end of life also play an important role in nucleosynthesis. The merger of two neutron stars, known as a kilonova, is a favourable site for the synthesis of heavy, neutron-rich nuclei [58; 59].

1.2 Importance of Nuclear Physics

1.2.1 Reaction rates

Definition

As seen in 1.1.2, the rate of energy production q requires a nuclear parameter: the nuclear reaction rate r. The latter is the rate at which a nuclear reaction takes place, proportional to the concentration of the reactants in a defined volume per time.

This parameter is determined from the considered nuclear reaction cross section, which can be derived by experimental measurements or theoretical determination.

The reaction rate generally used for the study of ^{12}C + ^{12}C fusion reaction was determined by Caughlan & Fowler [21], hereafter refered as CF88. This model is based on the fusion description by the penetration of an optical potential well.

The reaction rate r is given by:

$$R = N_x N_y \langle \sigma v \rangle (1 + \delta_{xy})^{-1}, \tag{1.26}$$

where N_x and N_y are the number of particles for species x and y respectively, δ_{xy} is the Kronecker delta, and prevents double counting when two identical particles are involved in the interaction, v is the relative velocity between both particles and σ is the reaction cross section.

In an astrophysical context, the stellar reaction rate is defined as:

$$r = N_A \langle \sigma v \rangle. \tag{1.27}$$

Indeed, in this context one consider, given the sheer number of particles that can interact with each other, that this number is the Avogadro number N_A, and double counting is neglected. The term describing the reaction probability, $\langle \sigma v \rangle$, can be written:

$$\langle \sigma v \rangle = \int_0^\infty \sigma(v)\ v\ \phi(v)\ dv, \tag{1.28}$$

where $\phi(v)$ is the velocity distribution of the particles. In a star, the available energy of the particles comes from thermal motion. Under normal stellar interior conditions, *i.e.* composed of non-degenerated and non-relativist matter, the gas is in thermodynamical equilibrium. The particles velocity can be described by the Maxwell-Boltzmann velocity distribution:

$$\phi(v_i) = 4\pi v_i^2 \left(\frac{m_i}{2\pi k_B T} \right)^{3/2} \exp\left(-\frac{m_i v_i^2}{2 k_B T} \right), \tag{1.29}$$

where k_B is Boltzmann's constant, T the temperature of the gas, and m_i and v_i the mass and velocity of the particle i.

By replacing the velocity dependence with the energy dependence *via* the formula:

$$E = \frac{\mu v^2}{2}, \tag{1.30}$$

where μ is the reduced mass of the system, the probability of interaction per pair of particles is:

$$\langle \sigma v \rangle = \left(\frac{8}{\pi\mu}\right)^{1/2} \frac{1}{(k_B T)^{3/2}} \int_0^\infty \sigma(E) E \exp\left(-\frac{E}{k_B T}\right) dE, \tag{1.31}$$

where E is the kinetic energy of the system, and $\sigma(E)$ the cross section of the reaction at the energy E considered. The understanding and knowledge of the dependence of the cross section on the energy is the main objective and main challenge of the nuclear physics experiments and theoretical models.

Gamow window and *S*-Factor

In order to calculate reaction rates for astrophysical interest, it is necessary to know in which energy range the associated cross section is determined.

Equation 1.29 describes the probability for a particle at the energy $E = \frac{1}{2}mv^2$ in a gas at the temperature T. The probability maximum is around the energy $E_{\text{th}} = k_B T$, which is generally much lower than the Coulomb barrier.

For example, for a core temperature of 10^9 K, which corresponds to the core temperature of a massive star during the C-burning, $E_{\text{th}} = 8.6 \times 10^{-2}$ MeV. To compare, the Coulomb barrier of the $^{12}C + ^{12}C$ system is $E_{\text{Coulomb}} = 6.6$ MeV.

Within a strictly classical frame, the carbon fusion is then impossible.

Therefore in astrophysical process, the cross section is mainly dominated by tunneling effect. In that case, as a first approximation the interaction probability decreases exponentially with the energy:

$$\sigma(E) \propto \exp(-2\pi\eta), \tag{1.32}$$

where η is the Sommerfeld parameter:

$$\eta \equiv \frac{Z_1 Z_2 e^2}{\hbar v}. \tag{1.33}$$

The geometric part of the cross section is proportionnal to the de Broglie wavelength λ:

$$\sigma(E) \propto \pi\lambda^2 \propto \frac{\pi h^2}{p^2} \propto \frac{1}{E}. \tag{1.34}$$

By combining both terms, the cross section can be written as:

$$\sigma(E) = \frac{1}{E} \exp(-2\pi\eta) S(E), \tag{1.35}$$

where $S(E)$, which is defined by this equation, is called the astrophysical S-factor. It contains the effects caused by strong interaction, that rules nuclear force. By removing the exponential dependence of the cross section, the S-factor varies less with energy, which favours the reading of astrophysical data and theoretical models.

By combining the Eq. 1.31 and 1.35, $\langle\sigma v\rangle$ can be written:

$$\langle\sigma v\rangle = \left(\frac{8}{\pi\mu}\right)^{1/2} \frac{1}{(k_B T)^{3/2}} \int_0^\infty S(E) \exp\left(-\frac{E}{k_B T} - \frac{b}{E^{1/2}}\right) dE, \tag{1.36}$$

where b, in $\mathrm{MeV}^{1/2}$, is defined:

$$b \equiv \frac{(2\mu)^{1/2}\pi e^2 Z_1 Z_2}{\hbar}. \tag{1.37}$$

Assuming a slow variation of the S-factor, the reaction propability is dominated by the exponential term, and will be maximum when the latter is minimum. By differentiating this term and setting the result to zero to find the minimum, one obtains:

$$\frac{1}{k_B T} - \frac{b}{2E^{3/2}} = 0. \tag{1.38}$$

The solution is given by the so-called Gamow energy E_0, defined as:

$$E_0 = \left(\frac{b k_B T}{2}\right)^{2/3}, \tag{1.39}$$

which corresponds to the maximum interaction probability between two particles of relative velocity v in the stellar medium.

Figure 1.12 illustrates the relative interaction probability between two particles, where the probability of fusion through tunneling is in red, and the Maxwell-Boltzmann energy distribution is in blue. The convolution between this two distributions gives a peak centered around E_0, called Gamow peak or Gamow window, with a characteristic width:

$$\Delta = \frac{4}{\sqrt{3}}\sqrt{E_0 k_B T}. \tag{1.40}$$

In other words, for a given system at a given temperature in a stellar medium, the majority of fusion reactions occurs in an energy range corresponding to the Gamow window. It is therefore within this energy range that nuclear experiments and theoretical models must seek to determine the cross section for astrophysical interests.

1.2.2 Deep sub-barrier cross section

As described previously, the reaction rate, and therefore the evolution of stars, are conditioned by the cross sections. The global and general behaviour of the latter, also influenced by nuclear structures effects.

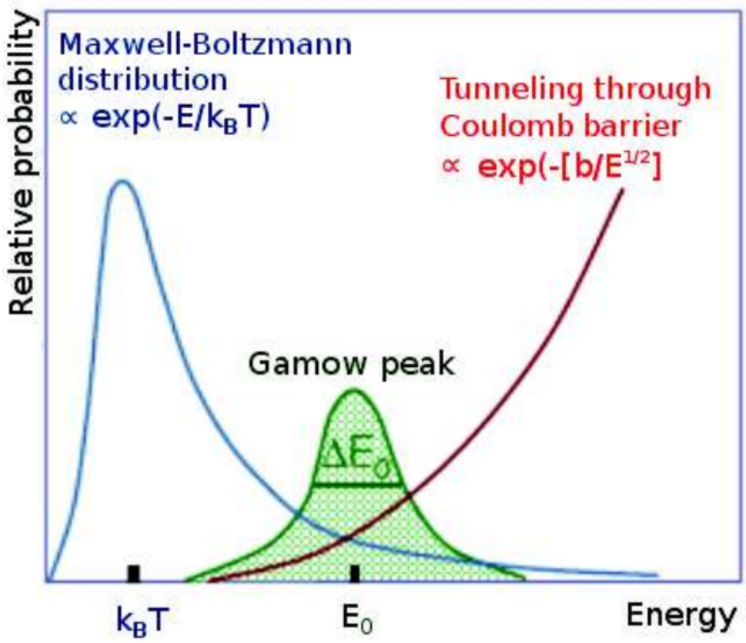

Figure 1.12: Representation of the Gamow peak (green), defined by the convolution of the Maxwell-Boltzmann distribution (blue) and the tunneling through the Coulomb barrier (red). The Gamow peak can be fitted by a gaussian, with a mean E_0. From [6].

In this work, two behaviours that have a important impact at deep sub-barrier energies are studied: resonances and fusion hindrance.

Resonances

A resonance is a structure in the cross section that can be seen as a strong local or broad increase at a specific energy. A cross section can have none, one or several resonances.

These structures have been observed since the first studies of the ^{12}C + ^{12}C system in the 1960s [20]. They have been measured at energies ranging from a few MeV/A down to deep sub-barrier energies, *i.e.* at energies of astrophysical interest. They are particularly pronounced around the Coulomb barrier, $E_{\text{Coulomb}} = 6.6$ MeV. However, the origin of these resonances is still under debate, and two possible interpretations will be discussed: molecular states, and the level density in ^{24}Mg.

Molecular states:

The first mention of a molecular state in the carbone was made in the 1950s by Hoyle [67], to explain the abundance of ^{12}C observed in the Universe. In fact, the cross section of the ^{8}Be(α,γ)^{12}C reaction, which is responsible for the formation of ^{12}C, is not high enough to explain its observed abundance. Considering the Q value of the reaction, Hoyle predicted an excited state in ^{12}C at an energy $E_{\text{ex}} = 7.6 - 7.7$ MeV for the reaction ^{8}Be(α,γ)^{12}C to take place. Soon later, a 0^+ state at $E_{\text{ex}} = 7654$ keV was measured [63; 64]. The nuclear structure at the origin of this excited state is still debated [68].

In the ^{12}C + ^{12}C cross section the resonant peaks around $E_{\rm com} = 5 - 7$ MeV are correlated in the different exit channels, suggesting the population of molecular configuration during the reaction, and ruling out statistical fluctuations [69].

This is reinforced by the width of the resonances, of the order of $\Gamma = 150$ keV, which are narrow and therefore associated with a long-lived state. The width of a resonance is related to the τ lifetime by:

$$\tau = \frac{\hbar}{\Gamma}, \tag{1.41}$$

which gives $\tau \approx 4.5 \times 10^{-21}$ s for a width of 150 keV. This lifetime is longer than the time for a nucleon to go through a nucleus at Fermi energy, which is $\sim 1.1 \times 10^{-22}$ s, suggesting that this resonant effects are not from surface effects. However, a compound nucleus takes around 10^{-18} s to stabilize. The lifetime of the resonances of the system ^{12}C + ^{12}C is thus in an intermediate situation.

One should note that the energy loss of the beam in the target is around 100 keV, *i.e.* of the same order than the measured resonances widths. These could be narrower, but the experimental resolution does not allow more precise measurements.

The first theoretical description associated with these results suggests the formation of a di-nuclear molecule, composed of two ^{12}C nuclei in the entry channel [70]. The potential considered then presents a shallow well in which the two ^{12}C nuclei keep their identity, before a possible penetration of the Coulomb barrier and the formation of a ^{24}Mg compound nucleus.

Such molecular structures were also suggested to exist in the vicinity of the emission threshold of the sub-systems. In our case, the emission threshold of two ^{12}C nuclei in ^{24}Mg is at $E_{\rm ex} = 13.93$ MeV, *i.e.* the minimum energy required for the formation of a ^{12}C-^{12}C state in ^{24}Mg. The description of these configurations and their associated energies has been carried out by Ikeda *et al.* [7], and is shown in the top panel of Fig. 1.13 for the α-conjugated nuclei.

More recently, the structure of these nuclei has been calculated from first principle by Energy Density Functional theory (EDF) by Ebran *et al.* [8]. The results can be seen in the bottom panel of Fig. 1.13. The first line represents the ground state of each nucleus, and as for the Ikeda diagram, the deformation increases with the excitation energy. The ^{12}C-^{12}C molecular configuration in ^{24}Mg is also reproduced and framed in black in the figure.

<u>^{24}Mg Level Density:</u>

Other approaches are being studied to understand the origin of the resonant structures observed in the ^{12}C + ^{12}C system. One of these is to exploit the differences

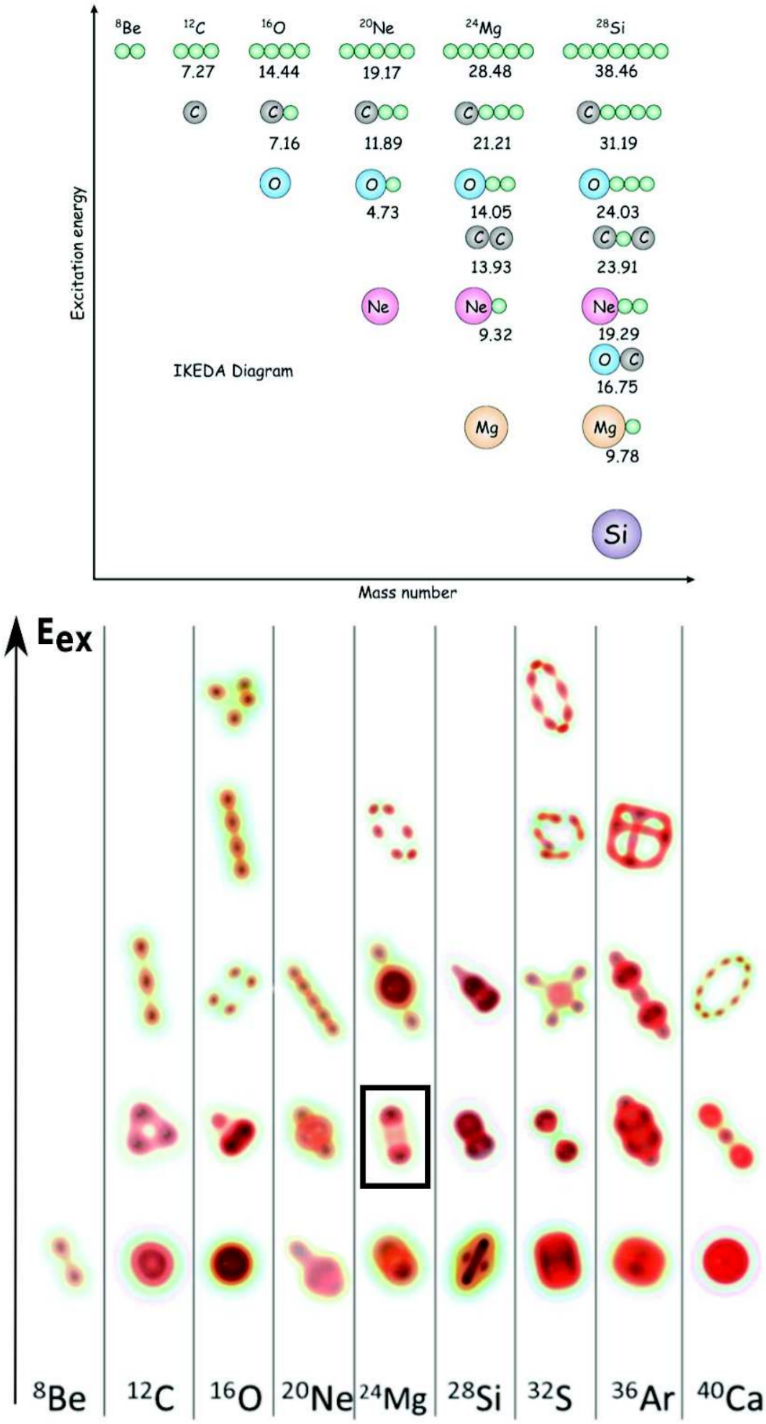

Figure 1.13: Top: Ikeda diagram showing α-cluster states in several nuclei, with their associated excitation energy in MeV. From [7]. Bottom: Molecular configurations computed with theory. The bottom lign corresponds to the ground state of each nuclei. The ^{12}C-^{12}C cluster state in the ^{24}Mg is framed in black. From [8].

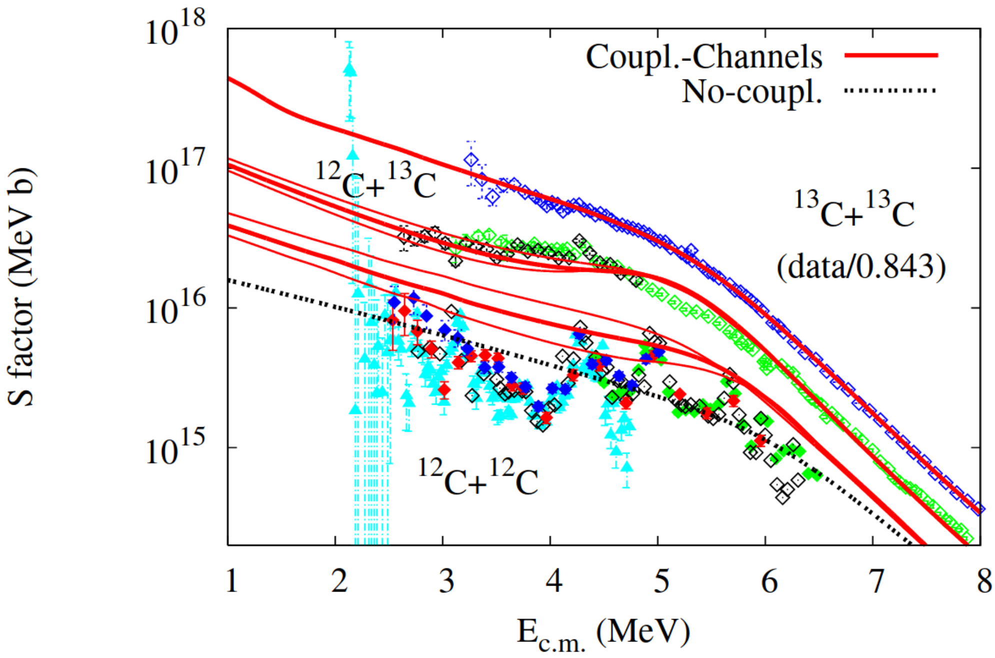

Figure 1.14: Comparaison of excitation functions for $^{12}C + ^{12}C$, $^{12}C + ^{13}C$ and $^{13}C + ^{13}C$ systems, with CC-calculations. From [9].

observed between the excitation function of the $^{12}C + ^{12}C$ fusion and those of neighbouring fusion reactions, the $^{12}C + ^{13}C$ and $^{13}C + ^{13}C$ reactions. In fact, the excitation functions of these last two systems do not show any apparent oscillations. The idea would then be to compare the nuclear structure properties of these systems with those of the $^{12}C + ^{12}C$ system, in order to find differences that would explain these contrasts in behaviour.

Calculations aimed at obtaining a description of the cross sections of these three systems simultaneously have been carried out by Esbensen *et al.* [9]. The results, employing Couple-Channels calculations (CC-calculations), are shown in Fig. 1.14. They show that the calculations can reproduce the experimental data for the systems $^{12}C + ^{13}C$ and $^{13}C + ^{13}C$, but not for $^{12}C + ^{12}C$. For the latter, the calculations are comparable with the experimental data only at the resonance peak, except for the last resonance at $E_{com} = 2.14$ MeV. One explanation put forward is the existence of a suppression of the cross section of the $^{12}C + ^{12}C$ fusion compared with other systems.

Following this, Jiang *et al.* [10] studied the density of levels present in the compound nuclei for each of the three reactions. The hypothesis proposed is that a deficit of states that can be populated in the ^{24}Mg during fusion causes this difference between theoretical calculations and experimental data observed in ^{12}C.

Figure 1.15 shows a comparison of the total density of state ρ_{tot} as a function of excitation energy U for ^{24}Mg, ^{25}Mg and ^{32}S, compound nuclei from $^{12}C + ^{12}C$, $^{12}C + ^{13}C$ and $^{16}O + ^{16}O$ fusion, respectively.

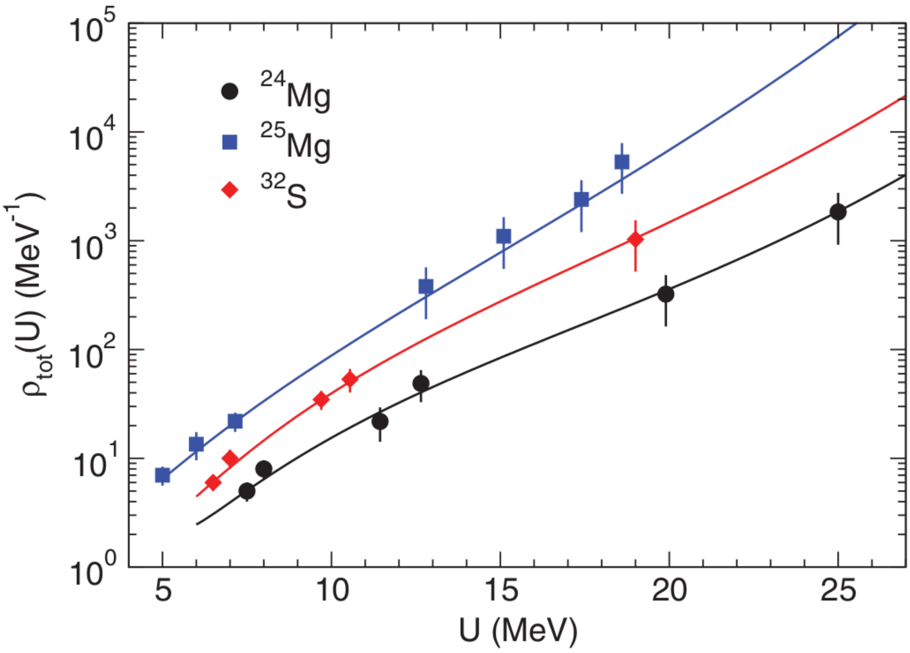

Figure 1.15: Level densities as a function of the excitation energy in ^{24}Mg, ^{25}Mg and ^{32}S. From [10].

The results obtained indicate that the ^{24}Mg nucleus has a density of levels approximately three times lower than that of ^{25}Mg.

There are several possible explanations for this lack of density in levels.

The first is due to the difference in Q value: the ^{12}C + ^{12}C reaction has the lowest value, followed by ^{12}C + ^{13}C and then ^{16}O + ^{16}O. This means that the zone explored in terms of energy in ^{25}Mg and ^{32}S will be higher, and therefore made up of a greater number of states that can be populated during fusion.

A second explanation comes from the fact that the ^{12}C + ^{12}C reaction involves the fusion of two $J^{\pi} = 0^+$ nuclei (bosons). Only positive even spin-parity states are accessible in the compound nucleus, which reduces the number of states available.

Consequently, the average spacing between two states, noted D, will be wider in the case of ^{24}Mg than ^{25}Mg and ^{32}S. For comparing the average spacing between states with the width Γ of the latter, the ratio Γ/D is used.

In the situation where $\Gamma/D > 1$, the width of the states is greater than their average spacing, and there is a strong overlap between the different levels of the compound nucleus.

If $\Gamma/D < 1$, then the spacing between the levels is larger than the width of the states, which do not overlap, thus limiting the possibility of compound nucleus formation.

The results obtained with Fig. 1.15 show that the first case corresponds to the ^{25}Mg and ^{32}S compound nuclei, while the second configuration ressembles more closely to the ^{24}Mg situation.

In this interpretation, a reduced phase space at sub-barrier energies is the origin of the cross section drops in $^{12}C + ^{12}C$. In this picture, resonances are isolated states in ^{24}Mg accessible during fusion.

Fusion hindrance

While resonances reflect local behaviour of the cross section, it is also important to considere the global trend of the excitation function. Knowing this is essential for extrapolating to energies of astrophysical interest.

The phenomenon of fusion hindrance predicts the suppression of the cross section at very low energies. This phenomenon has been observed experimentally in systems with intermediate masses, and studies are underway to determine its presence in the $^{12}C + ^{12}C$ system.

Discovery and theoritical hypothesis:

This phenomenon was first observed by Jiang *et al.* [71], with the measurement of the cross section of several systems. The results obtained were lower than those predicted by the theoretical models, CC-calculations and the Wong formula [72], which are known to describe the cross sections of intermediate-mass systems very well. Discrepancies between theoretical models and experimental data were observed from the Coulomb barrier.

This discovery was confirmed in 2004 with a study of the cross section of the $^{64}Ni + ^{64}Ni$ fusion reaction [11], shown in Fig. 1.16. Measurements were carried out around and below the Coulomb barrier, and two CC-calculations were added for comparison. The results of the calculations describe the experimental data very well down to an energy $E_{\text{lab}} \approx 176$ MeV. Below this energy, the experimental cross section decreases very rapidly, and the theoritical models cannot reproduce it. primordiales In order to explain this phenomenon of fusion suppression, various theoretical approaches have been employed, all seeking to modify the interaction potential used in the calculations.

The first attempt to explain fusion hindrance was proposed by Mişicu *et al.* in 2006 [12], by phenomenologically introducing the incompressibility properties of matter into the calculation of the M3Y (Michigan-3-Yukawa-Reid) potential. Indeed, nuclei are composed of fermions, and quantum state overlap is forbidden by Pauli's principle.

This property can be seen at very low interaction energies, when the two nuclei are at a small distance $r < R_1 + R_2$, where R_1 and R_2 are the radii of the two nuclei under consideration. Under these conditions, the density of fermions in a small volume is very high, and the idea behind this explanation is that this density cannot exceed a certain value. This has the effect of producing a repulsive core within the interaction potential. Jiang *et al.* [73] interpreted and studied this theoretical model with what is called the "sudden approximation": the reaction takes place so suddenly that the density is doubled on the overlapping region of the projectile and the target nuclei.

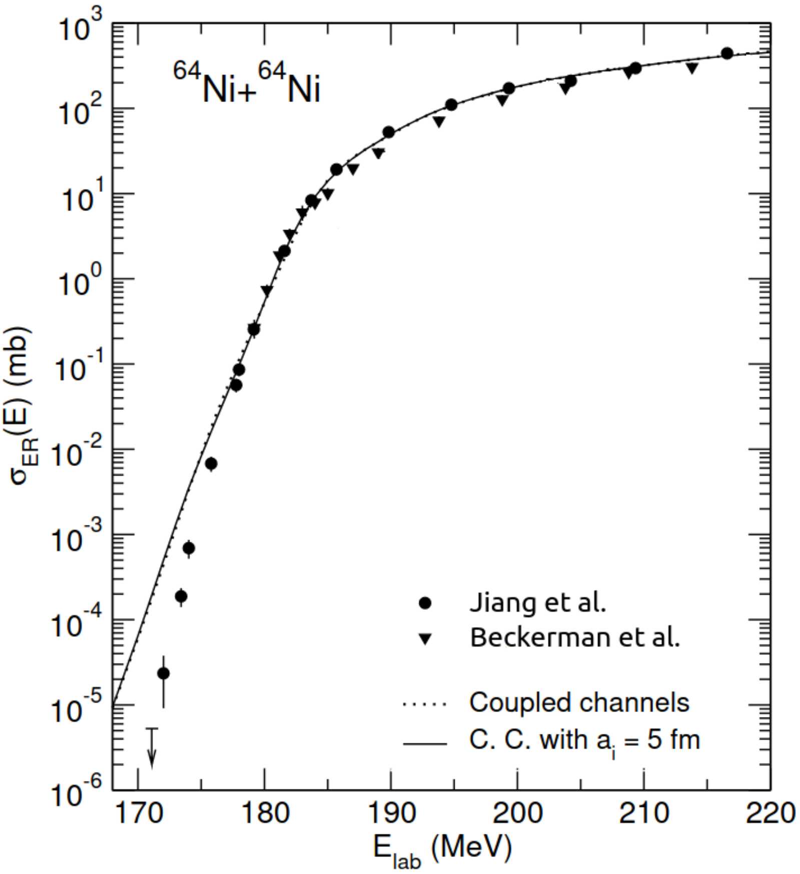

Figure 1.16: Cross section for ^{64}Ni + ^{64}Ni fusion reaction. Adapted from [11].

The resulting potential is shown in the upper panel of Fig. 1.17. The blue and black potentials do not take into account the incompressibility of matter, unlike the red potential. It is possible to note the appearance of a more shallow well in the nuclear potential, but also a widening of the Coulomb barrier. Thus, for collisions at energies below the Coulomb energy, the possibility of penetrating the barrier will be reduced.

The cross sections obtained with CC-calculations for these different potentials and their comparison with experimental measurements can be seen in the lower panel of Fig. 1.17. The red result, obtained with the potential containing the repulsive core, reproduces the data below the Coulomb barrier, unlike the other models. The green curve represents the uncoupled limit, where only the ground states of the target and projectile nuclei are taken into account.

In 2017, Simenel *et al.* [13] were also interested in this suppression of fusion. They explicitly introduced the Pauli exclusion principle into Hartree-Fock (HF) calculations. Thus, as in previous work, the density of nucleons in a restricted volume is limited, and so fusion will be reduced, in particular at sub-barrier energies. An interaction potential is derived from this method, called Density Constrained Frozen Hartree-

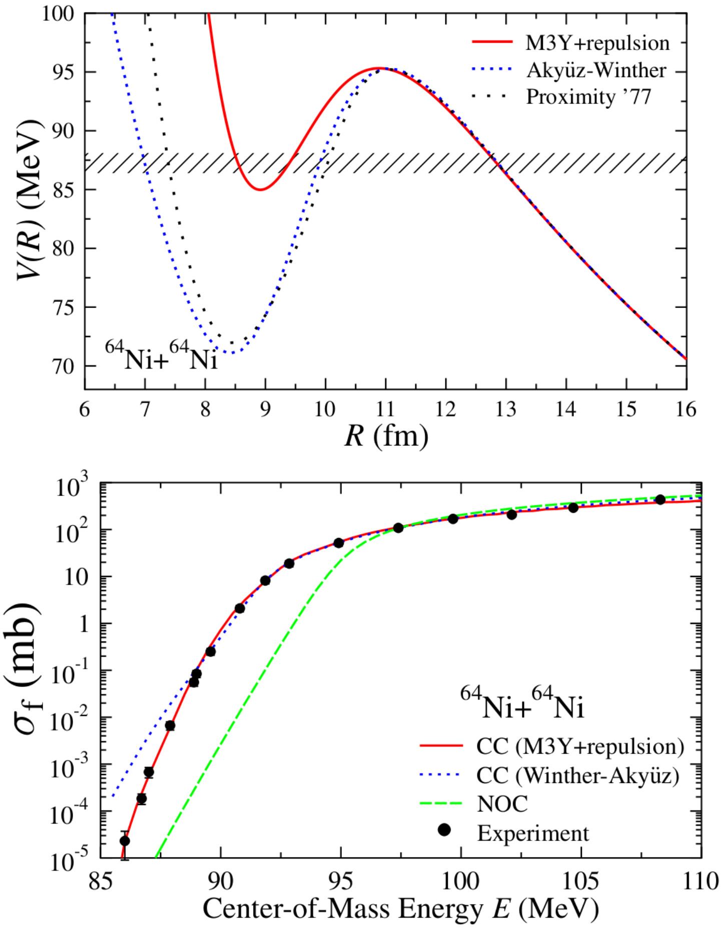

Figure 1.17: Top: Nuclear potential as a function of the distance for ^{64}Ni + ^{64}Ni system. Bottom: Cross section for ^{64}Ni + ^{64}Ni fusion reaction. Both figures are from [12].

Fock (DCFHF), and compared with HF calculations that do not explicitly include the Pauli principle, called Frozen Hartree-Fock (FHF) potential.

The effects of Pauli repulsion on the nucleus-nucleus potentials are shown in Fig. 1.18 for the ^{48}Ca + ^{48}Ca system. In the upper panel the DCFHF potential is shown in red, while the FHF is shown in blue. The associated cross sections are also shown in the lower panel. The potential obtained shows the appearance of a shallow pocket inside the potential well, and a widening of the barrier. Using the DCFHF potential gives a good reproduction of the experimental cross sections.

A dynamic approach was explored by Godbey *et al.* [14], the Density Constrained Time Dependent Harthree-Fock (DCTDHF), allowing the calculated ion-ion fusion barrier to take into account changes in the nuclear density.

The effects of dynamical proccesses do not affect high energy fusion, and give similar results as the frozen calculations, but impact the sub-barrier energies.

Fusion hindrance in ^{12}C + ^{12}C:

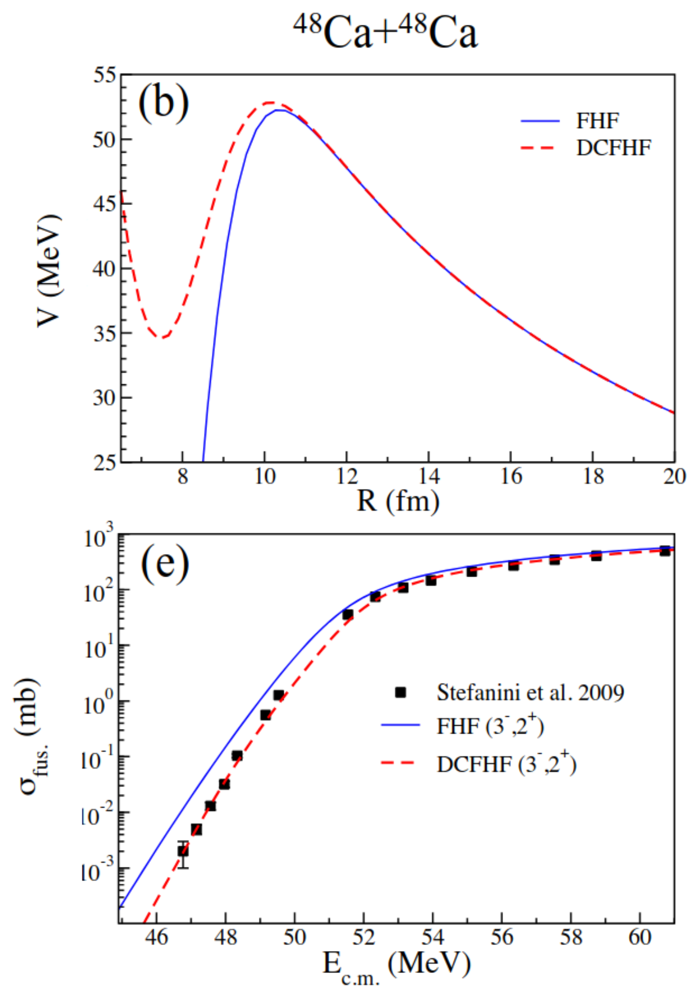

Figure 1.18: Top: Interaction potential for ^{48}Ca + ^{48}Ca. Bottom: Cross section for ^{48}Ca + ^{48}Ca fusion reaction. Both figures are from [13].

In this paragraph, the results will be discussed in term of S-factors. In fact, the latter has the characteristic of presenting a maximum at the energy when fusion hindrance begins to manifest itself.

The effects of fusion hindrance on the ^{12}C + ^{12}C system are still debated today.

With the CC-calculations, the M3Y and M3Y repulsive potentials only reproduce the maximum of the resonances, but do not show a maximum of the S-factor. The DCTDHF and DCFHF potentials do not predict a maximum of the S-factor either.

Figure 1.19 shows the S-factor of the ^{12}C + ^{12}C fusion reaction. Different theoretical models are displayed, DC-TDHF using two different forces in dashed black and dashed-dotted purple, DCFHF in plain black and FHF in dotted black. A phenomenological hindrance model proposed by Jiang *et al.* [17] is also represented in plain red.

It can be noted that the dynamical effects in the DCTDHF model seems to reduce

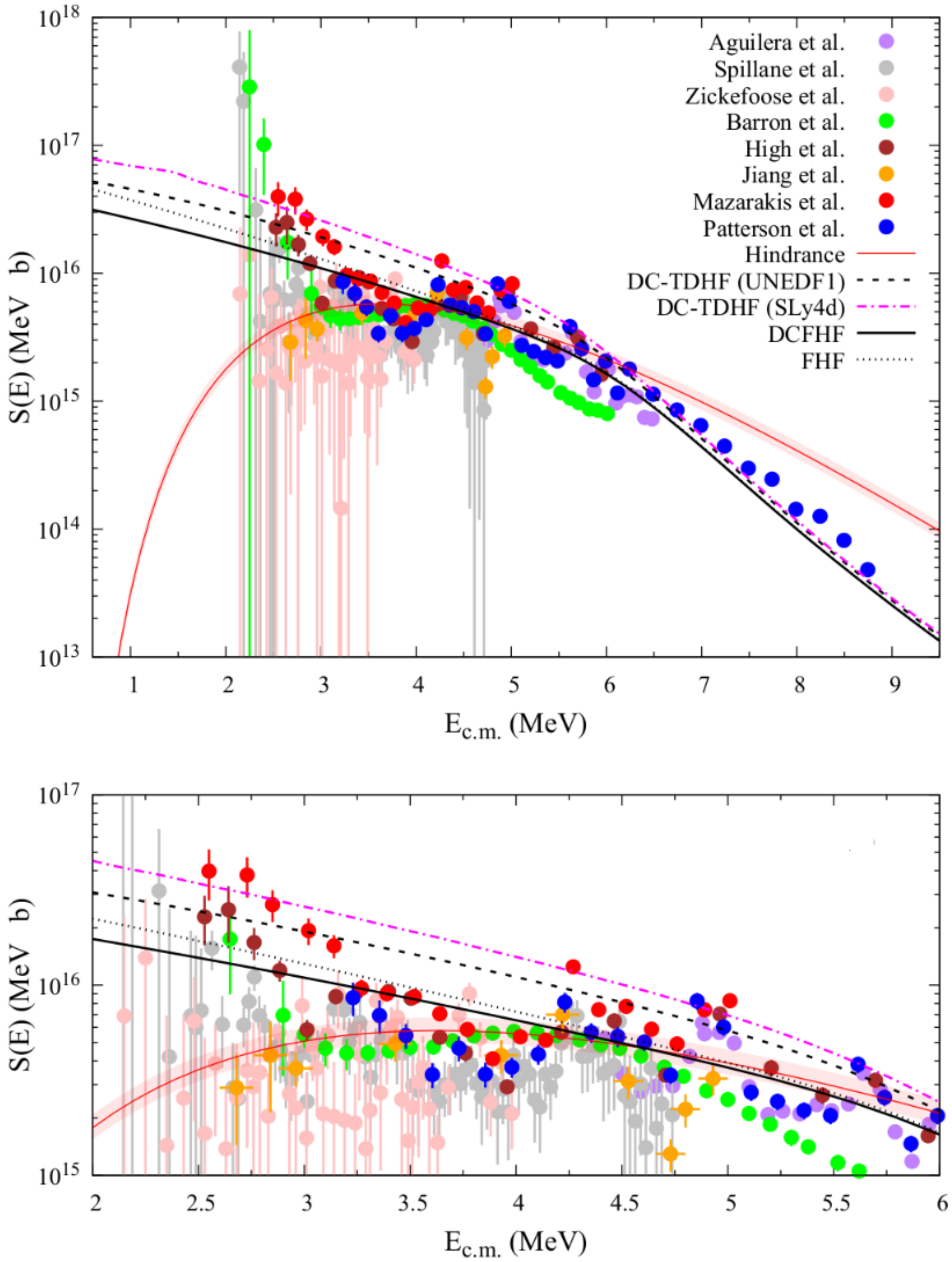

Figure 1.19: Top: S-factor for $^{12}C + ^{12}C$ fusion reaction, represented with different theoretical models. Bottom: Zoom on the sub-barrier measurements. From [14].

the Pauli repulsion in comparaison to the DCFHF one. The DCTDHF model, as the CC-calculations, follows the top of the resonances.

The hindrance model proposed by Jiang *et al.* was developed to describe the sub-barrier fusion hindrance. This model is based on a logarithmic derivative parametrised to fit data, with a boundary condition: when the energy approaches zero, the cross section must be finite and the logarithmic derivative diverges to infinity. The model also shows a maximum in S-factor.

The cross section hindrance parametrization is:

$$\sigma(E)_{\mathrm{Hin}} = \sigma_s \frac{E_s}{E} \exp\left(A_0(E - E_s) - \frac{2B_0}{\sqrt{E_s}}\left(\left(\frac{E_s}{E}\right)^{N_p-1} - 1\right)\right), \tag{1.42}$$

where the parameters E_s and σ_s are the center of mass energy in MeV and the total cross section in mb for which the astrophysical S-factor $S(E)$ is maximum, N_p has a fixed value at 1.5, and A_0 and B_0 are fit parameters.

Results from previous STELLA experimental campaigns [27; 28] with measurements of $^{12}C + ^{12}C$ fusion cross sections at energies of astrophysical interest are in good agreement with the hindrance model proposed by Jiang *et al.* in the energy range $E_{\mathrm{com}} = 2.1 - 5.5$ MeV.

1.2.3 Impact on astrophysical scenarios

As mentioned previously, standard models of stellar evolution commonly use CF88 reaction rates [21] for heavy/light ion fusion reactions. However, as seen in the previous section, the behaviour of the cross section at sub-barrier energies, *i.e.* at energies of astrophysical interest, such as resonances and the fusion hindrance phenomenon, can greatly influence this. The associated reaction rate can then increase or decrease, and thus have an impact on the astrophysical scenarios.

This is particularly the case for the $^{12}C + ^{12}C$ fusion reaction, which at low energies, and therefore at energies of astrophysical interest, potentially presents resonances as well as a fusion hindrance phenomenon.

Several studies have been carried out to understand these impacts on the evolution of massive stars or on the start of the explosive scenario linked to the accretion of matter by a compact object in a binary system.

Evolution of massives stars

The evolution of stars as a function of different reaction rates has been studied by Pignatari *et al.* [15], who worked on the different behaviours of the cross section on the evolution of a 25 $M_\odot$ massive star, on the nuclesosynthesis pre-supernova and on the explosive p-process.

Different reaction rates for the $^{12}C + ^{12}C$ fusion reaction were used. Figure 1.20 shows these reaction rates, with the upper panel showing the reaction rates as a function of the temperature T and the lower panel showing the reaction rates normalised to the CF88 reaction rate. The latter is shown in black, and is also multiplied and divided by 10, in thin and thick red respectively, in order to study the consequences. The lower limit is calculated taking into account the suppression of the fusion [17; 18] in dotted blue. The upper limit adopted, in blue, takes account of the resonance observed by Spillane *et al.* [24] at $E_{\mathrm{com}} = 2.14$ MeV and a hypothetical resonance at $E_{\mathrm{com}} = 1.5$ MeV [74].

The stellar model studied is the same in all five cases, with a 25 $M_\odot$ mass and a half solar metallicity.

The main result of this study is that the temperature and stellar density required to start the carbon combustion phase are linked to the reaction rates considered. Thus, for the lowest rates, as is the case for the reaction taking into account fusion hindrance, the temperature and density must be higher in order to ignite carbon fusion. The opposite is true for higher reaction rates, which require lower temperatures and densities.

This has an influence on the processes taking place during the C-burning phase. For example, the ^{22}Ne(α,n)^{25}Mg reaction, which is a source of neutrons, is more efficient at lower temperatures and densities. This will have an impact on the s-process in shell burning: the higher rates will have a stronger s-process than the lower rates, and therefore different chemical abundances at the end of C-burning, but also during advanced burning phases.

The impact of the ratio between the two main exit channels from carbon fusion, ^{12}C(^{12}C,α)^{20}Ne, ^{12}C(^{12}C,p)^{23}Na, was also studied. Different ratios R_α/R_p were used. The results show that this ratio has a direct impact on the production of elements *via* the quantity of neutrons or protons available in the interstellar medium that can induce the n-capture and p-capture processes.

Reaction rates are essential data for studying the evolution of massive stars, but also for determining the mass limit M_L, the mass at which a star can start the C-burning phase.

Figure 1.21 shows the results obtained by Straniero *et al.* [16] for the limit mass as a function of solar mass $M_\mathrm{L}/M_\odot$ following the metallicity of the star. The red curve represents the results obtained with the CF88 reaction rates, and the blue curve the results obtained for the CF88 reaction rate with a resonance at $E_\mathrm{com} = 1.4$ MeV.

These results indicate that the presence of the resonance around $E_\mathrm{com} = 1.4$ MeV reduces the value of M_L by about two solar masses. This lowering of the limiting value compared with standard calculations logically leads to an increase in the population of stars able to undertake the advanced combustion phases, while the number of white dwarfs is reduced, which decreases the number of systems able to explode in type Ia supernovæ (see next section) by a factor of about 4 [16].

Binary systems and type Ia supernovæ

Stars are frequently in pair bound by their mutual gravitationnal attraction. They are called binary stars, or binary systems, and appear to be the norm rather than the exception [53].

Stars in such systems often see their evolution strongly influenced by the presence of their companion, through mass transfer for example. This is particularly true when

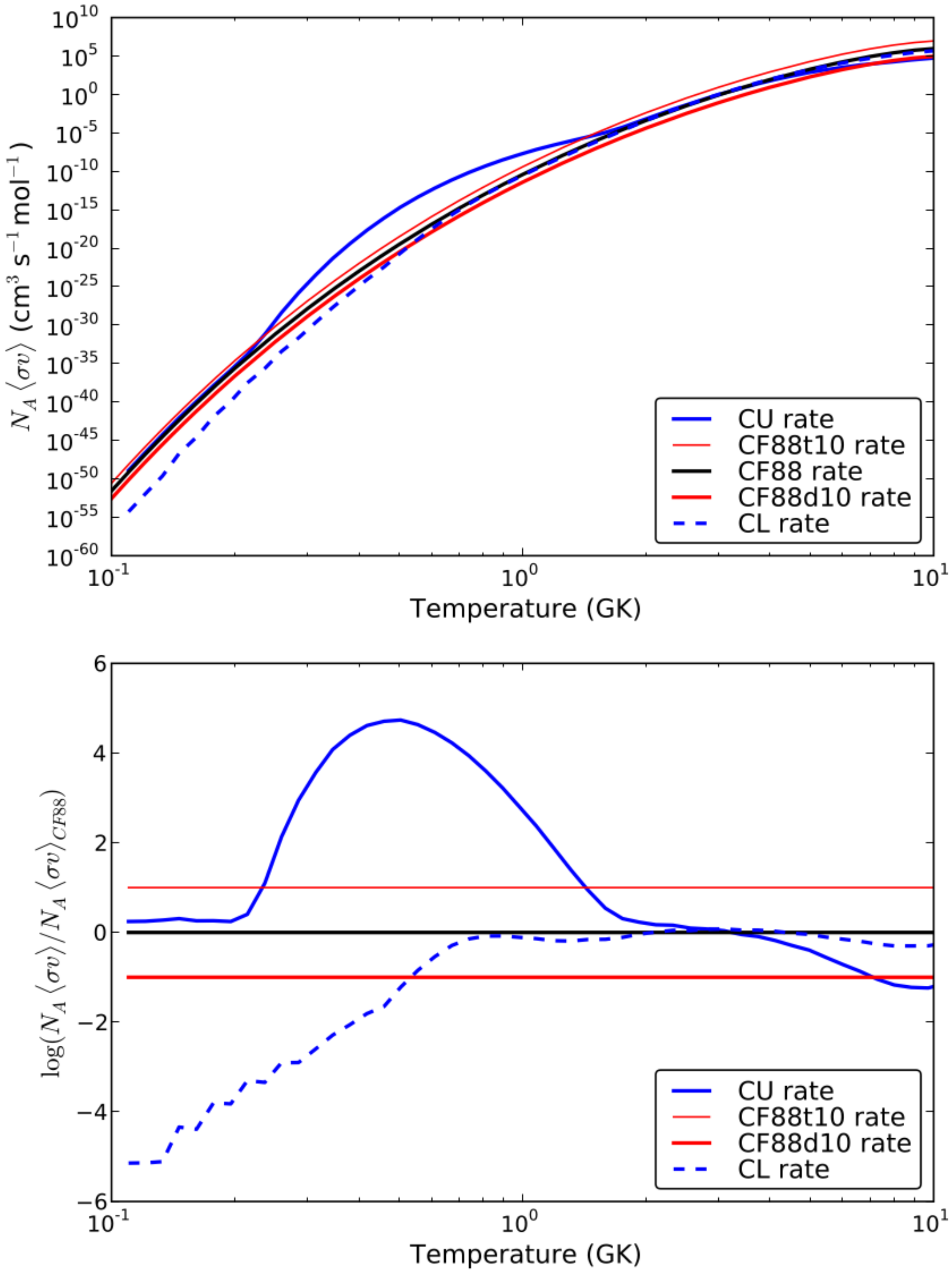

Figure 1.20: Top: Reaction rates for ^{12}C + ^{12}C obtained with different extrapolations. Bottom: Reaction rates for ^{12}C + ^{12}C obtained with different extrapolations normalized with CF88 rate. From [15].

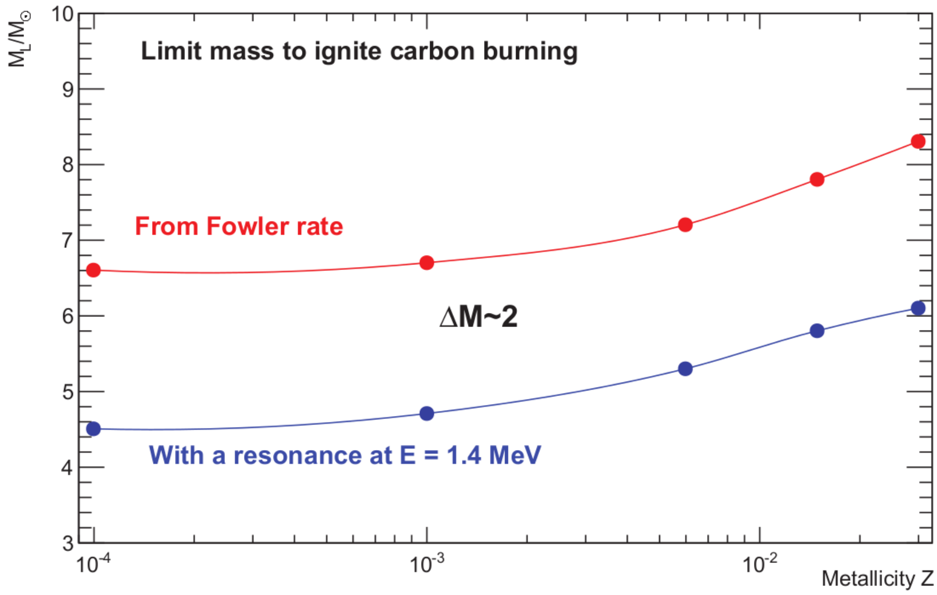

Figure 1.21: Limit mass $M_L/M_\odot$ for the carbon ignition as a function of the metallicity Z, following the CF88 reaction rate in red and the CF88 reaction rate with a resonance at $E_{com} = 1.4$ MeV. Figure from [6] and data from [16].

one of the two stars is a compact object, such as a white dwarf or a neutron star, while the other is located on the Main Sequence or on the Giant branch. The compact object will then accrete matter from its companion.

White dwarfs in binary systems are in many cases composed of a core of carbon and oxygen [2]. The accretion of matter can then cause it to exceed the Chandrasekhar mass, which is the maximum mass that the electronic degeneracy pressure of an object can withstand without gravitational collapse [53]. Exceeding this limit then induces an increase in temperature and density leading to the ignition of carbon burning, a key parameter in the triggering of type Ia supernovæ [52; 75]. These phenomena are at the origin of explosive nucleosynthesis, particularly of elements around manganese, iron, cobalt and nickel [2].

In this scenario, the carbon fusion ignition is supposed to take place around a temperature $T = 5{\times}10^8$ K, which corresponds to a Gamow window $E_{Gamow} = 1.5 \pm 0.3$ MeV. However, this interval corresponds to energies at which the cross section of the $^{12}C + ^{12}C$ reaction is poorly known: there are no direct experimental data and the various extrapolations considered differ by several orders of magnitude (see next chapter).

The main impact of the models governing these extraoplations are the temperature and density conditions required to ignite carbon fusion. Figure 1.22 represents the ignition curve in the ρ-T diagram of the $^{12}C + ^{12}C$ fusion reaction at the core of a massive ^{12}C-^{16}O white dwarf composed of 30% carbon. Two models are studied here, one following the CF88 reaction rate in bold and the second the fusion hindrance [17] in light.

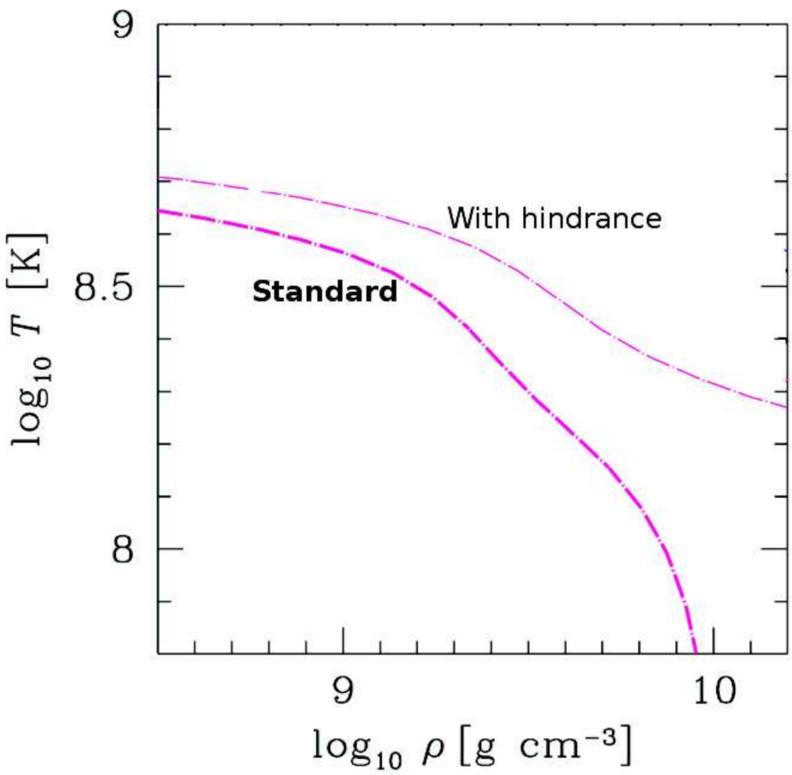

Figure 1.22: Carbon ignition curves in a core of a massive ^{12}C-^{16}O white dwarf, with CF88 model and fusion hindrance model [17]. Adapted from [18] by [6].

The results show that a higher density and temperature are necessary for the start of carbon burning in the model that takes into account fusion hindrance. This will change the physical conditions and dynamics of these explosive events.

Cooper *et al.* [52] were interested in the possible influence of a resonance in the Gamow window, *i.e.* around $E_{\text{com}} = 1.5$ MeV. In this case, the temperature and density required to ignite ^{12}C + ^{12}C fusion are reduced, which in turn leads to a less energetic explosion. This could reduce the amount of elements synthesised around the iron region in nucleosynthesis calculations.

In the same study, these authors also looked at the influence of this resonance on the accretion of matter by a neutron star. In neutron stars, this reaction is also the key parameter for triggering superbursts, highly energetic events visible in the X-rays range likely due to thermonuclear flashes occuring at the surface of neutron stars.

The presence of a resonance at $E_{\text{com}} = 1.5$ MeV decreases the density to be reached in the outer layers of the neutron star to start the ^{12}C + ^{12}C fusion reaction, which would be in agreement with astronomical observations [52].

1.3 Résumé du chapitre

La physique nucléaire, et les réactions nucléaires, ont un rôle primordial dans l'évolution de l'Univers, *via* leur impact sur les étoiles. Parmi les différentes réactions nucléaires, la fusion nucléaire joue un rôle clé dans l'évolution stellaire : comprendre les propriétés de ces réactions permet alors une meilleure compréhension des étoiles. En ce sens, la physique nucléaire expérimental, au travers de la détermination de grandeurs essentielles pour les astrophysiciens, tel que le taux de réaction, est primordiale pour l'astrophysique. De plus, des études récentes ont montré que le comportement des fonctions d'excitations a un impact direct sur le taux de réaction : la connaissance fine de ces dernières est également importante pour la compréhension de l'évolution des étoiles.

1.3.1 Contexte astrophysique

Les éléments chimiques sont produits au travers du processus appelé nucléosynthèse. Cette dernière a lieu au travers de différentes réactions nucléaires, à différents temps et lieux [37; 38; 57].

Les éléments les plus légers ont été formés lors des premiers instants de l'Univers, au cours de la nucléosynthèse primordiale : la haute pression et température ont permis la synthèse d'hélium et d'une faible quantité de lithium à partir de l'hydrogène existant [53].

La formation d'une majeure partie des éléments chimiques a lieu au sein de processus stellaire, et est donc appelée nucléosynthèse stellaire. Cette dernière est divisée en deux types de nucléosynthèse. La nucléosynthèse non explosive, qui a lieu dans le cœur est les couches des étoiles à l'équilibre hydrostatique, permet la formation des éléments les plus légers. Les éléments plus lourds que le fer sont formés au cours de la nucléosynthèse explosive, qui a lieu lors d'évènements stellaire impliquant le dégagement d'une importante quantité d'énergie.

Le dernier phénomène astrophysique conduisant à une nucléosynthèse est la spallation cosmique, ou nucléosynthèse interstellaire [37]. Un petit nombre d'isotopes légers sont ainsi formés, tels que le lithium, le béryllium et le bore.

La Figure 1.1 représente un tableau périodique coloré de façon à mettre en avant les différents processus aboutissant à la formation d'éléments chimiques, ainsi que leurs sites de production. Il permet ainsi de mettre en avant le lien profond entre la nucléosynthèse stellaire et l'évolution des étoiles.

La nucléosynthèse stellaire calme est le processus qui prend place lors de la majeure partie de la vie d'une étoile, et qui est l'une des cause de l'équilibre hydrostatique. Sous l'effet de sa propre gravité une étoile s'effondre sur elle-même et se contracte. Cette contraction mène à une augmentation de la température en son sein, qui atteint éventuellement des valeurs permettant le démarrage de réactions de fusion nucléaires. L'énergie libérée par ces réactions va alors compenser les effets de l'effondrement gravitationnel. Lorsque le combustible est épuisé, les réactions s'arrêtent et l'effondrement reprend. Les températures augmentent à nouveau, jusqu'à ce que d'autres réactions de fusion soient possibles. La structure de l'étoile prend alors la forme de couches successives de compositions chimiques différentes, appelée structure en couches. Cette dernière est représentée dans la fig 1.2, un schéma de la structure pré-supernova d'une étoile de masse initiale 25 $M_\odot$ [2]. Cette structure en couche est également discernable dans le diagramme de Kippenhahn fig. 1.3 [3].

Les éléments synthétisés au cours de la nucléosynthèse stellaire sont déterminés par la masse initiale de l'étoile. Comme indiqué sur la fig. 1.4 [4], il est possible de distinguer deux chemins évolutifs distincts. Les étoiles dont la masse initiale est inférieure à 8 $M_\odot$ vont seulement fusionner l'hydrogène en hélium puis ce dernier en carbone. Le rémanent de ce processus est une naine blanche. Les étoiles dont la masse initiale est supérieure à $10 - 12$ $M_\odot$, appelée étoile massive, vont fusionner tous les éléments jusqu'au fer, avant de finir sa vie en supernova dont le rémanent sera une étoile à neutrons ou un trou noir. L'évolution des étoiles dont la masse est comprise entre $8 - 10$ $M_\odot$ n'est pas prédite précisément : les modèles numériques ne convergent pas vers une seule réponse, car de nombreux paramètres entrent en compte dans ce cas. Les observations actuellement indiquent que ces étoiles peuvent évoluer en naines blanches, étoiles à neutrons et supernovæ [2].

L'évolution stellaire peut être décrite comme une succession de phases de combustion impliquant la fusion d'éléments précis.

La première phase de fusion est celle de l'hydrogène au cœur de l'étoile. Durant cette phase, qui est la plus longue phase de combustion, 4 noyaux d'hydrogène 1 vont fusionnés en un noyau d'hélium 4. Cette fusion peut avoir lieu selon deux processus : la chaîne proton-proton, qui ne nécessite au départ que des protons, ou les cycles CNO, qui nécessitent la présence de noyaux de carbone, oxygène et azote, qui vont jouer le rôle de catalyseur.

Après cette phase, l'étoile va entamer la combustion de l'hélium en son cœur, tandis que la combustion de l'hydrogène peut continuer dans une couche supérieure de l'étoile. Lors de cette phase de combustion, les deux principales réactions sont $^{4}\mathrm{He}(\alpha\alpha,\gamma)^{12}\mathrm{C}$ et $^{12}\mathrm{C}(\alpha,\gamma)^{16}\mathrm{O}$. La première réaction est appelée réaction 3-α est va prendre place au début de cette phase de combustion. Lors de ce processus, deux noyaux d'hélium 4 vont fusionner dans un premier temps en un noyau de béryllium 8, qui va capturer un autre noyau d'hélium afin de produire un noyau de carbone 12. Cependant, le temps de demi-vie du béryllium 8 est un très court, et seule la présence d'un état excité dans le noyau de carbone peut expliquer l'abondance de cet élément, comme indiqué sur la fig. 1.6 [2]. La seconde réaction, $^{12}\mathrm{C}(\alpha,\gamma)^{16}\mathrm{O}$, est favorisé par rapport à la réaction 3-α plus tard dans la phase de combustion, après changement des conditions de densité et température au cœur de l'étoile.

Les étoiles avec une masse initiale $< 8 - 10$ $M_\odot$ vont arrêter les réactions de fusion après la phase de combustion de l'hélium, et finir en naines blanches, un astre inerte dont l'équilibre hydrostatique est maintenu grâce à la pression de dégénérescence des électrons.

Les étoiles de masses initiales > 8 $M_\odot$ vont pouvoir entrer dans la phase de combustion du carbone, dont les réactions primaires sont $^{12}\mathrm{C}(^{12}\mathrm{C},\alpha)^{20}\mathrm{Ne}$, $^{12}\mathrm{C}(^{12}\mathrm{C},\mathrm{p})^{23}\mathrm{Na}$ et $^{12}\mathrm{C}(^{12}\mathrm{C},\mathrm{n})^{23}\mathrm{Mg}$. La fusion du carbone prend place à des températures comprises entre $0.6 - 1$ GK, avec une durée d'environs 1600 ans pour une étoile massive de 25 $M_\odot \dot{}$Dans ces conditions, la réaction ^{12}C(^{12}C,n)^{23}Mg est endothermique et donc négligeable. Les produits des réactions primaires vont être les combustibles d'un réseau de réactions secondaires. Ces réactions et les noyaux synthétisés sont représentés dans la fenêtre supérieure de la fig. 1.8. L'évolution de l'abondance chimique durant la phase de combustion du carbone est représentée dans la fenêtre inférieure de la fig. 1.8. Cette phase de combustion est largement dominé par les réactions nucléaires, et en particulier par la section efficace de la réaction ^{12}C + ^{12}C. Cependant, cette réaction est extrêmement difficile à étudier en laboratoire, et les résultats expérimentaux ne sont pas assez précis pour contraindre efficacement les différents modèles théoriques. Cela rend difficile la détermination de la msse limite des étoiles pouvant entamer la phase de combustion du carbone, et donc la compréhension de l'évolution des étoiles.

Après la phase de combustion du carbone les étoiles vont entamer une succession de phases de combustions dites avancées avant de finir en supernova. La première phase de combustion est celle du néon, qui va prendre place à $T > 1$ GK, et durer quelques centaines de jours pour une étoile massive de 25 $M_\odot\dot{}$La réaction primaire de cette phase est la photodésintégration du néon. L'évolution de l'abondance chimique durant cette phase est visible sur la fig. 1.9. Cette phase est suivie par la combustion de l'oxygène, à $T = 2.2$ GK et dont la durée est d'un peu plus d'une centaine de jours pour une étoile de 25 $M_\odot\dot{}$La réaction principale est la fusion ^{16}O + ^{16}O, ayant un grand nombre de voies de sorties possibles. L'évolution des abondances chimiques est représentée fig. 1.10. La phase de combustion suivante est celle du silicium, dont les réactions principales sont les photodésintégrations du silicium et du souffre. Cette phase prend place à $T = 3$ et dure quelques heures pour une 25 $M_\odot\dot{}$L'évolution chimique est montrée sur la fig. 1.11. Après cette phase de combustion les réactions nucléaires au centre de l'étoile vont stopper brusquement, et l'étoile va s'effondrer sur elle-même. La pression va alors atteindre des valeurs permettant la recombinaison des électrons du plasma avec les protons des noyaux afin de former des neutrons. Les couches supérieures de l'étoile vont alors rebondir sur cœur : cet évènement est appelé supernova. Cette fin de vie, dont le rémanent est une étoile à neutrons ou un trou noir, participe grandement à l'enrichissement du milieu interstellaire.

1.3.2 Importance de la physique nucléaire

Les simulations d'évolution stellaire nécessite un paramètre découlant directement de la physique nucléaire : le taux de réaction nucléaire. Ce dernier est le taux auquel les réactions nucléaires ont lieu, proportionnellement à la concentration des réactifs dans un volume et une durée définies. Le taux de réaction communément utilisé pour la réaction de fusion ^{12}C + ^{12}C est celui de Caughlan & Fowler [21], aussi appelé CF88.

Le taux de réaction est déterminé à partir de la section efficace de la réaction considérée, cette dernière pouvant être issue mesures expérimentales comme de modèles théoriques. La section efficace est dépendante de l'énergie, et la compréhension et la connaissance de cette dernière et l'objectif et le défi principal de l'astrophysique nucléaire.

Afin de calculer des taux de réactions à des fins astrophysiques, il est nécessaire de savoir à quel intervalle en énergie la section efficace associée est déterminée. Dans les conditions normales d'un intérieur stellaire, c'est-à-dire quand la matière n'est ni dégénérée ni relativiste, la vitesse des particules est décrite par la distribution de Maxwell-Boltzmann. La fusion est impossible dans le cas de la mécanique classique, les énergies cinétiques des particules étant bien plus faible que la barrière de Coulomb des réactions de fusion considérés. Cependant, dans les processus astrophysiques, les sections efficaces sont largement dominées par l'effet tunnel quantique. La figure 1.12 montre la distribution de Maxwell-Boltzmann en bleue, et la probabilité de l'effet tunnel en rouge. La convolution de ces deux distributions donne lieu à un pic centré autour d'une énergie E_0, appelé pic ou fenêtre de Gamow. C'est dans cette fenêtre en énergie que, pour un système donné à une température fixe, la probabilité de fusion est la plus importante. Il est donc essentiel de déterminer les sections efficaces à ces énergies.

La détermination des sections efficaces passe par l'étude de leur comportement. Aux énergies d'intérêt astrophysique, des énergies profondément sous-coulombiennes, deux phénomènes ont été étudiés dans ce travail : les résonances et le phénomène de suppression de la fusion.

Une résonance est une structure de la section efficace qui peut être une forte et locale ou plus large augmentation de la section efficace à une énergie spécifique. Ces structures ont été observés pour le système ^{12}C + ^{12}C dès les années 1960 [20], des énergies de quelques MeV/A jusqu'aux énergies profondément sous-coulombiennes. Elles sont particulièrement prononcées autour de la barrière de Coulomb. Leur origine est toujours débattue, et deux interprétations sont présentées ici. La première est la présence d'état moléculaire dans le noyau de ^{24}Mg. Cette hypothèse est appuyée par la largeur des résonances considérées, de l'ordre de 150 keV. De plus, des simulations récentes basées selon sur les interactions fondamentales ont reproduit ces états moléculaires dans différents noyaux, résultats montrés sur la fenêtre inférieure de la fig. 1.13 [8]. La seconde interprétation est liée à la densité d'état dans le noyau de ^{24}Mg. Les résonance seraient alors causées par une diminution de la section efficace dans les régions en énergies où il y a un faible chevauchement d'états, effet accru par un nombre d'états disponibles limités par les états initiaux $J^\pi(^{12}\mathrm{C}) = 0^+$ [10].

Le phénomène de suppression de la fusion a été mis en avant pour la première fois récemment au travers de plusieurs systèmes lourds : aux énergies sous-coulombiennes, les sections efficaces expérimentales sont plus faibles que celles prédites par les modèles théoriques en voies couplées [71]. Cette découverte a ensuite été confirmée pour le système ^{64}Ni + ^{64}Ni, visible sur la fig. 1.16 [11]. Plusieurs hypothèses ont été avancées pour expliquer ce phénomène, comme l'incompressibilité de la matière [12] et donc l'ajout du principe d'exclusion de Pauli dans les calculs en voies couplées. Cet ajout permis la reproduction des mesures expérimentales, montrées sur la fig. 1.18 [13]. Dans le cas de la réaction ^{12}C + ^{12}C, les effets de la suppression de la fusion sont toujours débattus aujourd'hui. En effet, les modèles théoriques mentionnés précédemment ne reproduisent pas les données expérimentales, et semblent suivre le haut des résonance, visible sur la fig. 1.19 [14]. Afin d'étudier ce phénomène dans les données expérimentales, un modèle phénoménologique a été développé [17]. Les résultats des précédentes campagnes expérimentales de STELLA sont en accord avec ce modèle phénoménologique [27; 28].

Plusieurs travaux ont déjà été menés pour comprendre les impacts des résonances ou de la suppression de la fusion sur les étoiles.

L'évolution des étoiles selon différents taux de réactions pour la réaction ^{12}C + ^{12}C a été étudiée pour une étoile de 25 $M_{\odot}$, montrée sur la fig. 1.20 [15]. Le résultat principale de ce travaux est que la température et la densité requises pour commencer la phase de combustion du carbone sont liées au taux de réaction considéré. Ainsi, dans le cas de la suppression de la fusion, où le taux de réaction est plus faible, la température et la densité doivent être plus élevées pour allumer la fusion du carbone. Ces conditions différentes auront un impact sur les abondances chimiques. L'impact du rapport entre les différentes voies de sorties de la fusion du carbone a également été étudiée. La masse limite de l'allumage de la combustion du carbone a aussi été analysée [16]. Les résultats indiquent que la présence d'une résonance abaisse la masse limite, et modifie donc la distribution entre étoiles peu massives et étoiles massives, voir fig. 1.21.

Chapter 2

Carbon fusion measurement

Contents

2.1 $^{12}C + {}^{12}C$ fusion reaction 51

2.1.1 Exit channels 51

2.1.2 State of the art 53

2.2 Detection methods 55

2.2.1 Distinct measurement 55

Charged particles 55

Gamma rays 57

Limits and challenges 57

2.2.2 Coincidence method 59

2.3 The STELLA experiment 60

2.3.1 Reaction chamber 61

2.3.2 Carbon targets 63

2.3.3 Charged particle detectors 65

DSSSD 66

PIXEL 68

Monitor 70

2.3.4 Gamma-ray detectors: UK-FATIMA collaboration 72

$LaBr_3$(Ce) detectors 72

Geometric configuration 73

2.3.5 Vacuum system 74

2.3.6 Acquisition systems and synchronization 77

STELLA acquisition system 77

UK-FATIMA acquisition system 79

Time synchronization 80

2.3.7 Andromede facility 82

2.4 Résumé du chapitre 83
2.4.1 La réaction de fusion $^{12}C + ^{12}C$ 84
2.4.2 Méthodes de détection 84
2.4.3 L'expérience STELLA 85

The ^{12}C + ^{12}C fusion reaction is a nuclear reaction which has always been of great interest for the nuclear community. In fact, as mentioned in the previous chapter, it plays a key role in stellar evolution: it is the main reaction during the C-burning phase, which is the first phase that only stars that are going to evolve into supernova reach.

Moreover, one should add to this a keen interest in this reaction linked to features that are more closely related to nuclear physics. Indeed, the excitation function of the carbon fusion reaction seems to show two interesting features: the presence of a large number of resonances [20], and a suspected fusion hindrance at deep sub-barrier energies [25; 27; 26; 28].

Numerous experiments have been carried out to study this reaction, using different types of set-ups to detect the reaction products. Yet, none of them was precise enough to accurately determine the behaviour of the excitation function of carbon fusion at deep sub-barrier energies, *i.e.* at energies of astrophysical interest.

In fact, the ^{12}C + ^{12}C reaction, due to its very low cross section of the order of pi-cobarns in the astrophysical range of interest, is heavily contaminated by background. Consequently, this system presents huge experimental and data analysis challenges.

To address these challenges, a coincidence detection method was set up for this system by Jiang *et al.* [76], with the collaboration of the STELLA team. This method has then been used for the construction of the STELLA experiment [29].

2.1 ^{12}C + ^{12}C fusion reaction

2.1.1 Exit channels

The ^{12}C + ^{12}C fusion reaction is the main reaction that occurs during the carbon burning phase, as seen in 1.1.3.

Depending to the initial mass of the star, the core temperature during the carbon burning phase varies. It is $T \approx 0.9$ GK for a 25 $M_{\odot}$, which corresponds to a Gamow energy for the carbon fusion of $E_{\text{Gamow}} = 2.25 \pm 0.48$ MeV; and $T \approx 0.5$ GK for a $8 - 10$ $M_{\odot}$, which corresponds to $E_{\text{Gamow}} = 1.5 \pm 0.30$ MeV. In all cases the Gamow window is lower than the ^{12}C + ^{12}C reaction Coulomb barrier $E_{\text{Coulomb}} = 6.6$ MeV.

Carbon fusion leads to the formation of a compound nucleus ^{24}Mg* with a Q value $Q = 13.93$ MeV. Taking into account the energy of the centre of mass of the collision, the excitation energy of ^{24}Mg is of the order of $E_{\text{ex}} = 16 - 20$ MeV in the range of astrophysical interest. The ^{24}Mg* releases its energy in three main exit channels, as mentionned in the previous chapter:

$$\begin{aligned}
{}^{12}\mathrm{C} + {}^{12}\mathrm{C} \rightarrow {}^{24}\mathrm{Mg}^* &\rightarrow {}^{20}\mathrm{Ne}^* + \alpha && (Q = 4.62\,\mathrm{MeV}), && (2.1)\\
&\rightarrow {}^{23}\mathrm{Na}^* + p && (Q = 2.24\,\mathrm{MeV}), && (2.2)\\
&\rightarrow {}^{23}\mathrm{Mg}^* + n && (Q = -2.62\,\mathrm{MeV}). && (2.3)
\end{aligned}$$

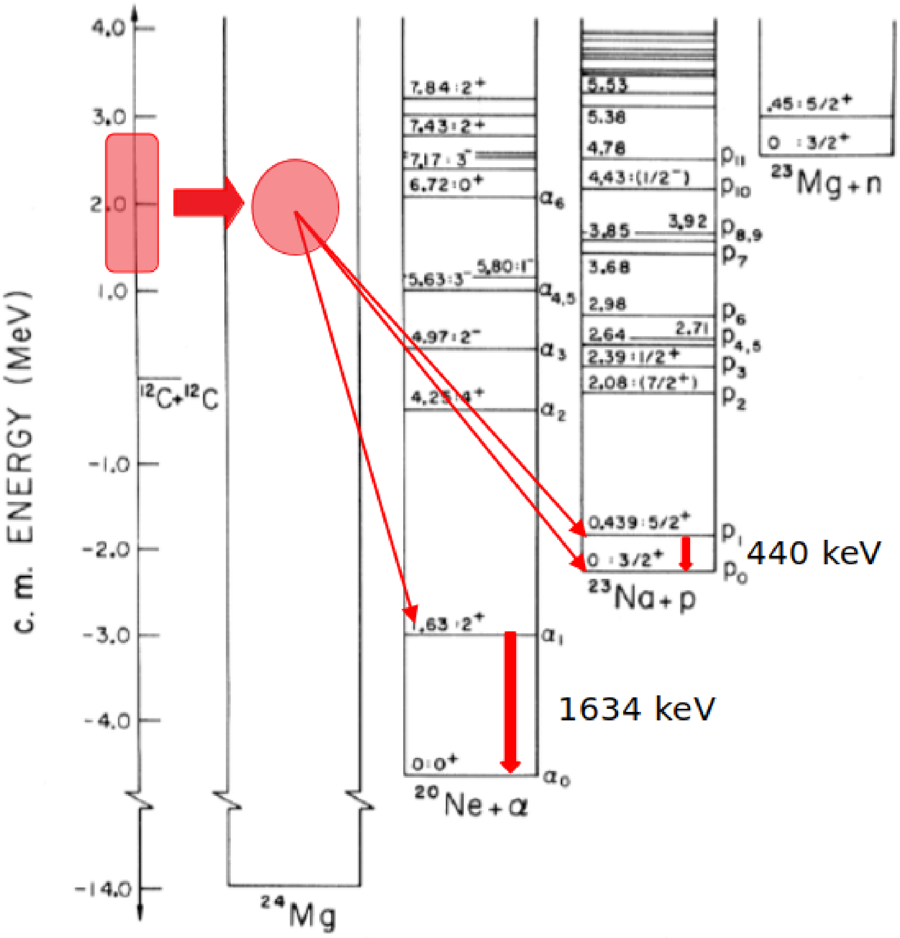

Figure 2.1: Energy level diagram of the ^{12}C + ^{12}C fusion reaction at $E_{\text{com}} \approx 1.2 - 2.8$ MeV. Adapted from [19].

The fusion reaction that involves α, p and n are called α-channel, p-channel and n-channel, respectively.

In an astrophysical context, the dominant exit channels are the p and α ones, the n-channel being largely endothermic [65]. In addition, the evaporation residues, ^{20}Ne neon or ^{23}Na sodium, can be formed in excited states, and emit one or several γ rays to decay into a the ground state (see Fig. 2.1). Their first excited states are usually the most populated ones, and the associated γ rays are at the energies $E_\gamma = 440$ keV for ^{23}Na and $E_\gamma = 1634$ keV for ^{20}Ne.

When the evaporation residues are synthesised in an excited state, the light particle emitted at the same time is indexed: we then have particles denoted α_i and p$_i$, where $i = 1, 2, 3, 4, ...$, represent the excitation level of the daughter nucleus, $i = 0$ being associated to the ground state.

Figure 2.1 represents the energy level diagram of the the ^{12}C + ^{12}C fusion reaction at $E_{\text{com}} \approx 1.2 - 2.8$ MeV. This energy range covers the Gamow window for stars with masses between $8 - 10$ and 25 $M_\odot$. The different exit channels are shown, with the

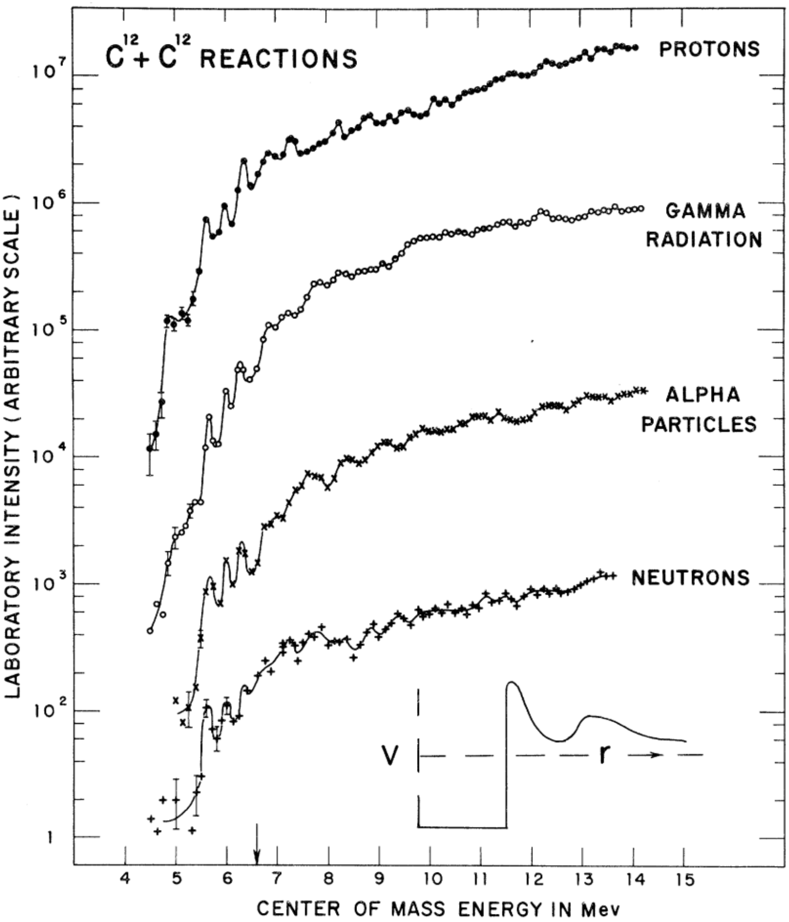

Figure 2.2: Excitation fonctions for the ^{12}C + ^{12}C reaction from [20], for the different fusion reaction channels. The black arrow indicate the Coulomb barrier at $E_{\text{Coulomb}} = 6.6$ MeV. The inset shows a suggested 1D quasi-molecular potential.

excitation levels in the daughter nuclei. The thin red arrows indicate some of the desintegration of the excited magnesium ^{24}Mg*, and the thick red arrows represent the emitted γ ray during the de-excitation of the daughter particle, with their energy noted alongside.

2.1.2 State of the art

Since the 1960s and the emergence of stable beams up to the present day, the ^{12}C + ^{12}C fusion reaction has been studied on numerous occasions, showing the strong interest of the scientific community for this rich subject of research.

The first study of the ^{12}C + ^{12}C fusion reaction was made by Almqvist *et al.* [20]. The results, represented in Fig. 2.2, show the excitation functions for the different reaction products: protons, α particles, γ rays and neutrons, for energies in the center of mass $E_{\text{com}} \approx 4.5 - 14$ MeV. The black arrow indicate the Coulomb barrier at

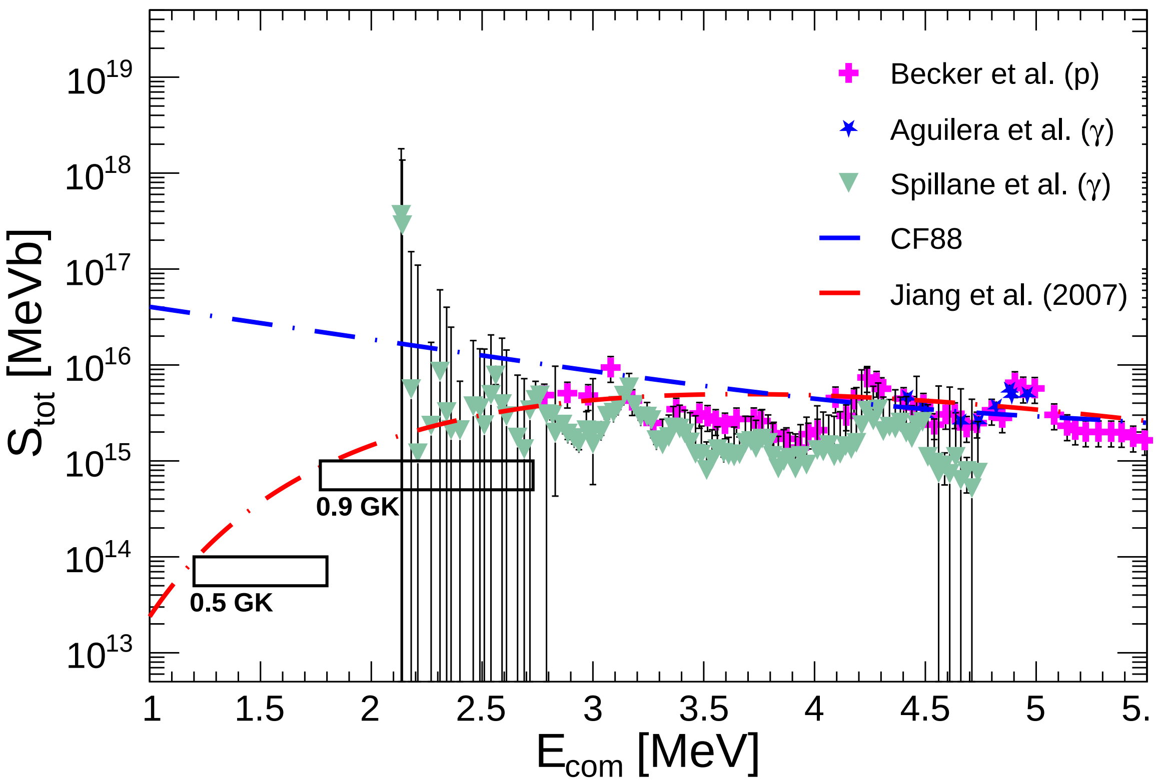

Figure 2.3: Compilation of total astrophysical S(E)-factors of the ^{12}C + ^{12}C reaction obtained with direct measurements. The theoretical models are from [17; 21]. Experimental data are taken from [22; 23; 24]. The letter in brackets indicates the reaction product detected: light particle (p) or γ rays (γ). The two black rectangles indicate the position of the Gamow window for the stellar temperatures $T = 0.5$ GK ($E_{\text{Gamow}} = 1.5 \pm 0.3$ MeV) and $T = 0.9$ GK ($E_{\text{Gamow}} = 2.25 \pm 0.48$ MeV).

$E_{\text{Coulomb}} = 6.6$ MeV.

The excitation functions reveal several structures that seem to be correlated in all the exit channels. They are decreasing proportionally with the energy, with a sharp drop just below the Coulomb barrier. The different curves also show several resonances, which are more pronounced under the Coulomb barrier.

Figure 2.3 summarises the state of the art for this reaction at the end of the 2010s. The different experimental results are obtained with direct measurements, using the detection of light particles (α and protons) or γ rays. The curves are two different extrapolations, and the black boxes indicate the position of the Gamow windows for the stellar temperatures $T = 0.5$ GK and $T = 0.9$ GK, which correspond to $E_{\text{Gamow}} = 1.5 \pm 0.3$ MeV and $E_{\text{Gamow}} = 2.25 \pm 0.48$ MeV, respectively.

The curves represent two different extrapolations. The blue one is based from the CF88 model [21], and the red ones from phenomenological model that takes into account the fusion hindrance and developed by Jiang *et al.* [17]. In this extrapolation, the S-factor is maximum at $E_{\text{S}} = 3.18$ MeV. These extrapolations represent the global tendency of the S-factor, and do not consider local behaviours such as resonances. Both extrapolations are similar at energies close to the Coulomb Barrier ($E_{\text{Coulomb}} = 6.6$ MeV), but diverge at the lowest energies, that can be called deep sub-barrier energies.

The different experiments show consistent S-factors: they all report the presence of resonances, as observed in [20]. In addition, in a range from $E_{\text{com}} = 5.5$ MeV to energies of around $E_{\text{com}} = 3.2$ MeV, the error bars are reasonable, and make it possible to constrain the various models and extrapolations on this interval. Both extrapolations show reasonable average agreement.

However, at deep sub-barrier energies, experimental data show error bars of several orders of magnitude, and for the lowest energies there is no data available. At these energies, the experimental measurements do not allow to validate or exclude different extrapolations. These uncertainties and lack of data come from the major challenges involved in the direct measurement of the carbon fusion reaction.

These sub-barrier energies cover the Gamow windows for stars with inital masses around $8 - 10$ and $25\ M_{\odot}$. As a result, these experimental data cannot be used to probe energies of astrophysical interest. New detection methods are required for this purpose.

2.2 Detection methods

2.2.1 Distinct measurement

The distinct measurement is based on the principle that an event is the detection of one fusion product, light particles or γ rays. For astrophysical purposes the reaction product detected are the protons, α particles or γ rays. This detection method is the only one which has been used during the XXth century for the measurement of the carbon fusion cross section.

Charged particles

Experiments measuring charged particles [20; 22; 19; 10] focus on the detection of the protons and α associated to different final states.

For these experiments, silicon detectors placed at angles $0 \leq \theta_{\text{lab}} \leq 90°$ are used. They are protected from scattered beam by aluminium or nickel foils thin enough to allow proton and α to traverse. Thin carbon targets of between 10 and 50 µg/cm^2 are used to determine the precise energy of the reaction. The particle detectors are placed at different angles to measure the angular distribution of the emitted particle, as shown in Fig. 2.4.

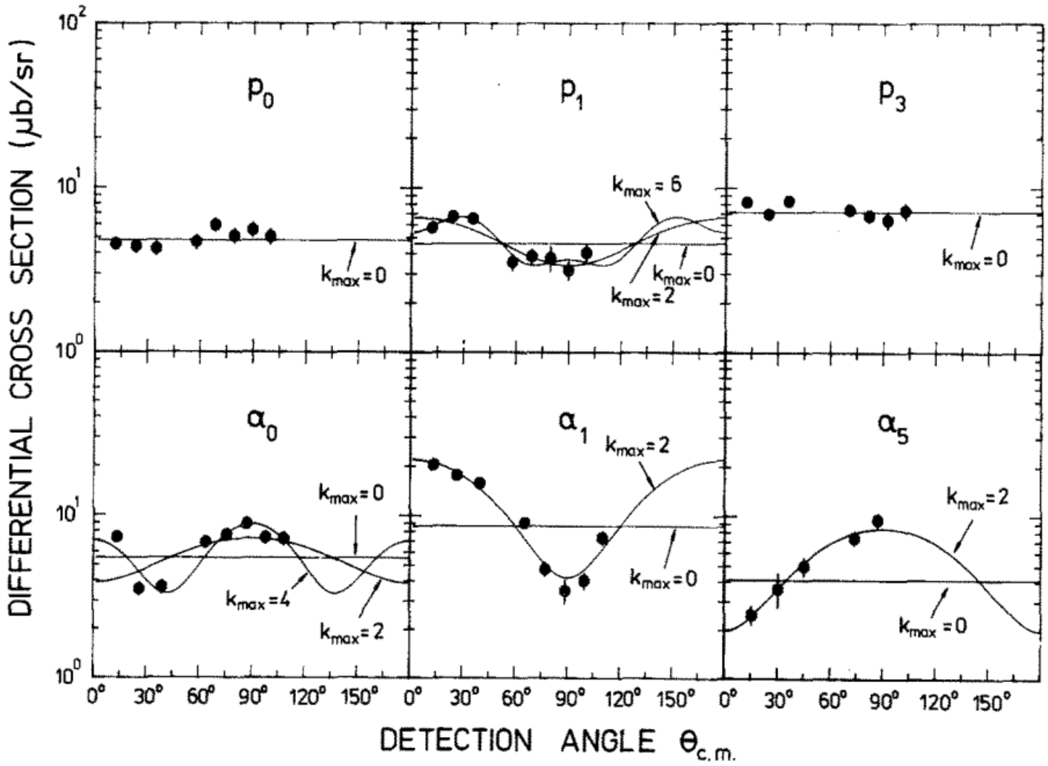

Figure 2.4: Angular distribution for protons and α particles, at $E_{\mathrm{com}} = 4.25$ MeV. From [22].

The angular distribution is generally more pronounced for α exit channel, as proton emission is often isotropic.

These distributions are fitted with the sum of Legendre polynomials, using the formula [77]:

$$\left(\frac{\mathrm{d}\sigma}{\mathrm{d}\Omega}\right)_i = \sum_{k=0}^{k_{max}} a_k P_k \cos(\theta_{\mathrm{com}}), \tag{2.4}$$

with k the order of the polynomial P_k and a_k the fitting parameter. The total cross section for one excited state i is $(\sigma_{\mathrm{tot}})_i$, and is then obtained from the integration over the entire solid angle of the 0^{th}:

$$(\sigma_{\mathrm{tot}})_i = 4\pi a_0. \tag{2.5}$$

The total cross section for the p-channel or α-channel is given by the sum of the cross sections of all the excited states available at the energy reaction. If some excited states cannot be extracted from the experimental data, a branching correction based on previous measurement has to be applied, in the form:

$$\sigma_{\mathrm{tot}} = \left[\sum^{i} (\sigma_{\mathrm{tot}})_i\right] \Gamma, \tag{2.6}$$

where Γ is the branching correction for the missing excited states. In this work, these branching corrections are from Becker *et al.* [22].

However, at energies around and below the Coulomb barrier, the cross section, and therefore the statistics, drops sharply and the background becomes dominant in the spectra, leading to large error bars. In addition, results may vary from one experiment to another, as shows in Fig. 2.3, indicating an additional systematic uncertainty.

Gamma rays

Experiments measuring γ rays [78; 79; 23; 80; 24] are based on the measurement of the fusion cross section through the detection of the γ of de-excitation of the daughter nucleus. To achieve this, detection is concentrated on the γ linked to the first excited states of ^{20}Ne and ^{23}Na, with energies $E_\gamma = 1634$ keV and $E_\gamma = 440$ keV, respectively. The branching ratios between the different excited states can be deduced from cascades.

Germanium detectors are generally used, often protected of the background by a lead shield. Thin (between 10 and 50 µg/cm^2) and thick ($\geq$ 1 mm) targets can be used, but in the latter case the beam is stopped in the target, allowing the use of very intense beam ($\geq$ 10 pµA). The effective energy of the reaction is then between E_{lab} and 0 MeV. In order to determine the fusion cross section at a given energy, several measurements are done with a small variation of the energy between each of them.

The excitation function for the carbon fusion is then determined *via* the derivation of the counting rate between two succesive energy steps, according to the formula [2]:

$$\sigma(E) = \frac{M_{\text{T}}\mathrm{d}Y}{fN_A\mathrm{d}E}\frac{\mathrm{d}E}{\mathrm{d}(\rho x)}, \tag{2.7}$$

where M_{T} is the molecular mass of the target, Y the measured counting rate, f the molecular fraction of the nucleus of interest in the target, N_A the Avogadro number and $\frac{\mathrm{d}E}{\mathrm{d}(\rho x)}$ the stopping power of the beam inside the target.

Likewise the detection of charged particles, experimental data from the detection of γ rays show deviations in the various excitation functions, but also large error bars at the lowest energies. This is due to a number of limits and challenges specific to distinct measurements for the study of the carbon fusion cross section at sub-barrier energies.

Limits and challenges

The main difficulty encountered in measuring the cross section of the ^{12}C + ^{12}C fusion reaction is due to its very low value, of the order of picobarns in the region of interest. As a result, the statistics are very low, and the background becomes dominant in the spectra, obscuring the relevant data.

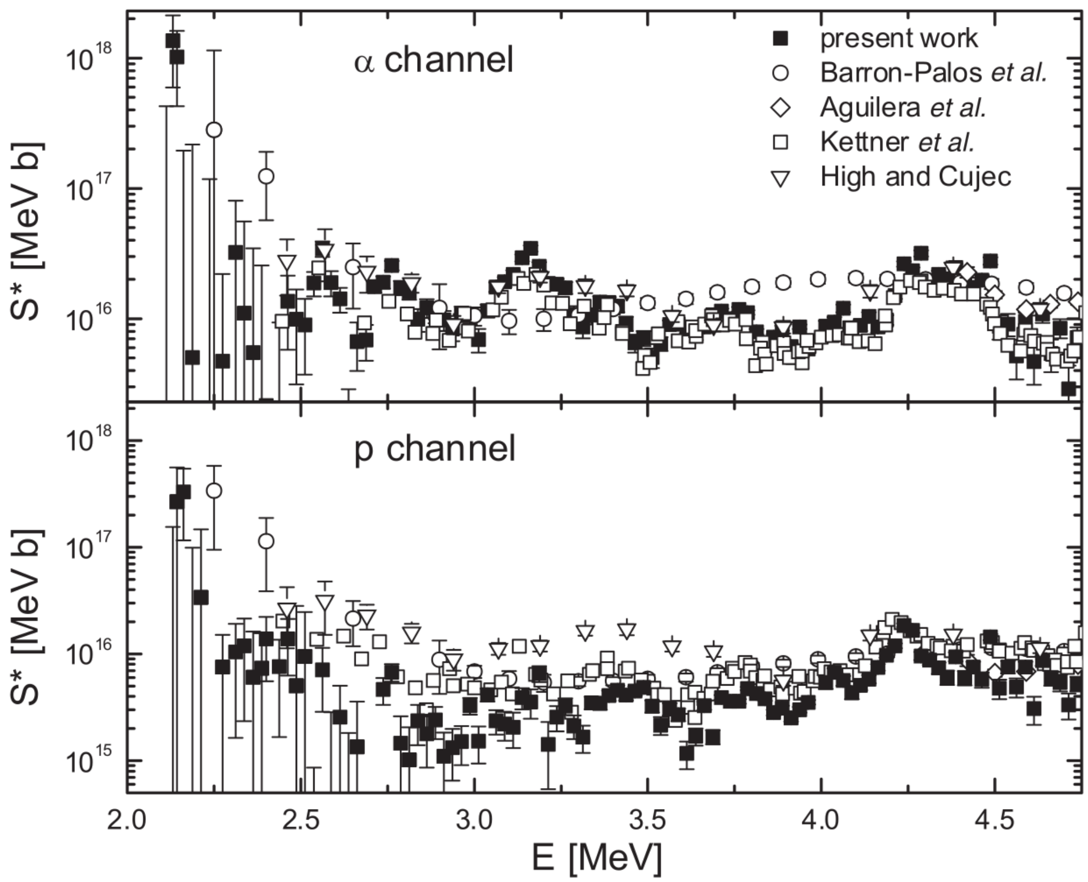

Figure 2.5: S^*-factor for proton and α channels at deep sub-barrier energies. From [24].

For the measurement of charged particles, the majority of the background comes from contaminants in the target.

The ^{13}C isotope naturally contained in the carbon targets leads to the emission of protons and α particles whose energies are close to those of particles resulting from the $^{12}C + {}^{12}C$ fusion. To address this, targets enriched in ^{12}C ($\geq 99.9\%$) are used.

Hydrogen isotopes, ^{1}H and deuterium (d), present in the water molecules trapped in the target, can also interact with the ^{12}C beam. They can be forward scattered, due to kinematics, generating events comparable to those resulting from carbon fusion. As the effective cross-section of $^{12}C + {}^{1}d$ scattering is much larger than that of $^{12}C + {}^{12}C$ fusion at low energies, this contribution can mask fusion events.

At deep sub-barrier energies, an important contamination of the spectra comes from the fusion reaction d(^{12}C,p)^{13}C: this produces protons with energies similar to the charged particles produced by the carbon fusion. It is therefore hardly possible to distinguish between particles coming from a reaction or the other, and the error bars at these energies are extremely large.

The spectra from γ detection are mainly contaminated by Compton background.

The contaminants present in the target are also responsible for the background.

The reactions ^{1}H (^{12}C,γ)^{13}N and d(^{12}C,pγ)^{13}C emit γ at the energies $E_\gamma = 2.36$ MeV and $E_\gamma = 3.09$ MeV, respectively. These γ rays will induce Compton background, and hide the γ of lowest energies.

This phenomenom is illustrated in Fig. 2.5. The error bars for the α channel S^*-factor are reasonable, but the ones for the proton channel are much larger. This can be explained by the fact that the γ rays from the first excited state of ^{20}Ne is at $E_\gamma = 1634$ keV and the one from the first excited state of ^{23}Na is at $E_\gamma = 440$ keV. The latter is in the energy range highly contaminated by the Compton background.

At the deep sub-barrier energies, the ^{12}C + ^{12}C cross section drops below the µb. The contamination from ambiant radioactivity and cosmic rays is then dominant in the spectra.

To adress all these difficulties, a detection allowing the suppression of the background, the coincidence method, is needed.

2.2.2 Coincidence method

The coincidence method can be described as the simultaneous detection of at least two particles from the same event. In the case of the ^{12}C + ^{12}C fusion reaction it is the detection of a charged particle and the associated γ ray.

This detection method is based on the fact that the ^{24}Mg* compound nucleus makes a two-body desintegration, leading into a well-known kinetic energy for both released particles. It is then possible to correlate the charged particles with the de-excitation γ and suppress all other signals and background.

This detection method has been set up for this system by Jiang *et al.* [25] at the Argonne National Laboratory in collaboration with the STELLA team.

During the last years, several experiments based on this coincidence method have been done. Their results are shown in Fig. 2.6. They indicate that this technique significantly increases the precision of the measurements, and allows measurements with reduced error bars defined where only upper limits could have been established without coincidences.

Limits of this method are the following. The detection of both fusion products is required to be recorded as a fusion event, and thus the statistics is significantly reduced. The latter being already low, the number of count can then be extremely small. In order to overcome this, very long beamtimes and high beam intensities are needed.

Because it eliminates the majority of the background and therefore significantly reduces measurement error bars, the STELLA collaboration has chosen to use this detection method to study carbon fusion at energies of astrophysical interest.

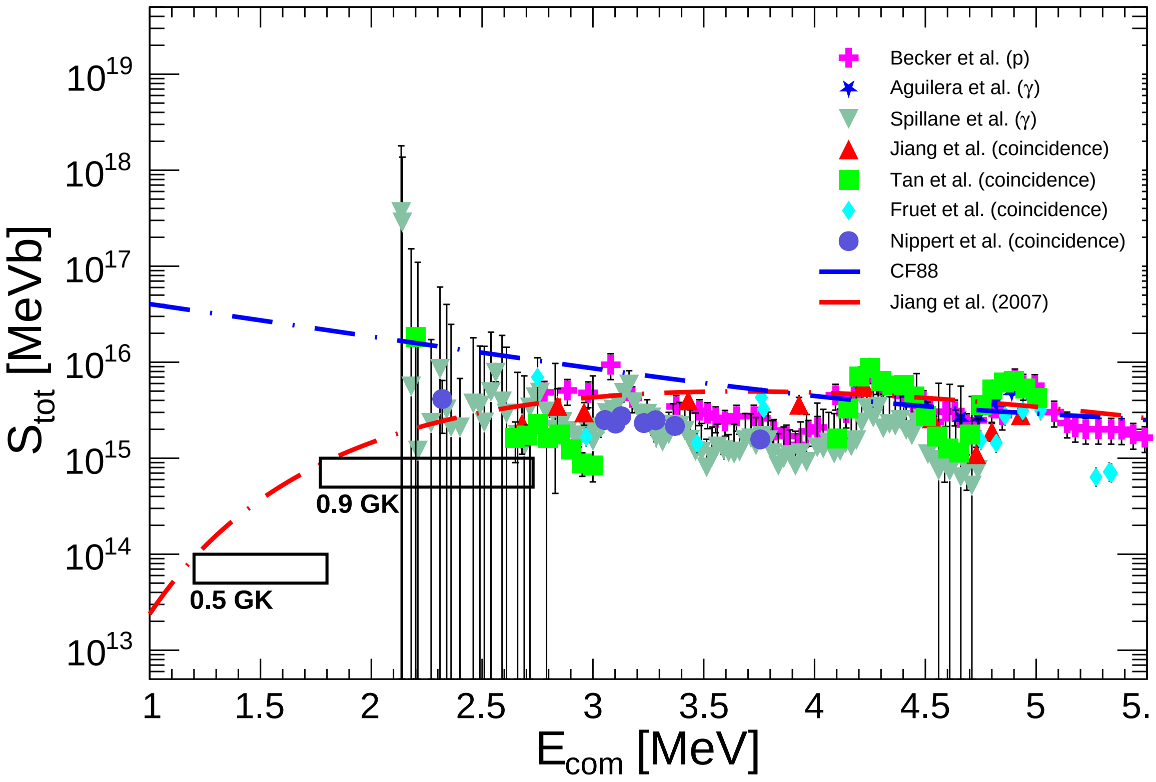

Figure 2.6: Compilation of total astrophysical factors S(E) of the ^{12}C + ^{12}C reaction obtained with direct measurements. The theoretical models are from [17; 21]. Experimental data are taken from [22; 23; 24; 25; 26; 27; 28]. The brackets indicates the reaction product detected: light particle (p), γ rays (γ) or both in coincidence (coincidence). The two black rectangles indicate the position of the Gamow window for the stellar temperatures $T \approx$ 0.5 GK ($E_{\text{Gamow}} = 1.5 \pm 0.3$ MeV) and $T \approx 0.9$ GK ($E_{\text{Gamow}} = 2.52 \pm 0.48$ MeV).

2.3 The STELLA experiment

The STELLA experiment, for STELlar LAboratory, is a nuclear physics experiment focused on the direct measurement of light-medium heavy ions fusion reactions at energies of astrophysical interest, and more specifically the ^{12}C + ^{12}C, ^{12}C + ^{16}O and ^{16}O + ^{16}O reactions, with the coincidence method. The reactions take place in "astrophysical conditions", *i.e.* at sub-coulomb energies. The determination of these reactions cross sections will allow a better understanding of the evolution of stars with initial masses $M_i > 8 - 12\ M_{\odot}$.

This project is a collaboration between the IPHC (Strasbourg, France), the University of York (England), the University of Surrey (England), the GANIL (France), the IJCLab (France) and the Texas A&M University (USA). It has been funded by the University of Strasbourg Institute of Advanced Studies (USIAS), the University of Strasbourg Initiative d'Excellence program (IdEx) and the CNRS-IN2P3.

The STELLA experiment, represented in Fig. 2.7, is a mobile structure, developed

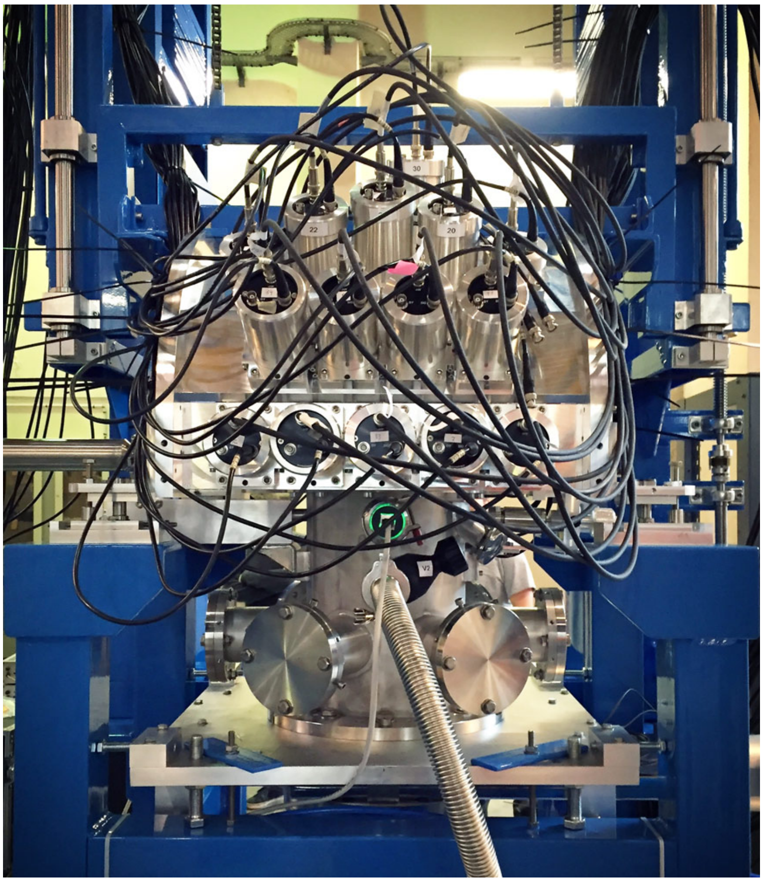

Figure 2.7: The STELLA experiment.

and built at the IPHC in Strasbourg, consisting of a high-vacuum reaction chamber operated by a system of mechanical and cryogenic pumps, and a thin-walled reaction chamber containing a rotating target system and Double Sided Silicon Strip Detector (DSSSD) charged particle detectors, a data acquisition system and $LaBr_3$ radiation detectors from the UK-FATIMA collaboration. The development of the STELLA apparatus and the commissioning experiment were performed during Guillaume Fruet's PhD [6], and the set-up is detailed in Heine *et al.* [29]. In this manuscript, the STELLA apparatus used during the 2022 experimental campaigns will be described.

Until now, the STELLA collaboration has studied the $^{12}C + ^{12}C$ fusion reaction at the Andromede accelerator, located in Orsay, France.

2.3.1 Reaction chamber

The reaction chamber of the STELLA apparatus was designed with the aim of measuring fusion reactions with coincidence method at sub-barrier energies, *i.e.* with very low statistics. In order to perform such a challenging measurement, it is required to use a compact design, that allows the placement of light particles detectors in the chamber and a set of γ detectors as close as possible of the target. Figure 2.8 shows a 3D CAD representation of the entire reaction chamber.

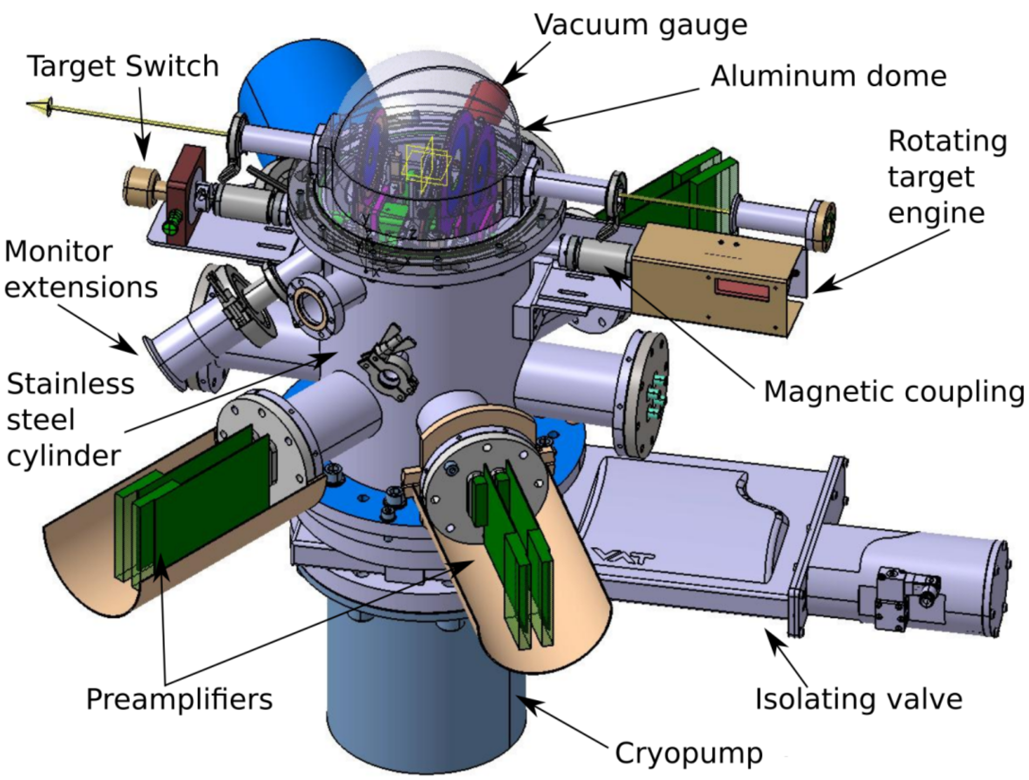

Figure 2.8: 3D CAD representation of the STELLA reaction chamber. From [6]

The reaction chamber is composed of a stainless steel cylinder, topped by a dome. In the cylindrical part differents exits have been machined: two forwards for the monitor extension, and four on the sides for the signals exit and the preamplifiers.

Several modules formed the vacuum system, required for experiment at low energies: the vacuum gauge, in red in Fig. 2.8 and 2.9, that measures the vacuum in the dome, a valve that isolates the chamber from the cryogenic pump, and a precision valve for air intake.

The dome is 2.5 mm thick, in order to minimize interections with γ rays from fusion reactions. A closer view of it is given in Fig. 2.9.

It contains two silicon detectors, noted S3F and S3B, placed on either side of the target, and a additional one, PIXEL, placed above the target (not represented here). The detector noted S1 has not been used during the 2022 experimental campaing.

The target support system, in green in Fig. 2.8 and 2.9, can hold two different types of target: large rotating targets, and small fixed targets. The position of the system, and therefore the target used, can be switched from the outside of the chamber with the target switch. The target rotation is provided by the rotating target motor, through a magnetic coupling.

The dome supports the tubes linking the chamber to the beamline, which traverses the chamber from end to end, passing through the target and the centre of the detectors, represented by the yellow arrow in Fig. 2.8 and 2.9. The beam in monitored by

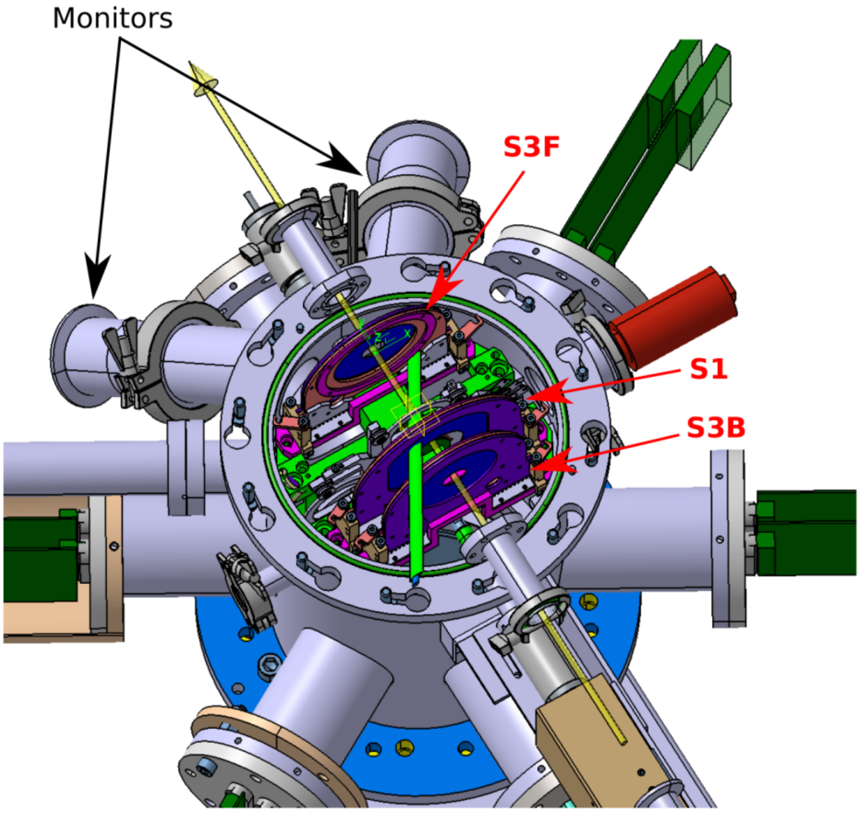

Figure 2.9: 3D CAD representation of the inside of the STELLA reaction chamber. From [29]

a Faraday Cup integrator placed after the reaction chamber, and two surface barrier silicon detectors placed at 45° with respect to the beamline, in the monitor extensions.

2.3.2 Carbon targets

To measure the carbon fusion reaction, the STELLA collaboration chose to use thin carbon targets. This type of target, here with a thickness between 30 and 75 µg/cm², minimises the loss of beam energy in the target, and therefore increases the accuracy of determining the interaction energy.

However, thin targets are very sensitive to the beam intensity, and can be damaged and break after a few tens of minutes of exposure. This is mainly due to the heat generated by the deposition of energy in the target, which is concentrated at a precise point. For example, a 5 MeV ^{12}C beam loses around 350 keV in a target 50 µg/cm² thick. With a 5 µpA beam, the intensity typically used during STELLA collaboration experimental campaigns, a total of 1.75 W is deposited at the heart of the target.

To address this problem, the STELLA team, in collaboration with GANIL (Grand Accélérateur National d'Ions Lourds), has developed a rotating target system, in Fig. 2.10. Thanks to the rotation of the target, this system increases the irradiation surface, and therefore the distribution of the energy deposit in the target, increasing

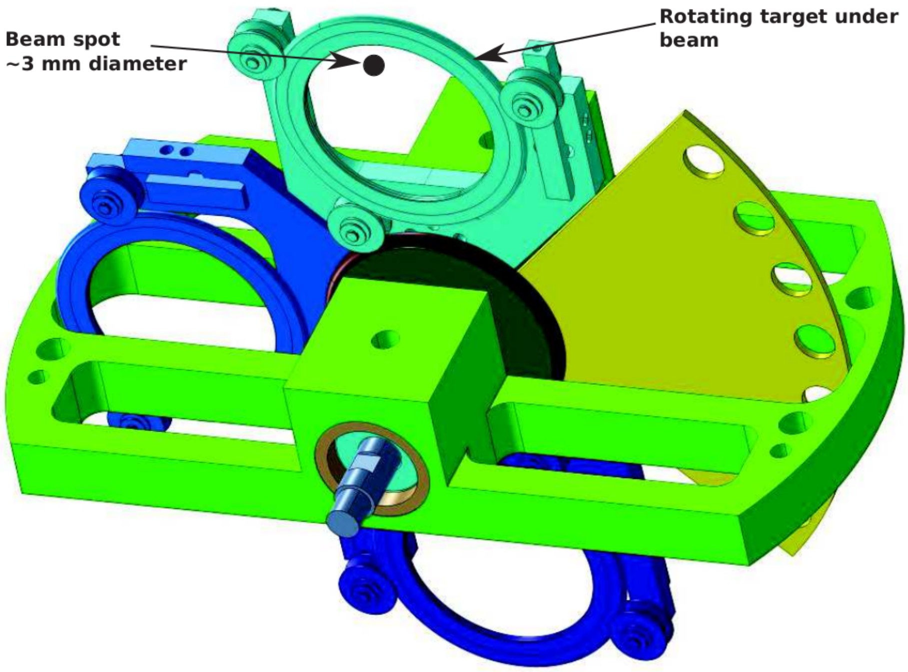

Figure 2.10: 3D CAD representation of the rotative targets system of the STELLA experiment. From [6]

its lifetime. Thermal studies have been performed by M. Krauth, from IPHC, during the development of STELLA [29].

The rotation system used by the STELLA experiment can accommodate three rotating targets held by the blue supports, and six fixed targets on the yellow support. The central position of the yellow support is reserved for the use of an empty, electrically-isolated target holder in the chamber, to allow control of the beam focus.

The fixed targets are mounted on target holders with a central aperture 9 mm in diameter. They were prepared by the INFN (Istituto Nazionale di Fisica Nucleare) in Legnaro, Italy, and enriched in ^{12}C.

The rotating targets are manufactured at GANIL, with thicknesses of between 30 and 60 µg/cm^2 for the 2022 experimental campaign. The carbon sheets, made of carbon containing 98.9% of ^{12}C, are deposited on a circular frame with an external diameter of 63 mm and an internal diameter of 46 mm. The beam impinges on the target about 8 mm from the inner edge of the frame, indicated by the black dot in Fig. 2.10. This provides a large irradiation area, visible in Fig. 2.11: the photo on the left shows a target before irradiation, and the one on the right after irradiation. The area subjected to the beam appears lighter than the untouched surface.

The targets are rotated by three small wheels holding each target support. The movement is provided by the bearing at the bottom of the support, connected to the

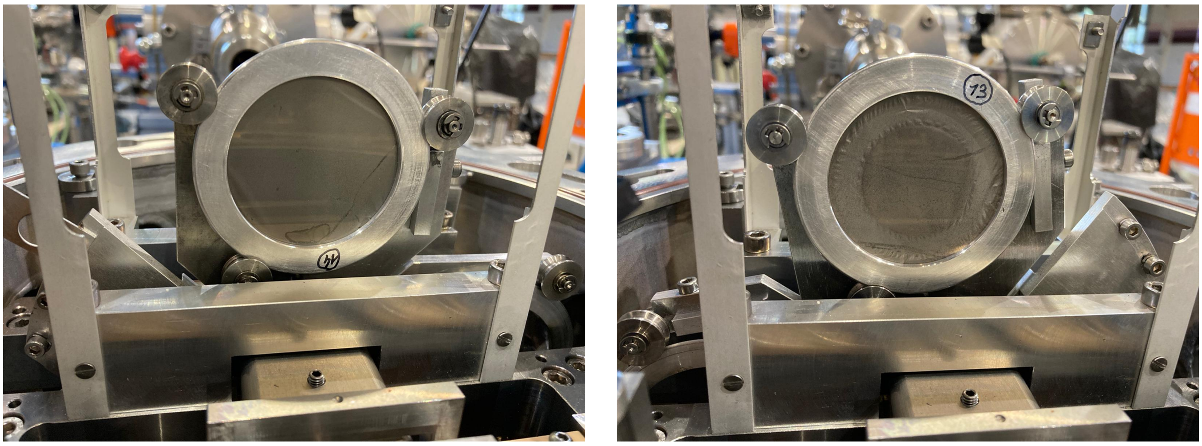

Figure 2.11: Left: Picture of a target in the target holder before irradiation. Right: Picture of a target after irradiation. The irradiated area is lighter than the area that is not impacted by the beam.

central bearing, shown in brown in Fig. 2.10. The axis of rotation, visible on the front of the figure, is connected to a motor located outside the chamber, shown on the right in Fig. 2.8. The connection is made via a magnetic coupling, developed by UHV Design Ltd [81], which maintains the ultra high vacuum in the chamber despite the movement of the axis. The target is thus able to reach a speed of around 1000 rpm.

Finally, the position of the rotation system, and therefore the choice of the target under the beam, is controlled by a second rotation axis located opposite to the one used to rotate the target. A graduated wheel on the outside of the chamber is used to choose between the three rotating targets and the six fixed targets.

2.3.3 Charged particle detectors

The detection of charged particles plays an essential role in the study of the fusion reaction $^{12}C + ^{12}C$. Indeed, it is only through their detection that it is possible to access the angular distributions for the excited states of the daughter nuclei, as shown in [22]. For its experimental set-up, the STELLA collaboration chose to use three detector systems: two type DSSSD silicon detectors and the PIXEL system, in order to obtain the largest possible angular coverage, and two so-called monitors, in order to control the state of the target during the experiment, but also to measure the elastic scattering of the reaction $^{12}C + ^{12}C$ for normalisation purposes.

Figure 2.12 is a photograph of the interior of the reaction chamber taken during the 2022 experimental campaign. It shows the PIXEL detector system on top of the target, and the silicon detectors on the beamline.

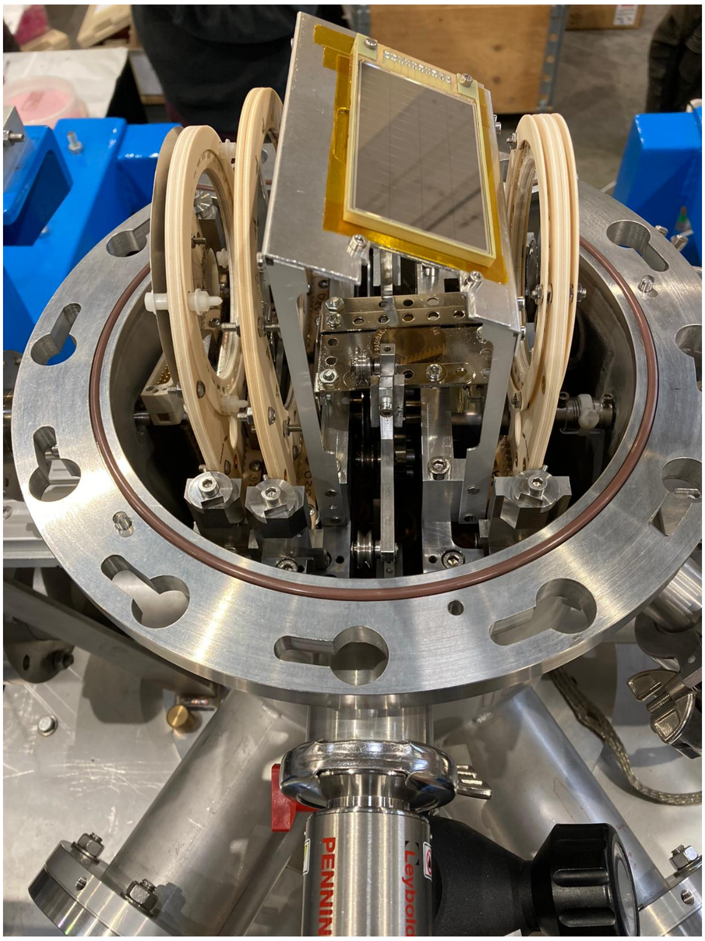

Figure 2.12: Photograph of the STELLA experiment's reaction chamber taken during the 2022 experimental campaign.

DSSSD

The DSSSD, for Double Sided Striped Silicon Detector, are S3 type silicon detectors with chips from Micron Semiconductor Ltd and mounted on PCB at IPHC.

These detectors have a cylindrical symmetry, with 32 sectors on the ohmic side and 24 rings on the junction side. The rings have a width of 986 µm with a 100 µm resistive separation. The active area has an intern and extern diameter of 22 mm and 70 mm, respectively, and a thickness of 500 µm. Figure 2.13 is a photograph of the junction face of a S3 type DSSSD used by the STELLA experiment. The 24 rings are visible, as are the mass connectors, the small black circles on the PCB plate, and the connections to the pins at the bottom of the detector.

The scheme of the S3 Printed-Circuit Board, called hereafter PCB, developed by the IPHC is shown in Fig. 2.14, with the ohmic side on the left and the junction side on the right. The ground points are represented by the green circles and the connectors by the pink lines. The sectors, visible on the left-hand side, are all connected to the mass. Each of the rings on the right of the figure is connected to a signal track, which

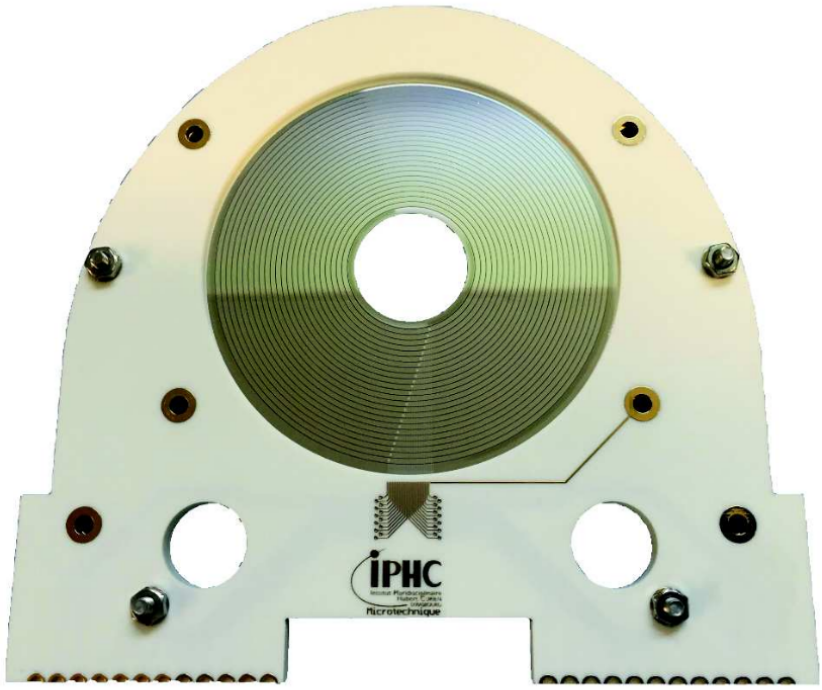

Figure 2.13: Photography of the junction side of a S3 type DSSSD. The 24 rings and the connections to the pins at the bottom of the detector are visible. From [6]

is distributed on either side of the PCB, towards the bottom, before being transmitted through connectors.

Two circles are visible on either side of the PCB, below the detection zone, and bypassed by the electronic tracks. Both openings allow the beam particles scattered in the target to be detected by the two monitors.

The S3 types DSSSD were tested with a 3α source. The results obtained indicate a rise time between 80 and 120 ns and a fall time between 15 and 20 µs. The resolution measured was FWHM = 0.5% at 5 MeV.

The materials used in the chamber were carefully chosen to be compatible with the ultra-high vacuum required to study the $^{12}C + ^{12}C$ fusion reaction.

The PCBs are made from RO4003C^{TM} from ROGERS Corporation, a patented ceramic-reinforced glass braided material, material known to have a low outgassing rate. The design chosen by the STELLA collaboration for the PCBs also minimises the volume of the reaction chamber, unlike the standard electronic boards supplied by Micron.

Connections to the preamplifiers are made from the bottom of the detectors, using pins that make electronic contact with the detector connectors. The signals are then transmitted using Kapton® cables, a material also known for its excellent compatibility with ultra-high vacuum.

The preamplifiers are Mesytec® MPR-16D differential cards, and are connected

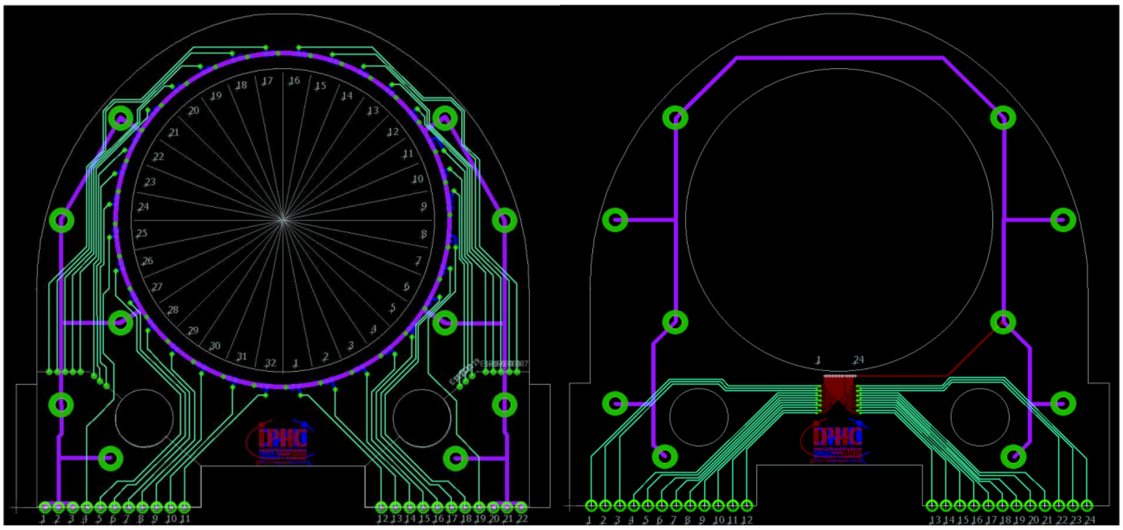

Figure 2.14: Scheme of the S3 Printed-Circuit Board (PCB), designed and mounted at IPHC. The ohmic side is on the left, the junction side on the right. From [6]

directly to the chamber, reducing electronic noise. The cards are contained in aluminium cylinders, used as Faraday cages, limiting electromagnetic noise. Finally, the signals are routed to the differential/single-ended converters via shielded cables.

The inside of the chamber houses two S3 DSSSDs: one forward the target and the other backward its, called S3F and S3B, respectively.

The S3F detector is positioned 59.2 mm from the target. It covers angles between $\theta_{\text{lab}} = 10.4°-30.3°$ with respect to the beam, which corresponds to a solid angle of 0.75 sr. The side facing the target is protected from the significant scattering of the beam in the target by a thick aluminium foil of 10 µm.

The S3B detector is positioned 55.6 mm from the target. It covers the angular range between $\theta_{\text{lab}} = 148°-169°$, which corresponds to a solid angle of 0.84 sr. It is covered at the front with a thin sheet of aluminium, 1.6 µm thick, to stop the electrons produced by the impact of the beam on the target.

The aluminium foils are mounted on RO4003C$^{\text{TM}}$ hoops and are attached to the detectors at the mass points. This allows them to evacuate the intense charge deposit.

To avoid any interaction and discharge of the foils on the detectors, these are attached to the ohmic faces of the DSSSDs, which are also connected to the mass.

PIXEL

The PIXEL detection system was added during the 2022 experimental campaign, with the aim of completing the angular coverage at angles between $\theta_{\text{lab}} = 60°-90°$. Two types of detector can be used: a BB10 and a SUPER-X3, both Position Sensitive Detectors produced by Micron Semiconductor Ltd.

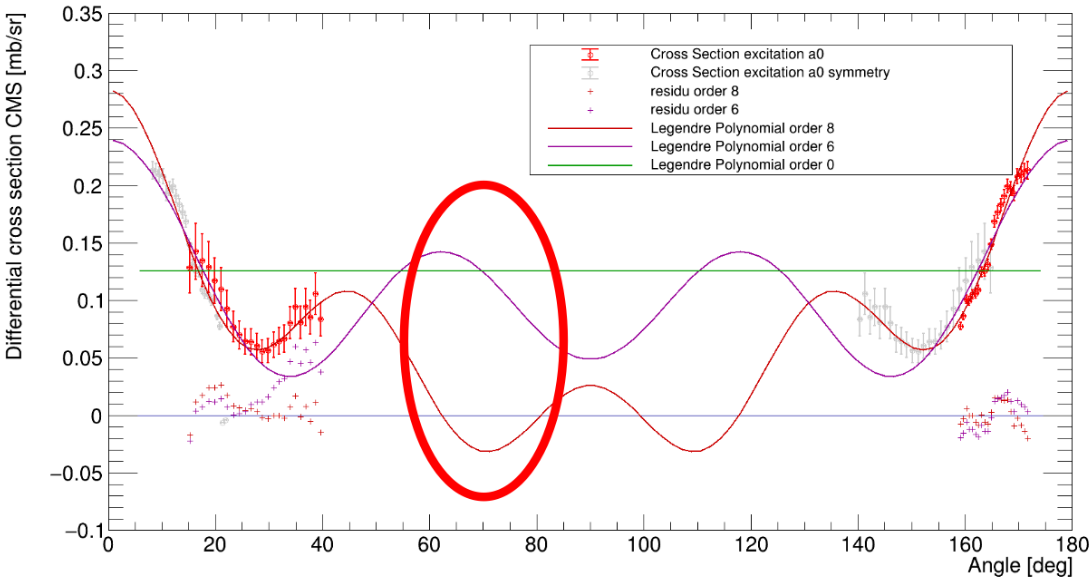

Figure 2.15: Angular distribution for α_0 for the ^{12}C + ^{12}C fusion, at E_{com} = 5.38 MeV by J. Nippert [28]. The red circle indicates the angular range probed by PIXEL.

This addition has two direct consequences: it increases the solid angle of the experiment, but also improves the accuracy of the determination of the angular distribution. Figure. 2.15 shows the angular distribution of the α_0 channel obtained from data from STELLA's 2019 experimental campaign [28]. The set-up used at the time, consisting of the two detectors S3F and S3B, did not cover the angular interval that would allow discrimination between the orders of the Legendre polynomials. The addition of PIXEL, whose angles are indicated by the red circle, solves this problem.

The data taken during the 2022 experimental campaing are currently under analysis.

The BB10 detector, shown in the left panel of Fig. 2.16, is a DC strip silicon detector without bias resistors.

It is composed of eight junction strips with junction pitch of 4944 µm, and a total active area of 39.45 × 74.15 mm², with a thickness ∼ 1 mm. The junctions and the strip connections to the pins, represented by the rectangles at top of each junction, can be identified.

This detector is used for its segmentation, the signal is collected at the beginning of each strip. The position of the event on the strip is then determined with a pulse shape analysis.

The response speed of this detector does not allow precise timing selection, so it is not the most suitable for a γ-particle coincidence study at low energies. However, its high angular accuracy makes it an excellent tool for the accurate measurement of angular distributions.

The SUPER-X3 detector is shown in the right panel of Fig. 2.16.

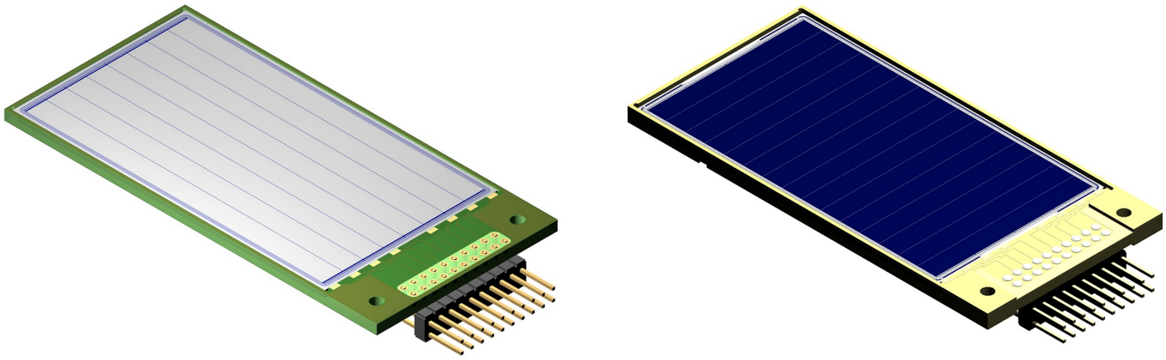

Figure 2.16: Left: 3D view of the BB10 detector. Right: 3D view of the Super-X3 detector. Both pictures are from [30].

It is composed of four junction strips and four ohmic sectors. The total active area is 40.30×75.00 mm$^{\mathbf{2}}$, with a thickness ~ 1 mm.

On the junction side the signal is collected from both side of the strip, allowing a good determination of the light particle impact on the detector.

The timing determination of this detector is more precise than with the BB10 detector.

During the 2022 experimental campaign, both detectors have been protected from beam scattering by aluminium foils with a thickness of 6 µm.

Monitor

To obtain an absolute normalisation of the effective cross section of the ^{12}C + ^{12}C fusion reaction, the STELLA collaboration chose to use the measurement of elastic scattering of the beam in the target. Two silicon detectors, called monitors, were installed in the chamber to monitor this scattering.

At sub-Coulomb energies the cross section of the elastic scattering of two identical bosons is described by the Mott formula [82] :

$$\left(\frac{\mathrm{d}\sigma}{\mathrm{d}\Omega}\right)_{\mathrm{com}} = \frac{Z^4 e^4}{4(4\pi\epsilon_0 E_{\mathrm{com}})} \times \left[\frac{1}{\sin^4(\frac{\theta_{\mathrm{com}}}{2})} + \frac{1}{\cos^4(\frac{\theta_{\mathrm{com}}}{2})} + \frac{2}{\sin^2(\frac{\theta_{\mathrm{com}}}{2})\cos^2(\frac{\theta_{\mathrm{com}}}{2})} \cos\left(\frac{Z^2 e^2}{4\pi\epsilon_0 \hbar\nu} \ln\left(\tan^2(\frac{\theta_{\mathrm{com}}}{2})\right)\right)\right], \tag{2.8}$$

where Z is the atomic number of the considered nucleus, e the elementary charge, ϵ_0 the dielectric constant, $\hbar$ the reduced Planck constant, and θ_{com} and E_{com} the scattering angle and the energy of interaction in the center of mass system, respectively.

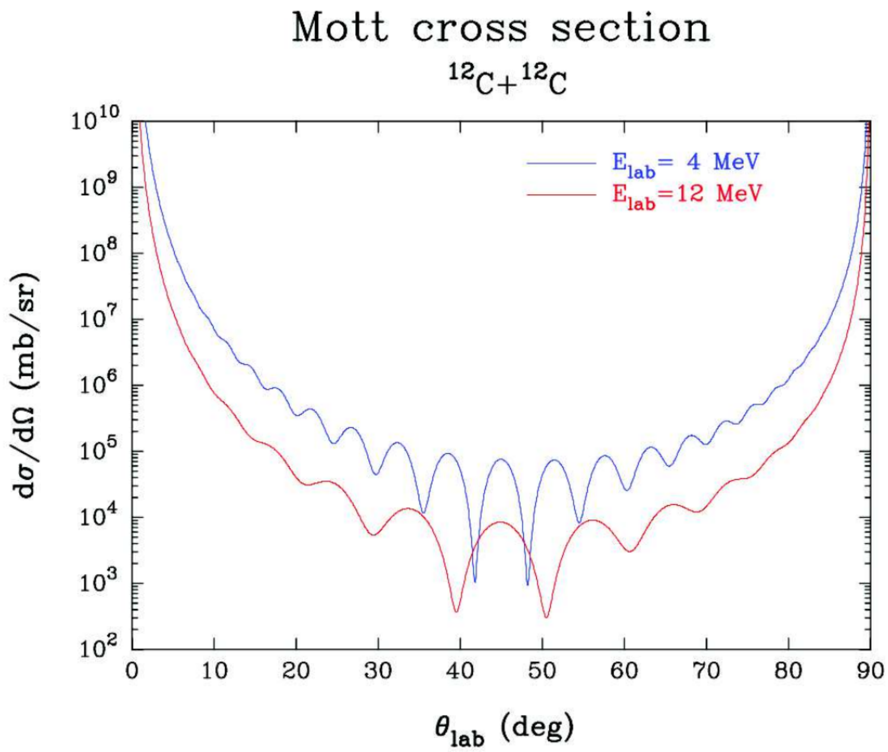

Figure 2.17: Angular distributions in the laboratory frame for the ^{12}C + ^{12}C Mott scattering. From [6].

The ^{12}C + ^{12}C system can be described by this formula, the ^{12}C being an even-even nucleus with a 0^+ spin-parity in its ground state.

Figure 2.17 presents angular distributions in the laboratory frame for the ^{12}C + ^{12}C Mott scattering for $E_{\text{lab}} = 4$ MeV in blue and $E_{\text{lab}} = 12$ MeV in red.

In this frame the diffusion is only in forward direction, because of the identical masses of the particles.

The interferences pattern, due to the quantum properties of identical bosons, shows different local maxima and minima depending of the energy of the scattering, except for the local maxima at $\theta_{\text{lab}} = 45°$, which appears to be independent of the energy. This angle is thus the best choice to place the monitors for a consistent monitoring and then normalization.

The monitors are placed in the monitor extensions, visible on the left in Fig. 2.8. They are located 23 cm away from the target, at an angle of 45°. A 1 mm diameter aluminium collimator is used to reduce the solid angle, and therefore the expected high count rate. Each monitor then has a total solid angle of 1.38×10^{-5} sr.

The collimator is designed so that the irradiated zone is located on the edge of the detector. It is then possible to change this irradiation zone by changing the rotation of the monitor, which means that it can continue to be used even if a zone is damaged, increasing its lifetime.

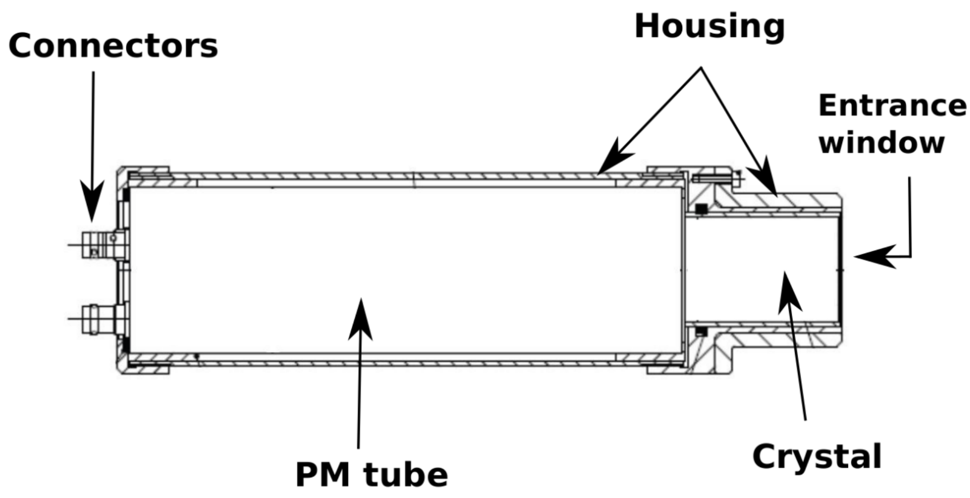

Figure 2.18: Schema of a $LaBr_3(Ce)$ scintillator. From [27]

The cross section of the elastic scattering of ^{12}C + ^{12}C is much higher than the ^{12}C + ^{12}C fusion cross section. This results in a very high count rate in the monitors, which leads to the deterioration of their energy resolution, and thus makes difficult to analyse the spectra for accurate data normalization.

Nevertheless, by combining the data from the monitors with that from the Faraday cup, it is possible to track the state of the target and the position of the beam.

2.3.4 Gamma-ray detectors: UK-FATIMA collaboration

The STELLA collaboration is using $LaBr_3(Ce)$ scintillation detectors from the UK-FATIMA (FAst TIMing Array) collaboration [83] to measure the γ rays produced by the ^{12}C + ^{12}C fusion reaction. These detectors, at the number of 36, are positioned as close as possible to the reaction chamber, in an optimised cylindrical configuration. These scintillators present an intrinsic efficiency; and a timing resolution better than germanium detectors, allowing a sub-nanosecond timing response.

$LaBr_3(Ce)$ detectors

The STELLA collaboration uses a total of 36 $LaBr_3(Ce)$ detectors during its experimental campaigns. Each detector is based on a cylindrical scintillator crystal, with a diameter of 3.8 cm and a length of 5.1 cm. The photons producted inside the crystal are collected by a photomultiplier tube with a diameter of 7.6 cm. The detectors are encapsuled in an aluminium box with a thickness $\sim$ 0.5 mm for the front panel and $\sim$ 2.2 mm on the side. A technical drawing of a $LaBr_3(Ce)$ detector is represented Fig. 2.18.

These detectors have a non-linear response to the energy of the γ measured: their calibration requires a polynomial of order 2. However, for the detectors used by

	Angular coverage [%]		
# Det	Spherical	Cylindrical	Wall
10	23.3	23.1	20.6
12	24.4	23.2	21.2

Table 2.1: Angular coverage (in % of 4π) of $LaBr_3$(Ce) scintillators according different configurations and number of detectors in the first ring. From [6].

STELLA, the ratio between the linear term and the quadratic term is about 10^{-6}. The resolution of these detectors is of the order FWHM $\approx 3\%$ at 1.33 MeV. $LaBr_3$(Ce) scintallors have a excellent time resolution: they present a precision better than 1 ns [84]. This time resolution is essential for the STELLA experiment in order to discriminate the protons and α.

$LaBr_3$(Ce) detectors are known to contain radioactive elements with intrinsic radioactive activity. Two isotopes are mainly responsible for this activity: ^{138}La and ^{224}Ac.

The natural abundance of the ^{138}La is of 0.0902%, and its half-life is of $T_{1/2} = 1.05 \times 10^{11}$ years [85]. The corresponding activity is around 90 Bq of background per crystal. The ^{138}La decays at 66.4% into ^{138}Ba by electron capture and at 33.6% into ^{138}Ce through β emission. In both cases, only the 2^+ will be populated in daughter nuclei, leading to a decay with γ emission, at energies $E_\gamma = 1436$ MeV and $E_\gamma = 789$ MeV for the electron capture and the β emission, respectively.

The ^{224}Ac, and its decay products, emit α particles at different energies, between $E_\alpha = 1600$ keV and $E_\alpha = 3000$ keV, that can be seen in γ spectra [86].

^{138}La scintillators therefore have a natural activity that produces a constant background in the γ spectra, a contribution that can be reduced using the coincidence method.

Geometric configuration

In order to determine the most optimal scintillator array configuration for the set-up, a Geant4 simulation was carried out [87]. Several parameters had to be taken into account: the angular coverage of the grid, its ease of construction and handling on the beamline and under experimental conditions, its compactness, and its detection efficiency.

Three geometries were studied: a wall configuration where the detectors are stacked in staggered rows, a spherical configuration where all the detectors point towards the target, and a cylindrical configuration where the detectors face the beamline. In the last two cases, studies with varying numbers of detectors on the first line have been carried out.

The angular coverage obtained for each configuration with isotropic γ emission of energy $E_\gamma = 10$ keV is summarised in Tab. 2.1. The spherical configuration is the one with the best angular coverage, unlike the wall configuration, which therefore has been discarded.

E_γ (MeV)	0.01	0.44	1.0	1.63	2.0	3.0	4.0	5.0	6.0	7.0
ϵ_{sing} [%]	23.1	8.0	3.5	2.2	1.8	1.1	0.7	0.5	0.4	0.4
ϵ_{sum} [%]	23.1	8.6	4.1	2.6	2.1	1.4	1.0	0.7	0.6	0.5

Table 2.2: Efficiency of the photoelectric peak with respect to the energy for 36 scintillators in the cylindrical configuration. ϵ_{sing} is the efficiency from single spectra analysis, and ϵ_{sum} is the sum of the total energy deposit in the array. From [6].

The geometric acceptances of the last two configurations are similar, and the number of detectors in the first ring does not significantly influence them. So, for reasons of practicality, the cylindrical configuration with ten detectors on the first ring was selected. A 3D CAD of the cylindrical configuration can be seen in the upper panel of the Fig. 2.19, and a 3D CAD of the first ring of detectors of this configuration is represented in the bottom panel.

To move the scintillators array upward and downward, the STELLA collaboration designed a lifting mechanism topping the reaction chamber. Figure 2.20 is a scheme of the structure built for the manipulation of the detectors array: a counterweight system allows the placement of the $LaBr_3$(Ce) scintillators as close as possible to the target during data acquisition, and its uplift to access the reaction chamber between runs.

The efficiency of the γ detection system has been studied for the cylindrical configuration simulation in by G. Fruet [6]. Two different cases have been investigated.

The first one, called ϵ_{sing}, considers only multiplicity-one events, it is therefore the study of each scintillator individually. An efficiency is associated to each detector, and the total efficiency of the whole system is the sum of the individual efficiencies.

The second case, called ϵ_{sum}, takes into account the Compton events, and the fact that a single γ can deposit energy in several scintillators. These partial energies can then by summed, and the global efficiency can be determined. This correction is more relevant for high-energy γ.

The results are presented in Tab. 2.2, for different incident E_γ.

For the γ of interest for the ^{12}C + ^{12}C fusion reaction, the efficiency is of the order $\epsilon = 8\%$ and $\epsilon = 3\%$ for $E_\gamma = 440$ keV and $E_\gamma = 1634$ keV, respectively.

2.3.5 Vacuum system

The vacuum in the reaction chamber is an important component of the experimental conditions. In order to reduce the background contaminating the data spectra as much as possible, it is necessary to minimise interactions between the beam and the particles making up the residual gas contained in the chamber (and the beam line). To achieve

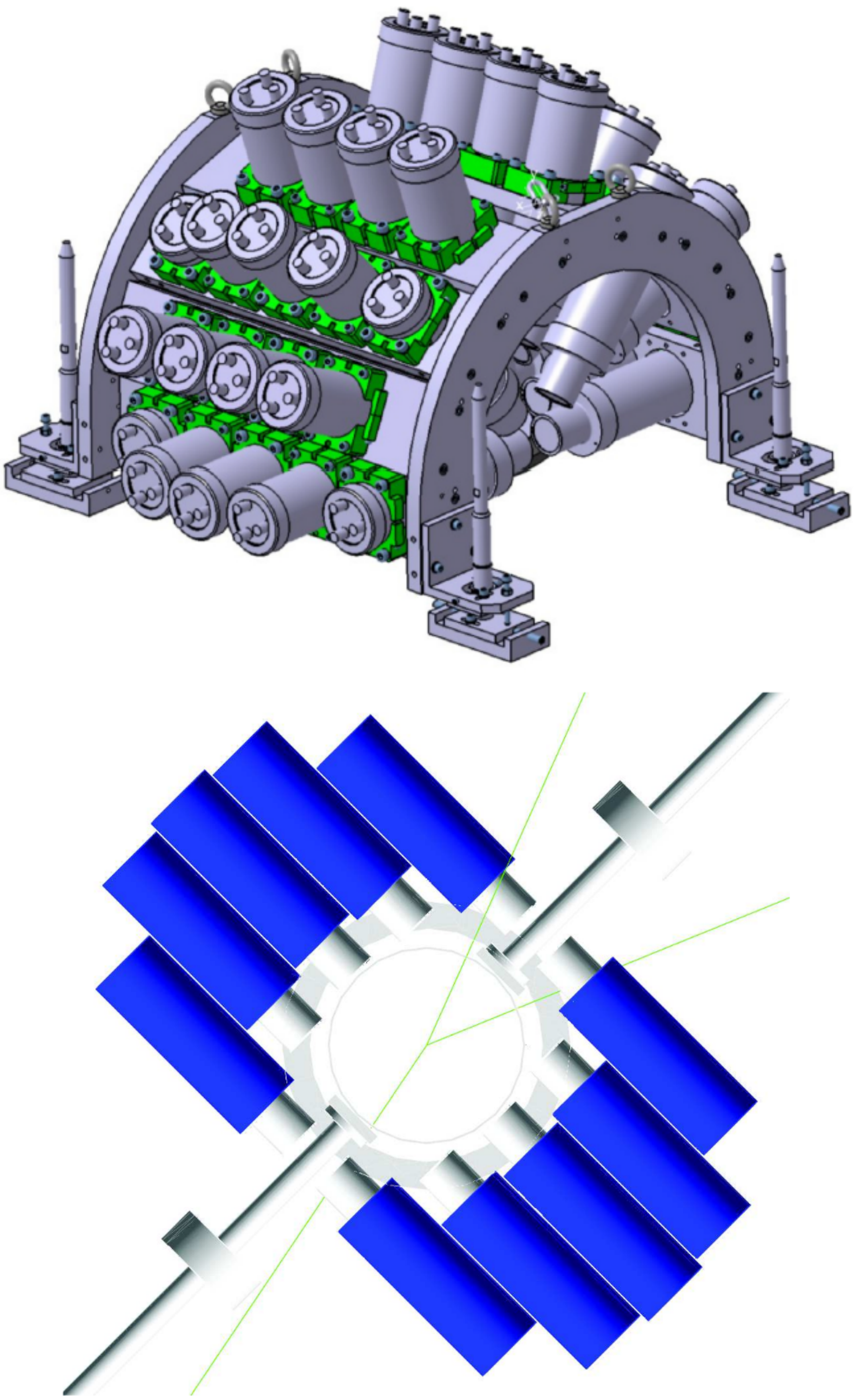

Figure 2.19: Top: 3D CAD representation od the UK-FATIMA detectors on the cylindrical configuration support. Bottom: 3D CAD representation of the first ring of detectors of the cylindrical configuration. The green lines show the trajectory of three γ rays from the target. Both figures are from [29]

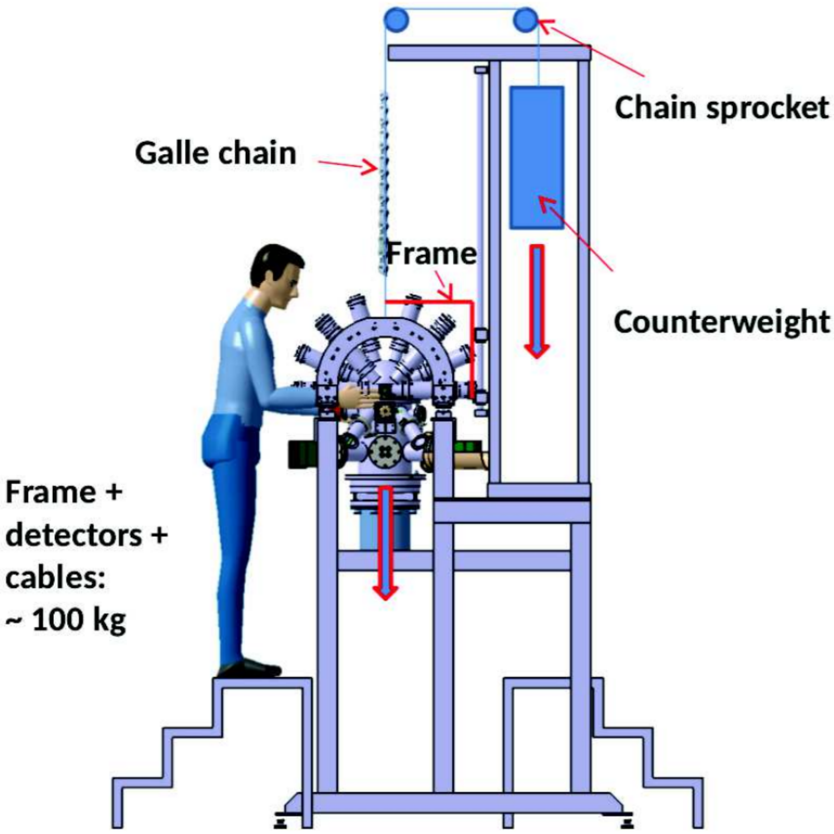

Figure 2.20: Scheme of the structure allowing the manipulation of the scintillators array. Fromé[6]

this, a pressure of $P \leq 10^{-7}$ mbar is required in the reaction chamber.

A combination of three pumping systems has thus been used: a primary dry pump, two turbomolecular pumps and a cryogenic pump.

The primary dry pump is directly connected to the chamber by one flange at the side of the stainless steel cylinder. This allows the gas flow to follow a trajectory parallel to the targets in the chamber, and with the precision of the valve it reduces the risk of damage not only to the thin carbon foil but also to the aluminium foils protecting the detectors. A primary vaccuum of the order 2×10^{-1} mbar is reached within few minutes.

When this primary vaccuum is reached, the turbomolecular pumps, placed on the beamline, on either sides of the reaction chamber, are switched on. A secondary vaccuum around 10^{-3} mbar is reached in few minutes.

After that the cryogenic pump can be started. It has a 20 cm diameter and is fixed at the bottom of the reaction chamber by an isolating valve. The cryogenic pump is a very cold trap, between 15 and 18 K, composed of plates cooled by liquid helium. The residual gas inside the chamber hits the plate, and transfers it kinetic energy to the helium circulating in the plates. The gas is then trapped, and a compressor ensures the cycling of the helium to maintain the temperature. With this last pump, the reaction chamber reaches a pressure of $P \sim 6 \times 10^{-8}$ mbar.

To facilitate the establishment of this vacuum, materials with low outgassing, such as specific PCB materials, are used inside the chamber. In addition, working above the chamber and its opening are made with caution.

2.3.6 Acquisition systems and synchronization

In order to convert the signals generated by the various detectors into usable data, it is necessary to evaluate them in terms of energy and time. This is done by the acquisition systems.

The STELLA experiment is based on two detection systems: two sets of DSSSDs (S3F/S3B and PIXEL), and scintillators from the UK-FATIMA collaboration. So there are two different acquisition systems, each adapted to the types of detectors under consideration. And to use the coincidence method, a time synchronisation is also required.

STELLA acquisition system

The STELLA acquisition system includes all the hardware and software used to process and record the data. It was developed by the "Système de Mesure et d'Acquisition" technical group at the IPHC in Strasbourg.

The detectors used in the reaction chamber, S3F, S3B and PIXEL, are silicon semiconductors. Depletion of the substrate is created by biasing it with a potential difference of −60 V applied to the junction side.

When a particle penetrates the polarised substrate, it creates electron-hole pairs along its path. The electric field applied in the detector will cause the migration of the electrons on the ohmic side and the holes on the junction side, in a direction perpendicular to the surface of the detector. The signal is then generated by the potential difference created by the movement of the charges.

Figure 2.21 illustrates how a silicon detector works: the incident particle trajectory is shown in black, the holes in red and the electrons in blue.

The signal generated is then transmitted to a differential preamplifier, where it is amplified. The shape of the resulting signal can be seen in the upper panel of Fig. 2.22.

The rise time corresponds to the collection of charges, and is generally between 80 and 120 ns. The maximum amplitude reached is representative of the total energy deposited in the detector. The fall time represents the discharge of the preamplifier and follows an exponential trend, usually between 15 and 20 µs.

Usually, a simple trigger threshold is applied to the signal at the output of the preamplifier: if the amplitude exceeds a certain value, the signal is processed and recorded. However, this method is sensitive to the long decay time of the signal, as well as to possible baseline fluctuations.

The STELLA collaboration has chosen to use a digital triggering system.

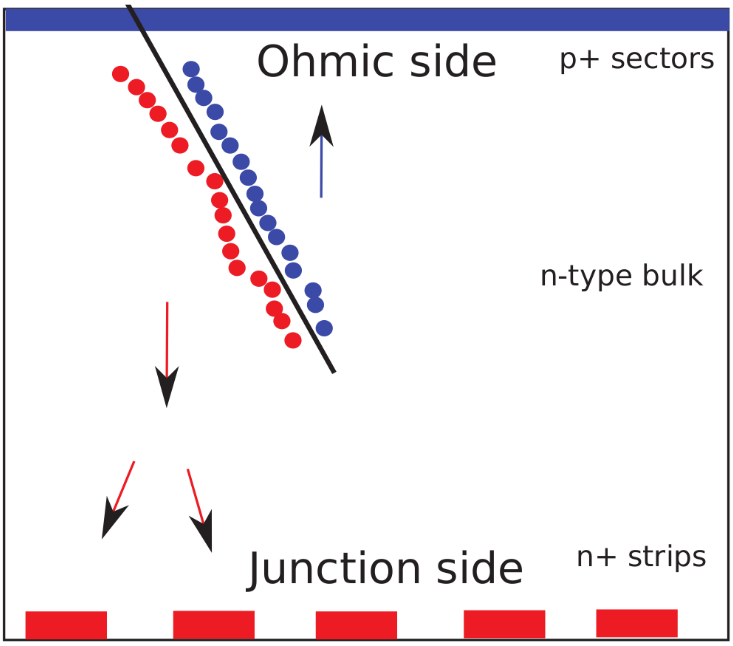

Figure 2.21: Scheme of the working principle of a polarized silicon particle detector. From [6].

To do this, the pre-amplified signal is sent to an electronic converter where it is transformed from a differential signal to a single ended signal. It is then sent to the STELLA data acquisition system.

It consists of 8 FMC112 cards contained in a commercial ABACO 125 µTCA crate. The cards are grouped two by two using 4 FC7 AMC cards, for Advanced Mezzanine Card. Each card contains 12 ADC channels, for a total of 96 channels, providing time and energy information. These channels manage a single ended signal.

In this acquisition system, the pre-amplified signal undergoes several transformations. First, a differentiation process: a time delay is applied to the received signal, and the difference with the raw signal is calculated. This result is then integrated over a defined number of samples, which is adjusted with the acquisition program. This integration reduces baseline dependency by averaging its fluctuations. The triggering of signal processing and recording then depends on a user-defined threshold. The resulting signal can be seen in the bottom panel of Fig. 2.22.

This processing method also reduces dead time by optimising the signal integration window.

This process of differentiating and integrating the signal from the silicon detectors is carried out continuously by the digital algorithm on the acquisition cards, with a sampling frequency of 8 ns. When the trigger threshold is reached, the signal is processed using Jordanov's algorithm [88] until a trapezoid is obtained, as shown in Fig 2.23.

The trapezoid is characterised by three parameters: its rise time, and the width and height of its platform. These parameters are controlled and adjusted by the user via the acquisition system interface, who can also define a digital gain. The energy of

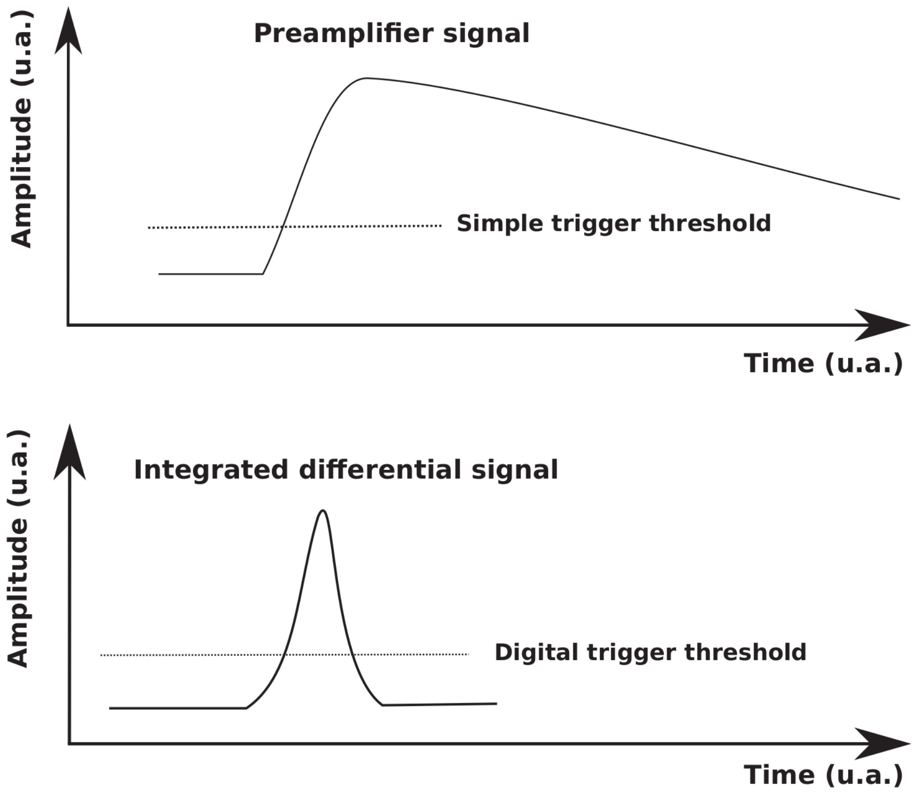

Figure 2.22: Top: Triggering system with a simple trigger threshold applied on a preamplifier signal. Bottom: Triggering system with a digital trigger threshold applied on an integrated differential signal. Both figures are from [6].

the signal is finally determined by averaging over the height of the trapezoid.

UK-FATIMA acquisition system

The γ produced during the ^{12}C + ^{12}C fusion reaction will penetrate and ionise the scintillator crystal. In response, the scintillator will emit light. The light enters the Photo Multiplier Tube (PMT) *via* a photocathode, which converts photons into primary electrons. The electrons are then accelerated through a series of dynodes between which potential differences are applied. This will generate an avalanche of electrons to amplify the signal read by the acquisition system.

A schematic diagram of a scintillator associated with a PMT is shown in Fig. 2.24. The incident γ is shown in purple, the low-energy light rays in red.

The signals from the $LaBr_3$(Ce) detectors are then transmitted to 1 GHz VME-based V1751 cards from Caen. Five boards, each accommodating eight acquisition channels, were used, which can also receive external signals, such as the time signals required for the coincidence method. The high voltage of 1000 V required for the PMTs is provided by a dedicated multi-channel module from Caen.

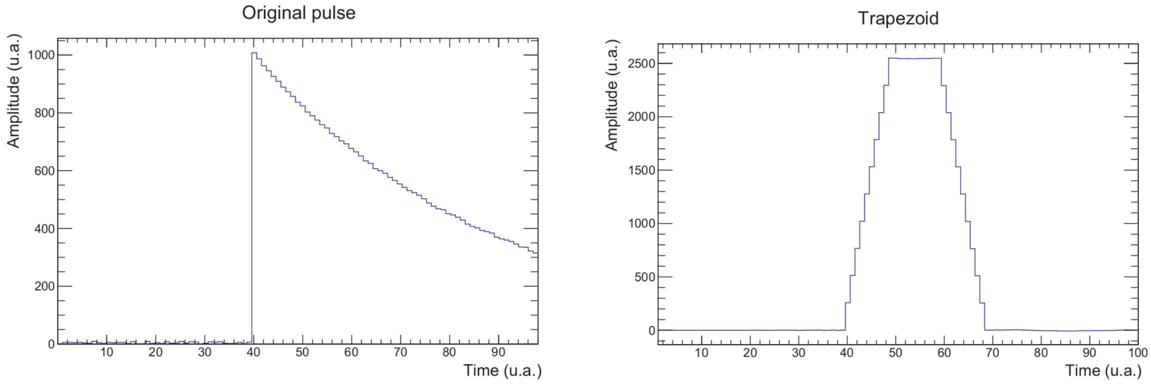

Figure 2.23: Left: Arbitrary signal with exponential decrease. Right: Trapezoid signal using the Jordanov algorithm. Both figures are from [6].

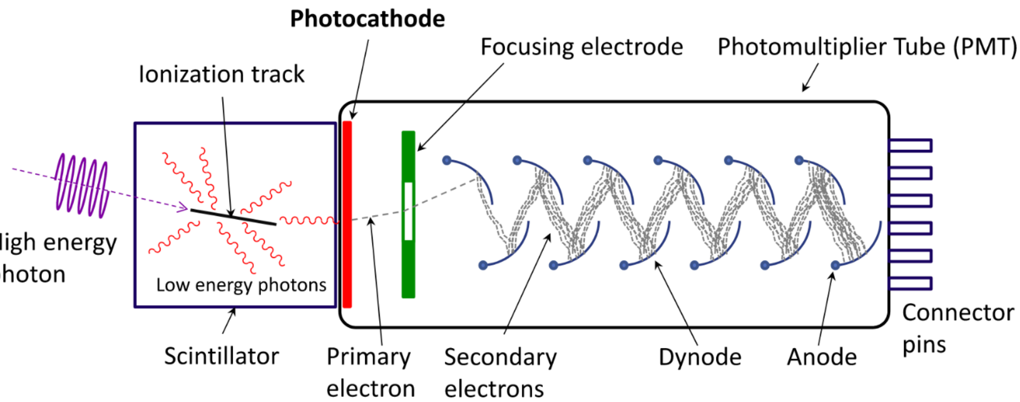

Figure 2.24: Scheme of a scintillator with the associated PMT. The scintillator converts the high energy incident γ in a low energy light, and the PMT convert this light into a electrical signal. From [31].

The acquisition software used to read and save the data was implemented in the STELLA acquisition framework for the 2022 experimental campaign.

Time synchronization

The coincidence method used by the STELLA experiment requires time synchronisation of the data collected by the STELLA and UK-FATIMA acquisition systems.

Time synchronisation is provided by a Gigabit Link Interface Board (GLIB), which is hosted by the same µTCA module as STELLA acquisition system FC7 boards.

The GLIB card continuously generates a 10 MHz clock which is delivered to the eight STELLA acquisition cards. Each of these eight cards then transmits a 125 MHz signal which is distributed to the two PIXEL system acquisition cards and five UK-FATIMA acquisition cards.

Figure 2.25 shows a diagram of the distribution of the clock used to synchronise the STELLA-FATIMA-PIXEL acquisition. The red maps are for the STELLA ac-

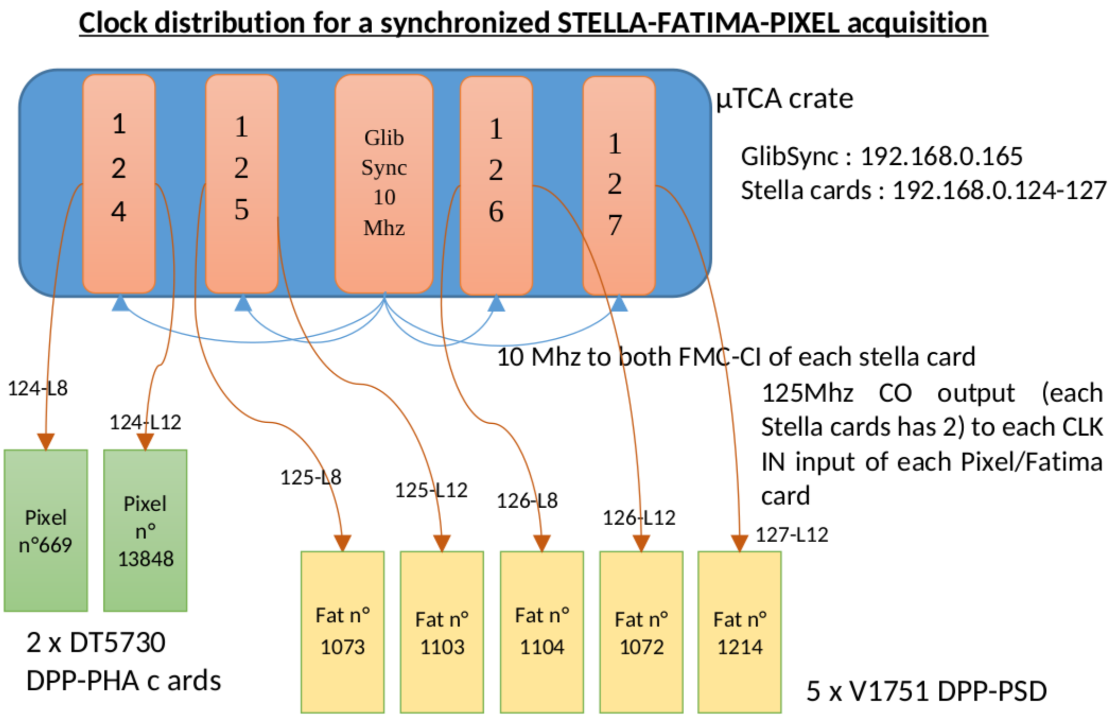

Figure 2.25: Scheme of the clock distribution for a synchronized STELLA-FATIMA-PIXEL acquisition. Credits M. Richer.

quisition, the green for PIXEL and the yellow for UK-FATIMA. The 10 MHz signals produced by the GLIB card are shown in blue, while the 125 MHz signals generated by the STELLA cards are shown in red.

Thanks to this system, a common clock is used for all the acquisition cards. However, the different internal clocks can be started with a slight delay of up to approximately 1 s.

To align the internal clocks, the GLIB card will generate a synchronization signal, here a positive square signal which is distributed over every acquisition card on a particular input or channel number. The synchronization can be done manually on the software, or automatically at regular intervals.

This synchronization system is represented in Fig. 2.26.

Finally, this acquisition system allows several parameters to be written to disk for each event: the number of the acquisition channel triggered, the energy and the time at which the trigger threshold was reached. Bits are also specially allocated for events exceeding the system's detection limit (saturated signals) as well as pile-ups due to excessively high count rates.

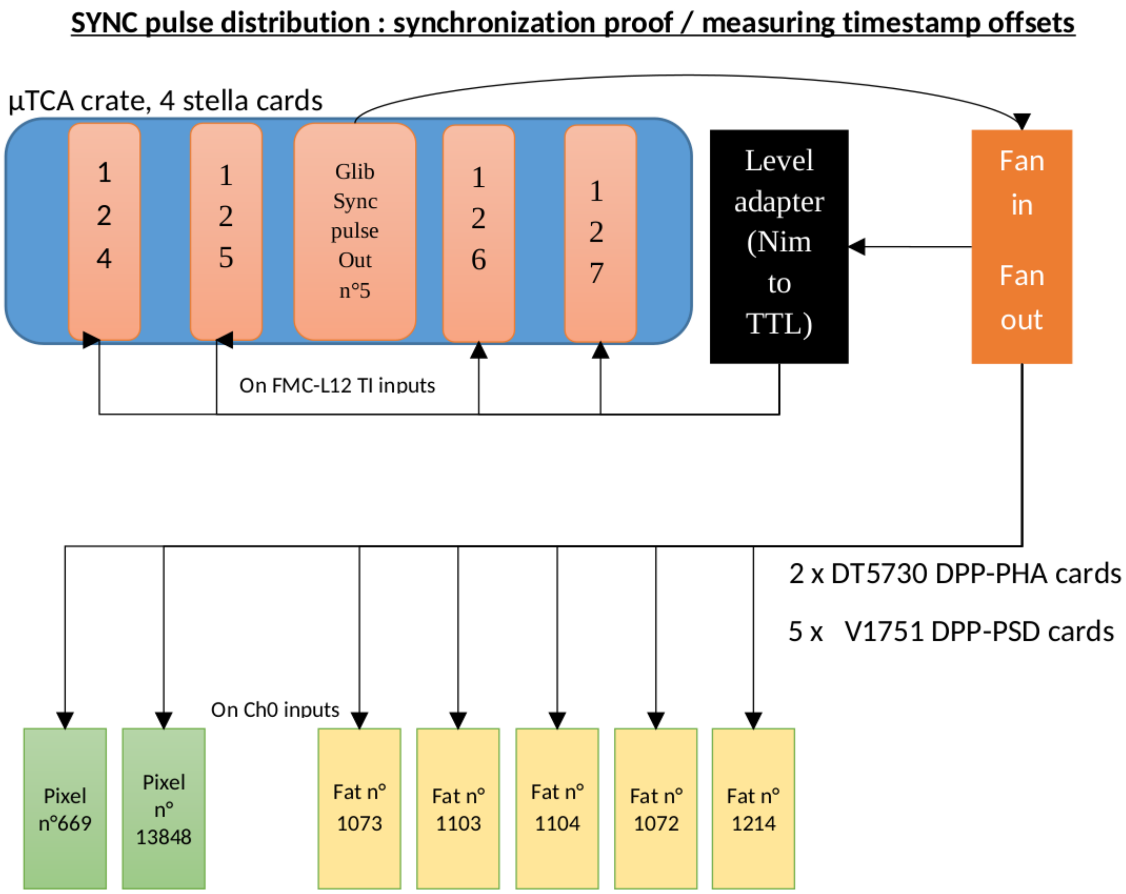

Figure 2.26: Scheme of the synchronization pulse distribution in the STELLA-FATIMA-PIXEL acquisition system. Credits M. Richer.

2.3.7 Andromede facility

The STELLA experiment is based at the Andromede facility at IJCLab in Orsay, France [89]. It is part of the MOSAIC platform. Andromede is a 4 MV electrostatic Pelletron©, made by NEC® company (National Electrostatique Corporation). Figure 2.27 shows a picture of Andromede. This accelerator can produce different types of beams, from light ions like ^{12}C to molecules, and can deliver stable beams at very high intensity ($\geq$ 10 pµA), a necessary feature for the studies of the STELLA collaboration.

For the STELLA campaing, the plasma is produced from a ECR source (Electron Cyclotron Resonance) which can deliver multiple charge states of the beam, 2^+ and 3^+ here. A CH_4 gas was used here, to limit possible contamination, by ^{16}O for example.

The acceleration process starts with frictions of chain carrying and deposits electrons along the acceleration tube, which will create potential differences and a electrostatic field. The accelerated ions are then selected by a Wien filter in a first step, and a magnetic dipole. The STELLA apparatus is placed at the 90° beamline, the magnetic dipole allowing the discrimination of the contribution that does not have the right ratio number of mass over charge state.

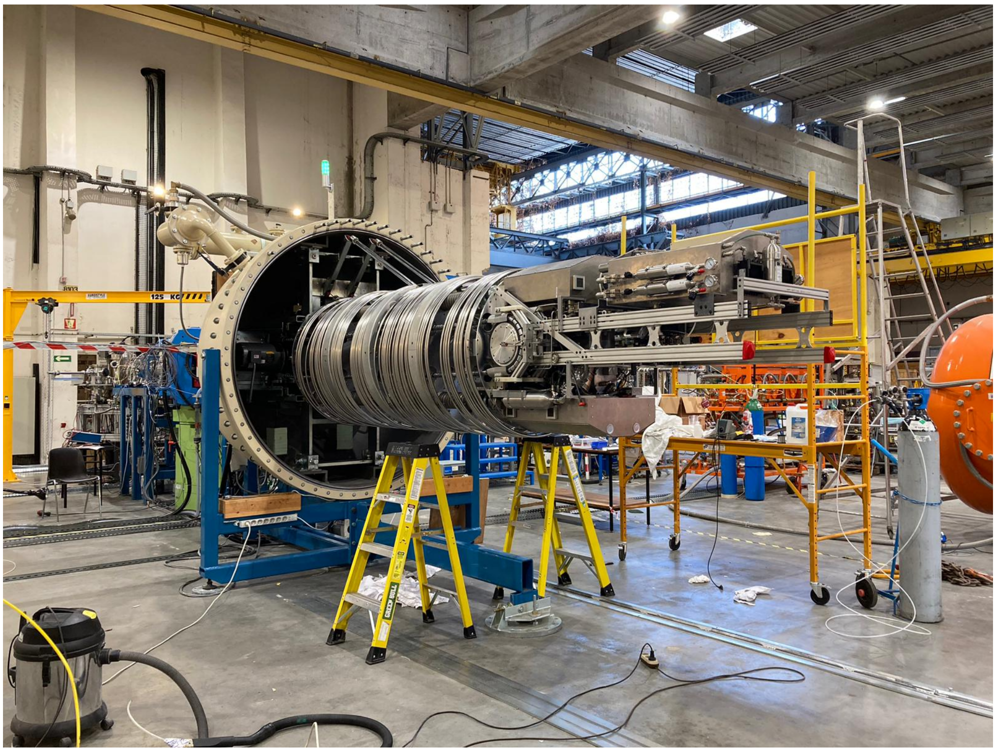

Figure 2.27: Andromede facility. In operation the tank is closed.

When the accelerator is operating, a tank covers it, filled with a isolant gas made of SF_6 at a pressure around 6 bar, in order to avoid discharging on metal elements.

The beam intensity delivered by Andromede is monitored by several Faraday cups, placed on either side of the reaction chamber. They were also used to control the beam transmission in the reaction chamber, and therefore the alignment of the beamline.
To avoid any electronic noise in the detectors or electronic devices, all the experimental setup, DAQ and the accelerator share the same ground, through the use of connected steel plates.

2.4 Résumé du chapitre

La réaction de fusion ^{12}C + ^{12}C est une réaction ayant une grande importance pour la communauté nucléaire. En effet, c'est non seulement une réaction clé dans l'évolution stellaire, mais sa section efficace présente également des structures de grand intérêt : les résonance et le phénomène de suppression de la fusion. Cependant, si de nombreuses expériences ont été menées afin de mesurer cette réaction, les résultats obtenus sont peu précis, avec de très larges incertitudes. Cela est du au fait que la mesure de cette réaction est un véritable défi, car sa section efficace est très faible, et le bruit de fond prédomine sur les spectres de particules. Afin de répondre à ces difficultés une méthode de détection en coïncidences a été mise en place pour ce système, en collaboration avec l'équipe STELLA. Cette méthode a été utilisée pour la construction de l'expérience STELLA.

2.4.1 La réaction de fusion ^{12}C + ^{12}C

La réaction de fusion ^{12}C + ^{12}C est la réaction principale de la phase de combustion du carbone. Selon la masse initiale de l'étoile, la température au centre varie, et donc l'énergie dans la fenêtre de Gamow. Cependant, dans tous les cas, elle reste inférieure à la barrière de Gamow.

La fusion du carbone présente trois voies de sorties : ^{12}C(^{12}C,α)^{20}Ne, ^{12}C(^{12}C,p)^{23}Na et ^{12}C(^{12}C,n)^{23}Mg, et sont appelées voie α, voie protons et voie neutrons respectivement. Cette dernière est endothermique aux énergies considérées [65]. De plus, les noyaux de ^{20}Ne et ^{23}Na peuvent être émis dans des états excités, et peuvent émettre des rayonnements γ pour atteindre leur états fondamentaux, comme montrés sur la Fig. 2.3.

La Figure 2.3 montre l'état de l'art de la fusion du carbone en mesures directes à la fin des années 2010. Les résultats ont été obtenus par la détection directe soit des particules légères (α et protons) soit des rayonnements γ associés. Deux extrapolations théoriques ont été ajoutées, l'une suivant le modèle CF88 et le second la suppression de la fusion. Ces deux extrapolations considèrent la tendance globale de la section efficace et ne prennent pas en compte les comportements locaux, telles que les résonances. Elles sont en accord aux énergies autour de la barrière de Coulomb, mais divergent aux plus basses énergies.

Les différentes expériences menées présentent toutes des résonances, et pour des énergies jusqu'à $E_{\text{cdm}} = 3.2$ MeV les incertitudes sont raisonnables, et permettent de contraindre les différents modèles théoriques et extrapolations. Cependant, aux énergies d'intérêt astrophysique, les incertitudes expérimentales sont de plusieurs ordres de grandeurs, et aux énergies les plus basses il n'y a pas de données : les mesures expérimentales ne permettent pas de valider ou d'invalider les différentes extrapolations. Ces difficultés sont directement issues des méthodes de détections utilisées et de leurs limites.

2.4.2 Méthodes de détection

La méthode de détection majoritairement utilisée pour la mesure de la fusion ^{12}C + ^{12}C est la mesure distincte, des particules légères ou des rayonnements γ.

Dans le cas de la détection des particules légères, des cibles fines de carbone sont utilisées et les particules chargées sont détectées par des détecteurs en silicium protégés par des fines feuilles d'aluminium ou de nickel. Ces détecteurs sont placés à différents angles pour mesurer la distribution angulaire de la particule émise, comme montré sur la Fig. 2.4. Cette méthode à l'avantage de pouvoir mesurer de très nombreuses voies de désexcitation ainsi que leurs rapports d'embranchement [22]. Cependant, aux énergies profondément sous-coulombiennes et d'intérêt astrophysique, la statistique chute exponentiellement, rendant la mesure sujette à un bruit de fond dominant. Ce dernier provenant notamment de réactions parasites avec des contaminants présents dans la cible, le deutérium et l'hydrogène majoritairement.

Pour la détection des rayonnements γ, des cibles fines et épaisses peuvent être utilisées. Les cibles épaisses ont la particularité de pouvoir arrêter le faisceau : les mesures sont effectuées en variant l'énergie pas à pas. Cependant, aux plus basses énergies, les spectres sont très sensibles au fond Compton venant de la radioactivité ambiante. Des réactions parasites vont également émettre des γ à des énergies semblables à celles des rayonnements d'intérêt.

Afin de répondre à ces problèmes, une méthodes par coïncidence à été développée pour le système ^{12}C + ^{12}C [25]. Cette technique repose sur la détection en simultanée d'une particule légère et de son rayonnement γ associé. Cette technique est possible pas le fait que le noyau composé de cette fusion fait une désintégration à deux corps, permettant une excellence connaissance de l'énergie cinétique de chacune des deux particules. Les résultats obtenus avec cette méthode sont montrés sur la Fig. 2.6. Ils présentent des barres d'erreurs réduites, indiquant que cette méthode augmente de façon significative la précision des mesures. Cependant, cette méthode réduit considérablement la statistique, nécessitant des temps de faisceau long auprès d'accélérateurs pouvant délivrer des faisceaux à haute intensité.

2.4.3 L'expérience STELLA

L'expérience STELLA, pour STELlar LAboratory, est basée sur la méthode de détection par coïncidence. Elle permet l'étude de réactions de fusion en ions lourds/légers aux énergies d'intérêt astrophysique. La description du montage correspond à celui utilisé lors de la campagne expérimentale de 2022.

La chambre à réaction est composée d'un cylindre inoxydable surplombé d'un dôme dont l'épaisseur permet de minimiser les interactions avec les rayonnements γ issues des évènements de fusion. Dans la partie cylindrique, plusieurs extensions ont été usinées, permettant l'installation de deux moniteurs et de quatre cartes préamplificatrices. Plusieurs modules attachés à la chambre forment le système de vide, requis pour les expériences à basse énergie.

La chambre contient un système de support de cibles fines, fixes et rotatives, dont la position peut être changée depuis l'extérieur de la chambre. Deux détecteurs en silicium sont placés de part et d'autre du système de cible, et un troisième système de détection, PIXEL a été ajouté au dessus de la cible.

Le dôme supporte également les tuyaux liant la chambre à la ligne de faisceau, qui la traverse de part en part. Une coupe de Faraday est placée à l'arrière de la chambre afin de contrôler l'intensité du courant.

Les cibles utilisées par l'expérience STELLA sont des cibles de carbone fines, de 30 à 75 μg/cm^2 d'épaisseur. Ces cibles sont cependant très sensible à l'intensité du faisceau. Pour que ce dernier ne les endommage pas, un système de rotation a été développé, permettant d'atteindre 1000 rpm. Cette rotation permet de dissiper la chaleur déposée dans la cible.

Deux types de cibles ont été utilisées : des cibles fixes, pour les mesures aux plus hautes énergies, avec une ouverture de 9 m de diamètre. Les cibles rotatives ont été préparées au GANIL, et sont déposées sur un cadre circulaire de 46 mm de diamètre interne et 63 mm de diamètre externe. Six cibles fixes et trois cibles rotatives peuvent être placées simultanément sur le support.

Pour la détection des particules légères chargées trois types de détecteurs en silicium ont été utilisés : deux détecteurs de types DSSSD, le système PIXEL et deux moniteurs.

Les DSSSD, pour Double Sided Striped Silicon Detector, sont deux détecteurs types S3 de Micron Semiconductor Ltd et montés sur des supports PCB à l'IPHC. Ils sont placés à l'avant et à l'arrière de la cible, permettant une couverture angulaire de $\theta_{\text{lab}} = 10.4°-30.3°$ et $\theta_{\text{lab}} = 148°-169°$ respectivement. Ils sont protégés de la diffusion élastique des noyaux de carbone et de la diffusion des électrons par des fines feuilles d'aluminium. Chacun de ces détecteurs est divisé en 24 anneaux angulaires.

Le système PIXEL, en phase de test en 2022, peut accueillir deux détecteurs en silicium : un type Super-X3 et type BB-10 de Micron Semiconductor Ltd, pouvant couvrir les angles $\theta_{\text{lab}} = 60°-90°$. Cet ajout a pour une meilleure mesure de la distribution angulaire de la fusion du carbone, grâce à l'augmentation de la couverture angulaire. Ces détecteurs sont également protégés par des feuilles fines en aluminium.

Les moniteurs, deux détecteurs en silicium, ont été utilisés afin d'obtenir une normalisation de la section efficace mesurée. Pour cela, ils permettant la mesure de la diffusion élastique $^{12}C + {}^{12}C$, décrite par la section efficace de Mott. Ils permettent également de contrôler en temps réel l'intensité du faisceau et l'état de la cible lors des prises de données.

Les rayonnements γ sont détectés grâce aux 36 scintillateurs $LaBr_3$(Ce) issus de la collaboration UK-FATIMA. Ils présentent une résolution suffisante, une bonne efficacité de détection et un temps de réponse inférieur à la nanoseconde, nécessaire pour la méthode par coïncidence. Ils sont positionnés dans une configuration cylindrique, optimisant la couverture angulaire et la mobilité de l'ensemble.

Ces scintillateurs sont sujets à de la radioactivité interne, comprenant de la radioactivité α, β et γ, permettant une auto-calibration sur toute la durée de l'acquisition de données.

La mesure en coïncidence requiert la synchronisation temporelle des détecteurs silicium et des scintillateurs. Cela est assurée par une carte Gigabit Link Interface Board, qui délivre un signal horloge à 10 MHz aux huit cartes d'acquisitions STELLA. Ces dernières cont générées un signal de 125 MHz distribué aux deux cartes PIXEL et cinq cartes UK-FATIMA. Toutes les cartes ne démarrant pas à la même vitesse, une signal de synchronisation est envoyé toutes les 15 secondes.

Le temps mort de l'acquisition, et donc la fenêtre considérée pour les coïncidence, est de 400 ns.

Le vide dans la chambre est assuré par un système de pompage composé de trois pompes : une pompe sèche primaire, deux pompes turbomoléculaires, et une pompe cryogénique. Ce système permet d'atteindre un ultravide $P \leq 10^{-7}$ mbar.

Lors de la campagne expérimentale de 2022, le faisceau a été délivré par l'accélérateur

Andromède, de la plateforme MOSAIC à l'IJCLab. Cet accélérateur est un Pelletron© de 4 MV muni d'une source ECR. La pûreté du faisceau est assuré par un filtre de Wien et un aimant à 90°, en amont de la chambre à réaction de STELLA.

Chapter 3

The ^{12}C + ^{12}C fusion reaction cross section with the STELLA project

Contents

3.1 Data analysis 90

3.1.1 Calibration 90

3α calibration 90

High energy calibration 91

3.1.2 Charge sharing 93

3.1.3 Angular distribution 98

3.2 Data normalization 99

3.2.1 Current integrator 100

3.2.2 Target thickness 102

3.2.3 Systematic uncertainties 102

3.3 Determination of the total fusion cross section at E_{rel} = 4.76 MeV 103

3.3.1 Event selection 103

3.3.2 Angular distribution 105

3.3.3 Total cross section 105

3.4 Résumé du chapitre 113

3.4.1 Analyse des données 113

3.4.2 Normalisation des données 114

3.4.3 Détermination de la section efficace totale à E_{rel} = 4.76 MeV 115

The STELLA experiment, described in the previous chapter, is an innovative experiment for measuring the cross section of the ^{12}C + ^{12}C fusion reaction at energies of astrophysical interest. The most recent experimental campaign took place in 2022.

In this chapter, data taken during this last campaign measured at an energy E_{com} = 4.8 MeV are discussed. For this energy only the DSSSD were used. To do this, the detectors were first calibrated in two stages. The spectra obtained were analysed in order to extract angular distributions. In order to obtain the best possible accuracy, data normalization was investigated. Finally, the total cross section was determined.

3.1 Data analysis

The data analysis carried out in this thesis is based on the detection of light particles. As seen previously, the ^{12}C + ^{12}C fusion reaction at energies of astrophysical interest takes place through two main exit channels:

$$
\begin{aligned}
{}^{12}\mathrm{C} + {}^{12}\mathrm{C} \rightarrow {}^{24}\mathrm{Mg}^{*} &\rightarrow {}^{20}\mathrm{Ne}^{*} + \alpha \qquad && (Q = 4.62\,\mathrm{MeV}), \qquad (3.1)\\
&\rightarrow {}^{23}\mathrm{Na}^{*} + p \qquad && (Q = 2.24\,\mathrm{MeV}). \qquad (3.2)
\end{aligned}
$$

The analysis will therefore be based on the detection of α and protons by the two DSSSD detectors, S3F and S3B.

3.1.1 Calibration

The two detectors S3F and S3B have 24 independent channels, each of which requires independent calibration. To achieve this, two methods were used: a calibration using a 3α source and a calibration based on an experimental fusion spectrum carried out at E_{lab} = 9.6 MeV, *i.e.* at a sufficiently high energy for the fusion cross section ($\sim$ 10 mb) to allow the identification of a large number of proton and α exit channels, known as high energy calibration.

3α calibration

The 3α source used for calibration contains three radioactive isotopes, ^{239}Pu, ^{241}Am and ^{244}Cm, with the main decay energies E_α = 5156.59 keV, E_α = 5485.56 keV and E_α = 5804.77 keV. This source therefore covers an energy range from 5 to 6 MeV.

The raw spectra from each of the 24 channels of the two detectors are fitted independently, and the three peaks obtained are associated with the main decay energy mentioned above. Figure 3.1 represents the energies of the α particles on the y-axis and the mean value of the associated peaks in the QDC spectrum (QDC channels) on the x-axis. The graph is then fit with a linear function, and the parameters obtained are used for calibration.

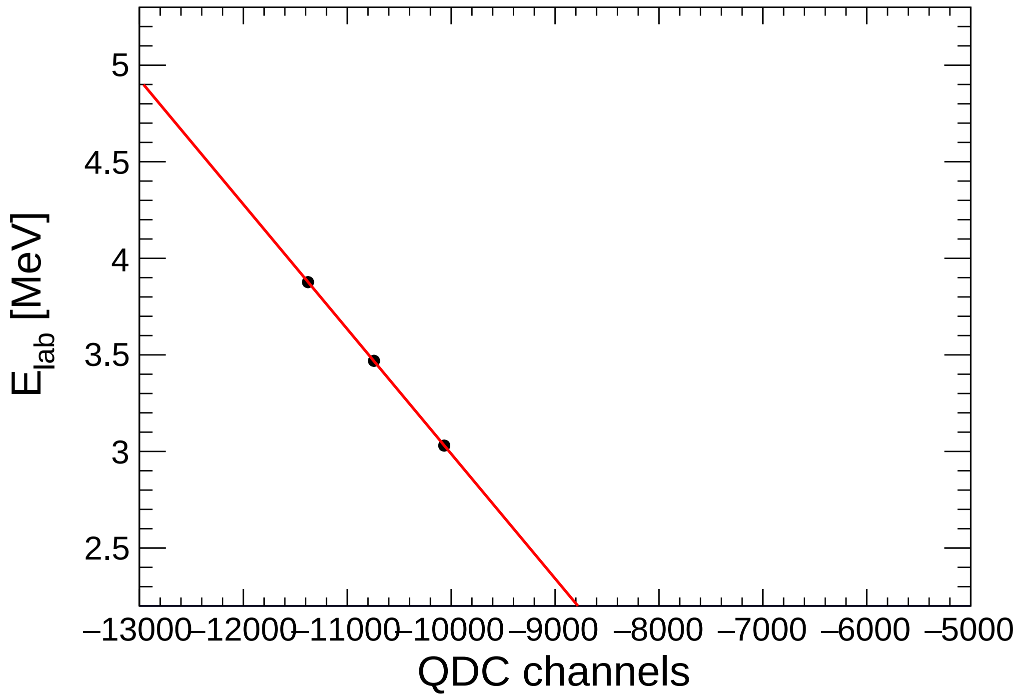

Figure 3.1: 3α calibration fit for a typical strip of the S3F detector. The obtained fit parameters are $p_0 = (6.458 \pm 0.001) \times 10^{-4}$ and $p_1 = -3.470 \pm 0.011$. The defaut QDC channel output is negative.

The spectra obtained with this calibration show a discrepancy between the kinematic calculations and the measured peaks. This can be explained by the precision of the linear calibration: as the calibration was carried out over an energy range of between 5 and 6 MeV, it is in this region that the calibration parameters obtained best describe the detector's response. This might explain the differences observed. This assumption is supported by the fact that the deviations are greater in the S3F detector, where the energies of the incident particles are furthest from those of the 3α source.

However, this method is not without interest. In view of the large number of exit channels detected in S3B, performing an initial 3α calibration provides a preliminary identification of peaks, which will, in conjunction with characteristic spacing between peaks, be used during the high energy calibration.

High energy calibration

For refining the 3α calibration, a high energy calibration was then carried out. This calibration is possible because the reaction kinematics can be calculated exactly, and the angle of emission of the protons and α is well defined.

Kinematic calculations performed for a beam energy $E_{\text{lab}} = 9.6$ MeV are shown in Fig. 3.2. The α exit channels are in black and the protons channels in red. The

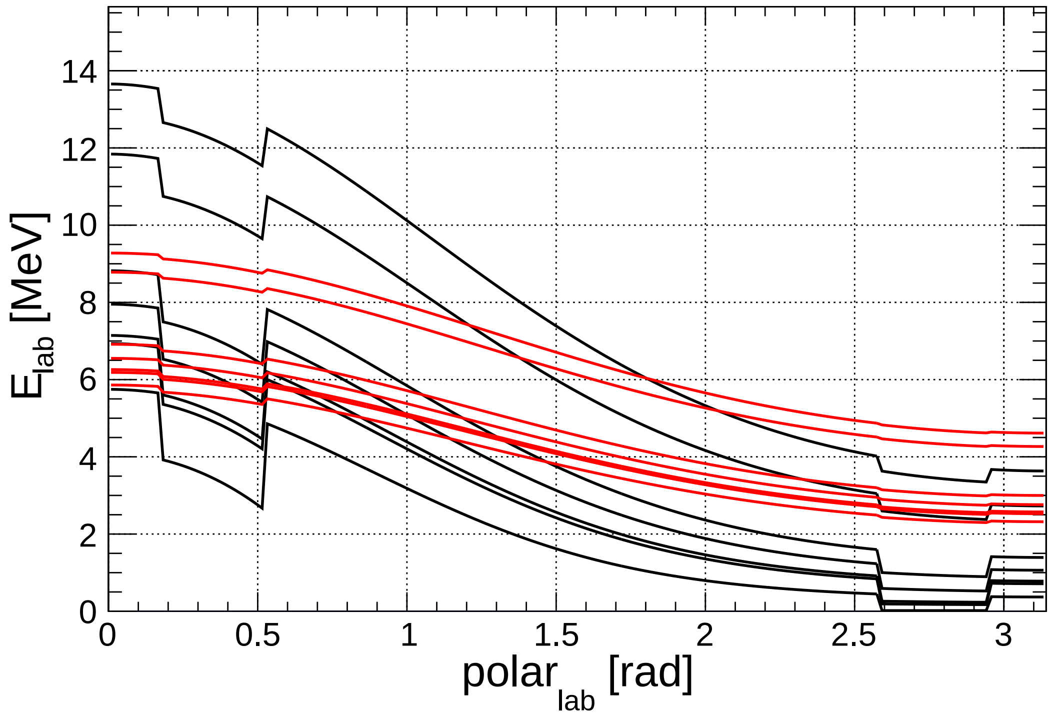

Figure 3.2: Kinematic energy calculation of α particules in black and protons in red producted at $E_{\text{lab}} = 9.6$ MeV.

various curves represent the different excitation levels at which the daughter nucleus is produced: thus, the most energetic α particle corresponds to α_0, the second highest to α_1... The same logics applies to protons.

The detectors S3F and S3B cover polar angles of 0.2 to 0.5 rad and 2.6 to 3 rad respectively. The drop of energy of the incident particles at these angles are due to the loss of energy of the particles as they pass through the aluminium foil protecting the detectors, which is accounted in the calculations. This energy loss is calculated from the stopping power in the aluminium of α particles and protons, extracted in the NIST data base [90].

By identifying the different particles in the spectra and knowing the precise angles at which each exit channel is located, it is possible to perform a calibration.

After identifying the different peaks in all the spectra of each strip, a linear calibration curve is obtained, as shown in Fig. 3.3 for a S3B channel. The energy of the particles are on the y-axis and the mean value of the associated peaks in the QDC spectrum (QDC channels) on the x-axis. The particles used for this calibration are indicated, and cover an energy range from 1.7 to 4.8 MeV. As before, the graphics are then fit with a linear function, and the parameters from Fig. 3.3 obtained are used for calibration.

Figure 3.4 shows the obtained results of this calibration, with angular differential

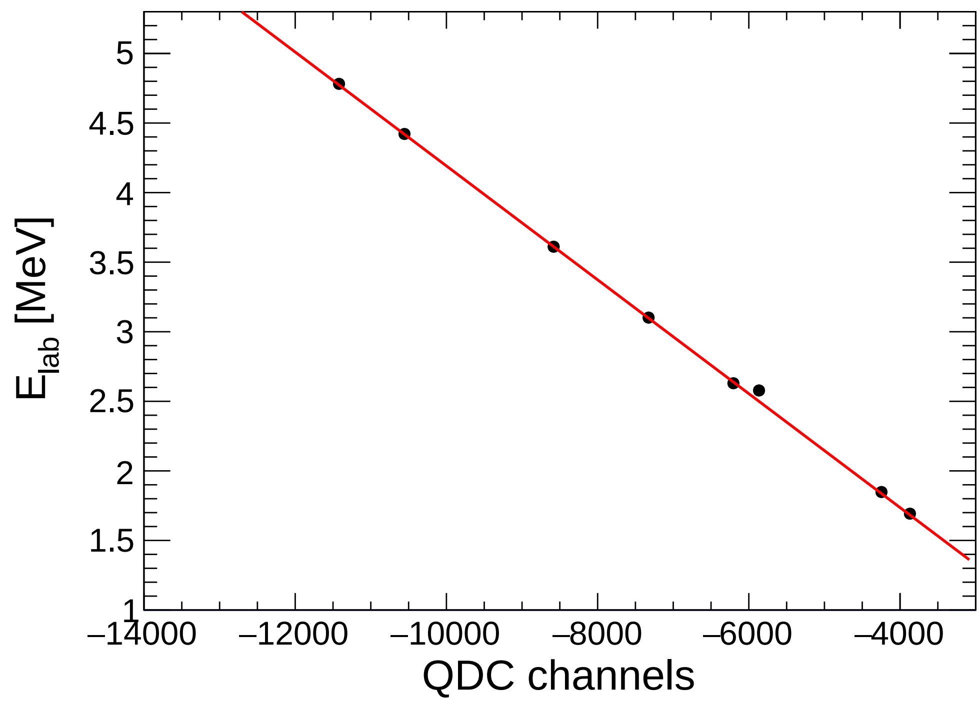

Figure 3.3: High energy calibration fit for a typical strip of the S3B detector at $E_{\rm lab}$ = 9.6 MeV. The obtained fit parameters are $p_0 = (4.092 \pm 0.004) \times 10^{-4}$ and $p_1 = (9.933 \pm 3.435) \times 10^{-2}$. The defaut QDC chnanel output is negative.

energy spectra for S3F in the upper panel and S3B in the bottom panel. Black and red lines represent the kinematics calculation for the α and protons, respectively. These spectra are for $E_{\rm lab}$ = 9.6 MeV and take into account the energy loss of the beam in the target.

3.1.2 Charge sharing

As seen in the technical description of the DSSSD in Sect. 2.3.3, the S3 detectors are divided into 24 rings of width of 986 mm. It is therefore possible that the cascades of charges generated by particles penetrating the detectors are not collected by one ring but are shared between neighbouring rings, in particular when particles impige close to the edge of a strip. This is known as charge sharing.

This phenomenon is illustrated in Fig. 3.5 [28]. The drawing on the left illustrates a case where all the charges are collected in the same strip: there is therefore no charge sharing. In the middle drawing, the charges are dispersed over two rings, and the graph on the right illustrates the quantity of charges collected by each of the strips. In order to reconstruct the correct energy of the particle, it is necessary to sum the two signals.

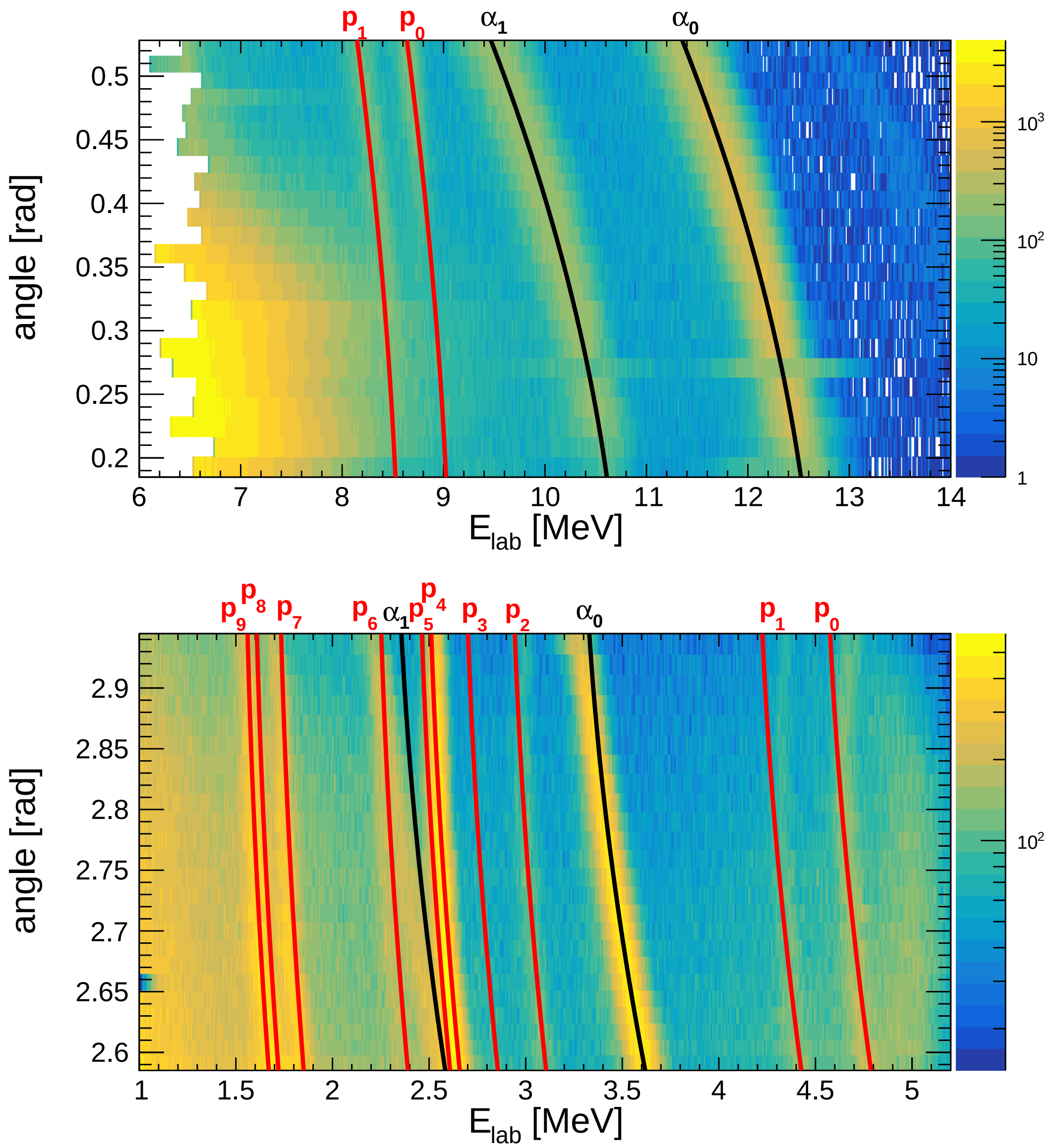

Figure 3.4: Angular differential energy spectra calibrated with high energy in S3F (top) and S3B (bottom) at $E_{\text{lab}} = 9.6$ MeV. Black and red lines represent the kinematics calculations for the α and proton exit channels, respectively. The ground state transitions are at the highest energy, followed by excitation levels with decreasing particle energy.

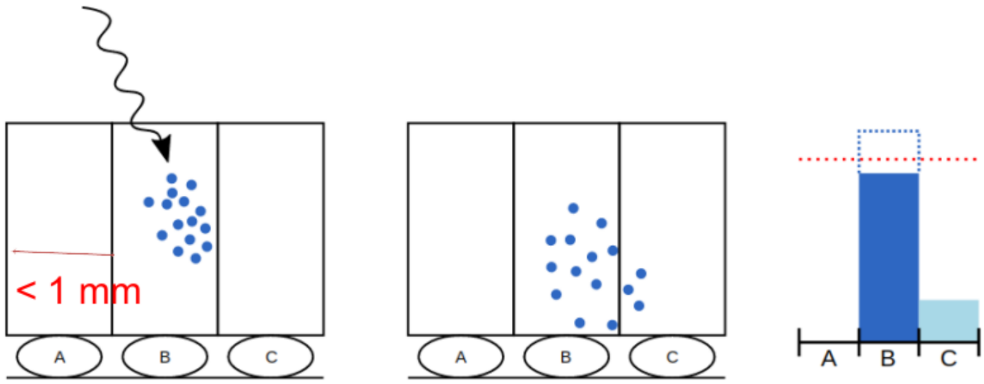

Figure 3.5: Scheme representing the principle of charge sharing: in the left drawing no charge sharing occurs, in the middle drawing the charges are distributed over two strips. The diagram on the right represents the amount of charges collected by every strips in the latter scenario. From [28].

It is therefore required to be able to identify and include charge sharing in the analysis. This can be done by recording the energy as well as the detection time of the events. The collection of charges from the same incident particle by two neighbouring rings takes place in an extremely short time window, $\sim$ 10 ns [28]. Determined by the dead time of the DAQ, two detections recorded with a time difference of less than 400 ns are considered from the same event, defined as being of multiplicity two. Events with a single detection will then be defined as being of multiplicity one.

Figure 3.6 shows the active rings when considering events of multiplicity two in the upper panel and the correlated energy E_1, E_2 in two consecutive rings on the lower panel, for S3B at $E_{\text{lab}} = 9.6$ MeV.

A correlation appears on these particle-particle coincidence matrices. On the upper panel, predominantly consecutive rings record events of multiplicity two. On the lower panel the correlation between two particles is indicated by the diagonal bands. The sum of the partial energies is equal to the total energy deposited by the incident particle.

The effects of charge sharing on particle spectra are shown in Fig. 3.7, with a particle spectrum of a S3F channel at the top and a SB3 channel at the bottom. The red curves represent events of multiplicity one, the blue curves those of multiplicity two, and the black curves the spectra obtained by summing the two types of events. Higher multiplicities can be neglected. The sum spectra are used to determine the cross sections.

These graphics illustrate the dependence of this phenomenon on the energy of the incident particle. For S3F, about 20% of particles with energies > 8 MeV deposit charges in two neighbouring rings. This value falls to less than 10% for particles with energies < 5 MeV in S3B. This can be explained by the fact that the lower energetic particles are stopped more quickly in the detectors, which limits the possibility of

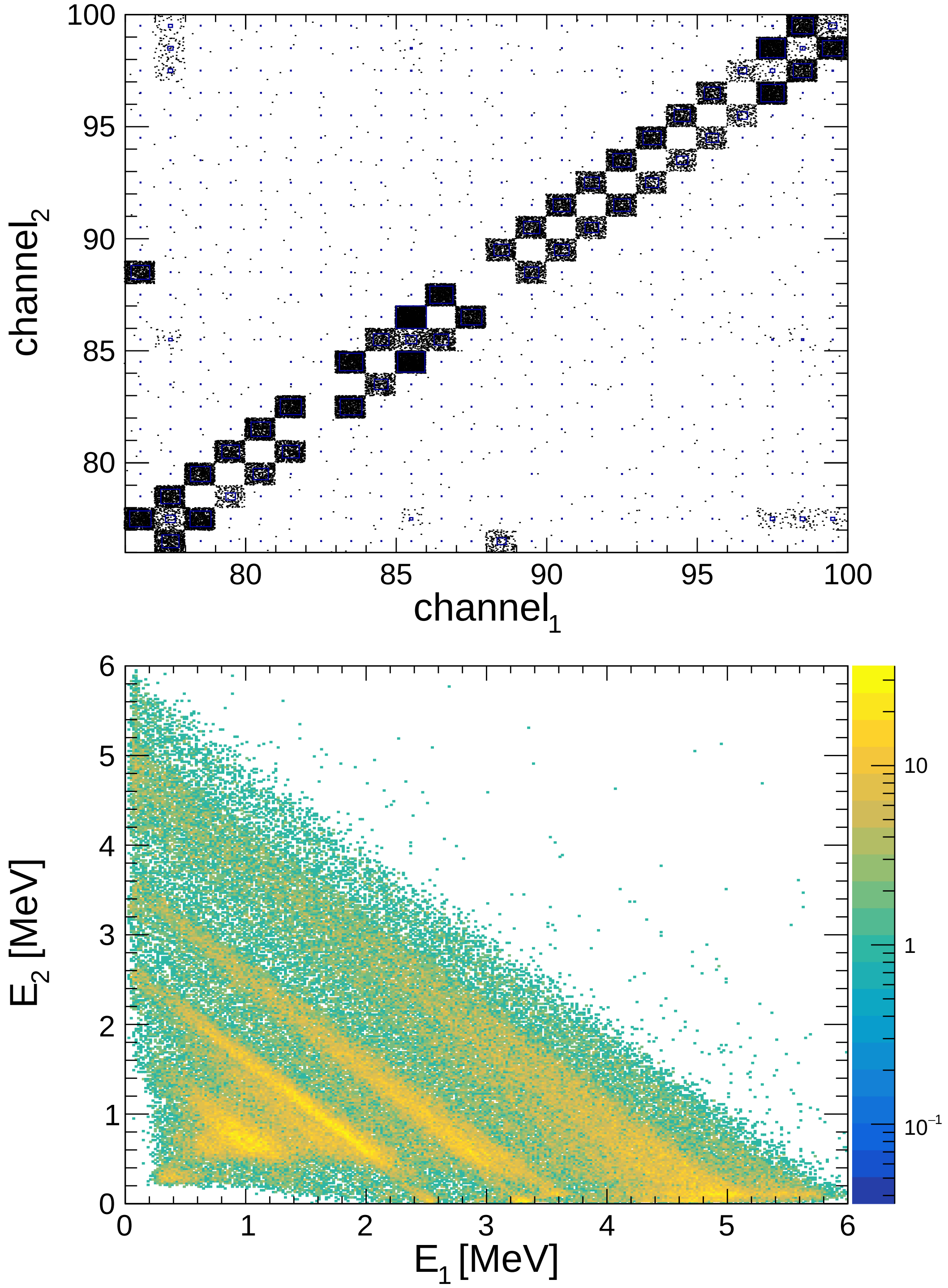

Figure 3.6: Top: Correlation of active rings of S3B for the detection of multiplicity-two events. Bottom: Correlation of particles energies for multiplicity-two events for S3B in neighbouring strips. $E_{\text{lab}} = 9.6$ MeV.

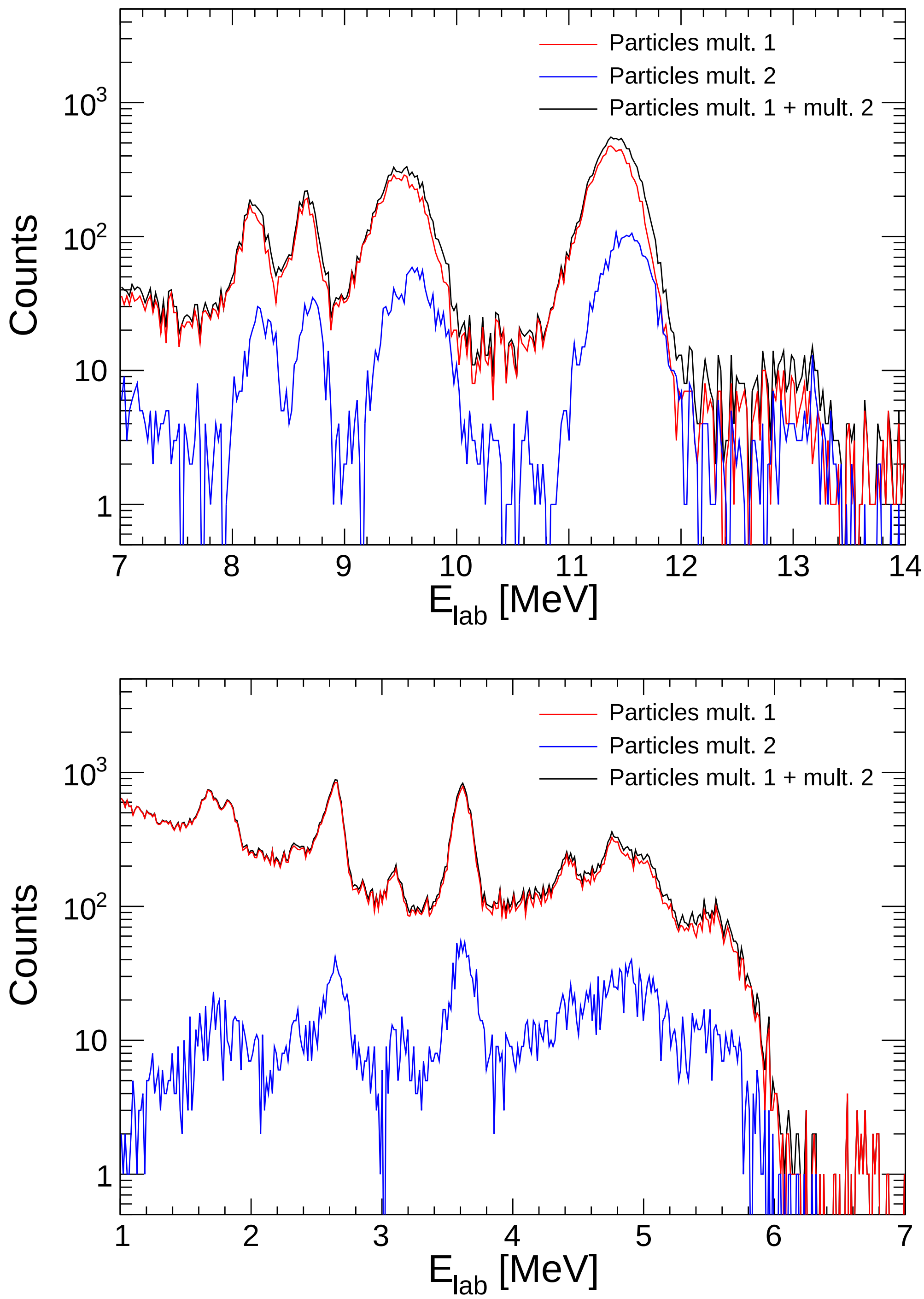

Figure 3.7: Effect of charge sharing on particles spectra, for S3F (top) and S3B (bottom). $E_{\text{lab}} = 9.6$ MeV.

charge sharing.

3.1.3 Angular distribution

After calibration and correction for charge sharing, it is possible to study the angular distribution of certain products of the ^{12}C + ^{12}C fusion reaction, for each of the 24 channels of the two detectors S3F and S3B. To do this, it is necessary to extract from the spectra the number of fusion events measured for each particle.

The adjustment performed on each of the peaks is made up of two components: a Gaussian function and background noise. The latter is linear or second-order polynomial, depending on the background considered. The energy interval over which this adjustment is made corresponds to $\mu \pm 6\sigma$, which include more than 99.99% of the events, in order to estimate the background as accurately as possible.

The number of events S is extracted from the amplitudes A and standard deviations σ of the Gaussian functions. It is determined using the Gaussian integral:

$$S = A\sigma\sqrt{2\pi}. \tag{3.3}$$

The statistical uncertainty on S is then given by:

$$\left(\frac{\Delta S}{S}\right)^2 = \left(\frac{\Delta A}{A}\right)^2 + \left(\frac{\Delta \sigma}{\sigma}\right)^2. \tag{3.4}$$

A cross section is thus obtained for each of the particles considered for all the channels using the formula:

$$\left(\frac{\mathrm{d}\sigma}{\mathrm{d}\Omega}\right)_{\mathrm{lab}} = \frac{S}{I \times N_T \times \Delta\Omega \times \Delta t}, \tag{3.5}$$

where I is the intensity of the beam, N_T the number of nuclei in the target, Δt the acquisition time and $\Delta\Omega$ the solid angle covered by the ring.

The transformation of the angles from the laboratory frame θ_{lab} to the angles in the center of mass frame θ_{com} is calculated for each channel using the relation [91]:

$$\sin(\theta_{\mathrm{com}}) = \frac{\sin(\theta_{\mathrm{lab}})[\delta_3 \cos(\theta_{\mathrm{lab}}) \pm (1 - \delta_3 \cos(\theta_{\mathrm{lab}}))]}{[1 + \delta_3^2 - 2\delta_3 \cos(\theta_{\mathrm{lab}})]^{1/2}}, \tag{3.6}$$

with δ_3 defined as:

$$\delta_3 = \left(\frac{A_1 A_3}{(A_1 + A_2)^2}\frac{E_1}{E_3}\right)^{1/2}, \tag{3.7}$$

where A_1 is the projectile of energy E_1, A_2 the target nucleus and A_3 the particle detected at an angle θ_{lab} and with an energy E_3. The differential cross section in the center of mass (in b/sr) is then expressed as [91]:

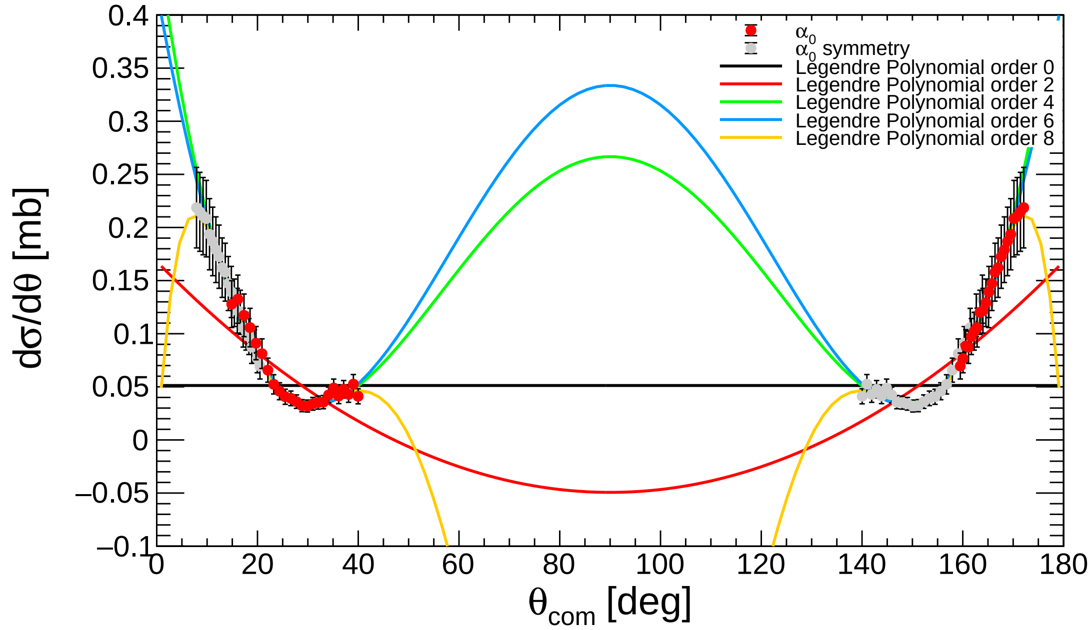

Figure 3.8: Angular distribution for α_0 at $E_{\mathrm{lab}} = 10.75$ MeV.

$$\left(\frac{\mathrm{d}\sigma}{\mathrm{d}\Omega}\right)_{\mathrm{com}} = \left(\frac{\mathrm{d}\sigma}{\mathrm{d}\Omega}\right)_{\mathrm{lab}} |1 - \delta_3 \cos(\theta_{\mathrm{lab}})|[1 + \delta_3^2 - 2\delta_3 \cos(\theta_{\mathrm{lab}})]^{1/2}. \tag{3.8}$$

Figure 3.8 shows the angular distribution obtained for α_0 at $E_{\mathrm{com}} = 4.8$ MeV. The data measured in S3F and S3B are shown in red, and their mirror points with respect to $\theta_{\mathrm{com}} = 90°$ in grey.

This angular distribution can be fitted with a Legendre Polynomial to extract information about the angular momentum carried away by the evaporated particle, and therefore possibly deduce information about the populated state in the compound nucleus before evaporation.

In this study, several fits were made, using only even orders for the ^{12}C + ^{12}C reaction fusion, because of the conservation of angular momentum of two 0^+ nuclei.

3.2 Data normalization

To determine the cross sections, it is necessary to know the normalisation parameters as accurately as possible. This requires knowledge of the number of nuclei involved in the measurement, the geometrical coverage and the detection efficiency. The former information is derived from two factors: the intensity of the current and the thickness of the target.

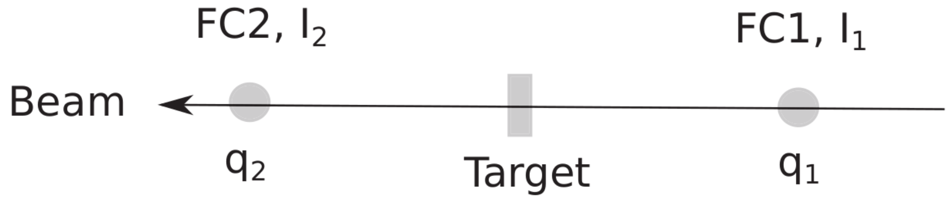

Figure 3.9: Scheme of the Faraday cups system used to measure the beam intensities I_1 and I_2 and charge state q_1 and q_2 before and after the target, respectively. From [6].

3.2.1 Current integrator

The current intensity used for data acquisition runs in the STELLA experiment can be determined in two different ways: by measuring the elastic scattering ^{12}C + ^{12}C in the monitors installed in the reaction chamber (see Sect. 2.3.3), and by using a system of Faraday cups.

This system enables the intensity delivered by the Andromede accelerator to be read and monitored using two Faraday cups, called FC1 and FC2, located upstream and downstream of the target with respect to the beam, respectively, as shown in Fig. 3.9. This facility allows the determination of the intensities I_1 and I_2 and of the charge state q_1 and q_2 before and after the target, respectively.

Before each run and at each energy change, a transmission check was carried out to characterise the beam alignment. A transmission of 100% means that the beam is not intercepted in the chamber and that its alignment is consistent with the reaction chamber. This verification is essential to ensure that the detectors are not impacted by the beam, which could damage them, or that the beam is scattered off the target frame.

For this purpose, an empty target holder with a diameter of 8 mm is used, electrically insulated from the reaction chamber, with the possibility of reading the current running off the target holder during beam focusing.

During data acquisition, the beam intensity is measured continuously with a digital current integrator from Ortec® [92] coupled to the FC2 Faraday cage. This module generates a box shaped signal as soon as a user-defined number of charges Q_{CI} is accumulated. This signal is then sent to a digital counter as the well at the STELLA DAQ, and the number of events recorded by the counter is therefore directly linked to the charge accumulated in FC2.

During the 2022 experimental campaign, the mode used generated a signal every $Q_{\mathrm{CI}} = 10^{-8}$ C.

Calibration runs of the current integrator were carried out, in order to control

Table 3.1: Correction factor f_{cor} in respect to the beam intensity I_{beam}.

I_{beam} [pnA]	f_{cor}
1.00E+02	0.30
2.50E+02	0.52
5.00E+02	0.67
7.50E+02	0.75
1.00E+03	0.78
1.20E+03	0.81
1.40E+03	0.82
1.60E+03	0.84
1.80E+03	0.85
2.00E+03	0.87
2.20E+03	0.87
2.40E+03	0.88
2.60E+03	0.89
2.80E+03	0.89
3.00E+03	0.89

possible deviations between the number of signals recorded by the measurement chain and the actual number of charges collected by the FC2 Faraday cup. These short runs (around 5 min) enabled the number of signals from the current integrator to be compared with the nominal beam intensity from FC1. The ratio between the expected intensity and the one measured was used to determine a correction factor f_{cor}. Several calibrations were done, and the various values of the correction factor as a function of the beam intensity taken at the start of the experimental campaign can be seen in Tab. 3.1.

In order to derive a current in units of particles per second, it is necessary to determine the average charge state of the beam after its passage through the carbon target. Depending on the target thickness and the beam energy, electrons can be stripped from the particles as they pass through the target, or electron can be picked up [93].

This average charge state is determined experimentally by comparing the intensity I_1, measured in FC1 with the intensity I_2 obtained in FC2, after the beam has passed through the target.

The beam leaving the accelerator is characterised by a known charge state q_1, and after passing through the target by an average charge state q_2. These two quantities are related by:

$$\frac{I_1}{q_1} = \frac{I_2}{q_2} \Leftrightarrow q_2 = \frac{q_1 \times I_2}{I_1}. \tag{3.9}$$

The intensities I_1 and I_2 are measured before and after each data acquisition to determine q_2.

The intensity integrated throughout the experiment I_{int}, in pnA or particle nanoampere, is given by the relation:

$$I_{\text{int}} = \frac{N_{\text{CI}} \times f_{\text{cor}} \times Q_{\text{CI}}}{q_2} \times 10^9, \tag{3.10}$$

where N_{CI} is the number of signals generated by the digital current integrator, Q_{CI} the number of charges to be accumulated to generate a signal, f_{cor} the correction factor determined by calibrating the integrator and q_2 the mean state of charge determined with Eq. 3.9.

The uncertainties considered for this quantity are due to fluctuations in the beam delivered by the accelerator, but also to the thickness of the target when q_2 is determined. They are estimated here at 12% [6].

3.2.2 Target thickness

The uncertainty of the target thickness, and therefore the number of particles contained in them, can be influenced in two ways: by uncertainties about their thickness during manufacture, and also by the thickening of targets during data acquisition runs.

The target thickness was precisely studied by J. Nippert [28], by measuring the energy loss of α particles of known energies through the targets. The aim of this work was the comparison of these measurements with the thicknesses given by GANIL, obtained by weighting each target separately. The results of this analysis indicate targets uncertainties of 10%.

The thickening of targets during runs was studied by G. Fruet [6]. The obtained results show that the impact of this thickening on the targets is negligible, and that no correction needs to be made for this phenomenon.

The uncertainty adopted for the target thickness are therefore 10%.

3.2.3 Systematic uncertainties

This section summarises all the systematic uncertainties taken into account in the normalisation of data from the STELLA experiment.

In Sect. 3.2.1, the uncertainty in the beam intensity used is 12%. The uncertainty on the thickness of the targets is 10% as seen in Sect. 3.2.2.

Two other uncertainties also need to be taken into account.
The first concerns the solid angle covered by the DSSSD detectors. The target-detector distance and the centring of the detector with respect to the beam position

are known to an accuracy of ±0.5 mm, leading to a relative uncertainty of 3% in the determination of the solid angle [6].

The second uncertainty is associated with the correction of the effective cross-sections with the branching ratios taken from [22]. It is estimated at 4.5%.

The total relative systematic uncertainty on the cross section is then calculated as:

$$\frac{\Delta\sigma^{syst}}{\sigma} = \frac{\sqrt{12^2 + 10^2 + 4.5^2 + 3^2}}{S}, \tag{3.11}$$

with S the measured signal defined in 3.3.

This uncertainty is quadratically added to the statistical uncertainties of the cross section results.

3.3 Determination of the total fusion cross section at $E_{\rm rel} = 4.76$ MeV

The data analysis developed in this work was used to determine a total cross section at $E_{\rm com} = 4.8$ MeV, *i.e.* at $E_{\rm rel} = 4.76$ MeV by taking into account the energy loss of the beam in the target. This energy allows the direct comparison with previous results from STELLA experiment [27; 28] and from Becker *et al.* [22].

3.3.1 Event selection

The first step of the determination of a cross section is the event selection on the spectra.

Figure 3.10 shows the particle spectra for a S3F channel in the upper panel and in a S3B channel in the bottom panel. The blue curves represent the total fit, including the particle-related Gaussian and the background noise, and the black curve represents the background noise. The vertical lines are derived from kinematic calculations for α and protons, in black and red respectively. The blue hatched boxes indicate the 3σ interval for the considered peaks.

These figures allow the identification of discernible particles. Thus, for S3F, only α_0 and α_1 can be studied in the 24 channels. This is because the p_0 and p_1 particles are only discernible in the outermost half of the detector, where the thickness through which they pass is sufficient for them to deposit all their energy, which is not the case at the smallest angles. The α and protons from the highest excitation levels are, in view of their kinematic energy, indistinguishable from the background noise.

For the α_0 and α_1 a linear background has been considered for all the spectra. For the p_0 and p_1 particles, the background fit has been adapted according the the angle considered. Indeed, at the smallest angles, *i.e.* when the channels are closest to the beam, the background is much greater, and a fit with a second-order polynomial was used. For more distant angles, this fit was not necessary and a linear background was

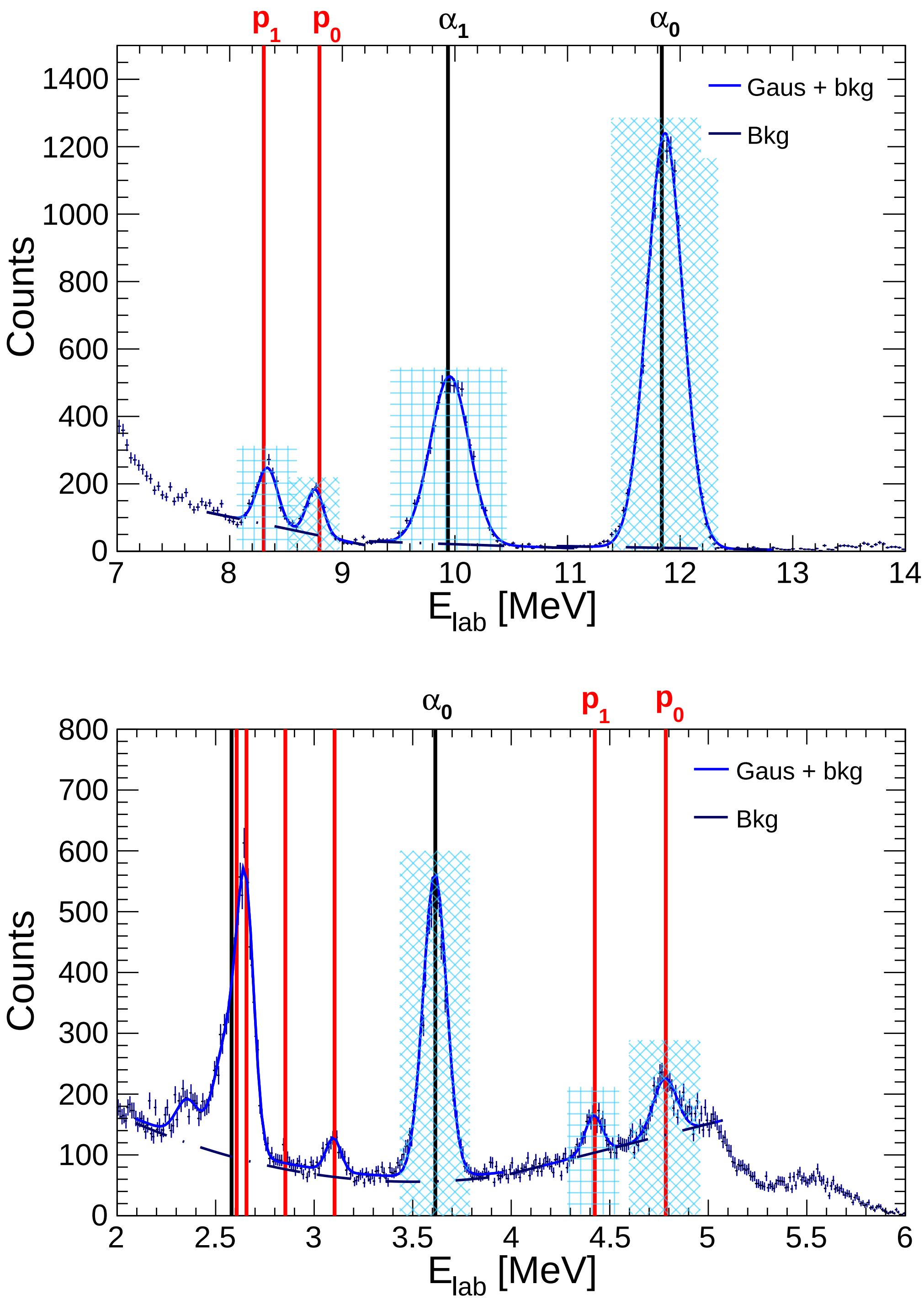

Figure 3.10: Particle spectra in S3F (top) and S3B (bottom). The vertical lines show the kinematic calculations for α in black and proton in red. $E_{\rm rel} = 4.76$ MeV.

used.

In the S3B detector, p_0, p_1 and α_0 can be studied. The statistics of the p_2 and p_3 particles do not allow them to be used, and p_4, p_5 and α_1 are indistinguishable from each other.

The same second-order polynomial background has been used in all the spectra. Indeed, the S3B detector is not exposed to the beam as the S3F detector, so the physics measured at each angle is the same.

All the particle spectra of S3B show a dominating background contribution at the typical energy of p_0, p_1. This can also be seen on the graphic on the bottom panel of Fig. 3.4, where an unidentified contribution is located at an energy slightly higher than that of p_0.

3.3.2 Angular distribution

After the selection of the fusion events, the differential cross section for each particles is calculated with Eq. 3.5. These distributions are fitted with the sum of Legendre polynomials, using the formula [77]:

$$\left(\frac{\mathrm{d}\sigma}{\mathrm{d}\Omega}\right)_i = \sum_{k=0}^{k_{max}} a_k P_k \cos(\theta_{\mathrm{com}}), \tag{3.12}$$

with k the order of the polynomial P_k and a_k the fitting parameter.

Figures 3.11 and 3.12 show the angular distributions obtained for α_0 and α_1, and p_0 and p_1, respectively. The data measured in the S3F and S3B detectors are in red, and their mirror points with respect to $\theta_{\mathrm{com}} = 90°$ are in grey. Legendre polynomials of orders zero, two, four, six and eight are also shown.

For all particles, order eight best fits the angular distribution at the probed angles. However, it gives a negative angular distribution at angles of the order of $55° \leq \theta_{\mathrm{com}} \leq 125°$ for α_0 and α_1, and at $85° \leq \theta_{\mathrm{com}} \leq 95°$ for p_0. This is impossible: the angular distribution may be null but not negative.

Thus, there is a real need for measurements at these angles to allow better determination of the main order parameters, which is the reason of the addition of the PIXEL system (see Sect. 2.3.3).

3.3.3 Total cross section

The total cross section for one excited state i is $(\sigma_{\mathrm{tot}})_i$, and is obtained from the integration over the entire solid angle of fitting parameter a_0 of the order zero of the Legendre polynomial:

$$(\sigma_{\mathrm{tot}})_i = 4\pi a_0. \tag{3.13}$$

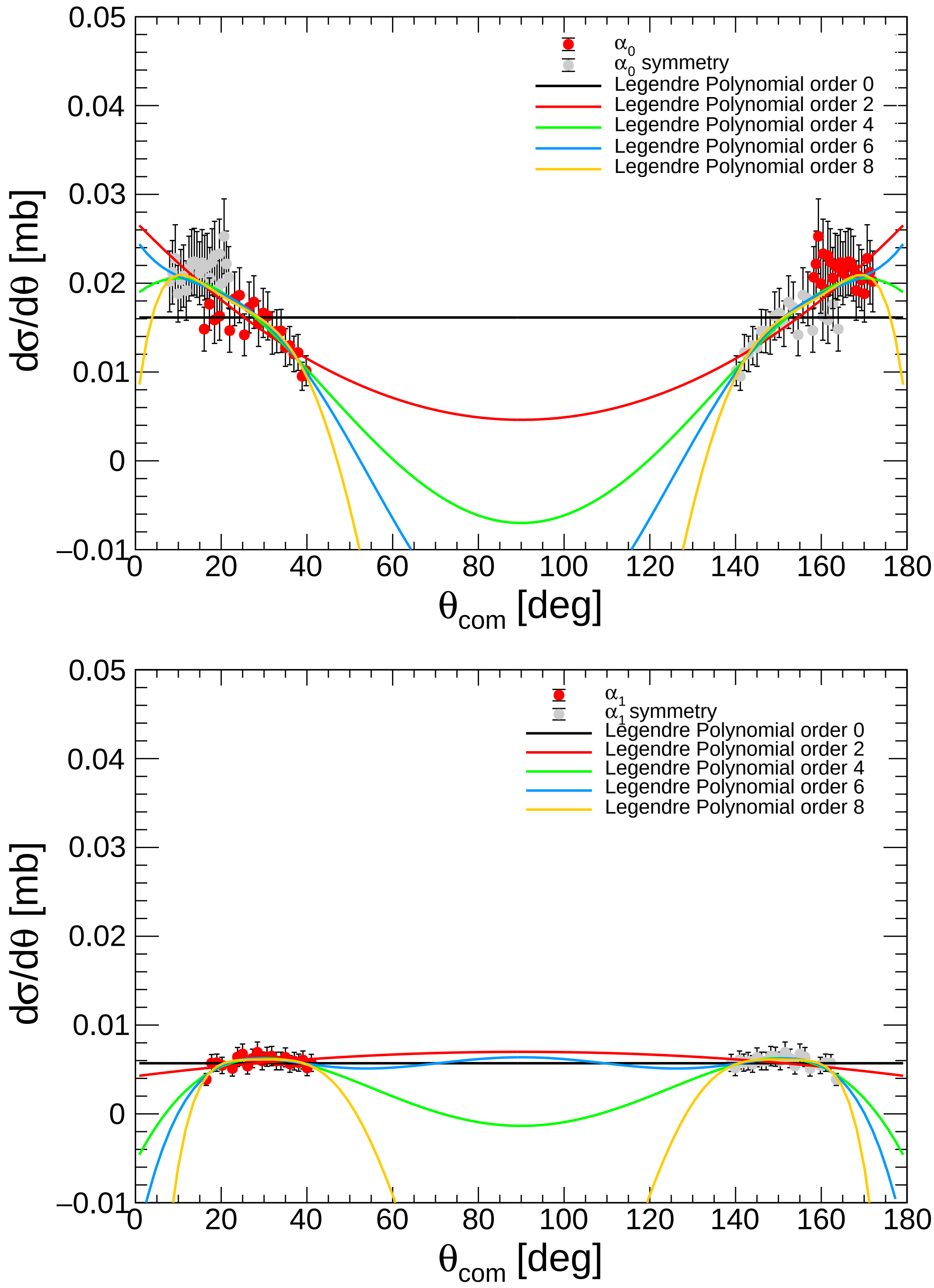

Figure 3.11: Angular distribution for α_0 (top) and α_1 (bottom). $E_{\mathrm{rel}} = 4.76$ MeV.

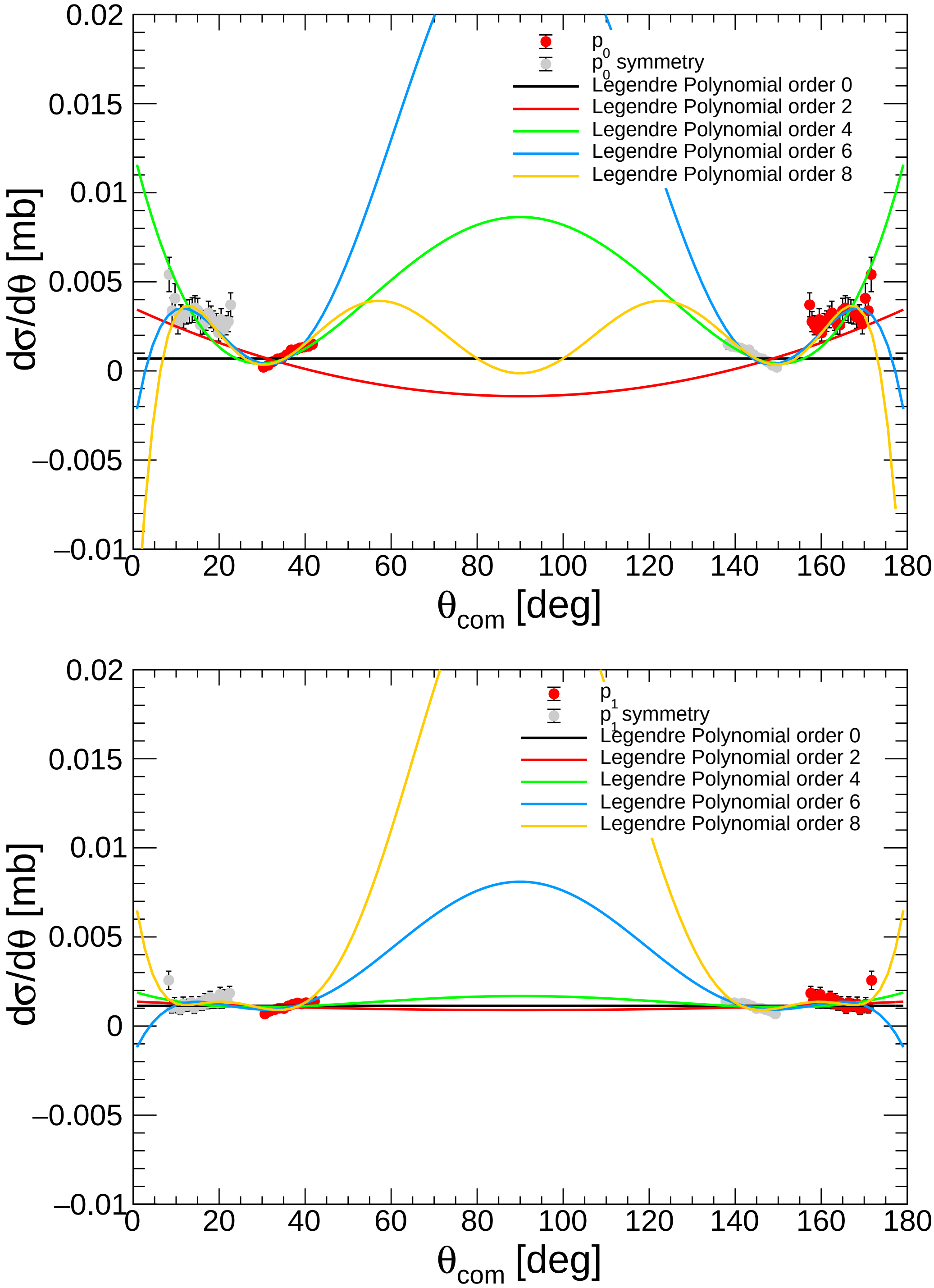

Figure 3.12: Angular distribution for p_0 (top) and p_1 (bottom). $E_{\mathrm{rel}} = 4.76$ MeV.

Measured excited state	Fraction of the total cross section
p_0	12%
p_1	15%
p_0, p_1	27%
α_0	16%
α_1	32%
α_0, α_1	48%

Table 3.2: Fraction of the measured excited states for the α and proton exit channels. Fusion data from [22].

The total cross section for the p-channel or α-channel is given by the sum of the cross sections of all the excited states accessible at the beam energy. If some excited states cannot be extracted from the experimental data, a branching correction based on previous measurement has to be applied, in the form:

$$\sigma_{\mathrm{tot}} = \left[\sum^{i} (\sigma_{\mathrm{tot}})_i \right] \Gamma, \tag{3.14}$$

where Γ is the branching correction for the missing excited states. In this work, these branching corrections are from Becker *et al.* [22], and are summarized in Tab. 3.2.

The total cross section for the α channel (top) and the proton channel (bottom) are in Fig. 3.13. These cross section have been obtained with α_0 and α_1, and p_0 and p_1, respectively. The points from this work are in red. Experimental data from [22; 27; 28] are also represented in blue, green and yellow.

It can be seen that the total cross sections obtained are lower than the previous experimental data: very slightly for α channel but more significantly for proton channel, with a difference of about an order of magnitude.

In order to understand this, the total cross sections were determined from a single state. This makes it possible to highlight problems associated with the spectra and fits achieved. The results obtained are shown in Fig. 3.14 for the α exit channel, with the total cross section determined from α_0 in the upper panel and α_1 in the lower panel, and Fig. 3.15 for the proton exit channel, with the total cross section determined from p_0 in the upper panel and p_1 in the lower panel. The legend used is the same as for Fig. 3.13.

The total cross section for the α channel obtained from the angular distribution of α_0 is in good agreement with the previous experimental data, unlike that obtained from the angular distribution of α_1, which is almost an order of magnitude smaller.

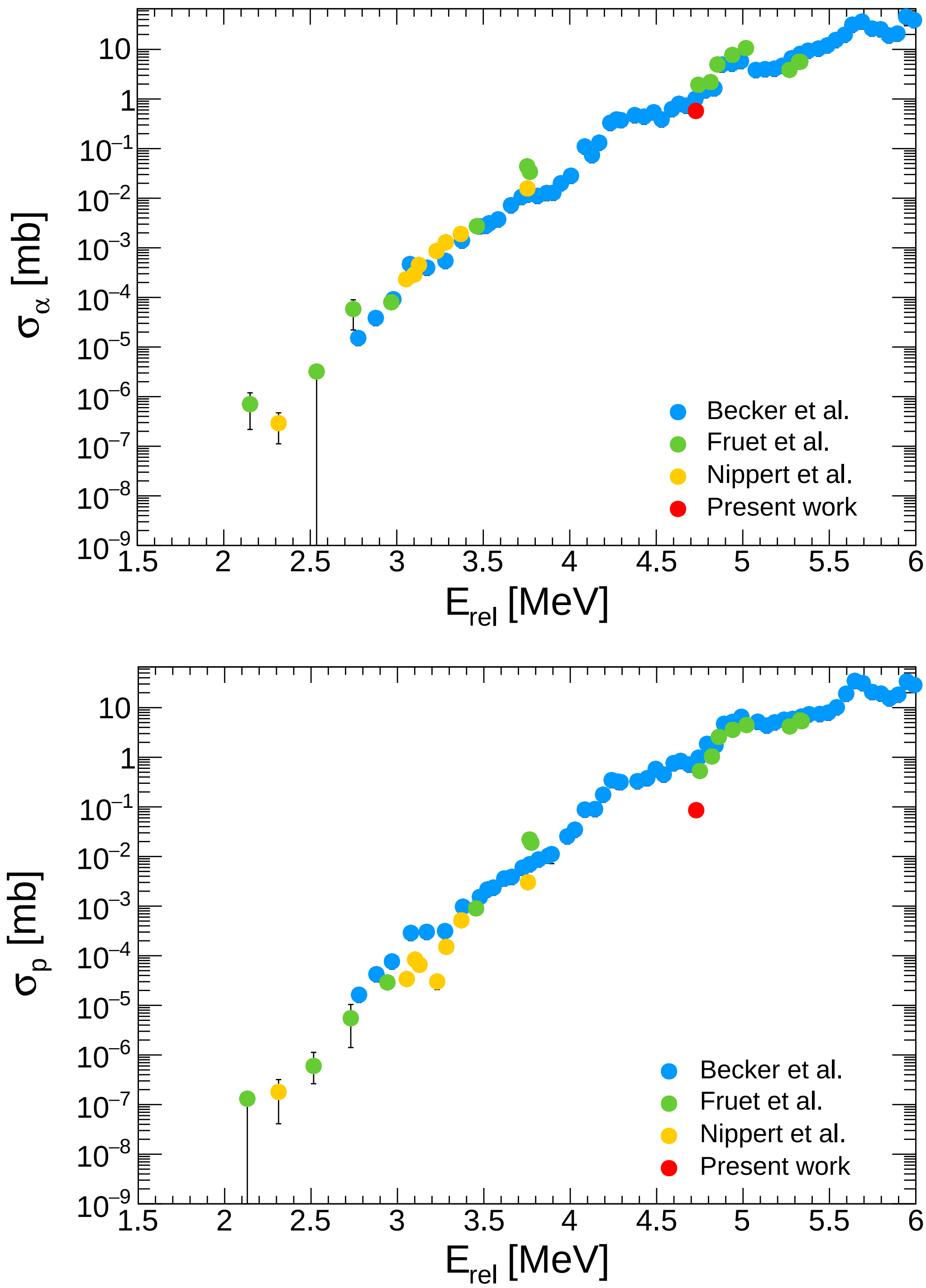

Figure 3.13: Total cross section for the α channel (top) and the proton channel (bottom). Experimental data from [22; 27; 28] are represented. $E_{\rm rel} = 4.76$ MeV.

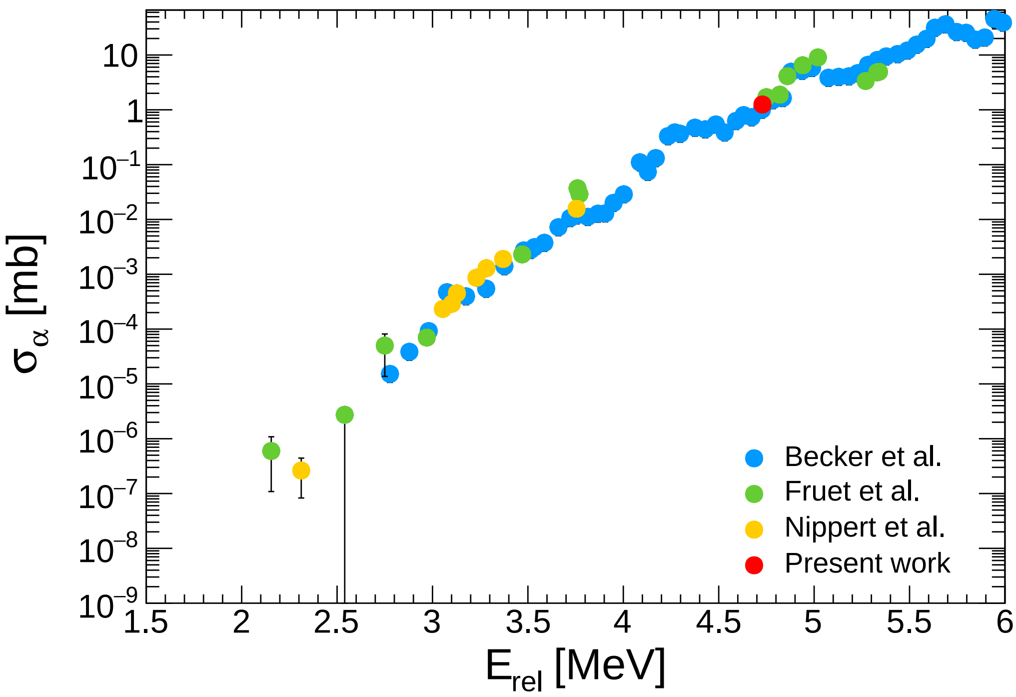

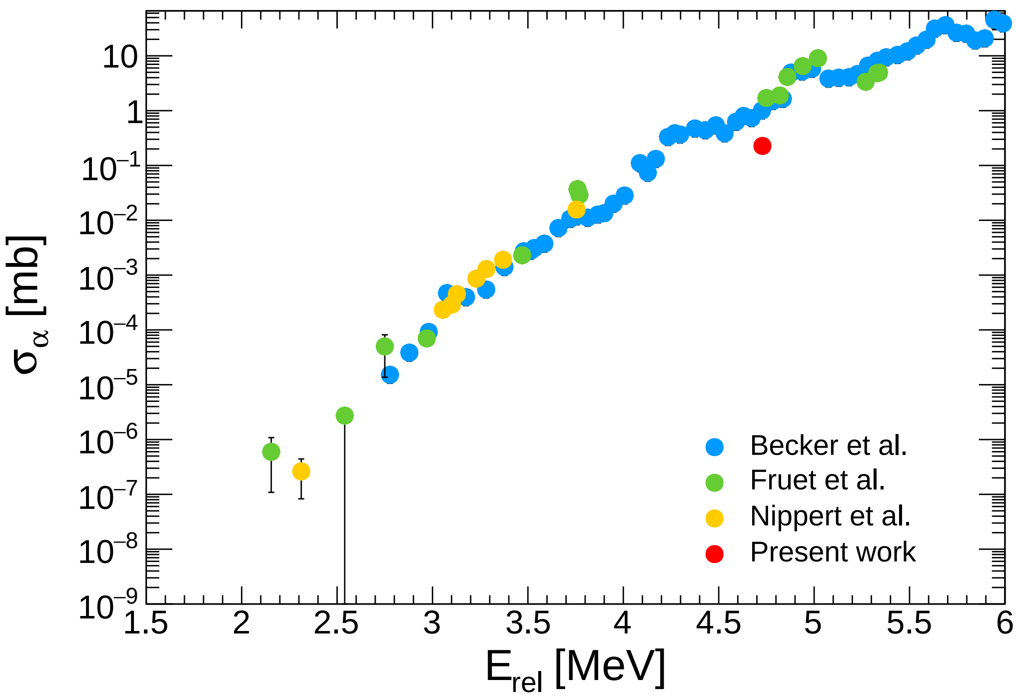

Figure 3.14: Total cross section for the α exit channel, determined with α_0 (top) and α_1 (bottom). Experimental data from [22; 27; 28] are represented. $E_{\text{rel}} = 4.76$ MeV.

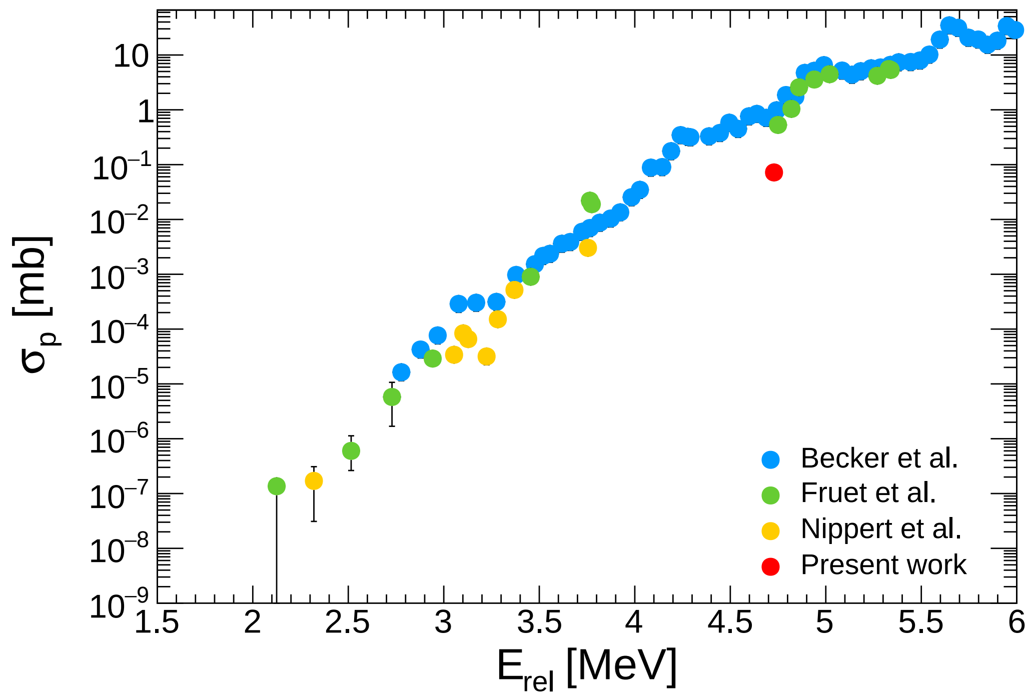

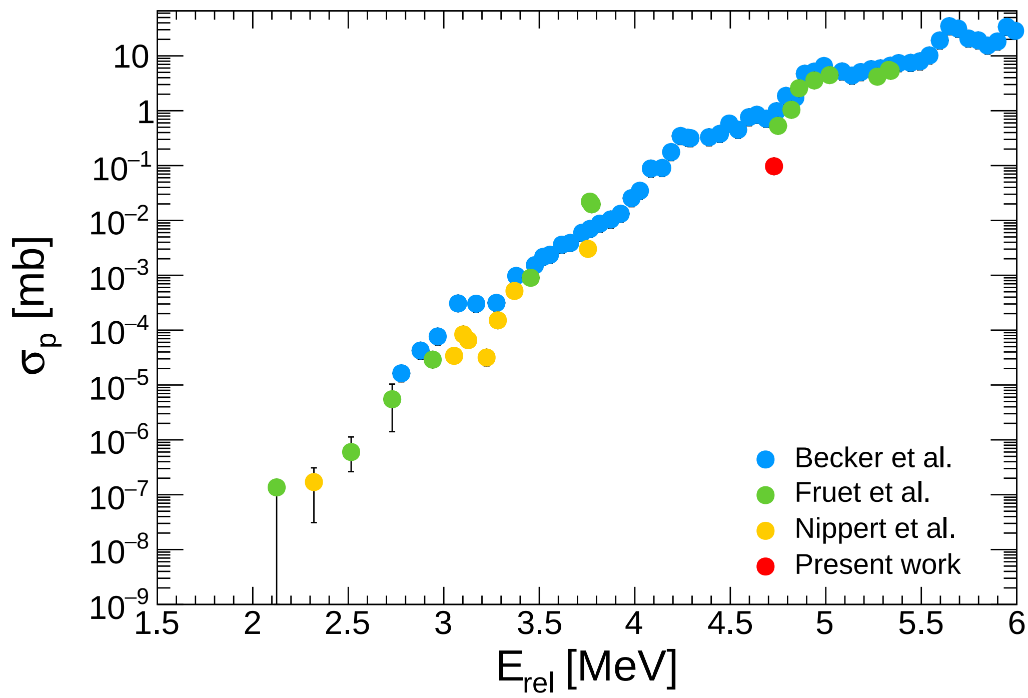

Figure 3.15: Total cross section for the proton exit channel, determined with p_0 (top) and p_1 (bottom). Experimental data from [22; 27; 28] are represented. $E_{rel} = 4.76$ MeV.

This can be explained by the angular coverage for each of the particles. Indeed, as mentioned in Sect. 3.3.1, α_0 is discernible in all the spectra, which is not the case for α_1, which is only discernible in the spectra from S3F. Thus, a lack of data can greatly influence the cross section, which is extracted from the zero order of the Legendre polynomial.

We can then deduce here that the difference between the cross section for the α channel determined in this work and visible in the upper panel of Fig. 3.13 is influenced by the lack of α_1 data.

The total cross sections for the proton exit channel obtained from the angular distribution of p_0 and p_1 are both lower than the previous experimental results, by more than an order of magnitude.

Since p_0 of p_1 are not discernible on all the S3F channels, we can assume that, as is the case for α_1, it is the lack of angular coverage that influences this result. However, this possibility should be ruled out. Indeed, as can be seen in Fig. 3.12, the angular distribution is much less marked for protons than for α, and it is more important, because fewer angles are covered. However, the difference between the cross sections obtained from this work and those from previous experiments is greater for p_0 and p_1 than for α_1, which should be the opposite.

A second lead comes from the spectra obtained from S3B. As seen in Sect. 3.3.1, there is a dominating background contribution at the typical energy of p_0 and p_1. Thus, if the adjustment of this background noise is not correctly estimated, it is possible to overestimate or underestimate the number of events. This seems to be the most likely explanation for the differences observed.

This contribution could have several origins. The first would be a contribution due to a fusion reaction involving contaminants in the target, and more specifically the d(^{12}C,p)^{13}C fusion reaction. Kinematic calculations were carried out to determine the energy of the protons produced by this reaction. The results can be seen in Fig. 3.16, where black, red and blue lines represent the kinematics calculations for the α exit channel, proton exit channels and from protons from reactions with deuterium contaminant, respectively. The ground state transitions are at the highest energy, followed by excitation levels with decreasing particle energy.

The result shows that the energy of the proton from the ground state of the reaction is too low to be the cause of this background.

The contamination could come from other contaminants, and in particular from the scattering of hydrogen isotopes in the target caused by interactions with the ^{12}C beam. However, this scattering is generated towards the front of the target, and not towards the back, where S3B is located.

A final cause could be electronic diffusion in the chamber. This has already been observed in low energy experiments, always in detectors positioned behind the target.

This analysis shows that angular coverage is an essential parameter for determining the total cross section of the $^{12}C + ^{12}C$ fusion reaction.

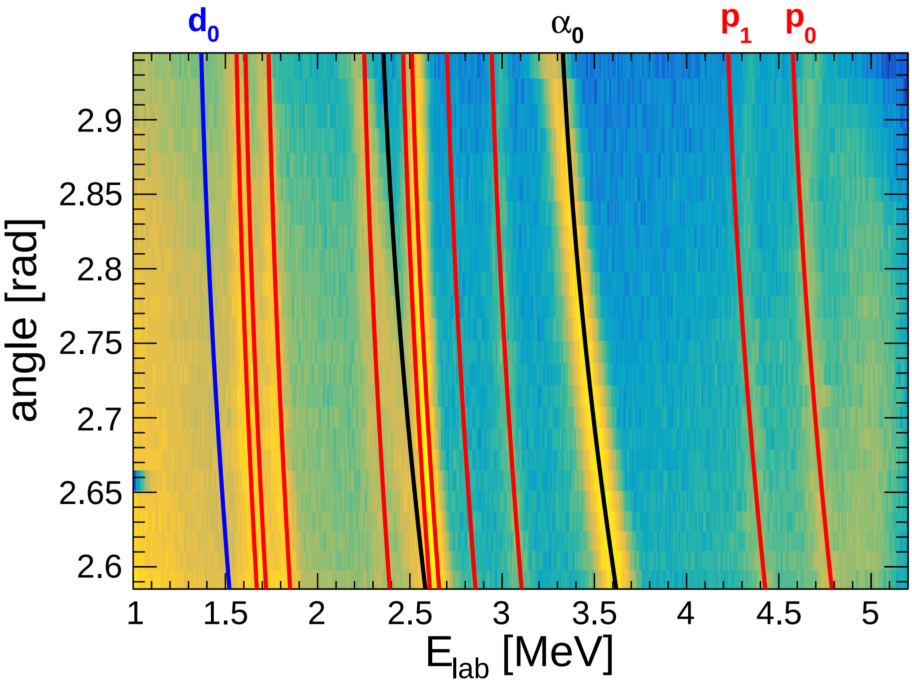

Figure 3.16: Angular differential energy spectra for S3B detector $E_{\text{lab}} = 9.6$ MeV. Black, red et blue lines represent the kinematics calculations for the α exit channel, proton exit channels and from deuterium contaminant, respectively. The ground state transitions are at the highest energy, followed by excitation levels with decreasing particle energy.

Thus, this work allows the calculation of a total cross section of the $^{12}\text{C} + ^{12}\text{C}$ fusion reaction for the α_0 path at $E_{\text{rel}} = 4.76$ MeV: $\sigma_\alpha(4.76) = 1.25 \pm 0.17$ mb.

3.4 Résumé du chapitre

Ce chapitre porte sur l'analyse des données mesurées à l'énergie $E_{\text{cdm}} = 4.8$ MeV lors de la campagne expérimentale de 2022. Pour cette énergie seuls les détecteurs DSSSD ont été utilisés. Afin d'effectuer cette analyse, les détecteurs ont d'abord été calibrés. Les spectres ont ensuite servi à extraire des distributions angulaires, avant l'obtention d'une section efficace totale. Les particules détectées ici sont les α et les protons issues des voies de sorties α et protons respectivement.

3.4.1 Analyse des données

L'analyse des données a été précédée de la calibration des détecteurs. Cette dernière a été effectuée en deux étapes : une première calibration à l'aide d'une source 3α, et une seconde calibration à haute énergie.

La calibration 3α a été effectuée avec une source contenant les isotopes ^{239}Pu, ^{241}Am et ^{244}Cm. Les spectres bruts ont été ajustés indépendamment, et les pics obtenus ont été associés avec les énergies des α émis. Des paramètres de calibration ont ainsi été obtenus *via* une régression linéaire, comme montré sur la Fig. 3.1. Les résultats obtenus montrent une différences entre les calculs cinétiques et les pics mesurés, expliquée par la précision de la calibration linéaire et le fait que les énergies des particules issues de la source 3α est différente de celles issues de la fusion du carbone. Cependant, cette calibration est utile pour obtenir une identification préliminaire des différentes particules.

La calibration à haute énergie est basée sur l'identification des pics grâce à des calculs d'énergies cinétiques, représentés sur la Fig. 3.2. Les spectres bruts sont ajustés indépendamment, et une régression linéaire est effectuée pour chacun d'entre eux, visibles sur la Fig. 3.3, afin d'obtenir un jeu de paramètres de calibration pour chacune des 24 pistes des deux DSSSD. Les distributions angulaires calibrées obtenues sont montrées sur la Fig. 3.8.

La calibration a été suivie d'une correction des données liée au partage de charge. Comme vu précédemment, les détecteurs sont divisés en 24 pistes angulaires : il est possible qu'une seule particule incidente génère une cascade de charges qui va être récoltée par deux pistes voisines, phénomène illustré Fig. 3.5 [28]. Dans ce cas d'un partage de charge, il est nécessaire de sommer le signal collecté par les deux pistes afin de reconstruire l'énergie de la particule incidente.

Afin d'identifier ce phénomène il est nécessaire d'enregistrer l'énergie de la particule mais également le temps de détection. En effet, dans le cas d'un partage de charge, la détection de la même particule incidente par les deux pistes voisines a lieu dans une courte fenêtre temporelle, 400 ns, valeur prenant en compte le temps mort de l'acquisition de STELLA [28]. Ces évènement sont appelés de multiplicité 2, tandis que les évènements détectés dans une seule piste sont de multiplicité 1.

Les effets du partage de charge et le rapport entre les évènements de multiplicité 1 et ceux de multiplicité 2 sont visibles sur la Fig. 3.7. L'importance du traitement de ce phénomène dans l'analyse y est ainsi illustrée.

L'étude la distribution angulaire de certains produits de la fusion du carbone a été effectuée, pour chacune des 24 pistes des deux détecteurs. Pour cela, extraire le nombre d'évènements de fusion pour chaque particule, des ajustements des pics ont été réalisés. Ils sont faits de deux parties : une fonction Gaussienne décrivant le pic et une fonction décrivant le bruit de fond, et sur un intervalle en énergie permettant la meilleure estimation de ce dernier. Les sections efficaces obtenues ont ensuite été transformées du référentiel laboratoire à celui du centre de masse.

Les distributions angulaires ont été ajustées avec des polynômes de Legendre, comme visible sur la Fig. 3.8, afin d'extraire des informations sur le moment angulaire de la particule légère.

3.4.2 Normalisation des données

La détermination de la section efficace nécessite une normalisation des paramètres la plus précise possible. Dans le cas de l'expérience STELLA, l'efficacité de détection est dérivée de deux grandeurs : l'intensité du faisceau et l'épaisseur des cibles.

L'intensité de faisceau est obtenue grâce aux mesures effectuées par deux coupes de Faraday, l'une placée en amont de la chambre, et l'autre en aval, comme représenté sur la Fig. 3.9.

Avant chaque prise de données, une vérification de l'alignement du faisceau dans la chambre *via* la transmission du faisceau dans la chambre a été effectuée.

Durant l'acquisition des données, l'intensité du faisceau est contrôlée continuellement par un intégrateur de courant digital relié à la coupe de Faraday en aval de la chambre. Des calibrations ont été effectuées régulièrement afin de s'assurer de la présence ou non de déviations entre l'intensité intégrée mesurée par l'intégrateur de courant et celle réellement délivrée par l'accélérateur. A partir de ces données un facteur de calibration a pu être déterminé pour différentes intensités.

A partir de ce facteur de calibration, de la valeur donnée par l'intégrateur de courant, et de la connaissance de la charge moyenne du faisceau, il a été possible de déterminer la valeur de l'intensité intégrée sur le temps de l'acquisition, avec une incertitude de 12%.

L'incertitude sur l'épaisseur de les cibles a été étudiée dans un travail précédent [28], ainsi que leur l'épaississent au cours d'un acquisition [6]. Les résultats obtenus montrent que l'épaisseur des cibles ne varient pas lors des prises de données, et que leur incertitude est de 10%.

Les différentes incertitudes sont résumées dans l'équation 3.11.

3.4.3 Détermination de la section efficace totale à $E_{\text{rel}} = 4.76$ MeV

La sélection des évènements a été fait grâce aux ajustements présentés précédemment. La Figure 3.10 montre les spectres en particules obtenues pour une voie de S3B (détecteur en amont de la cible) et S3F (détecteur en aval de la cible), ainsi que les ajustements réalisés et les énergies cinétiques calculées pour chaque particule.

Dans S3F, seules α_0 et α_1 peuvent être identifiées dans les 24 voies, avec un bruit de fond linéaire. Dans S3B, les particules p_0, p_1 et α_0 peuvent être identifiées dans toutes les voies, avec un bruit de fond polynomial au second ordre. Cependant, tous les spectres de S3B montrent un bruit de fond dominant aux énergies typiques de p_0 et p_1.

Les distributions angulaires pour α_0, α_1, p_0 et p_1 sont représentées sur les Fig. 3.11 et 3.12, ainsi que les polynômes de Legendre jusqu'à l'ordre 8. C'est ce dernier ordre qui présente le meilleur accord avec les données expérimentales. Cependant il est négatif à certains angles pour α_0, α_1 et p_0. Cela est impossible, ce qui montre l'importance d'une couverture angulaire améliorée pour mesurer des données à ces angles, ce qui est l'objectif du système PIXEL.

La section efficace totale a été obtenue à partir de l'intégration sur l'angle solide total du paramètre d'ajustement à l'ordre 0 du polynôme de Legendre. Les sections efficace totales pour les voies protons et α sont données par la somme des sections efficaces de chacun des états excités. Dans le cas où tous ces états ne peuvent être déterminés, un rapport de branchement a été appliqué [22].

Les sections efficaces totales sont visibles sur les Fig. 3.13 pour les protons et les α. Les résultats montrent que les résultats de ce travail sont inférieurs à ceux de mesures précédentes.

Afin de comprendre cela les sections efficaces ont été déterminées à partir d'un seul état : α_0, α_1, p_0 et p_1. Les résultats obtenus sur les Fig. 3.14 et 3.15. Il est possible de constater que seule la mesure de α_0 est en accord avec les précédentes, et α_1 plus faible. Cela peut s'expliquer par la différences de couverture angulaire entre les deux particules.

Concernant les résultats de p_0 et p_1, cela est aussi du au manque de couverture angulaire : ils ne sont pas définis dans tous les détecteurs de S3F. Concernant les données de S3B, le bruit de fond ne pouvant être correctement estimé, il est alors probable de le surestimer ou sous estimer.

L'origine de ces contamination a été investigué, avec comme source la plus probable la diffusion électronique dans la chambre, phénomène déjà observé dans le détecteur situé à l'arrière de la cible dans des expériences à basses énergies.

Ainsi, cette analyse démontre l'importance de la couverture angulaire dans la détermination de la section efficace totale de la réaction de fusion ^{12}C + ^{12}C.

Chapter 4

New reaction rates and their impact on stellar evolution

Contents

4.1 Determination of $^{12}C + ^{12}C$ nuclear reaction rates 118
4.1.1 Fusion excitation response function 118
4.1.2 STELLA sensitivity 121
4.1.3 Reaction rate 125
4.2 Impact on stellar evolution 130
4.2.1 Impact on global stellar evolution 130
4.2.2 Impact on detailed nucleosynthesis 139
4.3 Résumé du chapitre 145
4.3.1 Détermination des taux de réactions pour $^{12}C + ^{12}C$ 145
4.3.2 Impacts sur l'évolution stellaire 146

The stellar reaction rate is a profound nuclear and astrophysical quantity: it can only be determined by nuclear physics, whether theoretically or experimentally, and can only be exploited by astrophysics. It is a perfect example of the profound link between these two disciplines, and of how they complement each other. Calculating it and studying its impact on stellar evolution is the logical next step after determining the effective cross section at energies of astrophysical interest.

In order to determine reaction rate from STELLA experimental data [27], the features of the sub-barrier ^{12}C + ^{12}C fusion excitation function have been studied. It exhibits a series of resonances [23; 20]. The present deep sub-barrier data suggest the existence of an energy region with hindrance trend [27; 28] and an onset of dominant resonance structure towards even lower energies, around 2.1 MeV. By taking into account both of these features, new reaction rates were computed, turning the resonance on and off to evaluate its impact.

Their impact on stellar evolution models was studied using two different simulation code: the Geneva stellar evolution code [94], and a 'one-layer code' [56] for a focus on detailed nucleosynthesis.

The results presented in this chapter are a detailed description of the study published in [32] and [33].

4.1 Determination of ^{12}C + ^{12}C nuclear reaction rates

4.1.1 Fusion excitation response function

In order to calculate the nuclear reaction rate, the first step is to determine the excitation functions from measured carbon fusion cross sections. To this end, two different physical scenarios were explored: the Hin and the HinRes model.

The Hin model is based on an empirical model of fusion hindrance with a set of parameters for carbon fusion by Jiang *et al.* [17]. It describes the global behaviour of the excitation function of a system, but does not take into account potential local fluctuations. The excitation function for the Hin model has been obtained by fitting data measured by the STELLA collaboration [27] with a dependency suggested by Jiang *et al.* [17]:

$$\sigma(E)_{\mathrm{Hin}} = \sigma_{\mathrm{s}} \frac{E_{\mathrm{s}}}{E} \exp\left(A_0 (E - E_{\mathrm{s}}) - \frac{2B_0}{\sqrt{E_{\mathrm{s}}}} \left(\left(\frac{E_{\mathrm{s}}}{E} \right)^{N_p - 1} - 1 \right) \right), \tag{4.1}$$

where the parameters E_{s} and σ_{s} are the center of mass energy in MeV and the total cross section in mb for which the astrophysical S-factor $S(E)$ is maximum, N_p has a fixed value at 1.5, and A_0 and B_0 are free parameters. It should be noted that none of the parameters are forced during the adjustment of the $\sigma(E)_{\mathrm{Hin}}$ function to STELLA data.

The formula describing the total cross section was scaled by the commonly used branching ratio [15], corresponding to 35% for the proton exit channel and 65% for the α exit channel.

In the second scenario, the HinRes model, a resonance is added on top of the Hin model at $E = 2.14$ MeV; the resonance energy and width were taken from [24]. The contribution from an isolated narrow resonance to a cross section is described by the Breit-Wigner cross section formula:

$$\sigma_{BW}(E) = \frac{\lambda^2}{4\pi}\frac{(2J+1)(1+\delta_{01})}{(2j_0+1)(2j_1+1)}\frac{\Gamma_a\Gamma_b}{(E_\mathrm{R}-E)^2+\Gamma_\mathrm{R}^2/4}, \tag{4.2}$$

where j_0 and j_1 are the spins of target and projectile respectively, J and E_R are the spin and the center of mass energy of the resonance, Γ_a and Γ_b are the resonance partial widths of entrance and exit channel, Γ_R is the total resonance width, and δ_{01} is the Kronecker delta, to account for the contribution of identical particles. Values of the resonance parameters are kept fixed throughout the rest of this work, in order to study if the resonance proposed by Spillane *et al.* shows good compatibility with STELLA experimental data. The cross section considered for this second scenario is the sum of the Hin model cross section and the Breit-Wigner cross section in a simultaneous fit.

The choice of the points from [27], shown in Tab. 4.1, used to make the adjustment, refers to two important information: the considered physics at a given energy, but also the energy range over which this physics is considered to be valid.

First indication to define this energy range is that the fusion hindrance on which is based the Hin model is adapted to deep sub-barrier energies from systematic studies of various nuclei [17]. Additionally, the ^{12}C + ^{12}C reaction is known to have a lot of resonances [23; 20]: cross sections measured on these resonances cannot be considered throughout the adjustment, because the physics that generates resonance is not the same that the one describing the cross section behaviour without resonance. It is the reason for which the five points measured at the highest energies, based on a resonance, have not been considered in the adjustment. Also, in the first scenario, the point measured at the lowest energy, $E_\mathrm{eff} = 2.16$ MeV, has been excluded too, as presence of an other resonance is supposed here.

Data measured by STELLA allow to determine a cross section for each studied exit channel: α-channel and p-channel (see Eq. 2.3). Thus, the adjustment could be done in two different ways: independently for each channel, or simultaneously on both channels. The compound nucleus hypothesis made here is that the same behaviour is observed, at different scaling, in all exit channels.

Values of the determined parameters by the adjustment are given in Tab. 4.2.

The obtained cross sections with both models are shown in Fig. 4.1. Cross sections predicted in CF88 model [21] are also represented to make the comparison easier. This model describing the total cross section reaction, was scaled by the branching ratio of each channel. Cross sections have been extrapolated down to energy of $E_\mathrm{rel} = 1.2$ MeV.

E_{eff} (MeV)	$\sigma_p(E)$ (mb)	$\sigma_\alpha(E)$ (mb)
2.16	$[0\ ,\ 1.36*10^{-7}]$	$[0.99*10^{-7}\ ,\ 10.75*10^{-7}]$
2.54	$[2.63*10^{-7}\ ,\ 11.30*10^{-7}]$	$[0\ ,\ 2.73*10^{-6}]$
2.75	$[1.90*10^{-6}\ ,\ 10.40*10^{-6}]$	$[1.86*10^{-5}\ ,\ 8.63*10^{-5}]$
2.97	$(2.90\pm0.61)*10^{-5}$	$(7.00\pm0.91)*10^{-5}$
3.47	$(9.00\pm0.73)*10^{-4}$	$(2.30\pm0.21)*10^{-3}$
3.76	$(2.20\pm0.15)*10^{-2}$	$(3.70\pm0.27)*10^{-2}$
3.77	$(1.90\pm0.13)*10^{-2}$	$(2.90\pm0.21)*10^{-2}$
4.75	$(5.30\pm0.15)*10^{-1}$	1.70 ± 0.06
4.82	1.04 ± 0.03	1.89 ± 0.05
4.86	2.57 ± 0.06	4.12 ± 0.15
4.94	3.57 ± 0.09	6.49 ± 0.27
5.02	4.46 ± 0.12	9.04 ± 0.33
5.27	4.18 ± 0.10	3.36 ± 0.10
5.33	5.55 ± 0.12	4.82 ± 0.12
5.34	5.34 ± 0.17	4.94 ± 0.11

Table 4.1: Cross sections measured by STELLA, for α exit channel and proton exit channel. Data from [27].

Table 4.2: Parameters of cross sections for ^{12}C + ^{12}C fusion reaction using different models from data interpolation. From [32].

Model	σ_s (10^{-2} mb)	E_s (MeV)	A_0 (MeV^{-1})	B_0 (10^1 MeV$^{1/2}$)	$((\omega\gamma)_R)_\alpha$ (meV)	$((\omega\gamma)_R)_p$ (meV)	Γ_R (keV)	E_R (MeV)
Hin	2.20±0.14	3.69±0.01	-1.16±0.03	5.13±0.02	∅	∅	∅	∅
HinRes	2.20±0.14	3.69±0.01	-1.11±0.03	5.09±0.02	0.11±0.03	0.02±0.03	12	2.138±0.006

The STELLA measurements shows a good compatibility with the resonance observed by Spillane *et al.*: it allows to include the experimental point measured at $E_{\text{eff}} = 2.16$ MeV to the local response for the cross section composed of a hindrance trend with a resonance at 2.14 MeV. It is worth noting that at energies near the Coulomb barrier (*i.e.* $E_{\text{Coulomb}} = 6.6$ MeV) the different models overlap, but diverge toward lower energies, where both the Hin and HinRes models are clearly below that of the CF88 model.

In the region of astrophysical interest for $T = 0.5$ GK, that is at vicinity of $E_{\text{eff}} = 1.5$ MeV, it is possible to note that if cross sections extrapolations from Hin model and CF88 model follow the same tendency, cross section from HinRes model shows an other one. In these energy ranges, the cross section is not known, because of the lack of experimental data, and nothing can validate or invalidate the different proposed models. Furthermore, the presence of several other resonances at lower energies are suspected [74; 15; 95], but has not yet been confirmed by direct measurements.

Thus, STELLA data are not enough to claim with certitude the presence of a

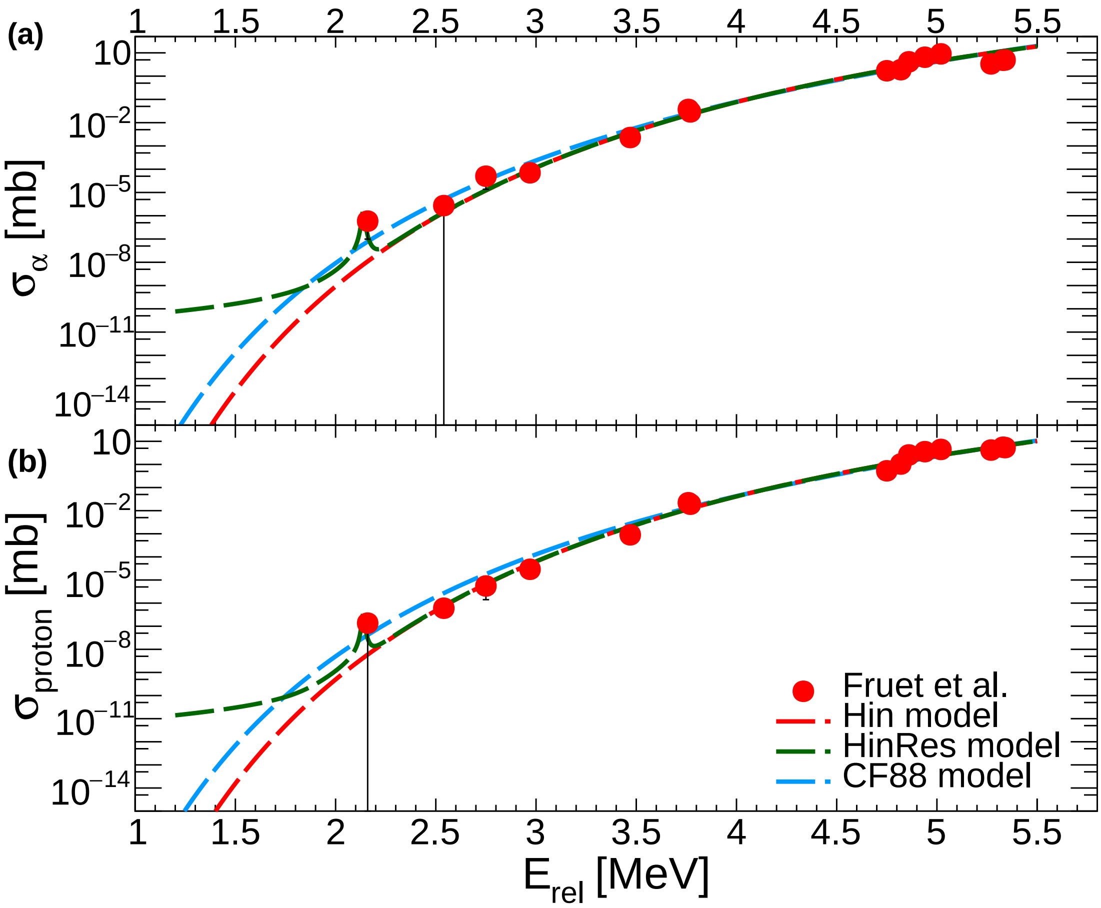

Figure 4.1: Cross sections for alpha (a) and proton (b) channel, obtained with STELLA (red points) [32]. Adjustments made for the Hin model (red curve) and HinRes model (green curve) are compared with the cross section from the CF88 model (blue curve) [21]. Data points at the lowest energy for protons and the second lowest for the α channel are upper limits (vertical black lines).

resonance like the one predicted in [24]: new measurements are required. It is necessary to note that these data does not allow, at lower energies, to know with precision the cross section tendency.

4.1.2 STELLA sensitivity

Since the reaction rate is a value computed from cross section, it is relevant to know the temperature range of the reaction rate experimentally probed by the STELLA experiment. Based on the energies at which the cross sections are measured, it is possible to determine the temperature interval where the reaction rate does not require extrapolation of the cross section. This range is called the STELLA sensitivity.

The minimum energy limit probed by the STELLA experiment was $E_{\text{rel}} = 2.03$ MeV (see supplements in Fruet *et al.* [27]), and was determined from the lowest energy at which measurements were made and the energy loss in the target. To determine the

Curve	Integral [0.5 , 4]	Integral $[E_0 - \sigma\ ,\ E_0 + \sigma]$	Ratio
Gamow peak	9.90E-41	6.74E-41	68.05%
Approximation	9.86E-41	6.73E-41	68.27%

Table 4.3: Integrals for the Gamow peak and the approximation from Illiadis [2], on an interval totally covering both peaks and the $E_0 \pm \sigma$ range, and ratio between these integrals for both curves.

temperature in the star at which fusion occurs at this energy, the definition of the Gamow window was used. Indeed, the Gamow window is defined as the energy interval in which, for a fixed temperature and a given system, the reaction has the highest probability of occurring, with a maximum at the Gamow energy E_0 [53; 2].

The reverse line of argument is: What is the temperature in a star corresponding to the measurements of a fusion reactions for a given system at a certain energy? To this end, the measured energy, E_{rel}, is equal to the Gamow energy for the required temperature. At $E_0 = 2.03$ MeV, this is $T = 0.77$ GK (see Fig. 4.2). This temperature is defined as the sensitivity limit of the present data set.

The lower limit of the sensitivity range is defined by the lower limit of the 1σ uncertainties of the Gamow energy.

To determine these uncertainties, the Gamow window for $T = 0.77$ GK, represented in Fig. 4.2, was used, based on an approximation proposed in [2], and employed in [6].

The Gamow peak may be approximated by a Gaussian function. The latter is centered at the energy $E = E_0$, and a maximum of the same size and of the same curvature at $E = E_0$. Both the Gamow peak and its Gaussian approximation are represented in Fig. 4.3.

In order to test the Gaussian approximation, different quantities were determined.

The width at 1σ was evaluated for both curves. The width is 0.599 MeV for the Gaussian function, and 0.600 MeV for the Gamow peak, which corresponds to a difference of 0.001 MeV between the two widths. The ratio between this difference and the width of the Gamow peak is 0.15%.

The Gamow peak is shifted by 0.0184 MeV with respect to the approximation, which corresponds to a ratio between this shift and the width of the Gamow peak of 3.07%. This shift in energy corresponds to a shift in temperature $T = 0.01$ GK, which was here assumed as negligible.

The integrals for different intervals and for both curves have been calculated and are reported in Tab. 4.3. These results show that the Gaussian approximation performed in [2] is a good approximation for the Gamow peak.

In conclusion, in this work it is assumed that the approximation proposed in [2] is suitable for the study of the Gamow peak.

Taking into account the width of the Gamow peak determined before, the minimum temperature corresponding to the $^{12}C + ^{12}C$ data set in Fruet *et al.* [6] for experimental

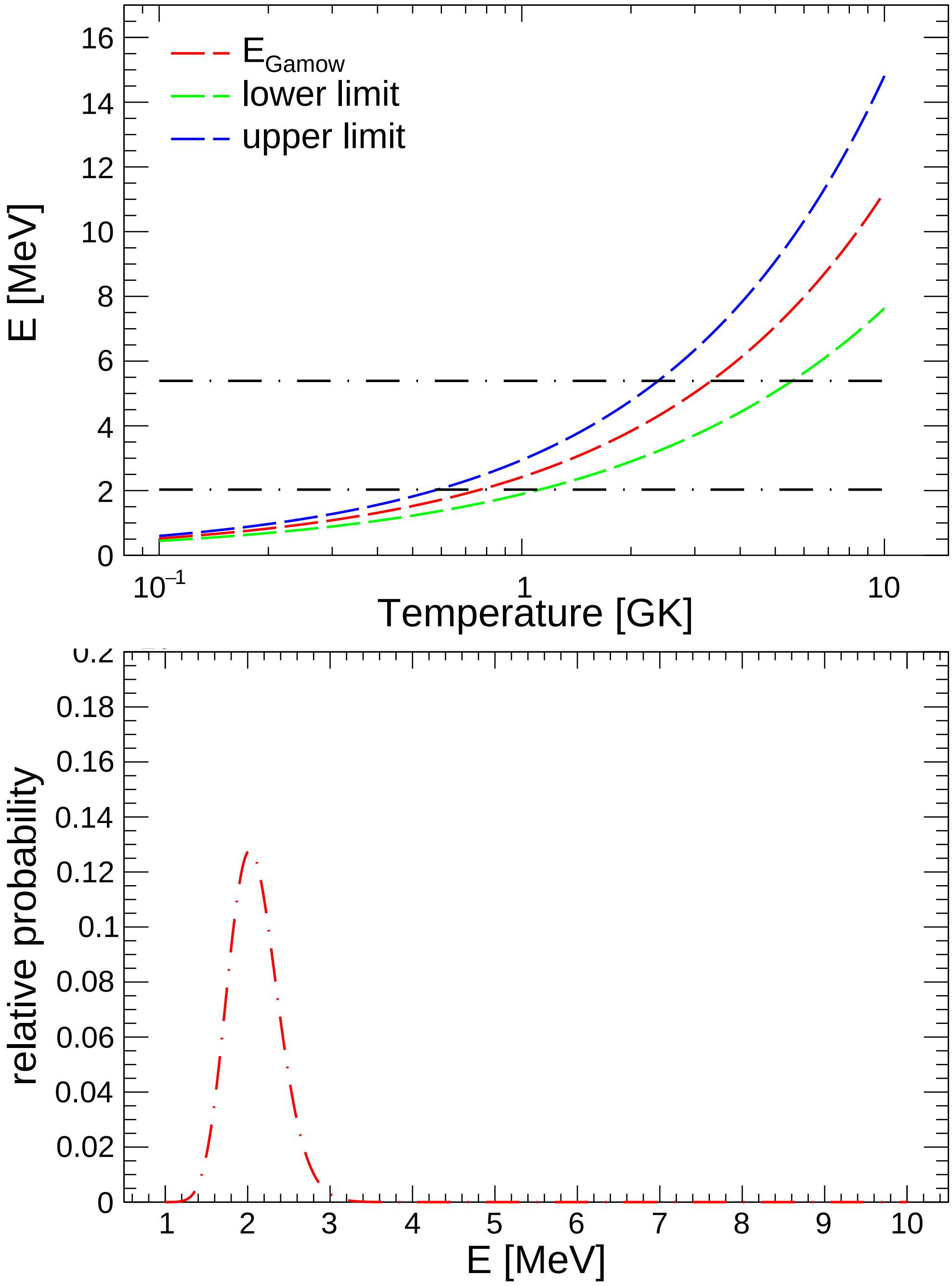

Figure 4.2: Top: Gamow energy as a function of the temperature. Lower and upper limit are given by a Gaussian approximation of the Gamow peak proposed in [2]. The two black lines represent the upper and lower limits energies reached by STELLA experiment. Bottom: Gamow window for the reaction fusion ^{12}C + ^{12}C at T = 0.77 GK, as a function of the relative energy.

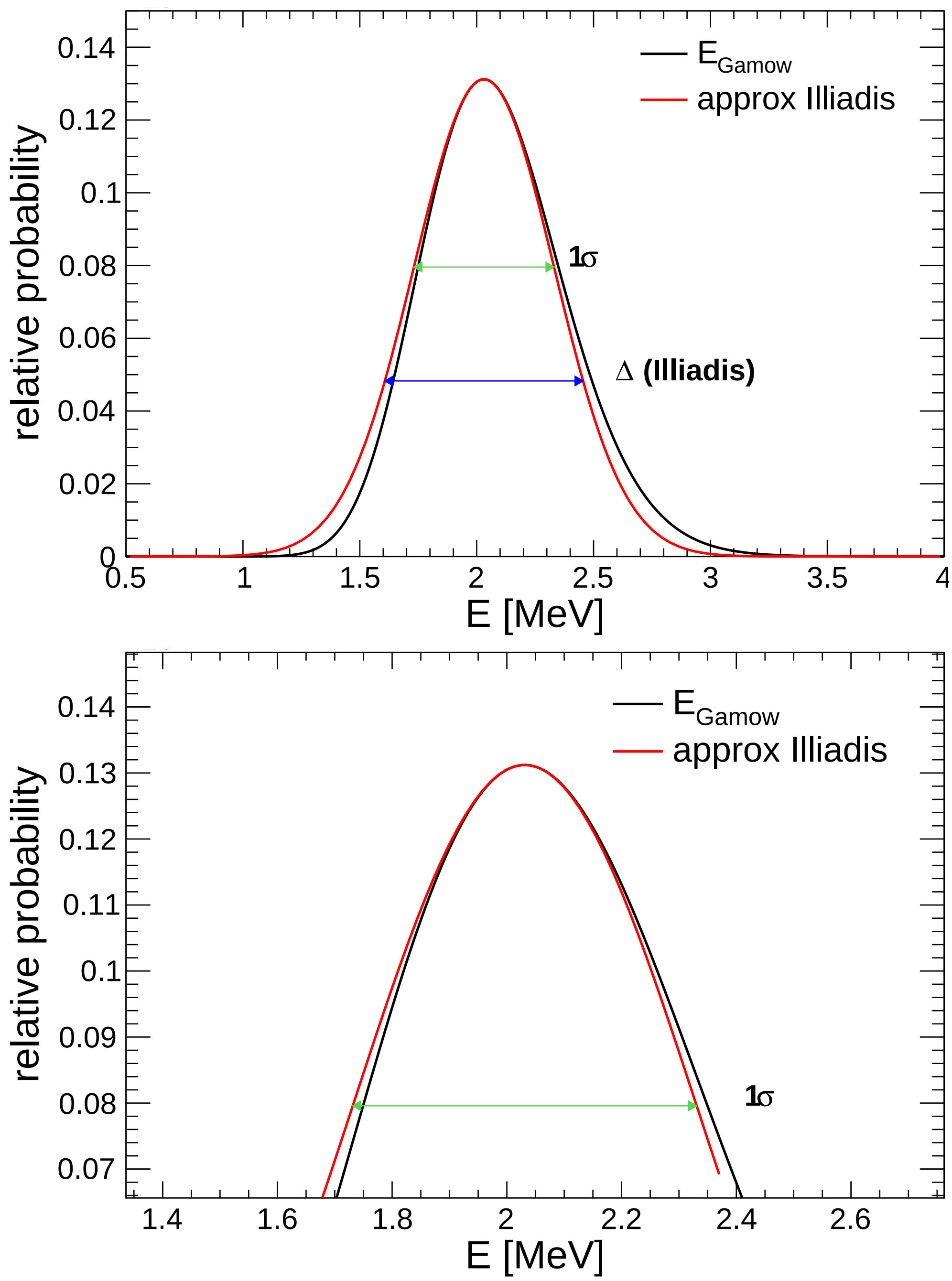

Figure 4.3: Top: Gamow window (black) and approximation from Illiadis [2] (red) for the reaction fusion $^{12}C + {}^{12}C$ at $T = 0.77$ GK. The 1/e width (here Δ) and the 1σ width are also represented for the approximation. Bottom: Zoom on the top of both curves.

determination of the reaction rate is $T = 0.6$ GK.

4.1.3 Reaction rate

Using the Hin and HinRes models from Sect. 4.1.1, reaction rates were computed.

Calculation of these reaction rates was done in two steps, corresponding to both physical scenarios. First step was about determination of reaction rate from the global tendency of cross section. Second was the addition, on this reaction rate without resonance, of an other reaction rate that only describes a resonance.

In the case of Hin model, two different ways to compute the reaction rate have been used. The first one is based on the general formula of a reaction rate, and the second one on an approximation describes by Gasques *et al.* [18].

In a general way, the stellar reaction rate ($N_A\langle\sigma v\rangle$) can be expressed as [53]:

$$(N_A\langle\sigma v\rangle) = \left(\frac{8}{\pi\mu}\right)^{1/2} \frac{N_A}{(kT)^{3/2}} \int_0^\infty \sigma(E) E \exp\left(-\frac{E}{kT}\right) dE, \tag{4.3}$$

where N_A is Avogadro's number, μ is the reduced mass of the system, k is the Boltzmann constant, T is the temperature at which the reaction occurs, $\sigma(E)$ is the reaction cross section, and E is the center of mass energy. The total cross section $\sigma(E)$ is obtained by summing the cross section from all exit channels.

The approximation from [18] can only describe non resonant reaction rates. It has the form:

$$(N_A\langle\sigma v\rangle) = 4N_A\sqrt{\frac{2E_{\mathrm{Gamow}}}{3\mu}} \frac{S(E_{\mathrm{Gamow}})}{kT} \exp(-\tau), \tag{4.4}$$

where $S(E_{\mathrm{Gamow}})$ the total astrophysical S-factor in MeV·b, or S-factor, at Gamow energy E_{Gamow} and τ can be written as:

$$\tau = \frac{3E_0}{kT}. \tag{4.5}$$

The total S-factor is obtained by summing S-factors from all exit channels, taking account their branching ratio from [15].

The two reaction rates from different calculations have been compared, with a mean deviation of 4% on the temperature range considered in this work. Due to this, the general formula of a reaction rate Eq. 4.3 has been chosen to calculate the reaction rate for the Hin model.

In the HinRes model, reaction rate was determined by adding to the hindrance trend a single narrow resonance at $E_{rel} = 2.14$ MeV. The reaction rate in the HinRes model $(N_A\langle\sigma v\rangle)_{\text{HinRes}}$ writes then:

$$(N_A\langle\sigma v\rangle)_{\text{HinRes}} = (N_A\langle\sigma v\rangle)_{\text{Hin}} + \sum_i (N_A\langle\sigma v\rangle)_{\text{res}_\text{i}}, \tag{4.6}$$

where $(N_A\langle\sigma v\rangle)_{\text{Hin}}$ is the reaction rate from Hin model, described in Eq. 4.3, and $(N_A\langle\sigma v\rangle)_{\text{res}_\text{i}}$ the reaction rate associated to the resonance i. Mathematically, the reaction rate obtained with hindrance model forms a continuum on which are added rates specific to each considered resonance.

The reaction rate $(N_A\langle\sigma v\rangle)_{\text{res}_\text{i}}$ formula from [2] is defined as:

$$(N_A\langle\sigma v\rangle)_{\text{res}_\text{i}} = \frac{1.5399 \times 10^{11}}{\left(\frac{M_0 M_1}{M_0+M_1} T_9\right)^{3/2}} \sum_i ((\omega\gamma)_R)_i \exp(-11.605(E_R)_i/T), \tag{4.7}$$

where i labels each resonance, $((\omega\gamma)_R)_i$ and $(E_R)_i$ are the resonance strength and energy, respectively. M_i is the reactant atomic mass, and T is the temperature in GK at which the reaction occurs. Values of these different parameters are from Spillane *et al.* [24].

The reaction rates obtained are shown in Fig. 4.4, in red for the Hin model and green for the HinRes model. The stellar reaction rate predicted in [21] (CF88 rate) is presented in blue. The hatched area in orange marks the STELLA sensitivity. The shaded areas around each curve show the total uncertainties of the reaction rates, determined through error propagation of the experimental uncertainties in the STELLA cross sections.

The Hin scenario yields a reaction rate significantly lower than predicted by the CF88 model at low temperatures, but is similar to it at high temperatures, which is consistent with the predictions of Jiang *et al.* [17].

In the HinRes scenario, the reaction rate is essentially the same as the one without a resonance, and it persists lower that the one predicted in CF88. However, two main effects can be identified. The existence of a resonance slightly increases the reaction rate at low temperatures, and, in an intermediate region between $T = 0.5 - 1.5$ GK, which corresponds to the C-burning of massive stars, it significantly increases the reaction rate to a level comparable with the CF88 rate.

The temperatures range for the C-burning phase (starting when 1% of the carbon abundance in the core is consumed and ending when the same abundance drops below 10^{-5}) determined with data from Fig. 4.5, are shown, for two stellar models detailed in the next section, and for both nuclear fusion scenarios considered in this work. This show that the STELLA sensitivity covers the temperature range needed in this study, *i.e.* stars of 12 and 25 $M_\odot$. The new reaction rates are therefore relevant for astrophysical purposes.

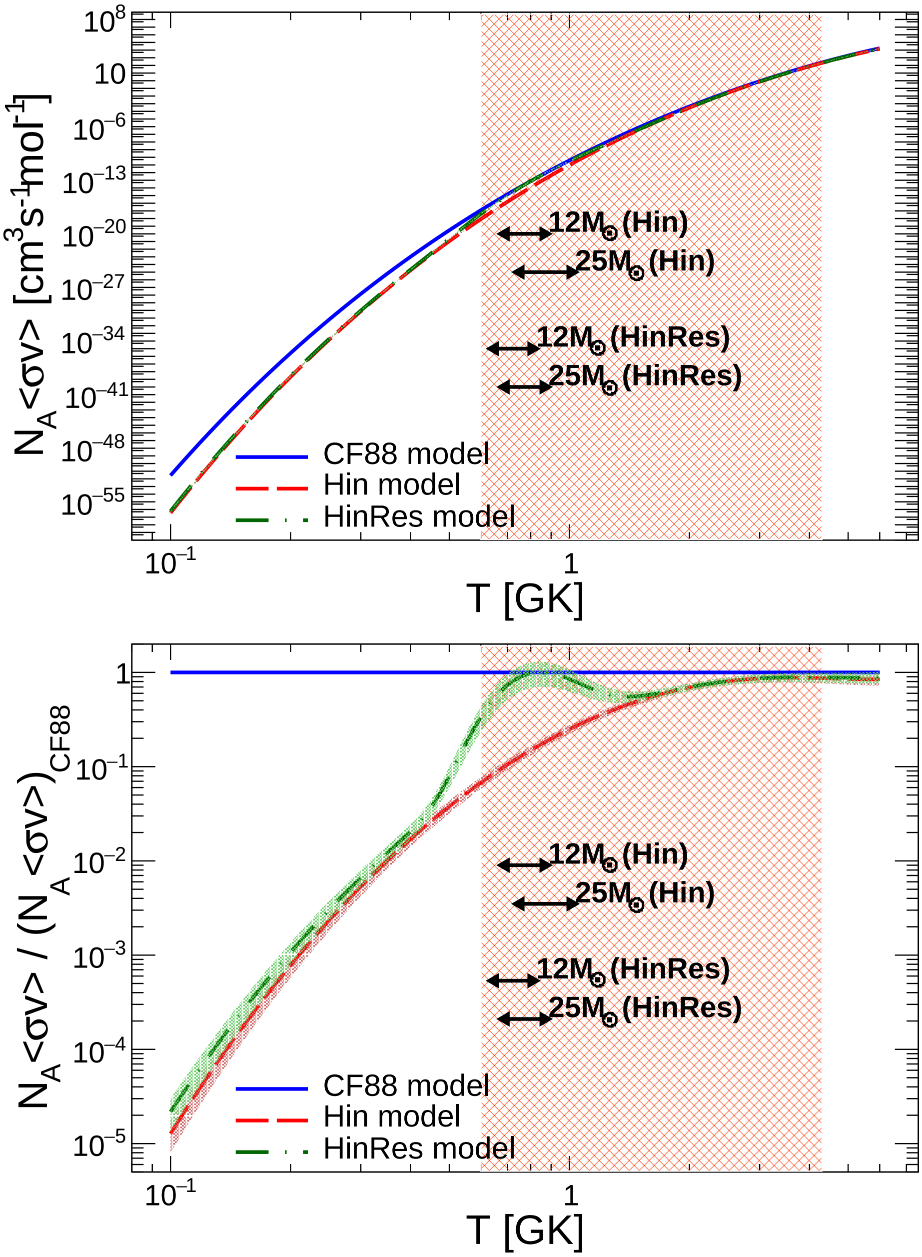

Figure 4.4: Reaction rates (top) and normalized reaction rates to $N_A\langle\sigma v\rangle)_{\mathrm{CF88}}$ (bottom), without (Hin; red curve) and with (HinRes; green curve) the added resonance [32]. The reaction rate from the CF88 model is also presented (blue curve). The shaded areas around the curves are the uncertainties (see text). Orange hatched areas show the temperature region explored by the STELLA experiment. The black arrows show the regions where carbon fusion occurs, for two stellar models (12 and 25 $M_\odot$), for both the Hin and HinRes models (see Fig. 4.5).

In the temperature range of $T = 0.6 - 4.3$ GK, the relative uncertainty of the fits for the Hin model is below 15% and only becomes 31% towards lower temperatures in the case of the HinRes trend due to the large uncertainties of the resonance parameters.

Recommended rates are based on a classical determination of the reaction rates using cross section extrapolation, and lower and upper rates represent the lower and upper limits of recommended rates, using their 1σ uncertainties. The latter comes from experimental uncertainties on cross sections measured by STELLA experiment [27]. Table 4.4 summarizes the values of the reaction rates between 0.11 and 6 GK.

Reaction rates have been fitted with a formula from [96], used in the REACLIB library:

$$\begin{aligned} N_A\langle\sigma v\rangle &= \sum_i \exp(a_{i0} + a_{i1}/T + a_{i2}/T^{1/3} + a_{i3}T^{1/3} \\ &\quad + a_{i4}T + a_{i5}T^{5/3} + a_{i6}\ln(T)), \end{aligned} \tag{4.8}$$

where a_i are fitting parameters and T is the temperature in GK. In the case of the Hin model, the best fit was obtained with $i = 1$, and for HinRes model with $i = 2$. The different parameters are reported in Tab. 4.5 and 4.6 for the Hin model and the HinRes model, respectively.

Table 4.4: Reaction rates for the $^{12}C + ^{12}C$ fusion reaction according to different models. Reaction rates are in $cm^3s^{-1}mol^{-1}$ and temperatures in GK. From [32].

T	Hin model			HinRes model		
	Recomm.	Lower	Upper	Recomm.	Lower	Upper
0.11	1.79E-54	1.15E-54	2.42E-54	2.94E-54	1.87E-54	4.00E-54
0.12	4.40E-52	2.89E-52	5.90E-52	7.02E-52	4.58E-52	9.46E-52
0.13	6.03E-50	4.05E-50	8.02E-50	9.39E-50	6.26E-50	1.25E-49
0.14	5.10E-48	3.48E-48	6.71E-48	7.75E-48	5.26E-48	1.02E-47
0.15	2.87E-46	1.99E-46	3.74E-46	4.27E-46	2.94E-46	5.60E-46
0.16	1.14E-44	8.03E-45	1.48E-44	1.67E-44	1.17E-44	2.17E-44
0.18	7.68E-42	5.54E-42	9.82E-42	1.08E-41	7.78E-42	1.39E-41
0.2	2.08E-39	1.53E-39	2.63E-39	2.86E-39	2.10E-39	3.62E-39
0.25	1.53E-34	1.17E-34	1.89E-34	1.98E-34	1.51E-34	2.45E-34
0.3	7.67E-31	6.05E-31	9.29E-31	9.54E-31	7.50E-31	1.16E-30
0.35	6.77E-28	5.45E-28	8.08E-28	8.16E-28	6.56E-28	9.77E-28
0.4	1.79E-25	1.47E-25	2.11E-25	2.16E-25	1.76E-25	2.57E-25
0.45	1.97E-23	1.64E-23	2.30E-23	2.77E-23	2.20E-23	3.34E-23
0.5	1.11E-21	9.37E-22	1.29E-21	2.34E-21	1.75E-21	2.92E-21
0.55	3.75E-20	3.18E-20	4.31E-20	1.27E-19	9.08E-20	1.63E-19
0.6	8.34E-19	7.15E-19	9.54E-19	4.13E-18	2.88E-18	5.38E-18
0.65	1.32E-17	1.14E-17	1.51E-17	8.30E-17	5.75E-17	1.09E-16
0.7	1.59E-16	1.38E-16	1.80E-16	1.11E-15	7.67E-16	1.45E-15
0.75	1.51E-15	1.32E-15	1.70E-15	1.06E-14	7.35E-15	1.39E-14
0.8	1.18E-14	1.03E-14	1.32E-14	7.70E-14	5.36E-14	1.00E-13
0.85	7.73E-14	6.81E-14	8.64E-14	4.46E-13	3.14E-13	5.79E-13
0.9	4.37E-13	3.87E-13	4.87E-13	2.15E-12	1.53E-12	2.77E-12
0.95	2.17E-12	1.93E-12	2.41E-12	8.93E-12	6.44E-12	1.14E-11
1	9.62E-12	8.57E-12	1.07E-11	3.28E-11	2.41E-11	4.15E-11
1.05	3.85E-11	3.44E-11	4.27E-11	1.09E-10	8.15E-11	1.36E-10
1.1	1.41E-10	1.26E-10	1.56E-10	3.34E-10	2.55E-10	4.12E-10
1.15	4.77E-10	4.27E-10	5.26E-10	9.58E-10	7.51E-10	1.16E-09
1.2	1.50E-09	1.34E-09	1.65E-09	2.61E-09	2.10E-09	3.13E-09
1.25	4.40E-09	3.96E-09	4.84E-09	6.81E-09	5.59E-09	8.03E-09
1.3	1.22E-08	1.10E-08	1.34E-08	1.71E-08	1.43E-08	1.99E-08
1.35	3.20E-08	2.88E-08	3.51E-08	4.14E-08	3.53E-08	4.76E-08
1.4	7.99E-08	7.21E-08	8.76E-08	9.72E-08	8.39E-08	1.11E-07
1.45	1.90E-07	1.72E-07	2.09E-07	2.21E-07	1.93E-07	2.49E-07
1.5	4.36E-07	3.94E-07	4.77E-07	4.87E-07	4.29E-07	5.45E-07
1.75	1.61E-05	1.46E-05	1.76E-05	1.65E-05	1.49E-05	1.82E-05
2	3.01E-04	2.72E-04	3.29E-04	3.02E-04	2.73E-04	3.31E-04
2.5	2.70E-02	2.44E-02	2.96E-02	2.70E-02	2.43E-02	2.96E-02
3	7.45E-01	6.69E-01	8.22E-01	7.48E-01	6.71E-01	8.25E-01
3.5	9.69E+00	8.63E+00	1.08E+01	9.79E+00	8.71E+00	1.09E+01
4	7.52E+01	6.65E+01	8.39E+01	7.65E+01	6.75E+01	8.54E+01
5	1.63E+03	1.42E+03	1.84E+03	1.68E+03	1.46E+03	1.90E+03
6	1.47E+04	1.26E+04	1.68E+04	1.54E+04	1.32E+04	1.77E+04

Table 4.5: Parameters for recommended, lower and upper reaction rates in the case of Hin model. From [32].

a_{ij}	Recomm.	Lower	Upper
a_{10}	7.72E+01	7.77E+01	7.68E+01
a_{11}	6.18E-02	6.39E-02	4.41E-02
a_{12}	-9.45E+01	-9.50E+01	-9.40E+01
a_{13}	-7.73E+00	-7.83E+00	-7.64E+00
a_{14}	-4.35E-01	-4.57E-01	-4.16E-01
a_{15}	3.11E-02	3.33E-02	2.88E-02
a_{16}	2.28E-01	1.64E-01	2.88E-01

Table 4.6: Parameters for recommended, lower and upper reaction rates in the case of HinRes model. From [32].

a_{ij}	Recomm.	Lower	Upper
a_{10}	7.63E+01	7.68E+01	7.58E+01
a_{11}	4.97E-02	5.12E-02	3.18E-02
a_{12}	-9.37E+01	-9.42E+01	-9.32E+01
a_{13}	-7.60E+00	-7.70E+00	-7.51E+00
a_{14}	-4.19E-01	-4.44E-01	-3.97E-01
a_{15}	2.97E-02	3.21E-02	2.72E-02
a_{16}	3.53E-01	2.95E-01	4.10E-01
a_{20}	3.42E-01	5.07E-01	-3.62E+00
a_{21}	-2.48E+01	-2.48E+01	-2.52E+01
a_{22}	3.25E-01	3.97E-01	3.94E+00
a_{23}	-3.65E-01	-3.32E-01	5.97E-02
a_{24}	1.64E-02	-7.59E-03	-1.45E-01
a_{25}	-7.65E-04	1.68E-03	1.23E-02
a_{26}	-1.29E+00	-1.24E+00	-4.16E-01

4.2 Impact on stellar evolution

4.2.1 Impact on global stellar evolution

The Geneva stellar evolution code, hereafter refered as GENEC, is a 1D simulation code used for the study of models of massive stars, and stars in different evolutionary stages. With about 50 000 lines, this code comes from the Göttingen code [97], and many optimisations have been made over the years. The version used here is described in Eggenberger *et al.* [55] and Ekström *et al.* [94].

A stellar model computes the evolution of the physical quantities at different positions (structure layers) inside the star as a function of time. In GENEC, the main variables are temperature, pressure, luminosity, radius, and chemical composition, while the independent variable is the mass coordinate. Other than the ^{12}C + ^{12}C reaction rates, the physics inputs used for the present study are the same as those described in [94].

Using GENEC, three sets of models have been computed using ^{12}C + ^{12}C reaction rates from [21] hereafter CF88, the Hin model, and the HinRes model. For each of these three sets, the evolution of a non-rotating 12 $M_\odot$ and 25 $M_\odot$ star at metallicity (the ratio between heavy elements abundances on hydrogen abundance) $Z = 0.014$ (solar) [60] has been computed until the end of the core C-burning phase. For a given initial mass, all the models evolve similary until the end of He-burning.

Figure 4.5 shows the evolution of central temperature during the C-burning phase as a function of the central ^{12}C abundance for both 12 $M_\odot$ and 25 $M_\odot$ stars. The Hin model is represented in red, the HinRest model in blue and the CF88 model in black.

The Hin model, the one with a lower rate, burns carbon at a slightly higher central temperature (the relative increase is about 10%). A lower rate implies less energy released per unit time. On the other hand, the energy lost per unit time at the surface of the star is not directly linked to nuclear reactions, but by the hydrostatic and radiative equilibrium. To compensate for these losses at the surface when the nuclear energy production is less efficient, the core contracts in order to achieve a new hydrostatic or radiative equilibrium. The contraction increases the central temperature and the nuclear reaction rate and, hence, the energy released per unit time. We note that since the dependence of the nuclear reactions on temperature is very high for the carbon fusion reaction (typically the rates depend on T^{27}), a moderate increase, 10% in the current case, is sufficient to restore the equilibrium. A similar effect is described in [15].

The situation with the HinRes model is not much different from the case with a CF88 rate. The resonance decreases the maximum temperature where the hindrance effect would be non-negligible and, as seen in Fig. 4.4, the rate at the peak of the resonance is of the order of the CF88 rates. We see here that at stellar conditions during C-burning, the central temperature is in a range where the contribution of the resonance is effective. The hotter medium for the 25 $M_\odot$ model shows even fewer differences than the 12 $M_\odot$ one between the CF88 rates and the HinRes rates.

The evolution of central conditions is shown in the temperature over density diagram in Fig. 4.6. The core C-burning phase occurs when the bump occurs along the tracks that is around 0.8 GK (Log $T = 8.9$). The bump in the 12 $M_\odot$ track is particularly well developed. This results from the fact that carbon-ignition occurs in a medium mildly degenerated (the grey straight line gives the positions in the plane where the perfect gas pressure is equal to the non-relativistic electronic degenerate pressure).

As seen in Fig. 4.6, the Hin model shows bumps that are shifted to slightly higher densities and temperatures with respect to the other models. This results from the fact that these models have more compact cores during the C-burning phase.

For comparison, the 25 $M_\odot$ model using the 'lower limit' from [15] is superimposed in green. This model uses rates close to our HinRes one and consistently follow a very similar path as the HinRes model.

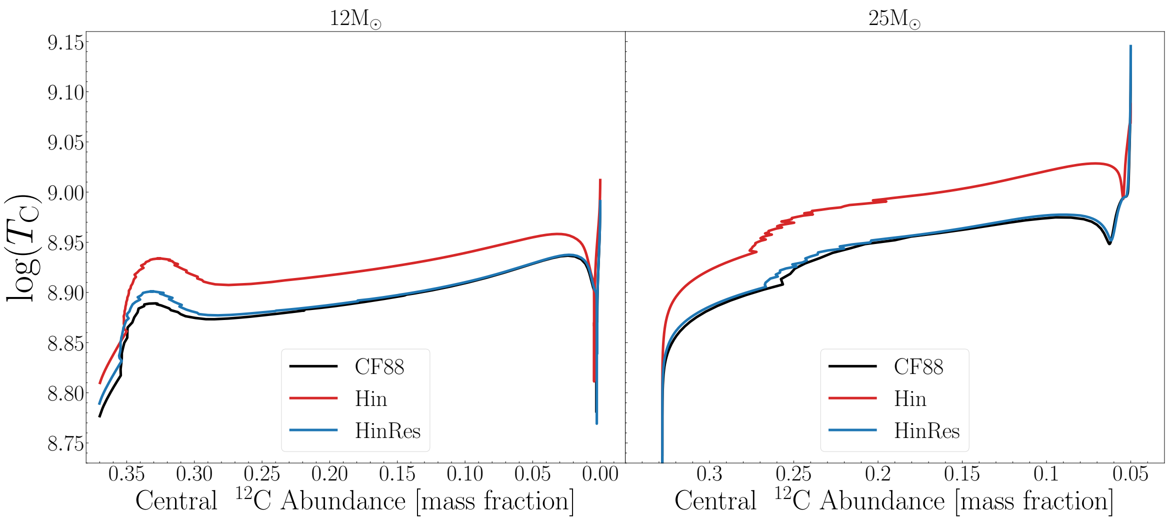

Figure 4.5: Central temperature evolution during the C-burning phase for 12 $M_{\odot}$ and 25 $M_{\odot}$ models with different $^{12}C + ^{12}C$ reaction rates. The evolution is given as a function of the mass fraction of carbon at the centre that decreases as a function of time. From [32].

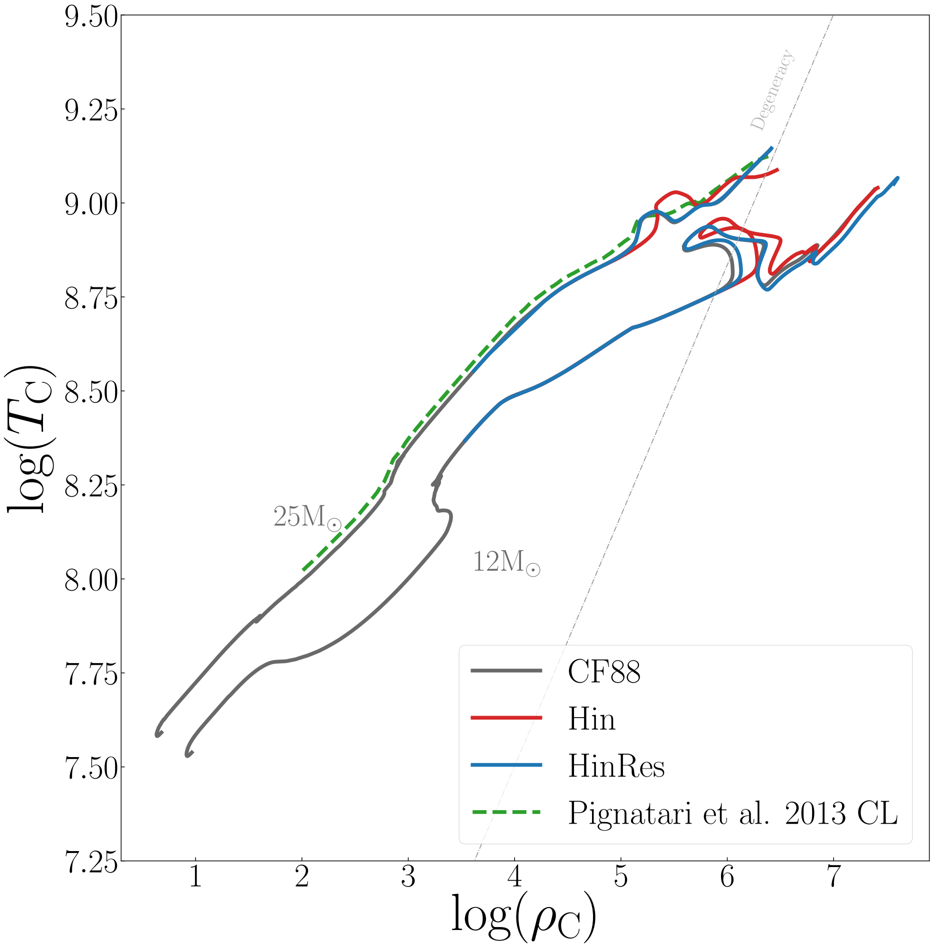

Figure 4.6: Evolution of central temperature as a function of central density for 12 $M_{\odot}$ and 25 $M_{\odot}$ models with different $^{12}C + ^{12}C$ reaction rates. From [32].

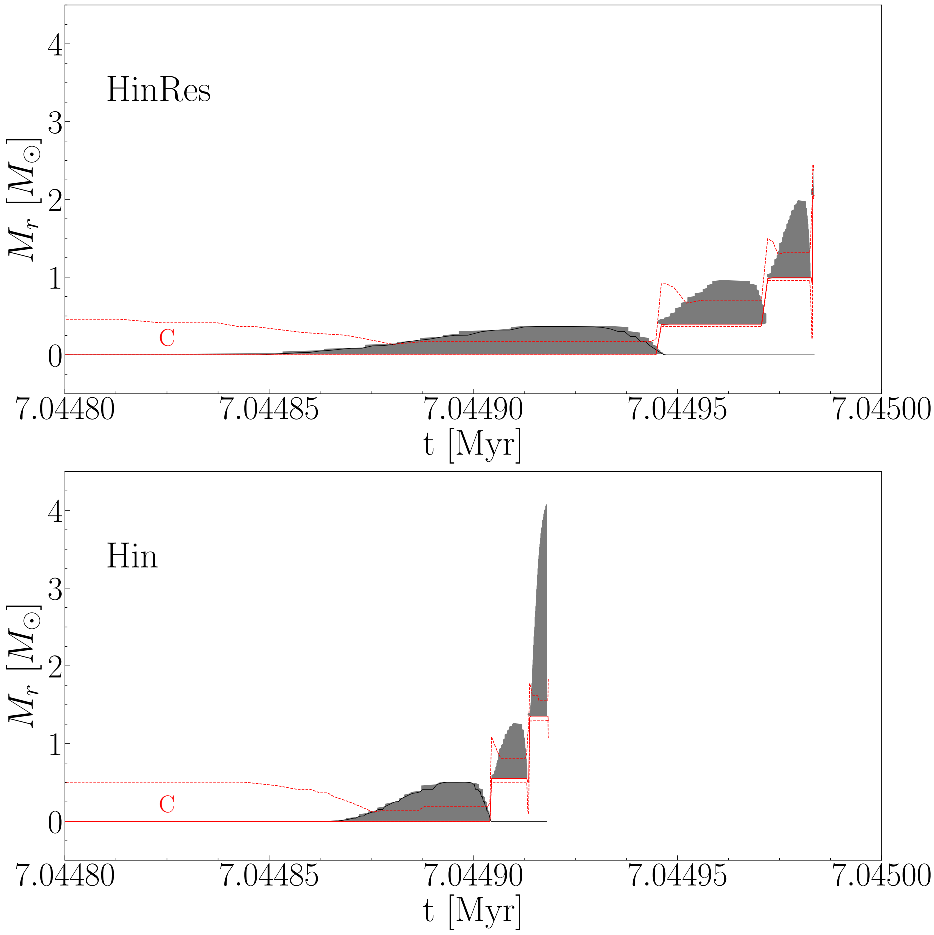

Figure 4.7: Kippenhahn diagrams for the centre of 25 $M_\odot$ models during the end of C-burning phase with Hin (top) and HinRes (bottom) $^{12}C + ^{12}C$ reaction rates. The grey shaded area shows the convective zones. The red dashed line shows the limits of the C-burning zones (defined where $\epsilon_C \geq 10^2$erg g^{-1}s^{-1}). From [32].

Figure 4.7 shows the Kippenhahn diagrams during the end of C-burning for the 25 $M_\odot$ models. The C-burning region (red, dashed lines) evolves in the same way for the different reaction rates. However, the convective zones developing in the inner regions of the star at the end of C-burning are quite different for the Hin model. Indeed, the convective zone, fueled by shell C-burning, extends much further away in the Hin model (see lower panel) compared to the HinRes model (upper panel). This effect is not present in the 12 $M_\odot$ models, hence, their Kippenhahn diagrams are not shown here. The largest convective zones in 25 $M_\odot$ the Hin model are due to the fact that, as already mentioned above, C-burning occurs at higher temperatures due to the lower nuclear energy generation rate in this temperature range. A stronger temperature gradient builds up that favors the occurrence of a larger convective zone.

The situation in the 12 $M_\odot$ model is different due to the fact that it is in a medium that is more affected by degeneracy.

In Fig. 4.8, the abundance profiles of the 12 $M_\odot$ and 25 $M_\odot$ models for different ^{12}C + ^{12}C reaction rates obtained at the end of the core C-burning phase (*i.e.* the last model before the central carbon abundance is lower than 10^{-5}) are compared. In the top panel, only the central region until $M_R = 1.75\ M_\odot$ are shown for the 12 $M_\odot$ model, beyond this region in outward direction, the models present no differences. In the bottom panel, like in the previous case, the central region until $M_R = 8\ M_\odot$ is shown for the 25 $M_\odot$.

The chemical structure at the end of the C-burning is not much affected by the changes of the rates in the 12 $M_\odot$ model with only slight differences between. The mass coordinate at which the carbon abundance changes abruptly (around 1.44 $M_\odot$) shifts outwards by about 0.1 $M_\odot$ passing from the Hin model to the CF88 model and by another 0.1 $M_\odot$ passing from the CF88 to the HinRes model. This abrupt change in abundance is due to presence of a convective C-burning shell.

These differences, although non-negligible, are not very significant when considering other uncertainties linked to the treatment of convection in stellar models [98; 99].

In the bottom panel in Fig. 4.8, a difference in the position of the sharp change of the carbon abundance in the 25 $M_\odot$ models depends on the rates used. For the Hin model, the step occurs at about 4 $M_\odot$ while for the CF88 and HinRes model, the step occurs around 2 $M_\odot$. Here, in the Hin model, the step is shifted outwards with respect to the other two models, while, as written above, it was shifted inwards in the 12 $M_\odot$. This difference between the 12 and the 25 $M_\odot$ models comes from the extension of the convective C-burning shell, which is slightly more extended for the CF88 and HinRes models in the 12 $M_\odot$ than the Hin one, while it is largely extended in the 25 $M_\odot$ Hin model compared to the CF88 and HinRes ones. Indeed, the size of the convective regions strongly impacts the chemical structure by imposing flat chemical gradients in them. The shift outwards beyond the sharp carbon abundance step in the 25 $M_\odot$ Hin model is linked to the extension of the last intermediate convective zone that can be seen in the bottom panel of Fig. 4.7. This convective shell indeed extends up to around 4 $M_\odot$, while its maximum extension in the HinRes model is limited to around 2 $M_\odot$ (see the upper panel of Fig. 4.7).

These two different behaviours for the 12 and 25 $M_\odot$ models illustrate the complex non-linear behaviour of the stars whose evolution results from many tightly interlinked processes.

It seems interesting to ask whether these differences of the chemical structure at the interior have an impact on the total quantity of an element in the star's outer envelope. At the end of the C-burning phase, the envelope has nearly reached its final chemical composition, because the subsequent burning phases will occur in regions well below this envelope and the time that remains before the explosion is short on stellar scales, that any changes have no time to be become significant in the envelope. Moreover, the explosive nucleosynthesis will affect mainly those layers near the core and the abundances of elements around the iron peak. Thus, it makes sense to look at the abundances of light elements in the outer layers, that is, in the layers that can be possibly ejected at the time of the supernova, and to evaluate changes depending on the rates used.

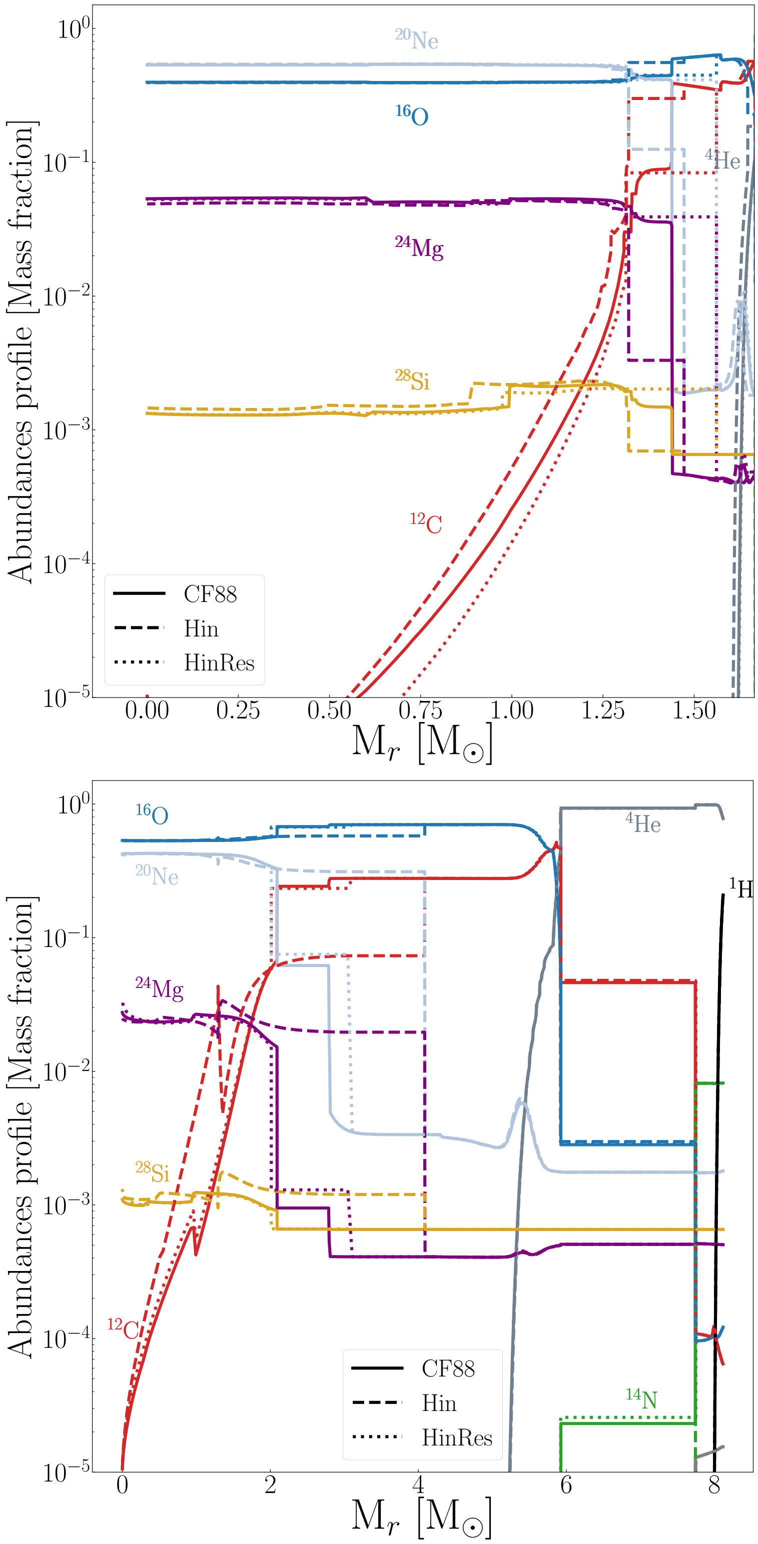

Figure 4.8: Top: Core abundance profile at the end of central C-burning for $12M_\odot$ models with different $^{12}C + {}^{12}C$ reaction rates. Bottom: Abundances profile at the end of C-burning for $25M_\odot$ models with different $^{12}C + {}^{12}C$ reaction rates. From [32].

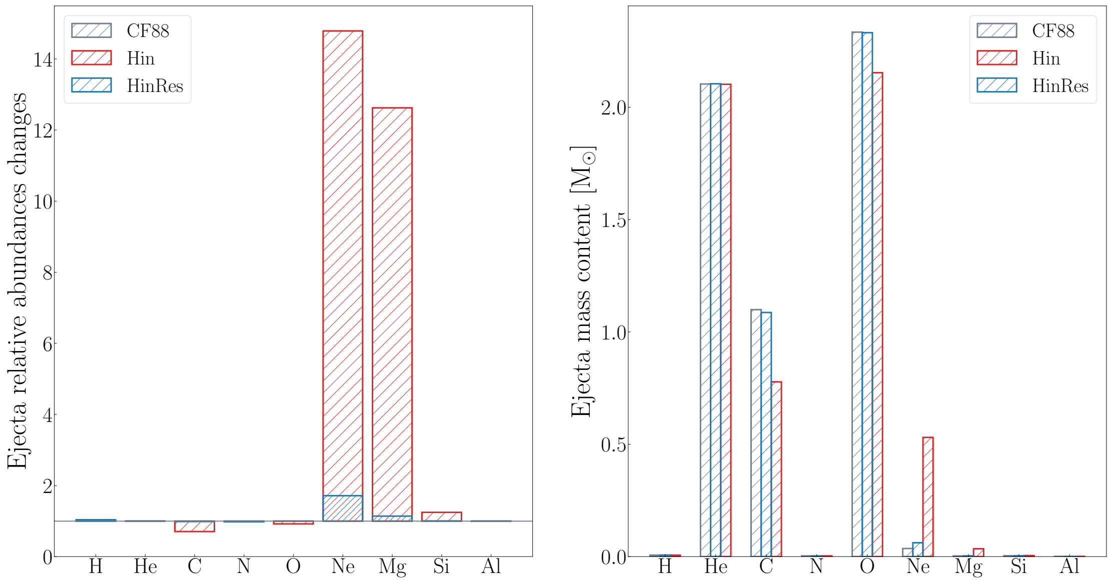

Figure 4.9: Left: Abundances relative to CF88 models in the supernova ejecta of the 25 $M_\odot$ models for different ^{12}C + ^{12}C reaction rates, based on the structure obtained at the end of the C-burning phase. Right: The same abundances but for the total mass content in the ejecta. From [32].

In Fig. 4.9, preliminary estimations on the chemical composition in the expected supernova-ejecta of our different models are compared. The structure of the envelope obtained at the end of C-burning is used as a proxy for its structure at the pre-supernova stage [100]. The CO-core masses of those models (5.9 $M_\odot$) being almost equal (less than 0.1% of difference), a common remnant mass of 2.4 $M_\odot$ is deduced from the relation between CO-core and the remnant mass given in [100]. The quantities of various isotopes present in all the layers above the remnant mass was computed with the resulting abundances displayed in Fig. 4.9. In the left panel, elements most affected are those which are the main products of C-burning, *i.e.* ^{20}Ne and ^{24}Mg. Their abundances are boosted in the Hin and HinRes models. This is likely the result of two effects: the first is due to the duration of the C-burning phase. It is slightly reduced in the HinRes model and significantly reduced in the Hin models, offering less time for these two elements to be destroyed by α captures (*i.e.* by the reactions ^{20}Ne(α,γ)^{24}Mg(α,p)^{27}Al). The second effect can be due to the transport of ^{20}Ne and ^{24}Mg to cooler regions by the extendted convection in the Hin model, where they cannot be destroyed.

Table 4.7 shows the central C-burning lifetimes, defined from the duration when 1% of central ^{12}C abundance has been burnt up to the central ^{12}C abundance reaching value lower than 10^{-5}. The C-burning lifetimes are very similar between models with the CF88 rates and models using the HinRes reaction rates. Using solely the Hin reaction rates halves the lifetimes in comparison to the other models, due to the higher central temperature regime.

Interestingly the authors in [101] using rates that are much higher than those of

Table 4.7: Central C-burning lifetime for different $^{12}C + ^{12}C$ reaction rates. From [32].

$^{12}C + ^{12}C$	CF88	Hin	HinRes
$12M_{\odot}$	7604 yrs	3856 yrs	6698 yrs
$25M_{\odot}$	820 yrs	403 yrs	717 yrs

CF88 in the $0.1 - 1$ GK range, find that C-burning occurs at lower densities. Indeed, since the nuclear rates are higher, a lower density is sufficient to reach the required amount of nuclear energy to counteract the contraction post He-burning. This means that the beginning of C-burning is in fact happening earlier after the end of He-burning. This leads to a C-burning lifetime longer than the ones obtained with the CF88 rates. This behaviour is consistent with that seen in Fig. 4.6, where lower reaction rates led to reaching larger densities to burn carbon, and hence a smaller C-burning lifetime.

It is a well-known fact that the C-burning phase is the longest phase of the evolution of massive stars when significant neutrino emissions occur [102; 103]. In Fig. 4.10, it can be seen that in the central regions of the 25 $M_{\odot}$ model at the middle of the C-burning phase, the energy evacuated through neutrino emissions is nearly always superior to that produced by nuclear burning. Thus, in that phase, the evolution of the stellar core is driven mainly by neutrino emissions. The total quantity of entropy lost by the central region during the whole C-burning phase depends on the product of the time-averaged rate of neutrino emission during that phase and its duration. In the Hin model, the duration is shortened, but on the other hand the entropy at the end of that phase depends also on the energy balance. In fact, the core in the Hin model loses more energy through neutrino emission than in the CF88 and HinRes models.

It can moreover be noticed in Fig. 4.6, that the Hin model crosses more rapidly the degeneracy limit than the other models, implying that it has lost more entropy than the other models during the C-burning phase and thus becomes sensitive to degeneracy effects at earlier stages. This may have important consequences for the ultimate fate of the star, the consequence of core collapse and the nature of the stellar remnant [103].

In conclusion, the difference between the reaction rates do not lead to major variation in the different stellar sets explored. The evolution of a star is mainly governed by gravity, which tends to contract the central regions. The contraction is stopped during the main nuclear phases, because the energy output of the nuclear reactions allows the pressure gradients to be maintained for long times. During the nuclear burning phases, the nuclear energy released per unit time and mass does not change much. Indeed, any decrease implies a contraction, thus an increase of the temperature (equation of state of an ideal gas) and thus an increase of the energy released by nuclear reactions. *Vice-versa*, an excess of energy produced by nuclear reactions causes an expansion, a cooling and thus a decrease of the nuclear reaction rate. Hence, at order zero, when a nuclear reaction rate important for the production of energy is changed, the energy released remains constant while the temperature changes. Of course, these temperature changes alter the structure of the star and numerical models are needed to deduce the

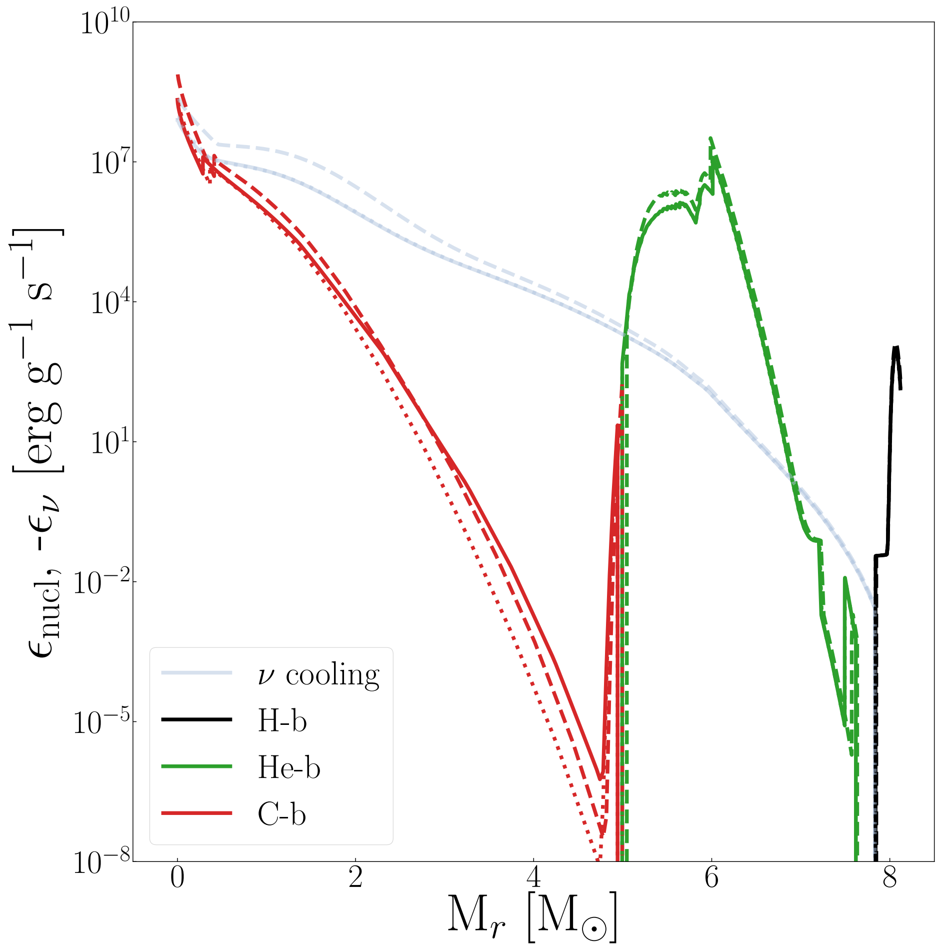

Figure 4.10: Energy production at the mid-point of C-burning (when half the central ^{12}C has been consumed since the beginning of C-burning) for 25 $M_\odot$ models for different ^{12}C + ^{12}C reaction rates. The CF88, Hin and HinRes models are plotted in solid, dashed, and dotted lines, respectively. From [32].

detailed composition. However, because nuclear reaction rates are very sensitive to very small change of the temperature, only a minor change of the temperature needs to occur to compensate for a given change of the rate. This reasoning allows one to understand why even significant change in a nuclear reaction rate may have only modest effect on the stellar structure.

The study of stellar models with GENEC and using the new reaction rates has been continued in Dumont *et al.* [34]. A grid of massive stars ranging from 8 to 30 $M_\odot$ at solar metallicity was computed. The results were explored using the same three different references for the rates, with or without rotation. The effect in terms of evolution, structure, and the critical mass limit between intermediate and massive stars was studied.

The impact of utilizing recent nuclear reaction rates, in accordance with the fusion hindrance hypothesis at deep sub-barrier energies, has been confirmed. Additionally, the mass-dependent effect of a resonance at 2.14 MeV with predominant feeding of the α exit channel of the ^{12}C + ^{12}C fusion reaction has been observed. These factors influence the characteristics of the stellar core from C-ignition throughout the core C-burning phase, including temperature, density, lifetime, size, and core convective/radiative properties. The alteration of nuclear reaction rates modifies the central nucleosynthesis of stars during the core-carbon burning phase, resulting in an underproduction of s-process elements, particularly when considering rotation-induced mixing, which exacerbates these effects, and will be discussed next.

4.2.2 Impact on detailed nucleosynthesis

In this section, the impact of changes in carbon fusion rates on the detailed composition resulting from C-burning is discussed. For this purpose, a 'one-layer model' [56] was employed. The evolution of abundances within a single layer was computed, allowing for the use of a much more extensive nuclear reaction network.

The nuclear reaction network in the 'one-layer model' tracked the evolution of the abundances of 1454 isotopes. An initial distribution of abundances, (*i.e.* the abundances at the onset of the core C-burning phase), and an evolutionary path in the temperature and density plane representative of the core C-burning phase in a star obtained with GENEC were taken as input.

These input are taken from the CF88 25 $M_\odot$ stellar model computed for this study. It should be noted that employing the 1454-nuclei network integrated in the construction of stellar models is possible. However, is this study this has not been choose, the purpose being here to obtain a first picture of the impact of the new reaction rate on stellar nucleosynthesis. The stellar models presented here were computed using a reduced nuclear reaction network that encompassed all reactions producing significant energy. Such reduced networks are adequate for computing reliable stellar structures. However, they may overlook reactions that are not energetically significant but have an impact on the abundances of certain elements. This is what was investigated here using a 'one-layer model'.

Three different 'one-layer models' are computed. The first one uses the CF88 rates for the reactions ^{12}C(^{12}C,α)^{20}Ne, ^{12}C(^{12}C,p)^{23}Na, and ^{12}C(^{12}C,n)^{23}Mg. The sec-

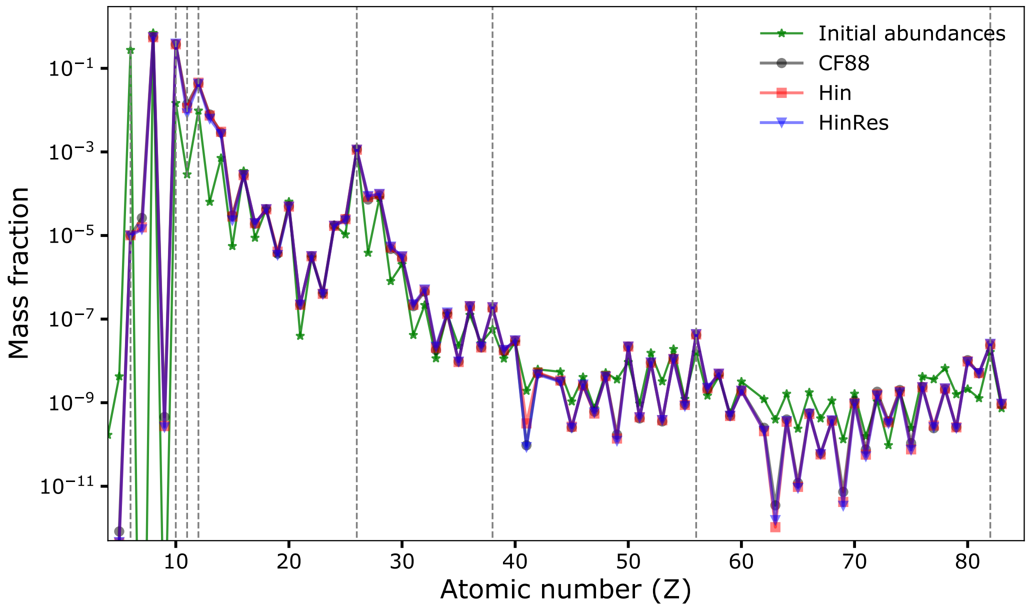

Figure 4.11: Comparisons between the abundances before (green) and at the end of the core C-burning phase (black, red and blue) obtained with three different sets of rates for the ^{12}C + ^{12}C reactions. The dashed vertical lines highlight from left to right the carbon ($Z = 6$), neon ($Z = 10$), sodium ($Z = 11$), magnesium ($Z = 12$), iron ($Z = 26$), strontium ($Z = 38$), barium ($Z = 56$), and lead ($Z = 82$). From [32].

ond and third models use rates from Hin model and HinRes model respectively for ^{12}C(^{12}C,α)^{20}Ne and ^{12}C(^{12}C,p)^{23}Na, and we use the recent experimental rates from Bucher *et al.* [65] for ^{12}C(^{12}C,n)^{23}Mg.

Figure 4.11 shows the mass fraction of the elements up to bismuth ($Z = 83$) at the beginning of the C-burning phase, see the green pattern, and at the end of it using CF88, Hin, and HinRes rates in black, red and blue, respectively. The comparison between the green and red, black and blue lines shows the impact of the C-burning.

As anticipated, it is observed that the two elements primarily produced by carbon burning are ^{20}Ne and ^{24}Mg; ^{23}Na is also generated during this phase, although as mentioned in the Sect. 1.1.3, most of it is transformed into ^{20}Ne. Interestingly, a slight enhancement in strontium ($Z = 38$) is observed during the C-burning phase. Strontium is formed through slow neutron capture, with the neutrons being released by the ^{13}C(α, n)^{16}O reaction and other minor source reactions [15]. Barium ($Z = 56$) and lead ($Z = 82$), also produced through neutron capture, show a slight enrichment as well.

When comparing the final abundances obtained with the different rates for the ^{12}C + ^{12}C reaction, it is observed that the overall changes remain quite modest and are scarcely discernible in Fig. 4.11.

Figure 4.12 represents the abundances normalised to the final abundances obtained using the CF88 rate. Only the elements with a significant mass fraction ($> 10^{-8}$) are shown. The final abundances obtained with the Hin rate exhibit less scatter normalized to the CF88 rate than the abundances obtained with the HinRes rate. The variations between the abundances obtained with the different rates never exceed a factor of 2. Above phosphorus (P), the most substantial differences are approximately 20% for Co and As.

To provide a more detailed analysis, it's important to note that, as expected, since situation after C-burning is considered, there are, by construction, no differences in carbon abundances. Other abundant α-nuclei such as ^{16}O, ^{20}Ne, and ^{24}Mg are modestly influenced in this 'one-layer' model. The most significant differences arise for N and Na. However, the N mass fraction is very small, $\sim 10^{-5}$, whereas the Na mass fraction is approximately ~ 0.1. Al and P also exhibit some variations. Notably, these differences are more pronounced for Al, which has a mass fraction of about 0.01 (while the P mass fraction is only around 10^{-5}). Overall, these 'one-layer' computations demonstrate that the most affected abundant element due to a change in the carbon fusion rate is ^{23}Na. For the high Z elements, the different rates do not significantly impact their abundances at the end of the C-burning phase.

The abundance differences obtained in Fig. 4.12 are too small to have an impact on the evolution and structure of the star during the last evolutionary stages. The nucleosynthesis may nevertheless be impacted: a different Na abundance after the end of core C-burning impacts the production of ^{26}Mg through ^{23}Na(α,p)^{26}Mg [104; 105]. The protons given by this reaction also increases the production of ^{26}Al through ^{25}Mg(p,γ)^{26}Al [35].

Within the 'one-layer model' similar C-burning lifetimes are obtained from the CF88 and the HinRes model, 0.31 and 0.37 kyrs respectively, due to comparable reaction rates within this temperature range. In contrast, the Hin model exhibits a lifetime approximately eight times longer than the CF88 model. This discrepancy arises from the absence of resonance in the Hin model, which reduces the ^{12}C + ^{12}C rate by roughly 1 dex at 0.8 GK (see Fig. 4.4). Consequently, more time is required for carbon burning. This outcome contrasts with stellar models with GENEC, where employing the Hin rate results in a shorter C-burning lifetime. The discrepancy stems from the fact that, in the 'one-layer model', there is no feedback between the energy generated by nuclear reactions and the path followed in the temperature and density plane. Regardless of the rate used, the path remains unchanged. Thus, the model with the lower rate simply requires more time to consume the carbon.

In [33], it can be note that in the GENEC simulations, the results of CF88 and HinRes are very similar as can be expected from comparable reaction rates at the temperatures during carbon burning (see Fig. 4.4). In contrary, the abundances from the 'one-layer model' of CF88 and Hin are closer, presenting a somewhat different situation. As the CF88 and HinRes rates are comparable with identical temperature trajectories during this run, the reasoning might be the branching with α and proton emission, that was adapted to the experimental findings given in Tab. 4.2 in the 'one-layer model', but could only be accounted for indirectly in the GENEC package [106].

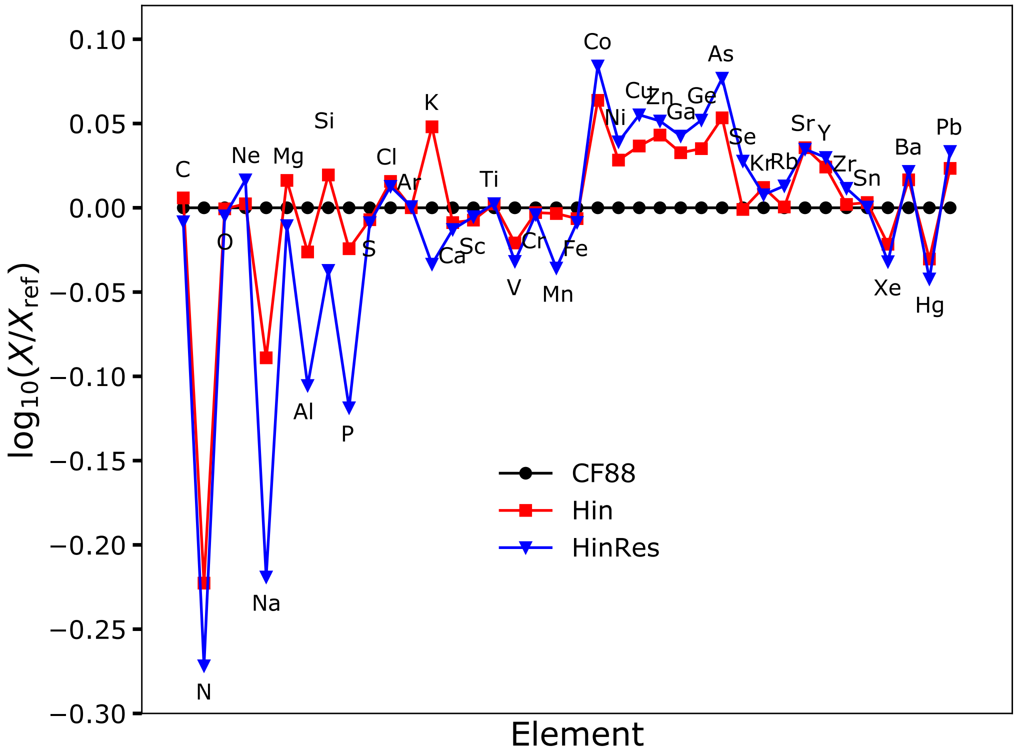

Figure 4.12: Abundances obtained at the end of the C-burning phase normalised to the final abundances obtained using the CF88 rate. Only the elements with a mass fraction greater than 10^{-8} (in either the first or second model) are considered. From [32].

Indeed, the branching during carbon burning from the 'one-layer model' given in Fig. 4.13, indicates a situation where the CF88 and Hin (is 0.65/0.35 [42]) are closer to each other than HinRes. The latter is given by the ratio of strengths of the resonance at $E_{\mathrm{com}} = 2.14$ MeV in the carbon-carbon system where α emission is dominating. This difference in strength of the resonance in α and proton channels has been discussed by Pignatari *et al.* [15]. However, the results need to be taken with care as the temperature trajectories need to be adapted to the actual hydrodynamics constraints in CF88, Hin and HinRes separately and different paths of nucleosynthesis might open with more realistic assumptions.

In conclusion, such a finding can demonstrate the sensitivity to resonances in the branching of reaction rates for key reactions during nucleosynthesis calculations where straight factorizing of entire energy regions might yield only approximate results.

In Dumont *et al.* [34], the impact of the evolutionary path choice on the nucleosynthesis has been studied with the 'one-layer model'. For each rate, the corresponding path choice have been extracted from the GENEC stellar models, and implemented in the 'one-layer model'. Results can be seen in Fig. 4.14.

When using consistent paths the Hin and HinRes models predict a smaller abundance of Na than the CF88 model. This is not the case for the Hin model using CF88 path, which is similar to CF88 model results. The other main product of C-burning,

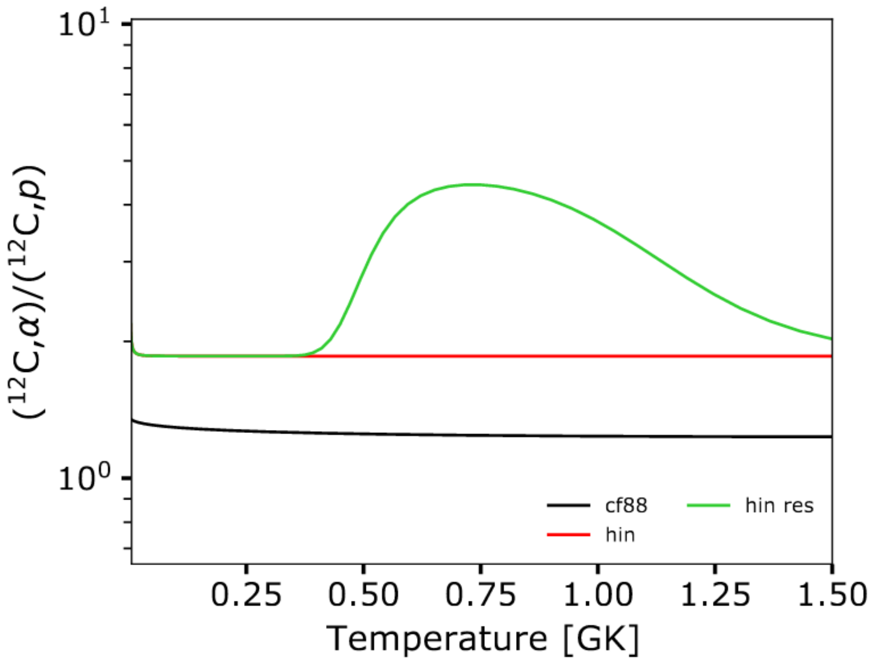

Figure 4.13: Ratio of the reaction channels in the valid temperature range for carbon burning for CF88, the Hin and HinRes in the One-Layer code. From [33].

Ne and Mg, are almost not affected in every case.

For the heavy elements, in both cases there is a modest production of s-elements in all models. This production is similar for the three models when using the CF88 paths, whereas notable differences are observed if using the dedicated paths: the production is higher in CF88 model, followed by the HinRes and then the Hin models. This reduces the efficiency of the s-process in the latter. This effect can be explained by the difference in neutron exposure in each of the models. Indeed, the C-burning lifetime of the CF88, Hin and HinRes models are 1480, 740 and 1450 yrs, respectively, with total neutron exposure of 0.19, 0.13 and 0.16 mbarn^{-1}. Therefore, the longest the C-burning lifetime, the highest the neutron exposure, and hence the greater the number of s-elements produced.

It is then possible to conclude that using the consistent path for computing the nucleosynthesis has a non-negligible impact.

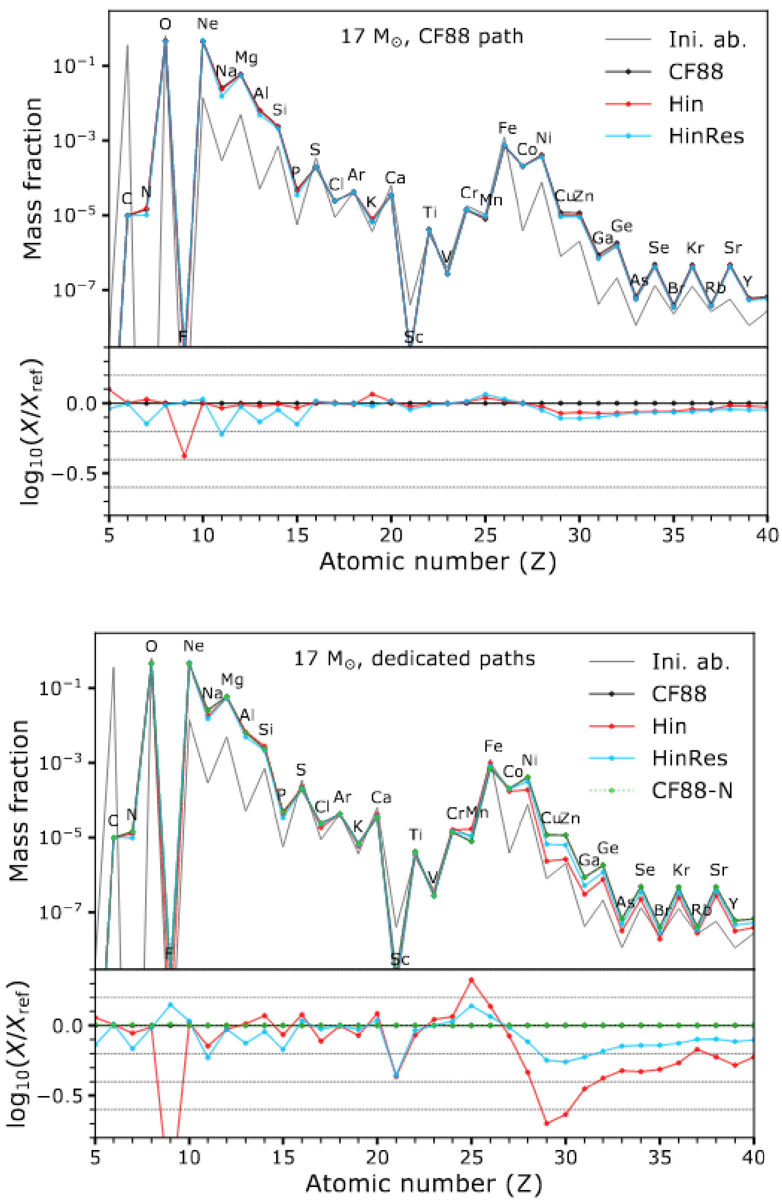

Figure 4.14: Mass fractions at the end of the core C-burning phase of a 17 $M_\odot$ star. The grey line refers to the initial abundances, extracted from the CF88 GENEC model at core C-ignition. The bottom panels show the abundances normalised to the ones of the CF88 model. Top: nucleosynthesis using the same (ρ, T) path from CF88 model. Bottom: nucleosynthesis using the consistent (ρ, T) paths from each GENEC model. From [34].

4.3 Résumé du chapitre

Le taux de réaction nucléaire est une grandeur à la fois nucléaire et astrophysique, qui permet comme aucune autre de lier ces deux disciplines. La calculer et étudier ses impacts sur l'évolution stellaire est dans la continuité logique de la détermination de sections efficaces aux énergies d'intérêt astrophysique. Afin de déterminer des taux de réactions à partir des données de STELLA, deux fonctions d'excitations, suivant chacune un scénario différent, ont été considérées. Les impacts de ses nouveaux taux ont ensuite été étudiés à l'aide de deux codes d'évolution stellaire, l'un permettant une vue d'ensemble sur l'étoile, et l'autre se concentrant sur la nucléosynthèse stellaire.

4.3.1 Détermination des taux de réactions pour $^{12}C + {}^{12}C$

Le calcul de taux de réaction commence par la détermination de fonction d'excitation à partir de section efficace mesurée. Pour cela, deux scénarios ont été considérés : le modèle Hin et le modèle HinRes.

Le modèle Hin est basé sur le modèle empirique de suppression de la fusion. Il décrit le comportement global de la section efficace, sans les potentielles fluctuations locales. La fonction d'excitation a été obtenue en ajustant les données expérimentales de STELLA [27] avec le modèle phénoménologique [17]. Durant cet ajustement aucun paramètre n'a été contraint. La formule décrivant la section efficace totale, elle a été corrigée par les rapport d'embranchements communément utilisés entre les voies α et protons [15].

Le modèle HinRes correspond au modèle Hin sur lequel une résonance à E = 2.14 MeV [24] a été ajoutée. Les paramètres de la résonance ont été maintenus fixes durant l'ajustement afin de tester la comptabilité de celle-ci avec les données de STELLA.

Les sections efficaces obtenues sont visibles sur la Fig. 4.1. Les mesures de STELLA sont en bon accord avec la résonance, en permettant l'inclusion d'un point expérimental. Il est important de noter que pour les énergies voisine de la barrière de Coulomb les deux modèles sont similaires, mais divergent aux plus basses énergies. Dans la région d'intérêt astrophysique, c'est-à-dire aux alentours de $E_{\text{eff}} = 1.5$ MeV, il est possible de remarquer que les extrapolations des modèles Hin et CF88 suivent la même tendance, contrairement au modèle HinRes. Cependant, l'absence de données expérimentales à ces énergies ne permet aucune contrainte des modèles. La présence de plusieurs résonances y a été prédite, mais sans aucune confirmation par mesure directe.

Afin de s'assurer de la pertinence des données mesurées par STELLA pours études d'intérêt astrophysique, la sensibilité de STELLA a été déterminée. Celle-ci peut être définie comme l'intervalle en température sondée par l'expérience STELLA, où aucune extrapolation de la section efficace n'est requise pour le calcul de taux de réaction.

L'énergie minimale sondée par STELLA est de $E_{\text{rel}} = 2.03$ MeV [27]. En utilisant la définition de la fenêtre de Gamow, il est possible d'identifier l'énergie minimale mesurée à l'énergie de Gamow liée à une température. Ainsi, pour $E_0 = 2.03$ MeV on obtient une température de $T = 0.77$ GK, comme montré sur la Fig. 4.2.

La limite basse de la sensibilité de STELLA a été définie comme étant la limite inférieure de l'incertitude à 1σ de l'énergie de Gamow. Pour cela, le pic de Gamow a été ajusté avec une fonction gaussienne, et la pertinence de cet ajustement a été testé *via* la comparaison de différentes grandeurs, visible Fig.4.3. Les résultats obtenus valident cette hypothèse et la limite inférieure à la sensibilité de STELLA a été déterminée à $T = 0.6$ GK.

Suite à cela les taux de réactions ont été déterminés pour les modèles Hin et HinRes.

Pour le modèle Hin, la formule utilisée est celle généralement utilisée pour ce calcul, servant à déterminer un taux de réaction issu d'une fonction d'excitation ne présentant pas de structure locale. Elle a été comparée avec une formule simplifiée décrivant les taux de réaction non-résonant [18], mais les deux formules présentées des résultats similaires, ne favorisant aucune des deux méthodes.

Le modèle HinRes est basée sur la même formule, mais auquel il est nécessaire d'ajouter un second taux de réaction dérivant de la résonance.

Les taux de réactions obtenus sont visibles sur les Fig. 4.3. La zone orangée représente la zone de sensibilité de STELLA, et les flèches noires indiquent les températures auxquelles les modèles stellaires décrits sont dans leur phase de combustion du carbone. Ces zones étant dans la zone de sensibilité de STELLA, il est possible de conclure de la pertinence de cette expérience à des intérêt astrophysiques.

Le taux Hin est inférieur au taux CF88 aux basses températures, mais similaires aux hautes températures, ce qui concorde avec de précédentes études [17]. L'impact de la résonance est visible sur le taux à HinRes à deux endroits : le taux est légèrement supérieur à basse température, et il est augmenté à des températures $T = 0.5-1.5$ GK, correspondant à la phase de combustion du carbone des étoiles massives.

Finalement, les incertitudes des taux de réactions dans la zone de sensibilité de STELLA sont de 15% pour le modèle Hin et 31% pour le modèle HinRes.

4.3.2 Impacts sur l'évolution stellaire

L'étude des impacts sur l'évolution stellaire des nouveaux taux de réactions a été commencé avec l'utilisation du GENEC, pour Geneva stellar evolution code. Ce code est une simulation 1D utilisée pour l'étude des modèles d'étoiles massives, et d'étoiles dans différentes phases évolutives [55; 94]. Avec le GENEC, trois taux de réactions int comparer : le taux Hin, le taux HinRes et le taux CF88. Pour chacun de ces taux, deux modèles stellaires ont été suivis, l'un de 12 et l'autre de 25 $M_\odot$, sans rotation, avec une métallicité solaire. Leurs évolutions ont été suivis jusqu'à la fin de la phase de combustion du carbone. Ce paragraphe va décrire les différences majeures générés par les nouveaux taux de réactions.

La Figure 4.5 montre l'évolution de la température centrale des deux modèles stellaires selon les taux de réactions. Les taux HinRes et CF88 présentent des températures similaires, tandis que le taux Hin a une température centrale plus élevée. Cela a pour conséquence direct la réduction par deux de la durée de la phase de combustion du carbone pour ce taux. Cette différence trouve son origine dans la valeur des taux de réactions : le taux de réaction Hin étant plus faible que les autres durant la combustion du carbone pour les modèle stellaires considérés, la température de l'étoile devra être plus élevée pour le qu'énergie nucléaire générée permette de contrebalancer l'effondrement gravitationnel. L'évolution des conditions centrales est montrée dans la Fig. 4.6. Il est possible de remarquer que la combustion du carbone se fait dans un milieu partiellement dégénéré pour le modèle stellaire de 12 $M_{\odot}$. Les diagrammes de Kippenhahn représentés Fig. 4.7 montrent l'impact de cet température plus haute sur la centre de la 25 $M_{\odot}$: dans le cas du taux Hin la zone convective est bien plus étendue, du à un gradient en température plus important.

Il est aussi possible de noter un impact sur l'effondrement du cœur et l anature du rémanent. En effet, la phase de combustion est la plus longue phase avec une émission de neutrinos importante, représenté sur la Fig. 4.10. La réduction de la durée de cette phase a donc un impact direct sur la quantité d'énergie emportée par les neutrinos.

L'étude de l'impact des nouveaux taux sur la nucléosynthèse a été réalisé à l'aide d'un "modèle à une couche", permettant le suivi d'un très grand nombre d'isotopes [56]. La distribution en abondance ainsi que les chemins évolutifs pris en entrée sont ceux correspondant au modèle stellaire de $25M_{\odot}$ avec le taux de réaction CF88 généré avec le GENEC dans l'étude précédente. Les taux utilisés sont ceux issus de ce travail pour les voies α et protons, et des taux récents pour la voie neutrons [65].

Les abondances obtenus à la fin de la phase de combustion sont représentés sur la Fig.4.12. Il est possible de noter des différences pour le sodium, l'aluminium ainsi que le phosphore, ainsi que des changement mineures pour les éléments les plus lourds. Ces légères variations vont avoir un impact modéré sur l'évolution stellaire mais un plus important sur la nucléosynthèse stellaire.

Cependant, il est possible de remarquer des différences de comportement entre les résultats donnés par le GENEC, où le taux HinRes est très proche de celui de CF88, tandis que le taux Hin est plus différent, alors que dans cette étude c'est le taux HinRes qui a les impacts les plus différents du taux CF88. Afin de comprendre cela deux paramètres ont été investigués : l'impact du rapport entre la voie α et la voie protons, ainsi que le choix du chemin évolutif.

La Figure 4.13 représente le rapport entre les voies α et protons. Si les taux Hin et CF88 ont un rapport constant, ce n'est pas le cas pour le taux HiNRes qui présente une augmentation de la contribution de la voie α par rapport à la voie protons dans l'intervalle en température correspondant à l'impact de la résonance. Cela est du à la différence de force de la résonance dans les deux voies de sortie. Cette différence de contribution peut avoir un impact sur l'abondance des éléments lourds.

Comme vu sur la Fig. 4.6 les taux de réactions conduisent à chemins évolutifs pour un même modèle stellaire initial. Les chemins générés par les taux HinRes et CF88 sont semblables alors que celui généré par le taux Hin est décalé. Ainsi, les conditions centrales des étoile seront différentes selon le taux considéré, menant à la synthèse d'élément différents et en proportions également différentes. Le choix du chemin évolutif semble donc un paramètre non négligeable.

Cette dernière hypothèse a été testé récemment [34], avec les mêmes modèle stellaires et les même taux, mais en associant à chaque taux le chemin évolutif correspondant. Les résultats, visible sur la Fig. 4.14, montre que l'impact sur le sodium, néon et magnésium n'est pas affecté, mais que celui sur les éléments lourds l'est. Cela pourrait être du à la différence en temps d'exposition aux neutrons : dans le cas d'une phase de combustion du carbone plus courte, les éléments se formant par capture neutronique verront leurs abondances être restreinte. L'impact du choix du chemin évolutif est donc montré.

Conclusion

Dans quelques décennies, nous ne serons plus, mais nos atomes existeront toujours, poursuivant ailleurs l'élaboration du monde.

Hubert Reeves, *Poussière d'étoiles*

This thesis focuses on the contribution of the $^{12}C + ^{12}C$ fusion reaction to stellar evolution and nucleosynthesis. To this end, the cross section of this fusion reaction at energies of astrophysical interest, *i.e.* at sub-barrier energies, $E_{\text{Coucomb}} = 6.6$ MeV in this system, was measured. A new stellar reaction rate was determined for this reaction, and its impact on stellar evolution and nucleosynthesis was studied. The ultimate aim was to determine new reaction rates relevant to stellar astrophysics, and thus increase our knowledge of the pivot C-burning phase.

This thesis took place within the STELLA collaboration, and the measurements at the STELLA station took place during the 2022 experimental campaign. This installation is based on the particle-γ coincidence detection method, in order to significantly reduce the contamination of the spectra by the various sources of background, dominant at the energies of astrophysical interest.

With this method, the experimental set-up is composed of two sets of detectors: particle detectors of the DSSSD type, to measure light evaporation residues (α and protons), and a set of $LaBr_3$(Ce) scintillators from the UK-FATIMA collaboration to detect the de-excitation γ. In order to support the high beam intensities required for this system, a system of rotating targets is being used.

The data analysis carried out in this work concerns the determination of the total fusion cross section at $E_{\text{com}} = 4.8$ MeV from the detection of light charged particles. The cross section obtained for the α_0 exit channel is in good agreement with previous results.

This analysis has also shown that the study of the cross section of the carbon fusion reaction requires good angular coverage to be relevant. Indeed, a reduced angular coverage does not allow to distinguish between different angular distributions, which strongly influence the extracted total cross section.

A second major part of this thesis was dedicated to the experimental data collected during the first acquisition campaign of the STELLA experiment in 2016 [27], in order to extract reaction rates that can be used in stellar evolution codes. To obtain these rates, it was first necessary to determine the excitation functions of the carbon fusion. Two scenarios were considered: the Hin model, following the fusion hindrance [17], and the HinRes model, involving the addition to this same model of a resonance located at $E_{com} = 2.14$ MeV [24]. The STELLA measurements are consistent with the fusion hindrance predictions, and although they also appear to be consistent with the resonance, the data collected are not sufficient to confirm its existence.

The reaction rates obtained for the Hin and HinRes models are lower than those obtained from CF88 model [21], except for the temperature interval between $T = 0.5 - 1.5$ GK, where the presence of the resonance slightly increases the rate of the HinRes model to the level of that obtained from CF88. The uncertainties of these rates are 15% for the Hin model and 31% for the HinRes model in the STELLA sensitivity range, $T = 0.6 - 4$ GK, in which the interpolation of the cross section measured by STELLA is the only input required to determine the reaction rate. This interval corresponds with the temperatures of the 12 and 25 $M_{\odot}$ stellar models studied in this work.

The impact of these rates has been studied using stellar evolution codes.

The results obtained with the Geneva stellar evolution code indicate slight changes in the combustion phase depending on the rates used. This is because stars are objects that maintain hydrostatic equilibrium during quiescent burning phases: the energy released per unit of time must reach a certain value, and to do this the star can either contract further, and so see its temperature rise, along with the energy released. And *vice-versa*, an excess of energy released will cause it to expand, and therefore to cool down... Changes in temperature can therefore have repercussions on the fine structures of the star, but only modest effects on the overall structure. However, the duration of the C-burning phase is halved with the Hin model, which could have an impact on the type of remnant.

The results obtained with the 'one-layer' code do not describe the overall evolution of the star, but detail the nucleosynthesis during the different phases. The changes between the different models are also modest here, even if a weakening of s-process could occur in the Hin model. However, the work carried out in this manuscript demonstrates the importance of the choice of evolution path for the star, but also the strong impact that the ratio between the α and the proton exit channel can have.

The study of the impact of these new reaction rates is continued by Dumont *et al.* [34], with the consideration of a larger grid of stellar models and also of stellar rotation. The mass limit of stars for carbon burning has also been studied, as by De Gerónimo *et al.* [43]: the new rates confirm the predicted values.

Experimental data from the 2019 STELLA campaign are currently being analysed (Nippert *et al.*, in prep), and should enable a reaction rate to be determined with greater precision, but also, thanks to the detailed study of a resonant structure at $E_{\mathrm{com}} = 3.2$ MeV, a better understanding of the impact of the ratio between the α and the proton exit channel.

The work carried out during the data analysis showed the need for sufficient angular coverage to study the $^{12}C + ^{12}C$ fusion reaction. The data provided by the new PIXEL detection system will complete the picture of this fusion reaction.

Finally, the collaboration is actively working on adapting the STELLA experiment to measure the cross sections of the $^{12}C + ^{16}O$ and $^{16}O + ^{16}O$ reactions through the CarbOx project. A future experimental campaign focusing on these reactions is planned for the coming months and years.

Bibliography

[1] *The periodic table from CHANDRA, NASA*, 2024. Https://chandra.harvard.edu/chemistry/. vii, 7

[2] C. Iliadis. Nuclear Physics of Stars. Wiley-VCH, 2 edition, 2015. ISBN 978-3-527-33648-7. vii, xi, xiii, 8, 9, 14, 15, 16, 17, 18, 19, 20, 21, 22, 23, 24, 41, 44, 57, 122, 123, 124, 126

[3] R. Hirschi, G. Meynet and A. Maeder. *Stellar evolution with rotation - XII. Pre-supernova models*. Astronomy&Astrophysics, **425**(2):649–670, 2004. doi:10.1051/0004-6361:20041095. vii, 9, 10, 44

[4] *Stellar evolution cycles from Wikipedia Commons*, 2024. Https://commons.wikimedia.org/wiki File:Star_life_cycles_red_dwarf_-en.svg. vii, 11, 44

[5] *Hertzsprung-Russell Diagram from ESO*, 2024. https://www.eso.org/public/france/images/eso0728c/. vii, 12

[6] G. Fruet. Structure des ions lourds et nucléosynthèse dans les étoiles massives : la réaction 12C + 12C. Thesis, University of Strasbourg, 2018. Thèse de doctorat dirigée par Courtin, Sandrine Physique Strasbourg 2018. viii, ix, x, xiii, 28, 41, 42, 61, 62, 64, 67, 68, 71, 73, 74, 76, 78, 79, 80, 100, 102, 103, 115, 122

[7] K. Ikeda, N. Takigawa and H. Horiuchi. *The Systematic Structure-Change into the Molecule-like Structures in the Self-Conjugate 4n Nuclei*. Progress of Theoretical Physics Supplement, **E68**:464–475, 1968. ISSN 0375-9687. doi:10.1143/PTPS.E68.464. arXiv:https://academic.oup.com/ptps/article-pdf/doi/10.1143/PTPS.E68.464/5216547/E68-464.pdf. viii, 29, 30

[8] J.-P. Ebran, E. Khan, T. Nikšić and D. Vretenar. *Density functional theory studies of cluster states in nuclei*. Physical Review C, **90**:054329, 2014. doi:10.1103/PhysRevC.90.054329. viii, 29, 30, 46

[9] H. Esbensen, X. Tang and C. L. Jiang. *Effects of mutual excitations in the fusion of carbon isotopes*. Physical Review C, **84**:064613, 2011. doi:10.1103/PhysRevC.84.064613. viii, 31

[10] C. L. Jiang et al. *Origin and Consequences of* $^{12}\mathbf{C} + ^{12}\mathbf{C}$ *Fusion Resonances at Deep Sub-barrier Energies.* Physical Review Letters, **110**:072701, 2013. doi:10.1103/PhysRevLett.110.072701. viii, 31, 32, 46, 55

[11] C. L. Jiang et al. *Influence of Nuclear Structure on Sub-Barrier Hindrance in* Ni + Ni *Fusion.* Physical Review Letters, **93**:012701, 2004. doi:10.1103/PhysRevLett.93.012701. viii, 33, 34, 46

[12] i. m. c. Mişicu and H. Esbensen. *Hindrance of Heavy-Ion Fusion due to Nuclear Incompressibility.* Physical Review Letters, **96**:112701, 2006. doi:10.1103/PhysRevLett.96.112701. viii, 33, 35, 46

[13] C. Simenel, A. S. Umar, K. Godbey, M. Dasgupta and D. J. Hinde. *How the Pauli exclusion principle affects fusion of atomic nuclei.* Physical Review C, **95**:031601, 2017. doi:10.1103/PhysRevC.95.031601. viii, 34, 36, 46

[14] K. Godbey, C. Simenel and A. S. Umar. *Absence of hindrance in a microscopic* $^{12}\mathrm{C} + ^{12}\mathrm{C}$ *fusion study.* Physical Review C, **100**:024619, 2019. doi:10.1103/PhysRevC.100.024619. viii, 35, 37, 46

[15] M. Pignatari et al. *The* $^{12}\mathrm{C}$ + $^{12}\mathrm{C}$ *Reaction and the Impact on Nucleosynthesis in Massive Stars.* The Astrophysical Journal, **762**(1):31, 2013. doi:10.1088/0004-637X/762/1/31. viii, 2, 6, 38, 40, 47, 119, 120, 125, 131, 140, 142, 145

[16] O. Straniero, L. Piersanti and S. Cristallo. *Do we really know Mup (i.e. the transition mass between Type Ia and core-collapse supernova progenitors)?* Journal of Physics: Conference Series, **665**(1):012008, 2016. doi:10.1088/1742-6596/665/1/012008. viii, 39, 41, 47

[17] C. L. Jiang, K. E. Rehm, B. B. Back and R. V. F. Janssens. *Expectations for* $^{12}\mathrm{C}$ *and* $^{16}\mathrm{O}$ *induced fusion cross sections at energies of astrophysical interest.* Physical Review C, **75**:015803, 2007. doi:10.1103/PhysRevC.75.015803. viii, ix, 36, 38, 41, 42, 46, 54, 60, 118, 119, 126, 145, 146, 150

[18] L. R. Gasques et al. *Implications of low-energy fusion hindrance on stellar burning and nucleosynthesis.* Physical Review C, **76**(3):035802, 2007. doi:10.1103/PhysRevC.76.035802. viii, 38, 42, 125, 146

[19] M. G. Mazarakis and W. E. Stephens. *Experimental Measurements of the* $^{12}\mathrm{C}$ + $^{12}\mathrm{C}$ *Nuclear Reactions at Low Energies.* Physical Review C, **7**:1280–1287, 1973. doi:10.1103/PhysRevC.7.1280. viii, 52, 55

[20] E. Almqvist, D. A. Bromley and J. A. Kuehner. *Resonances in* C^{12} *on Carbon Reactions.* Physical Review Letters, **4**:515–517, 1960. doi:10.1103/PhysRevLett.4.515. viii, 28, 46, 51, 53, 55, 118, 119

[21] G. R. Caughlan and W. A. Fowler. *Thermonuclear Reaction Rates V.* Atomic Data and Nuclear Data Tables, **40**:283, 1988. viii, ix, xi, 1, 25, 38, 45, 54, 60, 119, 121, 126, 131, 150

[22] H. W. Becker, K. U. Kettner, C. Rolfs and H. P. Trautvetter. *The 12C+12C reaction at subcoulomb energies (II)*. Zeitschrift für Physik A Atoms and Nuclei, **303**:305–312, 1981. ISSN 0939-7922. doi:10.1007/BF01421528. viii, ix, xi, xiii, 54, 55, 56, 57, 60, 65, 84, 103, 108, 109, 110, 111, 115

[23] E. F. Aguilera et al. *New γ-ray measurements for* ^{12}C+^{12}C *sub-Coulomb fusion: Toward data unification*. Physical Review C, **73**:064601, 2006. doi:10.1103/PhysRevC.73.064601. viii, ix, 54, 57, 60, 118, 119

[24] T. Spillane et al. ^{12}C + ^{12}C *Fusion Reactions near the Gamow Energy*. Physical Review Letters, **98**:122501, 2007. doi:10.1103/PhysRevLett.98.122501. viii, ix, 38, 54, 57, 58, 60, 119, 121, 126, 145, 150

[25] C. L. Jiang et al. *Reaction rate for carbon burning in massive stars*. Physical Review C, **97**:012801, 2018. doi:10.1103/PhysRevC.97.012801. ix, 6, 51, 59, 60, 85

[26] W. P. Tan et al. *New Measurement of* ^{12}C+^{12}C *Fusion Reaction at Astrophysical Energies*. Physical Review Letters, **124**:192702, 2020. doi:10.1103/PhysRevLett.124.192702. ix, 51, 60

[27] G. Fruet et al. *Advances in the Direct Study of Carbon Burning in Massive Stars*. Physical Review Letters, **124**:192701, 2020. doi:10.1103/PhysRevLett.124.192701. ix, xi, xiii, 2, 3, 38, 46, 51, 60, 72, 103, 108, 109, 110, 111, 118, 119, 120, 121, 128, 145, 150

[28] J. Nippert. Réactions de fusion par effet tunnel quantique et leurs impacts sur les étoiles massives avec STELLA. Thesis, University of Strasbourg, 2023. Thèse de doctorat dirigée par Courtin, Sandrine Physique Strasbourg 2023. ix, x, xi, 2, 38, 46, 51, 60, 69, 93, 95, 102, 103, 108, 109, 110, 111, 114, 115, 118

[29] M. Heine et al. *The STELLA apparatus for particle-Gamma coincidence fusion measurements with nanosecond timing*. Nuclear Instruments and Methods in Physics Research Section A: Accelerators, Spectrometers, Detectors and Associated Equipment, **903**:1–7, 2018. ISSN 0168-9002. doi:https://doi.org/10.1016/j.nima.2018.06.058. ix, 2, 51, 61, 63, 64, 75

[30] *Micron Semiconductor Ltd website*, 2024. https://www.micronsemiconductor.co.uk/. ix, 70

[31] *Photomultiplier scheme from Wikipedia*, 2024. Https://en.wikipedia.org/wiki/Photomultiplier_tube#/media/File:PhotoMultiplierTubeAndScintillator.svg. x, 80

[32] E. Monpribat et al. *A new 12C + 12C nuclear reaction rate: Impact on stellar evolution*. Astronomy&Astrophysics, **660**:A47, 2022. doi:10.1051/0004-6361/202141858. xi, xii, xiii, 118, 120, 121, 127, 129, 130, 132, 133, 135, 136, 137, 138, 140, 142

[33] E. Monpribat et al. *A new 12C+12C reaction rate: Impact on stellar evolution.* EPJ Web of Conferences, **279**:11016, 2023. doi:10.1051/epjconf/202327911016. xii, 118, 141, 143

[34] T. Dumont et al. *Massive stars evolution with new C12+C12 nuclear reaction rate – the core carbon-burning phase.* 2024. arXiv:2404.18662. xii, 139, 142, 144, 147, 150

[35] C. Iliadis, A. Champagne, A. Chieffi and M. Limongi. *The Effects of Thermonuclear Reaction Rate Variations on ^{26}Al Production in Massive Stars: A Sensitivity Study.* The Astrophysical Journal, **193**(1):16, 2011. doi:10.1088/0067-0049/193/1/16. arXiv:1101.5553. xiii, 13, 14, 141

[36] H. Reeves. Poussières d'étoiles. Le Seuil, 1984. 1

[37] E. M. Burbidge, G. R. Burbidge, W. A. Fowler and F. Hoyle. *Synthesis of the Elements in Stars.* Reviews of Modern Physics, **29**:547–650, 1957. doi:10.1103/RevModPhys.29.547. 1, 6, 7, 43

[38] A. G. W. Cameron. *NUCLEAR REACTIONS IN STARS AND NUCLEOGENESIS.* Publications of the Astronomical Society of the Pacific, **69**(408):201–222, 1957. ISSN 00046280, 15383873. 1, 6, 43

[39] C. Angulo et al. *A compilation of charged-particle induced thermonuclear reaction rates.* Nuclear Physics A, **656**(1):3–183, 1999. ISSN 0375-9474. doi:https://doi.org/10.1016/S0375-9474(99)00030-5. 1

[40] Y. Xu et al. *NACRE II: an update of the NACRE compilation of charged-particle-induced thermonuclear reaction rates for nuclei with mass number A<16.* Nuclear Physics A, **918**:61–169, 2013. ISSN 0375-9474. doi:https://doi.org/10.1016/j.nuclphysa.2013.09.007. 1

[41] Siess, L. *Evolution of massive AGB stars - I. Carbon burning phase.* Astronomy&Astrophysics, **448**(2):717–729, 2006. doi:10.1051/0004-6361:20053043. 2

[42] M.E. Bennett *et al. The effect of 12C +12C rate uncertainties on the evolution and nucleosynthesis of massive stars.* Monthly Notices of the Royal Astronomical Society, **420**(4):3047–3070, 2012. ISSN 0035-8711. doi:10.1111/j.1365-2966.2012.20193.x. 2, 20, 142

[43] De Gerónimo, Francisco C., Miller Bertolami, Marcelo M., Plaza, Francisco and Catelan, Márcio. *The composition of massive white dwarfs and their dependence on C-burning modeling.* Astronomy&Astrophysics, **659**:A150, 2022. doi:10.1051/0004-6361/202142341. 2, 150

[44] C. Raiteri, M. Busso, R. Gallino and G. Picchio. *S-process nucleosynthesis in massive stars and the weak component. II-Carbon burning and galactic enrichment.* The Astrophysical Journal, **371**:665–672, 1991. 2

[45] C. Raiteri, R. Gallino, M. Busso, D. Neuberger and F. Käppeler. *The weak s-component and nucleosynthesis in massive stars.* The Astrophysical Journal, **419**:207, 1993. 2

[46] L.-S. The, M. F. E. Eid and B. S. Meyer. *s-Process Nucleosynthesis in Advanced Burning Phases of Massive Stars.* The Astrophysical Journal, **655**(2):1058, 2007. doi:10.1086/509753. 2

[47] H. Saio and K. Nomoto. *Off-Center Carbon Ignition in Rapidly Rotating, Accreting Carbon-Oxygen White Dwarfs.* The Astrophysical Journal, **615**(1):444, 2004. doi:10.1086/423976. 2

[48] C. N. Augustine, D. E. Willcox, J. Brooks, D. M. Townsley and A. C. Calder. *SN Ia Explosions from Hybrid Carbon–Oxygen–Neon White Dwarf Progenitors that Have Mixed during Cooling.* The Astrophysical Journal, **887**(2):188, 2019. doi:10.3847/1538-4357/ab511a. 2

[49] C. Wu, B. Wang and D. Liu. *The outcomes of carbon–oxygen white dwarfs accreting CO-rich material.* Monthly Notices of the Royal Astronomical Society, **483**(1):263–275, 2018. ISSN 0035-8711. doi:10.1093/mnras/sty3176. arXiv:https://academic.oup.com/mnras/article-pdf/483/1/263/26996713/sty3176.pdf. 2

[50] S. E. Woosley, A. Heger and T. A. Weaver. *The evolution and explosion of massive stars.* Review of Modern Physics, **74**:1015–1071, 2002. doi:10.1103/RevModPhys.74.1015. 2

[51] T. E. Strohmayer and E. F. Brown. *A Remarkable 3 Hour Thermonuclear Burst from 4U 1820–30.* The Astrophysical Journal, **566**:1045, 2002. doi:https://doi.org/10.1086/338337. 2

[52] R. L. Cooper, A. W. Steiner and E. F. Brown. *POSSIBLE RESONANCES IN THE 12C + 12C FUSION RATE AND SUPERBURST IGNITION.* The Astrophysical Journal, **702**(1):660, 2009. doi:10.1088/0004-637X/702/1/660. 2, 41, 42

[53] C. Rolfs and W. Rodney. Cauldrons in the Cosmos. The University of Chigaco Press, 1988. ISBN 0-226-72456-5. 2, 6, 20, 22, 23, 24, 39, 41, 43, 122, 125

[54] B. B. Back, H. Esbensen, C. L. Jiang and K. E. Rehm. *Recent developments in heavy-ion fusion reactions.* Review of Modern Physics, **86**:317–360, 2014. doi:10.1103/RevModPhys.86.317. 2

[55] P. Eggenberger et al. *The Geneva stellar evolution code.* Astrophysics and Space Science, **316**:43–54, 2008. doi:10.1007/s10509-007-9511-y. 3, 130, 146

[56] A. Choplin, A. Maeder, G. Meynet and C. Chiappini. *Constraints on CEMP-no progenitors from nuclear astrophysics.* Astronomy&Astrophysics, **593**:A36, 2016. doi:10.1051/0004-6361/201628083. arXiv:1606.02752. 3, 118, 139, 147

[57] A. G. W. Cameron. *On the origin of the heavy elements.* The Astrophysical Journal, **62**:9–10, 1957. doi:10.1086/107435. 6, 43

[58] S. R. Kulkarni. *Modeling Supernova-like Explosions Associated with Gamma-ray Bursts with Short Durations*. 2005. arXiv:astro-ph/0510256. 7, 24

[59] B. D. Metzger et al. *Electromagnetic counterparts of compact object mergers powered by the radioactive decay of r-process nuclei*. Monthly Notices of the Royal Astronomical Society, **406**(4):2650–2662, 2010. ISSN 0035-8711. doi:10.1111/j.1365-2966.2010.16864.x. arXiv:https://academic.oup.com/mnras/article-pdf/406/4/2650/3356185/mnras0406-2650.pdf. 7, 24

[60] M. Asplund, N. Grevesse, A. J. Sauval and P. Scott. *The Chemical Composition of the Sun*. Annual Review of Astronomy and Astrophysics, **47**(Volume 47, 2009):481–522, 2009. ISSN 1545-4282. doi:https://doi.org/10.1146/annurev.astro.46.060407.145222. 8, 131

[61] M. Limongi, O. Straniero and A. Chieffi. *Massive Stars in the Range 13-25 M: Evolution and Nucleosynthesis. II. The Solar Metallicity Models*. The Astrophysical Journal Supplement Series, **129**(2):625, 2000. doi:10.1086/313424. 8

[62] A. Maeder. Physics, Formation and Evolution of Rotating Stars. Astronomy and Astrophysics Library. Springer Berlin, Heidelberg, 1 edition, 2009. 11

[63] D. N. F. Dunbar, R. E. Pixley, W. A. Wenzel and W. Whaling. *The 7.68-Mev State in* C^{12}. Physical Review Journal Archive, **92**:649–650, 1953. doi:10.1103/PhysRev.92.649. 15, 29

[64] C. W. Cook, W. A. Fowler, C. C. Lauritsen and T. Lauritsen. B^{12}*,* C^{12}*, and the Red Giants*. Physical Review Journal Archive, **107**:508–515, 1957. doi:10.1103/PhysRev.107.508. 15, 29

[65] B. Bucher et al. *First Direct Measurement of* $^{12}C(^{12}C, n)^{23}Mg$ *at Stellar Energies*. Physical Review Letters, **114**:251102, 2015. doi:10.1103/PhysRevLett.114.251102. 18, 52, 84, 140, 147

[66] C. Ouellet and B. Singh. *Nuclear Data Sheets for* $A = 32$. Nuclear Data Sheets, **112**(9):2199–2355, 2011. ISSN 0090-3752. doi:https://doi.org/10.1016/j.nds.2011.08.004. 23

[67] F. Hoyle. *On Nuclear Reactions Occuring in Very Hot STARS.I. the Synthesis of Elements from Carbon to Nickel.* The Astrophysical Journal, Supplement, **1**:121, 1954. doi:10.1086/190005. 28

[68] M. Chernykh, H. Feldmeier, T. Neff, P. von Neumann-Cosel and A. Richter. *Structure of the Hoyle State in* ^{12}C. Physical Review Letters, **98**:032501, 2007. doi:10.1103/PhysRevLett.98.032501. 29

[69] P. Adsley et al. *Extending the Hoyle-State Paradigm to* ^{12}C+^{12}C *Fusion*. Physical Review Letters, **129**:102701, 2022. doi:10.1103/PhysRevLett.129.102701. 29

[70] E. Vogt and H. McManus. *"Molecular" States Formed by Two Carbon Nuclei*. Physical Review Letters, **4**:518–520, 1960. doi:10.1103/PhysRevLett.4.518. 29

[71] C. L. Jiang et al. *Unexpected Behavior of Heavy-Ion Fusion Cross Sections at Extreme Sub-Barrier Energies*. Physical Review Letters, **89**:052701, 2002. doi:10.1103/PhysRevLett.89.052701. 33, 46

[72] C. Y. Wong. *Interaction Barrier in Charged-Particle Nuclear Reactions*. Physycal Review Letters, **31**:766–769, 1973. doi:10.1103/PhysRevLett.31.766. 33

[73] C. L. Jiang et al. *Heavy-ion fusion reactions at extreme sub-barrier energies*. The European Physical Journal A, 2021. 33

[74] R. Perez-Torres, T. L. Belyaeva and E. F. Aguilera. *Fusion and elastic-scattering cross-section analysis of the 12C + 12C system at low energies*. Physics of Atomic Nuclei, 2006. 38, 120

[75] Bravo, E. et al. *Type Ia supernovae and the 12C+12C reaction rate*. Astronomy&Astrophysics, **535**:A114, 2011. doi:10.1051/0004-6361/201117814. 41

[76] C. Jiang et al. *Measurements of fusion cross-sections in 12C+12C at low beam energies using a particle- coincidence technique*. Nuclear Instruments and Methods in Physics Research Section A: Accelerators, Spectrometers, Detectors and Associated Equipment, **682**:12–15, 2012. ISSN 0168-9002. doi:https://doi.org/10.1016/j.nima.2012.03.051. 51

[77] J. M. Blatt and L. C. Biedenharn. *The Angular Distribution of Scattering and Reaction Cross Sections*. Review Modern of Physics, **24**:258–272, 1952. doi:10.1103/RevModPhys.24.258. 56, 105

[78] M. High and B. Čujec. *The 12C + 12C sub-coulomb fusion cross section*. Nuclear Physics A, **282**(1):181–188, 1977. ISSN 0375-9474. doi:https://doi.org/10.1016/0375-9474(77)90179-8. 57

[79] K. U. Kettner, H. Lorenz-Wirzba, C. Rolfs and H. Winkler. *Study of the Fusion Reaction* ^{12}C + ^{12}C *below the Coulomb Barrier*. Physical Review Letters, **38**:337–340, 1977. doi:10.1103/PhysRevLett.38.337. 57

[80] L. Barrón-Palos et al. *Absolute cross sections measurement for the 12C + 12C system at astrophysically relevant energies*. Nuclear Physics A, **779**:318–332, 2006. ISSN 0375-9474. doi:https://doi.org/10.1016/j.nuclphysa.2006.09.004. 57

[81] *UHV Design Ltd website*, 2024. Https://www.uhvdesign.com/. 65

[82] F. Dalidchik and Y. Sayasov. *Theory of Coulomb excitation in the collision of identical nuclei*. Nuclear Physics, **58**:145–157, 1964. ISSN 0029-5582. doi:https://doi.org/10.1016/0029-5582(64)90528-0. 70

[83] O. J. Roberts et al. *A LaBr3: Ce fast-timing array for DESPEC at FAIR*. Nuclear Instruments and Methods in Physics Research Section A: Accelerators, Spectrometers, Detectors and Associated Equipment, **748**:91–95, 2014. ISSN 0168-9002. doi:https://doi.org/10.1016/j.nima.2014.02.037. 72

[84] P. Regan. *Precision measurement of sub-nanosecond lifetimes of excited nuclear states using fast-timing coincidences with LaBr3(Ce) detectors*. Radiation Physics and Chemistry, **116**:38–42, 2015. ISSN 0969-806X. doi:https://doi.org/10.1016/j.radphyschem.2015.01.029, proceedings of the 9th International Topical Meeting on Industrial Radiation and Radioisotope Measurement Applications. 73

[85] J. Chen. *Nuclear Data Sheets for A=138*. Nuclear Data Sheets, **146**:1–386, 2017. ISSN 0090-3752. doi:https://doi.org/10.1016/j.nds.2017.11.001. 73

[86] B. Milbrath et al. *Characterization of alpha contamination in lanthanum trichloride scintillators using coincidence measurements*. Nuclear Instruments and Methods in Physics Research Section A: Accelerators, Spectrometers, Detectors and Associated Equipment, **547**(2):504–510, 2005. ISSN 0168-9002. doi:https://doi.org/10.1016/j.nima.2004.11.054. 73

[87] S. Agostinelli et al. *Geant4—a simulation toolkit*. Nuclear Instruments and Methods in Physics Research Section A: Accelerators, Spectrometers, Detectors and Associated Equipment, **506**(3):250–303, 2003. ISSN 0168-9002. doi:https://doi.org/10.1016/S0168-9002(03)01368-8. 73

[88] V. T. Jordanov and G. F. Knoll. *Digital synthesis of pulse shapes in real time for high resolution radiation spectroscopy*. Nuclear Instruments and Methods in Physics Research Section A: Accelerators, Spectrometers, Detectors and Associated Equipment, **345**(2):337–345, 1994. ISSN 0168-9002. doi:https://doi.org/10.1016/0168-9002(94)91011-1. 78

[89] M. J. Eller et al. *Andromede project: Surface analysis and modification with probes from hydrogen to nano-particles in the MeV energy range*. Nuclear Instruments and Methods in Physics Research Section B: Beam Interactions with Materials and Atoms, **365**:367–370, 2015. ISSN 0168-583X. doi:https://doi.org/10.1016/j.nimb.2015.07.090, proceedings of the 19th International Conference on Ion Beam Modification of Materials (IBMM 2014). 82

[90] *National Institute of Standard and Technologies - Physical Measurement Laboratory - USA*, 2024. Https://www.nist.gov/pml/stopping-power-range-tables-electrons-protons-and-helium-ions. 92

[91] R. Bass. Nuclear Reactions with Heavy Ions. Springer-Verlag Berlin, Heidelberg, 1 edition, 1980. 98

[92] *Ortec Digital Current Integrator*, 2024. Https://www.ortec-online.com/products/electronic-instruments/digital-current-integrator/439. 100

[93] K. Shima, N. Kuno, M. Yamanouchi and H. Tawara. *Equilibrium charge fractions of ions of Z = 4–92 emerging from a carbon foil.* Atomic Data and Nuclear Data Tables, **51**(2):173–241, 1992. ISSN 0092-640X. doi:https://doi.org/10.1016/0092-640X(92)90001-X. 101

[94] S. Ekström et al. *Grids of stellar models with rotation. I. Models from 0.8 to 120 M at solar metallicity (Z = 0.014).* Astronomy&Astrophysics, **537**:A146, 2012. doi:10.1051/0004-6361/201117751. arXiv:1110.5049. 118, 130, 131, 146

[95] A. Tumino et al. *An increase in the 12C + 12C fusion rate from resonances at astrophysical energies.* Nature, **557**:687–690, 2018. ISSN 1476-4687. doi:10.1038/s41586-018-0149-4. 120

[96] F. K. Thielemann, M. Arnould and J. W. Truran. *Thermonuclear reaction rates from statistical model calculations.* In E. Vangioni-Flam, J. Audouze, M. Casse, J.-P. Chieze and J. Tran Thanh Van, editors, Advances in Nuclear Astrophysics, pages 525–540. 1986. 128

[97] R. Kippenhahn, A. Weigert and E. Hofmeister. Methods in Computational Physics, **7**, 1967. 130

[98] M. Gabriel, A. Noels, J. Montalbán and A. Miglio. *Proper use of Schwarzschild Ledoux criteria in stellar evolution computations.* Astronomy&Astrophysics, **569**:A63, 2014. doi:10.1051/0004-6361/201423442. arXiv:1405.0128. 134

[99] E. A. Kaiser et al. *Relative importance of convective uncertainties in massive stars.* Monthly Notices of the RAS, **496**(2):1967–1989, 2020. doi:10.1093/mnras/staa1595. arXiv:2006.01877. 134

[100] A. Maeder. *Stellar yields as a function of initial metallicity and mass limit for black hole formation.* Astronomy&Astrophysics, **264**(1):105–120, 1992. 136

[101] A. Chieffi et al. *The impact of the new measurement of the* $^{12}\mathrm{C} +^{12}\mathrm{C}$ *fusion cross section on the final compactness of the massive stars.* arXiv e-prints, arXiv:2106.00013, 2021. arXiv:2106.00013. 136

[102] W. D. Arnett. *Advanced Evolution of Massive Stars. II. Carbon Burning.* The Astrophysical Journal, **176**:699, 1972. doi:10.1086/151672. 137

[103] S. E. Woosley. *Nucleosynthesis and Stellar Evolution.* In J. Audouze, C. Chiosi and S. E. Woosley, editors, Saas-Fee Advanced Course 16: Nucleosynthesis and Chemical Evolution, page 1. 1986. 137

[104] W. D. Arnett. *Advanced evolution of massive stars. V. Neon burning.* The Astrophysical Journal, **193**:169–176, 1974. doi:10.1086/153143. 141

[105] D. P. Whitmire and C. N. Davids. *Reaction* $^{23}Na(\alpha,p)^{26}Mg$ *from* E_α=2.3-3.7 *MeV and the corresponding thermonuclear reaction rate.* Physical Review C, **9**(3):996–1001, 1974. doi:10.1103/PhysRevC.9.996. 141

[106] R. Hirschi. Massive rotating stars : the road to supernova explosion. Thesis, Université de Genève, 2004. Thèse de doctorat : Univ. Genève, 2004, no. Sc. 3550. 141

Université de Strasbourg

Emma MONPRIBAT

École doctorale
Physique, chimie-physique
ED 182
Université de Strasbourg

Contribution of the subcoulomb fusion reaction to the stellar evolution and nucleosynthesis

Résumé

La physique nucléaire joue un rôle primordiale dans l'évolution stellaire, et donc de l'évolution de l'Univers, au travers de la nucléosynthèse. Elle est essentielle via la détermination de grandeurs essentielles tel que le taux de réaction nucléaire stellaire. De plus, des comportements des fonctions d'excitations, telles que les résonances ou le phénomène de suppression de la fusion, ont été récemment montrés comme ayant un impact sur l'évolution stellaire. Parmi les réactions ayant lieu dans les étoiles, la réaction de fusion 12C + 12C revêt un intérêt particulier, de par son rôle clé dans l'évolution stellaire. Cependant, l'étude de ce système en laboratoire est difficile, du fait d'une section efficace faible aux énergies d'intérêt astrophysique. Pour surmonter cela, la collaboration STELLA a mis en place une expérience permettant la mesure en coïncidence des particules produites lors des évènements de fusion jusque dans la fenêtre de Gamow des étoiles massives. Les données issues de la campagne expérimentale de 2022 de STELLA ont ainsi été analysées. Les sections efficaces issues de la campagne expérimentale de 2016 ont été utilisées pour déterminer des nouveaux taux de réactions stellaires, sans extrapolations des sections efficaces. L'impact de ces taux a été étudié avec deux codes d'évolution stellaire, restant modeste dans l'évolution globale d'une étoile, mais pouvant être plus important pour la nucléosynthèse stellaire.

Mots-clés : taux de réaction, fusion 12C+12C, section efficace, STELLA, résonance, suppression de la fusion, fenêtre de Gamow, nucléosynthèse, évolution stellaire, étoile massive, abondances

Abstract

Nuclear physics plays a fundamental part in the evolution of stars, and therefore in the evolution of the Universe, through nucleosynthesis. It is essential for determining essential quantities such as the stellar nuclear reaction rate. In addition, the behaviour of excitation functions, such as resonances or fusion hindrance, has recently been shown to have an impact on stellar evolution. Among the reactions that take place in stars, the 12C + 12C fusion reaction is of particular interest because of its key role in stellar evolution. However, it is difficult to study this system in the laboratory, due to its low effective cross-section at energies of astrophysical interest. To overcome this, the STELLA collaboration has set up an experiment enabling coincidence measurements of the particles produced during fusion events right up to the Gamow window of massive stars. The data from STELLA's 2022 experimental campaign have been analysed in this way. The cross sections from the 2016 experimental campaign were used to determine new stellar reaction rates, without extrapolating the cross sections. The impact of these rates was studied with two stellar evolution codes, remaining modest in the overall evolution of a star, but potentially more important for stellar nucleosynthesis.

Keywords : reaction rates, 12C+12C fusion, cross section, STELLA, resonance, fusion hindrance, Gamow window, nucleosynthesis, stellar evolution, massive stars, abundance